学位論文

X-ray Studies of the Central Engine in Active Galactic Nuclei with *Suzaku*

(X 線衛星「すざく」による活動銀河核
セントラルエンジンの研究)

平成 25 年 5 月　博士(理学)　申請

東京大学大学院理学系研究科
天文学専攻

野田　博文

Abstract

In the central engine of an active galactic nucleus (AGN), an accretion disk is formed around the central super massive black hole, and inner regions of the disk are considered to be covered by a hot electron clouds, often called corona. Primary X-ray emission from an AGN is generated when blackbody photons from the accretion disk are inverse-Compton scattered by the coronal electrons, while secondary X-ray emission is produced via Compton down-scattering and photo-absorption of the primary X-rays by materials surrounding the central black hole. The *ASCA* discovery of an (apparently) relativistically-broadened iron line feature, from the type I Seyfert galaxy MCG–6-30-15, greatly accelerated studies of the secondary X-ray components. However, in these studies, the primary X-ray continuum has always been approximated as a single power-law component (with a high-energy cutoff), and all spectral features deviating from the assumed continuum have been interpreted as secondary components. This assumption, clearly too simplified considering the strong spatial gradient in the gravitational field around a black hole, has apparently hampered our correct knowledge of the central engine. In addition, it has potentially caused incorrect understanding of the secondary emission, because it is not trivial to separate the primary and secondary components.

The main objective of the present thesis is to determine the spectral shape of the primary X-ray emission from disk-dominated AGNs, as model-independently as possible. For this purpose, we developed a novel variability-assisted spectral analysis technique (to be called C3PO method), which allows us to decompose a time-averaged X-ray spectrum of an AGN, accumulated over a certain period (typically a few days), into a variable and a stationary components. Since these studies of the primary X-ray continua require a wide-band coverage, we utilized the *Suzaku* archive, wherein many AGNs were detected with high statistics in a broad energy band typically from ~ 0.5 keV to ~ 50 keV.

We first applied the C3PO method to soft X-ray energies (< 3 keV) of several types of AGNs; Mrk 509, Fairall 9, MCG-2-58-22 (type I Seyfert galaxies), 3C382 (broad line radio galaxy), 4C+74.26 (radio-loud quasar), and MR2251-178 (radio-quiet quasar). In all of them, the C3PO-derived variable (and dominant) component had a power-law shape with a photon index $\Gamma \sim 1.8$. The C3PO-derived stationary component exhibited a much softer spectrum equivalent to $\Gamma \sim 4$, and was confirmed to be essentially the same as the previously known "soft excess" component. On time scales of several weeks, however, this component exhibited slow variations (at least in Mrk 509), independently of the dominant variable $\Gamma \sim 1.8$ emission. Therefore, the soft component is considered to be an additional primary emission, rather than a secondary component or contamination from the host galaxy. Interpreting the soft excess as thermal Comptonization emission, an electron temperature of ~ 0.5 keV and an optical depth of ~ 15 were obtained. Thus, the soft excess phenomenon is likely to be produced in a relatively cool and dense corona, which is clearly different from those producing the dominant power-law (with an electron temperature of $\gtrsim 100$ keV and an optical depth of $\lesssim 1$).

In the same manner as above, we next examined harder X-ray energies (3–45 keV) of several type I Seyfert galaxies, including NGC 3516 (2 data sets), NGC 3227 (6 data sets), NGC 4051 (3 data sets), MCG–6-30-15 (four data sets), Mrk 841 (4 data sets), NGC 5548 (7 data sets), and IC4329A (5 data sets). In all these AGNs, the C3PO-extracted variable component again had a weakly absorbed power-law shape with Γ =1.7–2.2. The C3PO-derived stationary components exhibited intense narrow Fe-K lines, with various continuum shapes. In some cases, it was well explained solely as reflection signals from a distant/neutral accretion disk or a torus, while in other cases it also included an additional featureless harder (Γ =1.4–1.7) continuum with strong absorption ($N_{\rm H} \sim 10^{23}$ cm^{-2}). The latter sometimes bears the Fe-K edge feature, but is not accompanied by Fe-K emission lines. In NGC 3516, this additional harder emission was observed on one occasion, and disappeared in the other observation when the source became fainter. In NGC 3227, inversely, the harder component was always present with slow intensity changes, while the rapidly variable steeper powerlaw disappeared when the source became fainter. Since the two featureless continua, namely the rapidly variable steeper one and the slowly varying harder/absorbed one, vary without correlation, we regard both of them as the primary emissions from the central engine.

Thus applying the novel C3PO method to the *Suzaku* data, we have revealed that the X-ray emission from AGNs consists of multiple primary components, with different spectral hardness, different absorption, and different variability characteristics. We can identify at least four of them; (1) the previously known, rapidly varying, power-law shaped continuum with rather low absorption; (2) the soft excess component, of which the presence itself was long known but was not necessarily recognized previously as a primary component; (3) the newly identified hard component with strong absorption and slow variation, and (4) the neutral and distant reflection component generated at an outer region of an accretion disk or a torus. In the present thesis, we call (1)–(3) the Broad-Band, Soft, and Hard Primary components, respectively. These results imply that the central engine consists of several distinct regions where physical parameters are different and independent. This makes a contrast to the so-far popular assumption, and urges significant revision to the current consensus on the X-ray emission from AGNs. The actual geometry and configuration of these multiple emission zones are yet to be clarified.

Contents

List of Figures

List of Tables

Chapter 1

INTRODUCTION

Almost every galaxy in the universe is considered to host, at its center, a super massive black hole (SMBH) with a mass of $\sim 10^{4-10}$ $M_{\odot}$ ($M_{\odot}$ being the solar mass), and when gas is accretes onto it, its vicinity is expected to shine as an active galactic nucleus (AGN), with a luminosity reaching 10^{39-47} erg s^{-1}. Around the SMBH of an AGN, the accreting gas is considered to form a gaseous accretion disk, where gravitational energy of the gas is efficiently converted to radiation. This mechanism is considered to be the origin of all the emission from an AGN, and is called the central engine.

Direct emission from the central engine appears in the X-ray energies, because the gas is heated by viscosity to attain high temperatures. Thus, X-rays are expected to provide valuable information about extreme conditions near the BH, and to be the most useful wavelength to study the central engine of AGNs. Such X-ray emission from AGNs has been studied with more than 20 X-ray satellites launched so far, including the 5 Japanese ones, *Hakucho*, *Temma*, *Ginga*, *ASCA*, and *Suzaku*, which were launched from 1979 to 2005. Japanese contributions to the X-ray study of AGNs with these satellites have been quite large.

When the primary X-rays from the central engine interact with surrounding materials, the spectrum is expected to be modified significantly, due to photoelectric and resonant absorption, Compton scattering, and the emission of fluorescent photons. Since Tanaka et al. (1995) detected a structure like a relativistically-blurred Fe-Kα emission line in an X-ray spectrum from the type I AGN MCG–6-30-15 with *ASCA*, the AGN X-ray emission has been attracting much attention as a probe to verify the general relativity. As a result, a large number of observational and theoretical studies have been done on this topic. In addition, various absorption features by mildly photo-ionized materials (often called "warm absorbers") and outflows have been observed in X-ray spectra of AGNs, and hence the geometry and physical conditions of such absorbers have been another popular research subject with instruments having high energy resolution.

In contrast to the rapid progress in the studies of the "secondary components" which are generated via reprocessing of materials around a central SMBH, much less effort has been performed to understand "primary emission", which is directly emitted form the AGN central engine. Consequently, the primary spectrum of an AGN has always been assumed to be a single power-law like continuum, and

any deviation from this simplified assumption has been attributed to the secondary processes. This was motivated, at least partially, by the intrinsic difficulty of separating the primary and the secondary emission components.

In the present thesis, we focus on the primary emission from type I AGNs, and utilize the fact that different (e.g., primary and secondary) components are likely to exhibit different time variability characteristics. By combining the superior broad energy coverage of *Suzaku* and a novel timing analysis method we developed, we apply a comprehensive "variability-assisted spectroscopy" to the data of a dozen AGNs. We thus aim to decompose, in a model-independent manner, their overall X-ray emission into different components. This kind of data-oriented approach has been quite rare in the past.

Chapter 2

REVIEW

2.1 Active Galactic Nuclei

A few persent of total galaxies in the universe have a strong radiation source at their central region, with its luminosity of 10^{41-48} erg s^{-1}. They are called Active Galactic Nuclei (AGNs). Surprisingly, the AGN luminosity is comparable to, or sometimes higher than the sum of those of the remaining regions of the galaxy. From their discovery, AGNs have deeply attracted many astronomers, and have become one of the hottest and most important topics in astronomical fields.

2.1.1 Discovery

Seyfert galaxies and quasars, which are today regarded as representatives of AGNs, were first discovered in different ways. In 1943, C. Seyfert reported a group of galaxies including NGC 1068, NGC 3516, and NGC 4151, which commonly have a central region within ~ 100 pc emitting strong highly-ionized emission lines. They have broad line widths, which translate to a gas cloud velocity of more than a thousand km s^{-1}. This velocity is much higher than that of a galactic rotation, which is at most ~ 500 km s^{-1}. This implied the presence of something anomalous in their central regions, and later it was recognized as an AGN phenomenon.

Quasars were first discovered, in the late 1950's, as strong radio sources without obvious optical counterpart. Helped by lunar-occultation experiments, a few of them were identified, in the early 1960', with star-like objects with strange broad emission lines. They hence became to be called "quasi-stellar objects" (QSOs), and then quasars. In 1963, M.Schmidt hit upon an idea that the unidentified strong emission lines seen in one such object, 3C273, can be identified with Hydrogen Balmer series, if an amazing high redshift (for a common sense at that time) of 0.158 is assumed. After a lengthy debate (e.g., Field, Arp & Bahcall 1974) it became a consensus that quasars are objects at cosmological distances, and their high redshifts are a direct consequence of the expansion of the universe. This means that its luminosity is $\sim 10^8$ times higher than the Solar value, and ~ 10 times higher than a sum of luminosities of all stars included in a galaxy. After that, similar sources were found one after another, and they faint galaxy images later became detectable around some of them. Therefore, quasars were confirmed to reside in galaxies, and became recognized as AGNs.

Table 2.1: Classification of AGNs, except Blazars.

Luminosity	Radio-loud sources	Radio-quiet sources
$\gtrsim 10^{45}$ erg s^{-1}	Radio-loud quasars	Radio-quiet quasars
$\sim 10^{43}$–10^{45} erg s^{-1}	Radio galaxies	Seyfert galaxies
$\lesssim 10^{43}$		LINERs

2.1.2 Classification

AGNs may be classified with respect to several characteristics. Tow major ones are the luminosity and the radio loudness. Broadness of their optical emission lines may be employed as a third attribute. In Table 2.1, we summarized a typical AGN classification, and explain individual types, bellow.

Seyfert galaxies

Seyfert galaxies are AGNs with comparatively low luminosities of 10^{41-44} erg s^{-1}. As a definition, their B-band absolute magnitudes should be larger than $-21.5 + 5 \log h_0$, where h_0 is the Hubble constant in units of 100 km s^{-1} Mpc^{-1} (Schmidt & Green 1983). They emit time-variable continua which become particularly strong in the ultra-violet band. Their host galaxies can be easily seen, and most of them are spiral galaxies. Their optical spectra show high-excitation ionized emission lines, which allows further classification into two sub classes, type I and type II, in reference to velocity widths of the emission lines (Khachikian & Weedman 1974). As shown in Fig. 2.1 (a), a type I sources show both broad and narrow emission lines with velocity widths of $\sim 10^4$ km s^{-1} and $\sim 10^2$ km s^{-1}, respectively. On the other hand, a type II sources show only narrow emission lines (Fig. 2.1 b). Sometimes finer sub classes are defined between type I and II, like e.g., type 1.5, 1.8 and 1.9 (Osterbrock 1981).

Radio galaxies

Radio galaxies are AGNs with relatively large radio robes. Their luminosities are $\sim 10^{43-45}$ erg s^{-1}, and almost all of their host galaxies are elliptical. The large robes are considered to be generated when jets from the nucleus collide with surrounding dense gases. The lobes are filled with relativistic electrons, which makes the lobes luminous synchrotron radio sources. This radio loudness provides a major difference between Seyferts and radio galaxies. The robes often appear point-symmetrically, and their sizes sometimes reach ∼Mpc which largely exceeds that of its host galaxy, ~ 10 kpc. Similar to Seyferts, radio galaxies can be divided into two sub classes, type I and type II as shown in Fig. 2.1 (c, d). Type I radio galaxies are called Broad-Line Radio Galaxies (BLRGs), while type II sources Narrow-Line Radio Galaxies (NLRGs).

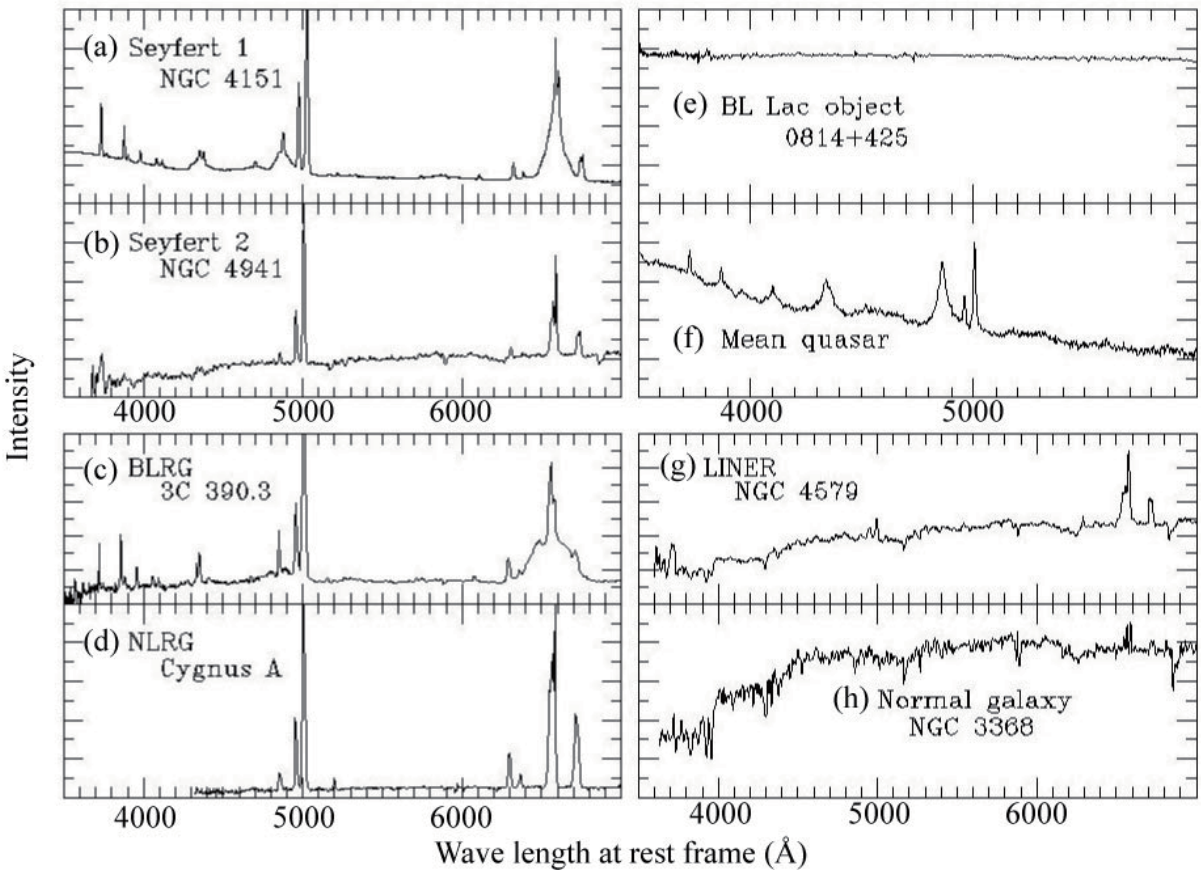

Figure 2.1: Optical spectra of (a) the type I Seyfert galaxy NGC4151, (b) the type II Seyfert galaxy NGC 4941, (c) the broad-line radio galaxy 3C390.3, (d) the narrow-line radio galaxy Cygnus A, (e) the Blazer 0814+425, (f) the Quasars in average, (g) the LINER NGC 4579 and (h) the normal galaxy NGC 3366. These figures are from the Bill Keel's slide set (URL: http://www.astr.ua.edu/keel/agn/spectra.html) and some labels are altered.

Quassrs

Quasars are the most luminous class of AGNs radiating 10^{44-48} erg s^{-1}, with their B-band absolute magnitudes less than $-21.5 + 5 \log h_0$ as a definition. The co-moving space density of quasars exhibit significant evolution, becoming maximum of redshifts of $z = 1$–2, and decreasing both to lower and higher redshifts. Their optical spectra are similar to those of Seyfert galaxies, and exhibit broad emission lines (Fig. 2.1 f). Their continuum spectra are also like those of Seyfert galaxies, with high time variability and strong enhancements in the ultra-violet band. Unlike Seyfert galaxies, quasars include radio-loud and radio-quite sources. A radio intensity of the radio-loud quasars is approximately three orders of magnitude higher then that of radio-quiet ones. Although the fist discovered quasar 3C273 is radio-loud (§2.2.1), the number of radio-loud quasars is only $\sim 5\%$ of the entire population, and the rests are all radio quite.

Blazars

Blazars are radio-loud AGNs characterized by high variability in a broad band and strong optical polarization. Roughly speaking, a Blazer is considered to be a radio galaxy or a radio-loud quasar that are observed nearly end-on to its jets, so that non-thermal (synchrotron, inverse-Compton, and synchrotron-self-Compton) emission components are significantly enhanced. Because the non-thermal emission dominates their broad-band spectra, optical emission lines become too weak to be detected (Fig. 2.1 e), and thermal emission usually becomes undetectable in the X-ray band. A νF_ν continuous spectrum of Blazers shows two peaks; one is in the radio–optical band, while the other in the γ-ray band, which are due to a synchrotron and synchrotron self-Compton emission, respectively.

LINER

LINERs (Low-Ionization Nuclear Emission-line Regions) are AGNs characterized with low luminosities and emission lines from low-ionized gases (Heckman 1980). The optical spectrum is similar to that of type II Seyfert galaxies, except low-ionized emission lines (Fig. 2.1 g). Ho, Filippenko, & Sargent (1994) reported that a half of spiral galaxies, particularly those in nearby universe, are considered to be LINERs. The very low luminosities of LINERs are considered to be a result of rather low accretion rate, rather than a low BH (e.g., Ishisaki et al. 1996). Luminous AGNs in distant universe may have evolved into LINERs (Iyomoto et al. 1998).

2.1.3 Spectral energy distribution

Spectral Energy Distributions (SEDs) of AGNs extend from radio to γ-ray wavelengths, and the spectral shape can be approximated by a power low as $\nu F_\nu \propto \nu^{-(\alpha-1)}$, where α is between $\sim$0–1. Figure 2.2 shows SEDs of radio-loud AGNs and radio-quiet AGNs, excluding Blazars, in a νF_ν form. They reveal some important spectral structures; a hump appearing between $\sim 1000 - 4000$ Å, called the big blue bump, a hump at $\sim 10\mu$m, called the infrared bump, and a drastic downturn below an infrared band, called the sub-millimeter break. The first structures is attributed to a black body emission from an accretion disk formed around the central black hole. Although this feature presumably extends to a soft X-ray band (above 0.1 keV) directly, the energy range between UV and X-ray cannot be observed in principal, because of neutral absorptions by interstellar medium. The second one is thought to be thermal emission from warm dusts with temperatures of $T \lesssim 2000$ K, while the last one can be explained by a spectral cutoff in the thermal dust emission.

Figure 2.2 shows that a radio intensity of the radio-loud quasars is approximately three orders of magnitude higher than that of radio-quiet ones (§2.1.2). The radio signals of radio-loud AGNs are contributed by synchrotron radiation, unlike the optical-UV and Infrared frequencies dominated by thermal emissions. In the hard X-ray to γ-ray energies, radio-loud AGNs can have stronger signals than radio-quiet ones, due to contribution from synchrotron-self-Compton emission in the jets. In the most extreme jet-dominated AGNs, namely Blazers, the non-thermal signals become dominant even

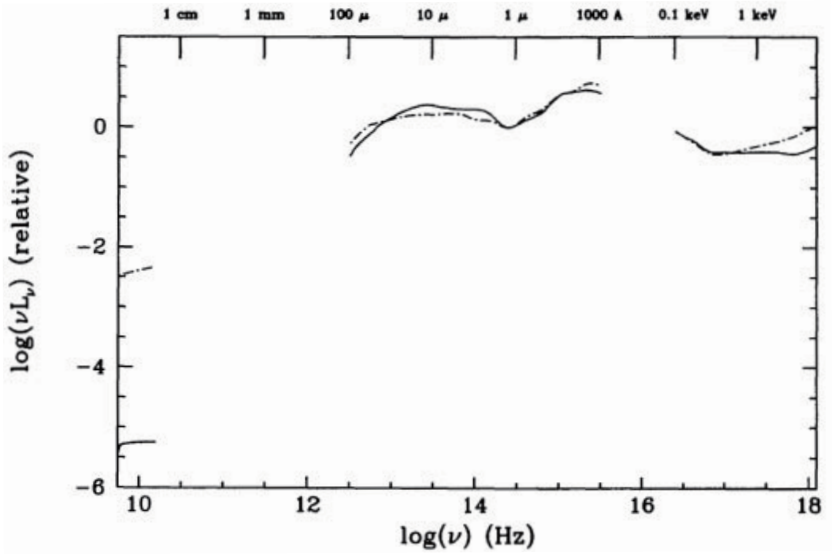

Figure 2.2: The mean quasar energy distribution at a rest frame in νF_ν form, for radio-loud (dash-dotted line) and radio-quiet (solid line) quasars , with the intensity normalized at 1.25 μm (Elvis et al. 1994).

in the IR to UV frequencies. However, how the AGN jets are generated, and what makes the three orders of magnitude gap between radio-loud and radio quiet AGNs, has so far been unknown.

2.1.4 The unified model

Regardless of their radio loudness, AGNs can be divided (§2.1.2) into type I objects exhibiting both broad and narrow emission lines, and type II ones showing only the latter. When the line width of $\sim$ 500 km s^{-1}, an ionized gas would need to have a temperature of $\sim$5 million K, which is much higher than the value of $\sim$10 thousand K, estimated from intensity ratios of the emission lines. Thus, we cannot explain the line width by the thermal broadening, and must consider two different regions; one with a dynamical motion with a velocity of $\sim$ 1000 km s^{-1} and the other with that of $\sim$ 100 km s^{-1}, which are called Broad-Line Region (BLR) and Narrow-Line Region (NLR), respectively. In 1985, Anntonucci & Miller detected a broad line component in polarized light from type II AGNs, and showed that they host BLR obscured from our direct view and observed only in scattered light. Therefore, the type I/type II classification of an AGNs depends on whether both BLR and NLR can be seen or only the NLR can.

The above discovery led astronomers to propose a unified model of AGNs, which is illustrated in Fig. 2.3. It assumes that an AGN is surrounded by torus-like materials with an equivalent hydrogen column density of $\sim 10^{27}$ cm^{-2} obscuring both the AGN central engine and the BLR, and the difference of type I/type II is attributed to the observing angle: AGNs seen from a direction of the torus openings are considered as type I, while those from a side of the torus are type II. Because the NLR is located outside regions covered by the torus, the narrow emission lines can be observed in both types.

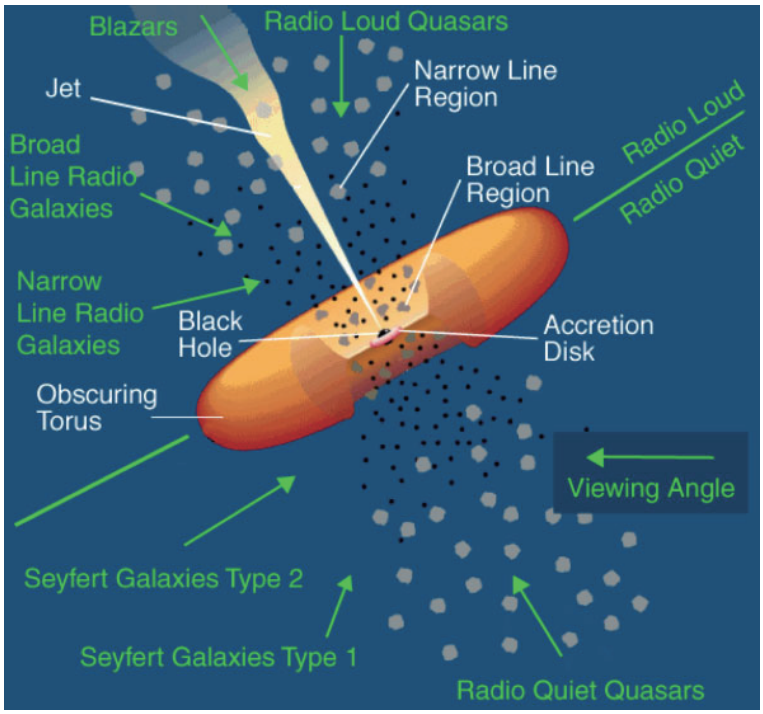

Figure 2.3: The AGN unified model proposed by Urry & Padovani (1995).

Through X-ray observations with *Ginga*, Koyama et al. (1989, 1992) and Awaki et al. (1990, 1991) discovered that type II AGNs are indeed significantly more absorbed than type I objects, and gave an observational support toward the unified model. Table 2.2 summarizes components which are invoked by the AGN unified picture.

Table 2.2: Components in the AGN unified model.

Component	Size (pc)	Density (cm^{-3})
Jet	0.1–10^6	
NLR	1–1000	10^2–10^6
Dust torus	1–100	
BRL	0.01–1	10^8–10^{11}

2.2 The central engine of AGNs

AGNs generate a $\sim 10^{12}$ times higher luminosity than the Solar value, from a central region within $\lesssim 1$ pc. According to the contemporary consensus, this is because a super massive black hole (SMBH) with its mass of $10^{5-10}\ M_\odot$ forms an gaseous accretion disk around it, and works as the central engine which efficiently converts gravitational energy of accreting matter into radiation (Zel'dovich & Navikov 1964; Salpeter 1964).

2.2.1 Super massive black holes (SMBHs)

The SMBH interpretation of AGNs has been constructed from many pieces of observational evidence, starting form Young et al. (1978) who studied the giant elliptical galaxy M87. They found quit a sharp peak in the surface brightness distribution at the central region of M87, which is much narrower than those of ordinary elliptical galaxies. This means that more stars gather at the central region of M87 than in other ellipticals, and the gathering was considered due to presence of a SMBH at the center. They estimated its mass to be $2.6 \pm 0.5 \times 10^9\ M_\odot$, which was the first estimate ever obtained.

Kormendy (1988) discovered that velocity dispersion and rotation curve of stars in the nearby spiral galaxy M31 deviate from the galactic rotation at the central region within 50 light years, exhibiting a sharp anomaly, even though M31 shows no AGN activity. This gave strong evidence for the presence of a dormant SMBH therein, of which the mass was, in 1988, estimated to be $\sim 3 \times 10^7\ M_\odot$. Harms et al. (1994) spectroscopically observed a gas disk at the nucleus of M87 found by Ford et al. (1994), and reported that two different locations with an distance of 60 light years in the center region emitted [OIII] and [NII] lines with Doppler red and blue shift, corresponding a velocity of 500 ± 50 km s^{-1}. This indicates that the center region harbors a strong gravity source, which caused the fast rotation of the gaseous disk. In this study, an estimated SMBH mass of $2.4 \pm 0.7 \times 10^9$ M$_\odot$ was obtained.

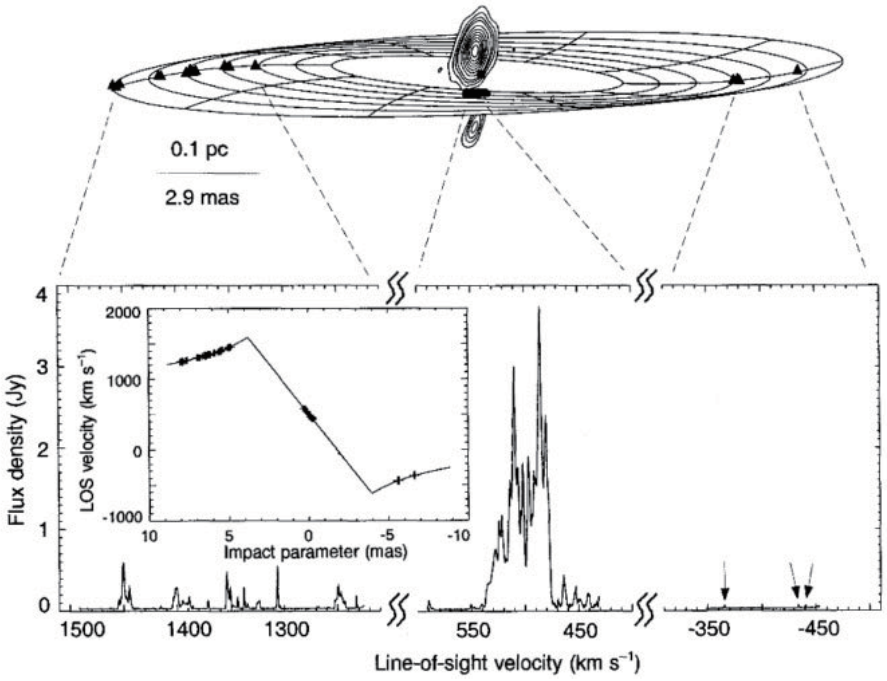

Figure 2.4: Simultaneous VLBI measurements of high-resolution ($\sim$ 0.1 milli-arcsec) positions and line-of-sight velocities of H_2O maser emission from the nucleus of NGC 4258 (Miyoshi et al. 1995). The inset shows plots between line-of-sight velocities of the masers and distances of their sources from the center, with a line representing a model of a Kepler rotation.

By far the most convincing evidence for the presence of SMBH was obtained in the LINER galaxy NGC 4258 utilizing strong H_2O maser emission (Miyoshi et al. 1995). As shown in Fig. 2.4, positions

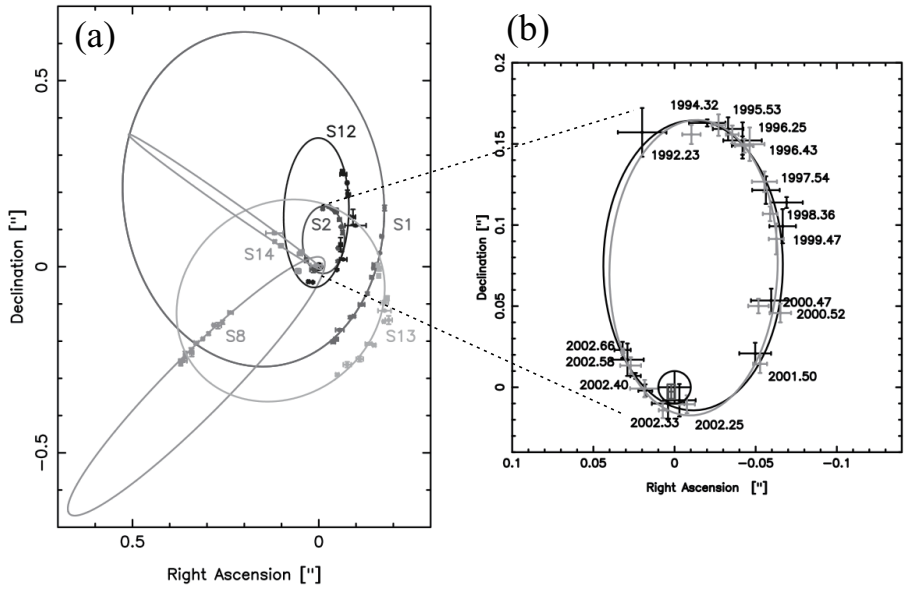

Figure 2.5: (a) Time-dependent positions and the determined projected orbits of the stars S1, S2, S8, S12, S13, and S14, which all have orbital rotations around Sgr A*. (b) The zoomed orbit of S2 star with a cross representing the position of Sgr A* determined by radio observations with a 10 milli arc second error circle. Black is from Shodel et al. (2003), while gray from Schodel et al. (2002).

and line-of-sight velocities of H_2O maser sources within ~ 0.13 pc from the center were accurately and simultaneously measured with the VLBI (Very Long Baseline Array) technique. Then, maser-emitting blobs were found to follow exactly a Keplarian motion, presumably located on a gaseous disk seen nearly edge-on, and the central gravitating mass was determined very accurately as $3.8 \pm 0.1 \times 10^7\ M_\odot$. Since this huge mass is confined within a radius of ~ 0.1 pc, it cannot be anything other than an SMBH. This result is considered far more reliable than the previous M87 measurement, because the Keplerian motion of the gaseous disk was found at many points in NGC 4258, while only two in M87. In fact, the nucleus of NGC 4258 has been established as a low-luminosity ($\sim 4 \times 10^{40}$ erg s^{-1}) AGN, with *ASCA* (Makishima et al. 1994) and *Suzaku* (Yamada et al. 2009) observations. Even our Milkey-Way Galaxy is believed to harbor an SMBH at the point of Sgr A*. As shown in Fig. 2.5, Schodel et al. (2002 and 2003) reported orbital motions of several stars strongly accelerated by a compact (within a few pc) gravity source. This is ascribed to an SMBH with a mass of $\sim 4 \times 10^6\ M_\odot$. Since Sgr A* exhibits rather weak activity (mainly in radio and X-ray signal), it is considered to be a nearly dormant SMBH. However, some X-ray reflection signals form regions within ~ 100 pc of Sgr A* suggest a very interesting possibility that it was highly active ~ 300 years ago (Koyama et al. 1996; Nobukawa et al. 2010).

Recently, almost all galaxies are believed to harbor SMBHs at their centers, and they are considered to become AGNs if a sufficient amount of accretion fuel is available. Although the origin of SMBH is a long-lasting puzzle since 1980' (e.g., Rees 1978 suggesting several routes of a SMBH formation shown in Fig. 2.6), an intriguing clue may be provided by the discovery of a tight correlation between

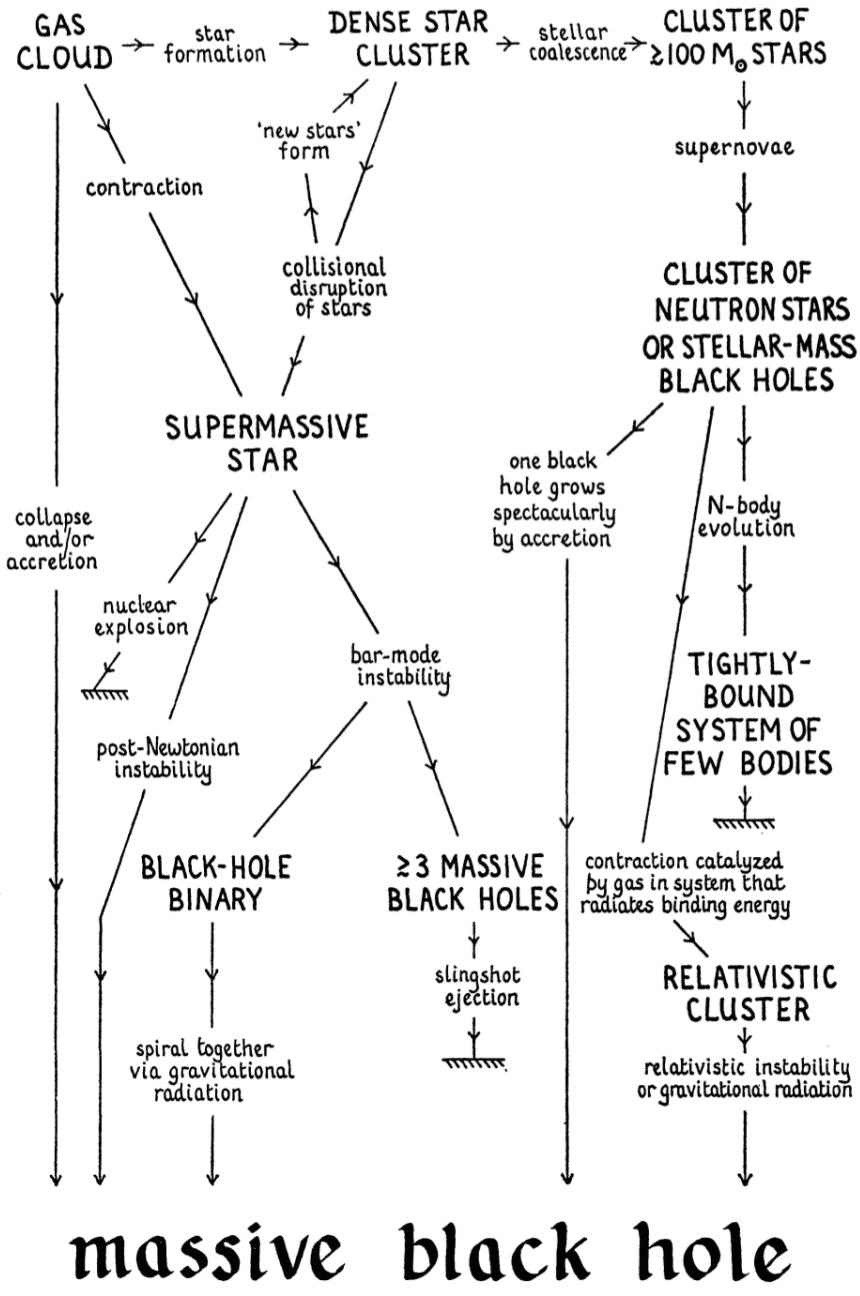

Figure 2.6: The Rees diagram (Rees 1978).

the SMBH mass and its host-galaxy bulge mass (e.g., Magorrian et al. 1998, Gebhardt et al. 2000, Merritt & Ferrarese 2001). This property is called "co-evolution" of SMBHs and their host galaxies.

2.2.2 Eddington ratio of super massive black holes

Around SMBHs, accreting gases are heated by their intense gravity, and radiation may get strong enough to make its pressure comparable to the gravitational force. When a spherically-symmetric geometry is assumed for simplicity, the luminosity which makes them equal is called "Eddington luminosity" and expressed as

$$L_{\rm E} = \frac{4\pi c G M \mu m_{\rm P}}{\sigma_{\rm T}} = 1.25 \times 10^{46} \left(\frac{M}{10^8 M_\odot} \right) \mu \quad ({\rm erg/s}), \tag{2.1}$$

where $\sigma_{\rm T} = 6.65 \times 10^{-25}$ cm^2 is the Thomson cross section and μ is the number of baryons per electron; $\mu = 1.0$, 2.0, and 1.2 for pure Hydrogen, pure Helium and gases with Solar abundances. Substituting eq. (2.1) to an equation of $L = \zeta \dot{M} c^2$, we can define "critical mass-accretion rate" as

$$\dot{M}_{\rm E} = 1.4 \times 10^{25} \left(\frac{M}{10^8 M_\odot} \right) \zeta^{-1} \quad ({\rm g/s}). \tag{2.2}$$

Where ζ is the efficiency (typically $\sim \frac{1}{12}$; see §2.2.3) with which the rest mass energy of accreting matter is converted to radiation. Because the gas cannot fall in a spherically-symmetric manner any more when $\dot{M}$ exceeds $\dot{M}_{\rm E}$, a quantity called Eddington ratio, defined as

$$\lambda = \frac{L}{L_{\rm E}} = \frac{\dot{M}}{\dot{M}_{\rm E}} \tag{2.3}$$

becomes one of the most important parameters characterizing AGNs.

2.2.3 Accretion disk

When gravitational energy of accreting matter is fully converted to thermal energy around a black hole, the gas temperature can reach the virial value of

$$T_{\rm vir}(r) \sim \frac{2GMm_{\rm P}}{3k_{\rm B}r} = \frac{m_{\rm p}c^2}{3k_{\rm B}} \left(\frac{r}{R_{\rm S}} \right)^{-1} \sim 10^{13} \left(\frac{r}{R_{\rm R}} \right) \quad ({\rm K}), \tag{2.4}$$

where $k_{\rm B}$ is the Boltzmann constant. However, when the gas forms a geometrically-thin and optically-thick disk, called a standard accretion disk (Shakura & Sunyaev 1973), its temperature cannot reach the value of eq. (2.4), because half the released gravitational energy goes into Keplarian rotational energy rather than the thermal energy, and the disk temperature increases only up to a point where the emergent black body radiation carries away the remaining half. This is often called "radiatively cooled" condition. Then, the temperature at a radius r of the standard accretion disk becomes

$$T(r) \sim 6.3 \times 10^5 \left(\frac{\dot{M}}{\dot{M}_{\rm E}} \right)^{\frac{1}{4}} \left(\frac{M}{10^8\ M_\odot} \right)^{-\frac{1}{4}} \left(\frac{r}{R_{\rm S}} \right)^{-\frac{3}{4}} \quad ({\rm K}), \tag{2.5}$$

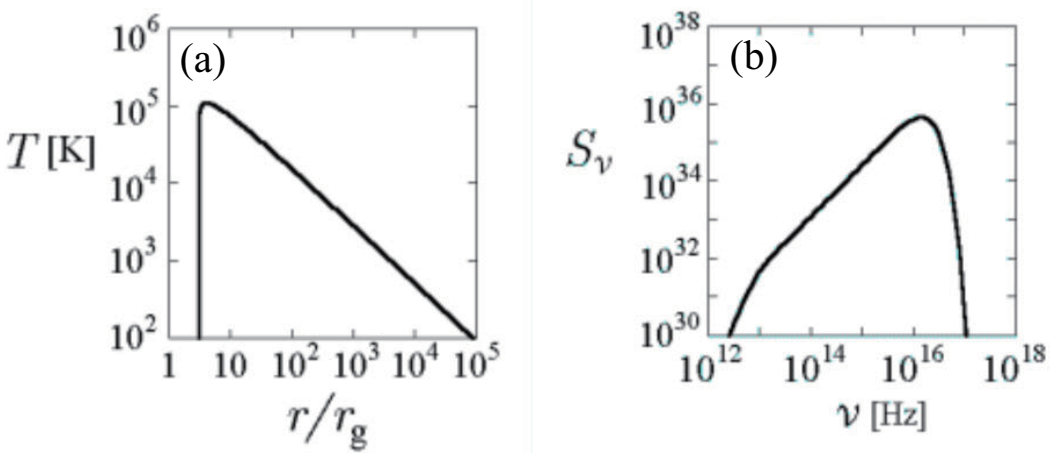

Figure 2.7: (a) A Temperature distribution in a standard accretion disk, in which abscissas is the radius in the units of R_S, while ordinate is temperature in units of K. (b) A disk spectrum as a superposition of various black body emissions from different radii on the accretion disk. The black hole mass and the accretion rate are assumed to be 10^8 $M_\odot$ and 0.1, respectively. These are from Fukue (2007).

where $R_S = 2GM/c^2$ is the Schwarzschild radius. This temperature profile of a standard disk is shown in Fig. 2.7 (a), Assuming a black hole mass of 10^8 $M_\odot$, an accretion ratio of 0.1 Eddington, and the inner radius of 6 R_S, the temperature of the inner edge of the accretion disk becomes ~ 10 eV. This highest temperature at the innermost radius appears in the UV band, while that at $\sim 10^3$ R_S in an optical band. Integrating these black body radiations from the innermost to an outermost radius of the accretion disk, an optically-thick spectrum, called disk-blackbody spectrum, is obtained as shown in Fig. 2.7 (b). This disk emission is considered to be the origin of the big blue bump shown in §2.1.3.

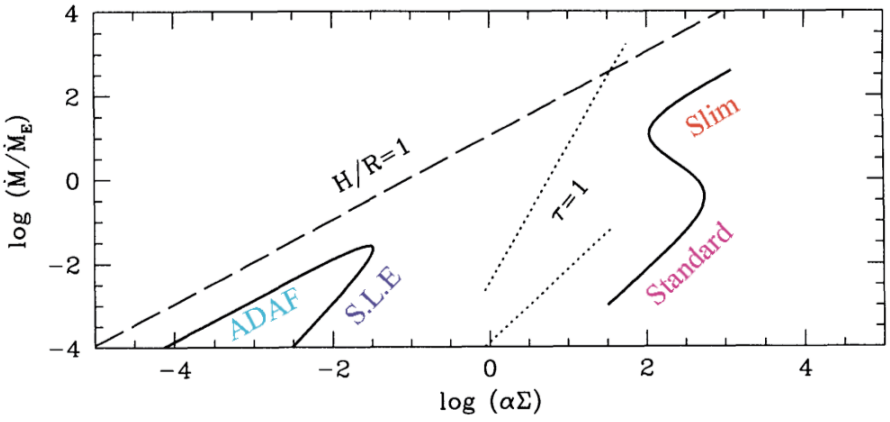

Figure 2.8: Thermal equilibria in an optically thick (right solid line) or thin (left solid line) disk, where the parameters are assumed as $M/M_\odot = 10$, $R/R_S = 2.5$, and the viscosity parameter $\alpha = 0.01$ (Abramowicz et al. 1995).

When the mass-accretion rate becomes lower, the gas in the accretion disk get rarefied, and the

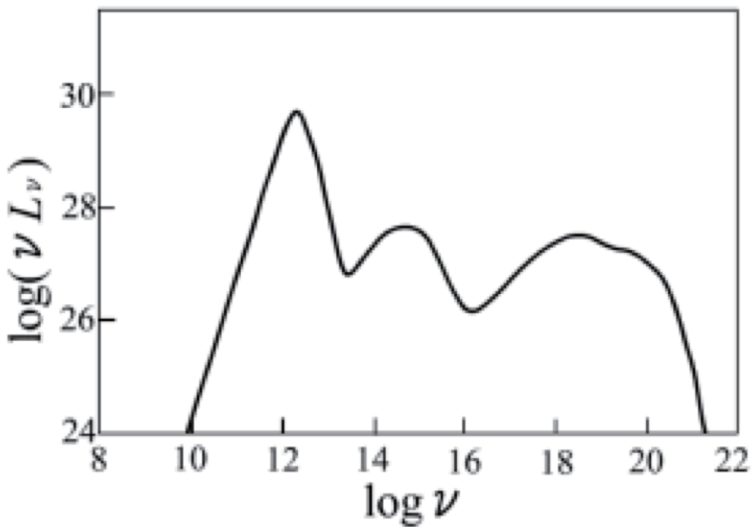

Figure 2.9: An expected spectrum which is emitted by RIAF with $M_{\rm BH} = 2.5{\times}10^6\ M_\odot$ and $\dot{M}/\dot{M}_{\rm Edd} = 3 \times 10^{-5}$ (Fukue 2007; Manmoto et al. 1997).

cooling does not work effectively. As a result, continuous heating by viscosity brings the gas temperature much higher, sometimes close to eq. (2.4), and the disk becomes thicker than the standard accretion disk. This condition is indicated in Fig. 2.8. The gas falls into the black hole without strong radiation, making the total disk emission quite faint. This is called Radiatively Inefficient Accretion Flow (RIAF; Narayan & Yi 1994), from which a spectrum shown in Fig. 2.9 is expected. In contrast to the black body spectrum of the standard accretion disk which appears in the UV–optical band like in Fig. 2.7 (b), the RIAF spectrum may be generated via thermal bremsstrahlung, thermal synchrotron, and inverse Comptonization processes, and appears in a higher energy band up to hard X-rays.

A mass-accreting stellar-mass black hole is known to take two distinct spectral states (Fig. 2.8); so-called High/Soft state where a standard accretion disk is present, and Low/Hard state wherein the accretion matter is close to the RIAF condition. However, it is not yet clear in which of these two states a typical AGN resides.

2.2.4 Black hole spin and ISCO

The Einstein equation predicts the presence of an Innermost Stable Circular Orbit (ISCO), within which any circular orbit becomes radially unstable, so that a test particle can no longer keep orbiting around the central black hole. Thus, the accretion disk must end at a radius equal to or larger than the ISCO, the gas rapidly falls into the black hole. As shown in Fig. 2.10, the ISCO radius in units of the gravitational radius $R_{\rm g} = GM/c^2 = 1/2\ R_{\rm S}$ depends on the black hole spin $a = J/cM_{\rm BH}$, where J is the angular momentum of the black hole. The normalized spin parameter a/M can take any value between 0 (Schwarzschild black hole) and 1 (Maximally spinning Kerr black hole), and correspondingly, the ISCO radius changes from 6 $R_{\rm g}$ to 1.24 $R_{\rm g}$.

When the black hole has a higher spin and hence the ISCO takes a smaller radius, the innermost

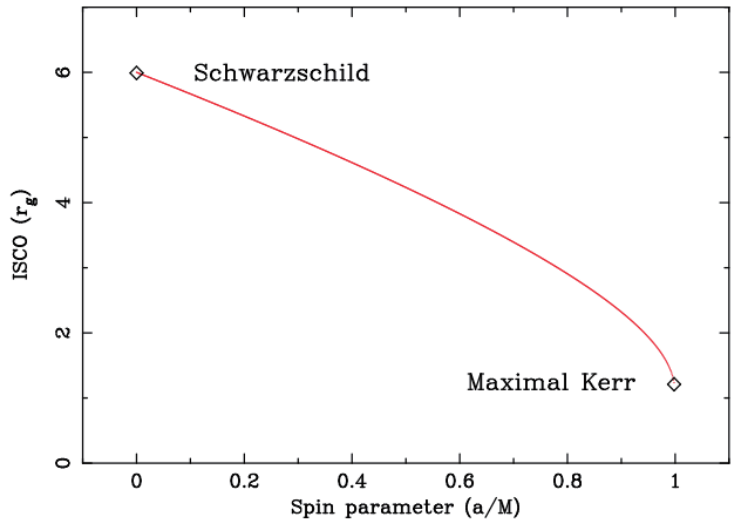

Figure 2.10: The dependence of the ISCO on the normalized black hole spin parameter. (Fabian & MIniutti 2005)

edge of the accretion disk can get closer to the central black hole. Then, the accretion matter becomes subject to stronger relativistic effects, including gravitational redshifts, as well as longitudinal and transverse Doppler effects. These in turn distort the X-ray spectrum emitted by the innermost disk region. In particular, the fluorescent Fe-K line is expected to be broadened, and the line profile provides a valuable information of the black-hole spin. Details of this issue are described in §2.3.4 and §2.3.5.

2.3 X-ray studies of type I AGNs

2.3.1 Past studies of primary X-ray continua

As illustrated in Fig. 2.11, an X-ray spectrum from the central region of AGNs is generally considered to consist of a Power-Law (PL) like primary continuum, a reflection component accompanied by an Fe-Kα line, and "soft excess" structure (§2.3.2). The primary component (Fig. 2.11 green), which is presumably generated via inverse Compton scattering in a corona (Haardt et al. 1994), can be approximated with a cutoff power-law function expressed as

$$\propto E^{-\Gamma} \exp(-E/E_{\rm c}), \tag{2.6}$$

where E is the energy, Γ is the photon index, and $E_{\rm c}$ is the cutoff energy. As given in Sunyaev & Titarchuk (1980), Γ is determined as

$$\Gamma = -1/2 + \sqrt{9/4 + 4/y}, \tag{2.7}$$

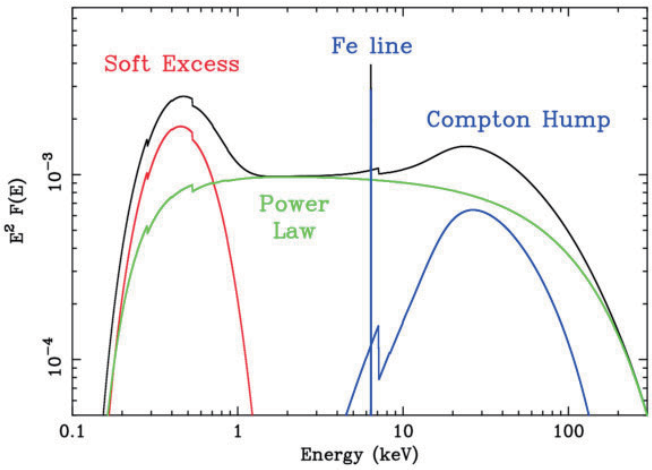

Figure 2.11: Schematic X-ray spectra of AGNs (Fabian & Miniutti 2005). Green shows a PL like primary continuum, while blue a reflection component accompanied by the Fe-Kα line at 6.4 keV. Red illustrates "soft X-ray excess" structure.

where y is the Compton y parameter defined by a product of the electron temperature $T_{\rm e}$ and the optical depth τ as

$$y \equiv \max(\tau, \tau^2) \times (4kT_{\rm e}/m_{\rm e}c^2). \tag{2.8}$$

From studies of the primary continua of bright Seyfert galaxies (e.g, Beckmann et al. 2009; Lubinski et al. 2010), a typical photon index and high energy cutoff are found to be ~ 1.8 and several hundreds keV, respectively, so the corona is generally characterized with an electron temperature of $\sim 10^9$ K and Compton y parameter (eq. 2.3) of ~ 1. Seed photons for the inverse Compton are considered to come from a black body emission of the standard accretion disk, which has a peak temperature of ~ 10 eV, when the BH mass is 10^8 $M_\odot$ and the Eddington ratio is 10% (eq. 2.5).

Geometry of the Comptonizing corona generating the PL-like primary continuum has been considered in various ways. As shown in the top panel of Fig 2.12, Haardt & Maraschi (1991 and 1993) suggested a simple model, where a uniform plane-like corona sandwiches the accretion disk in parallel. However, such a slab corona can be easily cooled by Comptonization, and cannot realize a temperature which is high enough to explain actually observed hard X-ray spectra (Stern et al. 1995). If the corona is formed within the inner disk edge like the middle two figures in Fig. 2.12, the Compton cooling does not work effectively, and the desired hard X-ray spectra can be obtained (Dove, Wilms & Begelman 1997). Alternatively, when the corona is patchy like the bottom figure in Fig 2.12, and the covering fraction of the corona against the accretion disk is relatively small, the Compton cooling becomes inefficient. Then, a hard X-ray spectrum like the observed one can be produced (Stern et al. 1995). Thus, the bottom three "photon starved" geometries in Fig. 2.12 are currently possible candidates for the corona in which the PL-like primary continuum is generated. Further attempts to identify the correct geometry are yet to be performed.

The heating mechanism raising the coronal temperature close to the virial value is also a mystery.

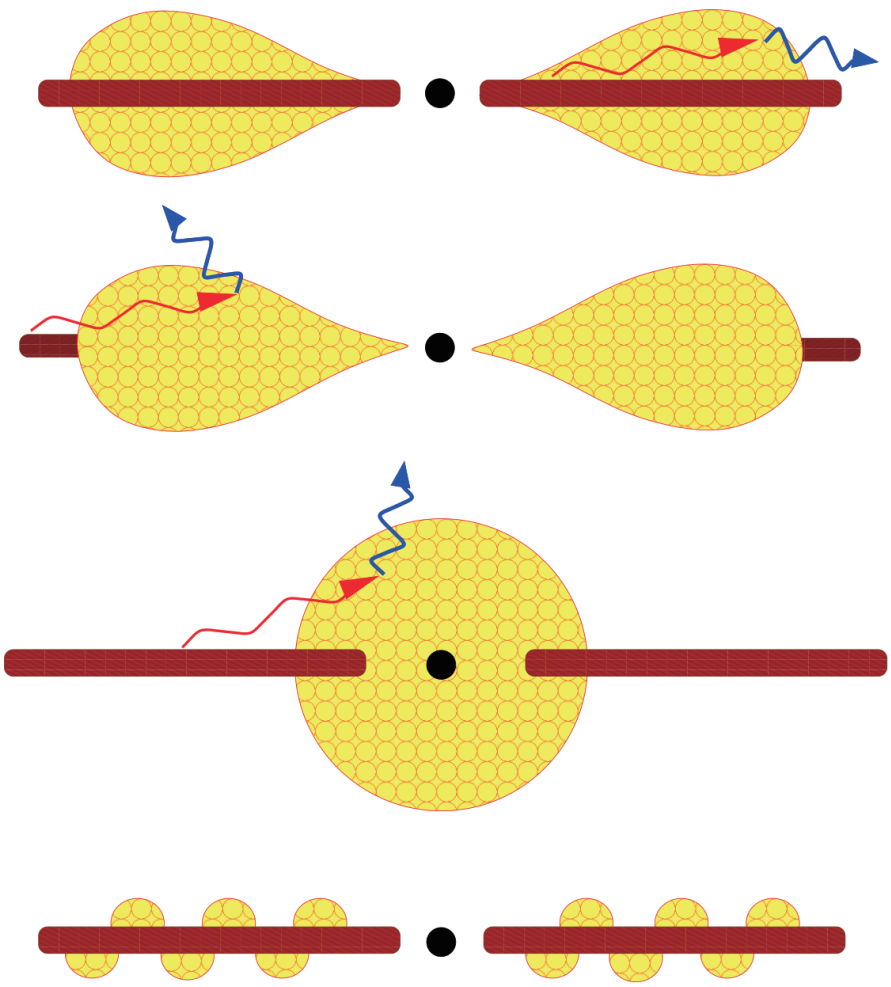

Figure 2.12: Geometries of the central black hole (black), the accretion disk (brown), and Comptonizing corona (yellow), proposed to explain the formation of the PL-like primary X-ray component. The top figure shows a sandwich geometry, the middle two show sphere+disk geometries, and the bottom a patchy corona (Reynolds & Nowak 2003).

Similar to the Solar coronae and Solar flares, magnetic processes may work to heat electrons (e.g., Di Matteo 1998; Miller & Stone 2000; Machida, Hayashi, & Matsumoto 2000). However, the corona around a black hole can energetically dominate the accretion flow, while that of the Sun contains only $\sim 10^{-13}$ of the entire self-gravitating energy of $\sim 10^{48}$ erg. Hence, the theory developed for the Sun may not be easily applied to these black hole systems. Alternatively, the RIAF (§2.2.2), which is a different state from the standard accretion disk, is considerable to make the sphere+disk geometry. In other words, the accretion disk becomes RIAF-like in the inner region, while it remains as an standard disk in the outer region. In this mechanism, most of seed photons for Comptonization come from synchrotron radiation internal to the radiatively inefficient flow, and the situation is slightly different form that illustrated by the second from top case of Fig. 2.12. Thus, a conclusive explanation of the coronal heating mechanism (in AGNs) has not been obtained yet. For reference, the most up-to-date

Suzaku data on the leading BH binary Cyg X-1 can be consistently explained assuming that the seed photons for Comptonization are supplied by the optically-thick disk (Makishima et al. 2008; Yamada et al. 2013).

2.3.2 Soft X-ray excess structure

AGN spectra often exhibit a phenomenon called "soft excess" (e.g., Arnaud et al. 1985; Turner & Pounds 1989), which appears in their soft X-ray spectra as a steep flux upturn towards lower energies. The simplest explanation of this structure would be direct black body emission from the accretion disk around the central black hole, like in the case of black hole binaries (e.g., Makishima et al. 2008; Yamada et al. 2013). However, as explained in §2.2.3, the peak temperature of the black body from AGNs should appear in the UV band, and it cannot explain the structure in the soft X-ray band.

Then, several different interpretations have been suggested, including thin-thermal plasma emission in the host galaxy, a part of relativistically-blurred reflection continuum (see §2.3.4), a part of primary X-ray continuum that is affected by ionized absorptions (see §2.3.6), and thermal Comptonizing signals arising in some corona that are not so hot as to produce hard X-rays. Nevertheless, none of them are conclusive, since all these interpretations can explain the same data similarly well, and degenerate (e.g., Cerrutti et al. 2011). Hence, the origin of the soft X-ray excess structure has also been a big mystery in the AGN studies.

2.3.3 Secondary signals: neutral- and ionized-disk reflection components

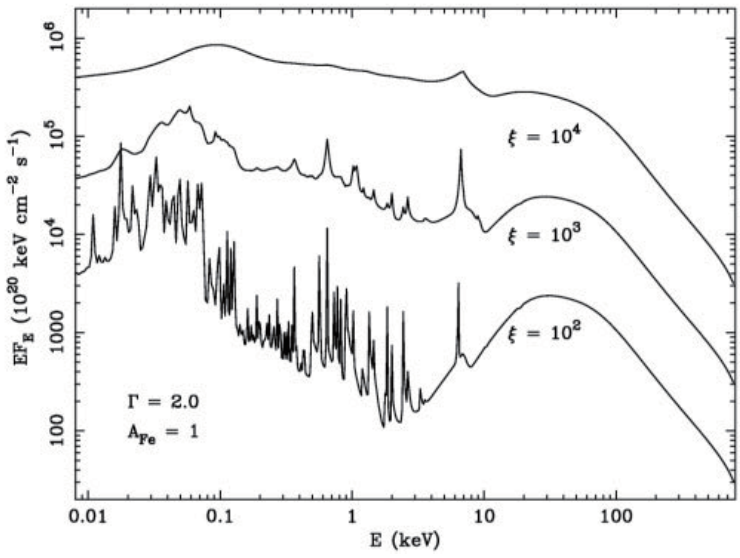

Figure 2.13: Reflection spectra for the ionized parameter of $\xi = 10^4$ (top), 10^3 (middle), and 10^4 (bottom), calculated by Ross & Fabian (2005). In all calculations, the photon index of the incident continuum, the hydrogen number density, and the Fe abundance of the reflecting material is assumed to be 2.0, 10^{15} cm^{-3} and 1 Solar, respectively.

A reflection component (Fig. 2.11 blue line) is generated when the primary continuum is Compton-scattered and/or photo-absorbed by neutral/ionized materials surrounding the central BH, including the accretion disk and the molecular torus (§2.1.4; George & Fabian 1991). In the high energy band, thus, the photons lose their energy due to the Compton down scattering. The photo-absorption process makes the reflection continuum with a hard spectral shape in the low energy band, and produces a deep Fe-K absorption edge at $\sim$ 7.1 keV. As a result, an Fe-Kα line inevitably sticks out at 6.4 keV with an equivalent width of $\sim$ 1–1.5 keV, when the scattering materials have an Fe abundance of 1 Solar and are cold and neutral (e.g., George & Fabian 1991). These strong Fe-K features are due to the high abundance ratio and fluorescence yield of Fe. Lighter elements also produce fluorescence lines.

The scattering gas in the accretion disk can be ionized due to strong illumination by the primary X-ray emission. The degree of ionization of the gas can be described by a quantity called ionization parameter, which is defined as

$$\xi = \frac{L}{nr^2} \quad (\text{erg cm s}^{-1}), \tag{2.9}$$

where L is the illuminating luminosity, n is the gas density, and r is the distance from the illuminating source to the reprocessing gas. When the scattering materials are ionized, the spectral shape of the reflection continuum changes like in Fig. 2.13. As the ξ value gets higher, the number of electrons bound in light atoms decreases, causing the photo-absorption cross section to decrease in lower energies. This softens the scattered continuum shape. Another effect of higher values of ξ is that the 0.98–3.0 keV range becomes dominated by Kα lines of highly ionized light atoms, and the lines get broader due to Compton scattering by electrons which become hotter. (The gas temperature is expected to be $\sim 10^6$ K at $\xi \sim 10^{3-4}$). At $\xi \sim 10^4$ erg cm s^{-1}, the ionized reflection component becomes like a featureless soft continuum except the H-like Fe feature peaking at $\sim$ 7 keV (top line in Fig. 2.13).

2.3.4 Relativistic effects on secondary components

When the X-ray reprocessing takes place at regions closer to the central black hole, the spectrum becomes affected more strongly by special and general relativistic effects, resulting in broadening/smearing of spectral features. Since the Fe-K line must be produced at various distances from the central BH, the observed line profile will be an weighted mean of those with different broadening strengths. Panels (I, II, and III) in Fig. 2.14(a) shows how the profile of an intrinsically narrow line produced in an optically-thick accretion disk is broadened under Neutonian (longitudinal Doppler), special relativistic (plus beaming and transverse Doppler), and general relativistic (plus gravitational redshift) schemes, respectively, and panel (IV) represents their overall combination. Figure 2.14(b) shows a simulated reflection spectrum generated by an ionized accretion disk with and without the relativistic broadening effects. In the relativistic reflection, every sharp spectral feature becomes smeared, and connects with neighboring structures, making the whole spectrum relatively smooth.

Since the strength of the relativistic effects strongly depends on the distance from the BH, the Fe-Kα line profile emitted from an accretion disk depends sensitively on the innermost disk radius,

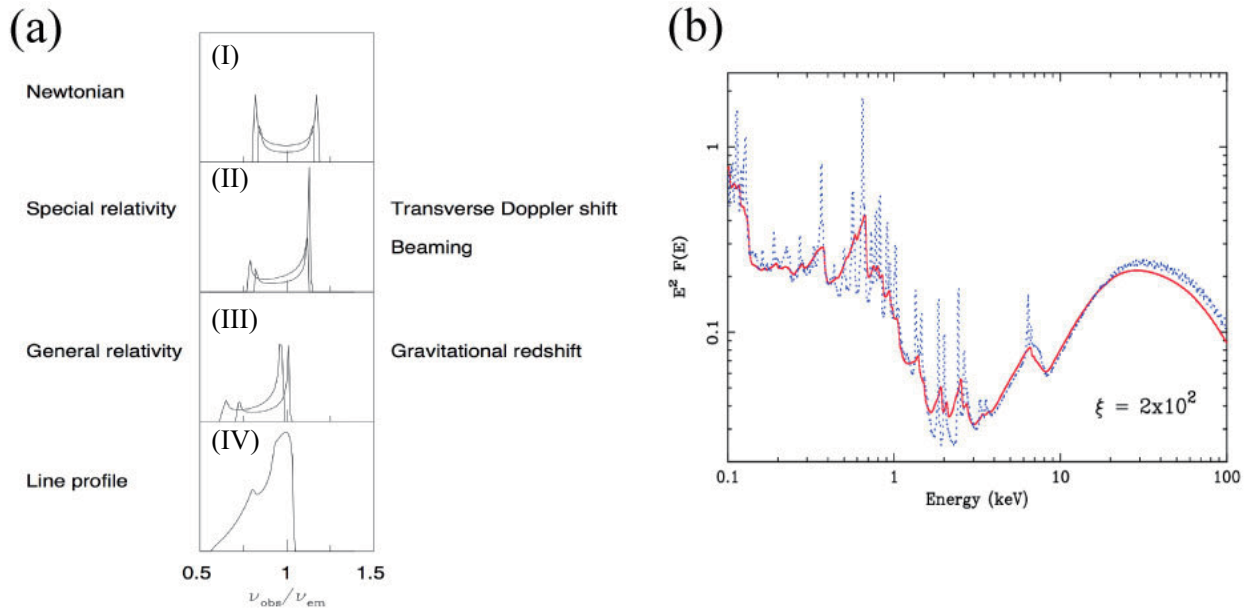

Figure 2.14: (a) The profile of an intrinsically narrow emission line is modified by the interplay of Doppler energy shifts, relativistic beaming, gravitational redshift, and the combination of them from top to bottom (Fabian et al. 2000). (b) Blue represents ionized reflection component with $\xi = 2 \times 10^2$ erg cm s^{-1}, while red that affected by the combination of the relativistic effects shown in panel (a), reported by Fabian & Miniutti et al. (2005).

inside which fluorescence can be neglected. Thus, an observed reflection spectrum, when compared with models like in Fig. 2.14(b), can give an estimate of the innermost disk radius, and hence an upper limit on the ISCO radius (§2.2.4) because the disk cannot be present inside the ISCO. Then, using the relation in Fig. 2.10, we can obtain the lower limit on the spin parameter of the black hole.

In an *ASCA* spectrum of the bright type I Seyfert galaxy MCG–6-30-15, a spectral feature like the relativistically-broadened iron line was detected by Tanaka et al. (1995). Figure 2.15 (a) shows this spectral feature fitted with the relativistic iron line model as presented in Fig. 2.14 (a). This feature was confirmed in the *Suzaku* spectrum by Miniutti et al. (2007), together with a strong hard X-ray hump (Fig. 2.15 b). The combination of the seemingly broad iron line and the apparently strong Compton hump was explained by the presence of a strong relativistic reflection component, wherein the Fe-K line is relativistically broadened and the Compton hump is enhanced due to "light bending" effects (§2.3.5), with a conclusion that the super massive black hole in MCG–6-30-15 is an almost maximally spinning one with $a/M_{\rm BH} \sim 1$ (Minitutti et al. 2007). In other type I AGNs, similar spectral features were reported, and they were also concluded to harbor a highly spinning black hole (Nandra et al. 2007).

Like the 0.1–1 keV band of the reflection spectrum shown in Fig. 2.14 (b), a soft-excess-like structure can be obtained in the soft X-ray band, by smearing the Fe-L edge and many emission lines from ionized lighter elements. As a result, many attempts were made to explain the soft-excess phenomenon (§.2.3.2) in terms of the relativistic reflection (e.g., Fabian et al. 2009). However, the

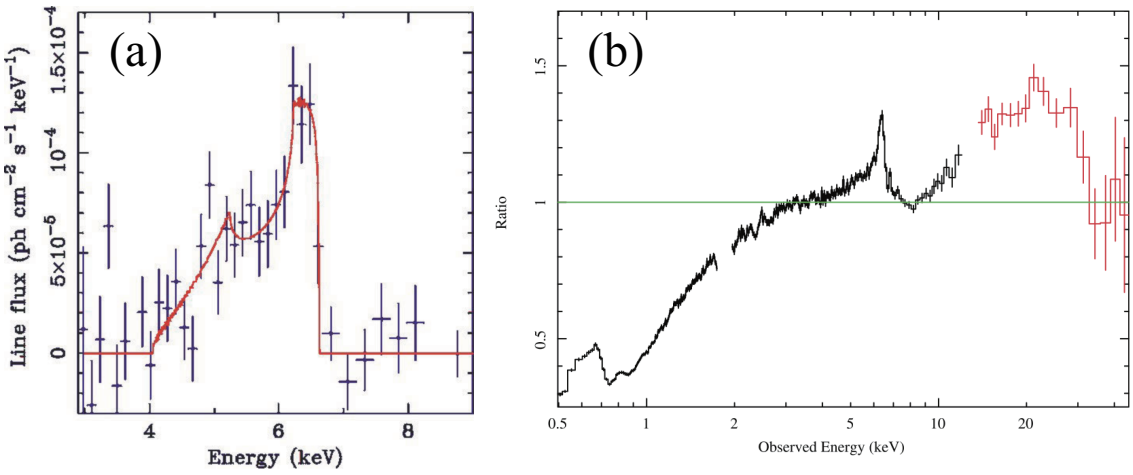

Figure 2.15: *ASCA* (panel a) and *Suzaku* (panel b) spectra of the type I Seyfert MCG–6-30-15, from Tanaka et al. (1995) and Miniutti et al. (2007), respectively. The *ASCA* result is presented often subtracting a PL-shaped continuum.

explanation of the broad band ($\sim$ 0.3–45 keV) X-ray spectrum by the relativistic reflection component requires a fine tuning in ξ, disk-emissivity index which described how the Fe-K line emissivity varies with the radius, and the disk inclination.

2.3.5 Light-bending effects on the relativistic reflection

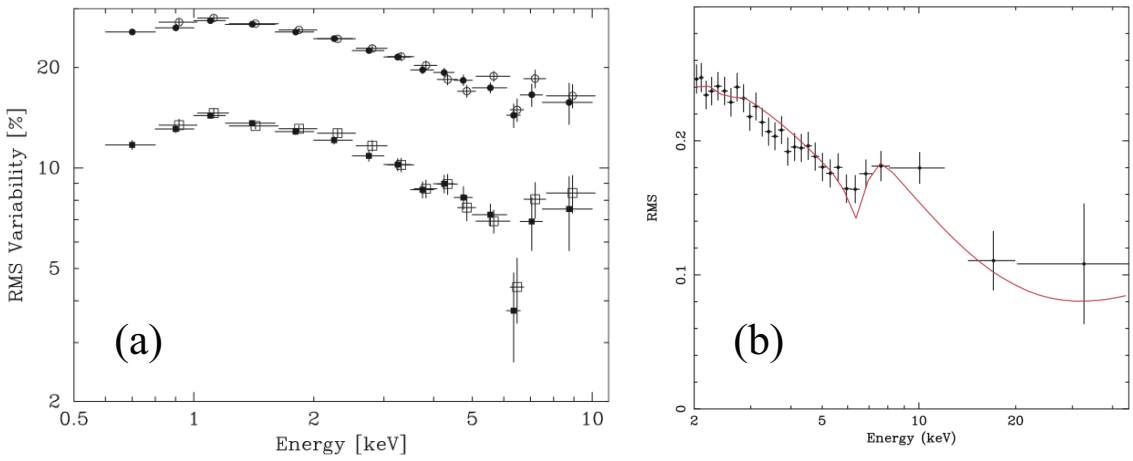

Figure 2.16: (a) An *ASCA* RMS spectrum of MCG–6-30-15 with binning of 180 ksec (open and filled circles) and 23 ksec (open and filled squares), from Matsumoto et al. (2003). (b) The same as panel (a), but the data are from *Suzaku*, and the binning is 45 ksec (Miniuttii et al. 2007).

The relativistically-blurred reflection hypothesis is apparently inconsistent with results of timing analyses, as represented by the root mean square (RMS) analysis. Figure 2.16 shows *ASCA* and *Suzaku* RMS (root-mean-square) spectra of MCG-6-30-15, from Matsumoto & Inoue (2003) and Miniutti et al.

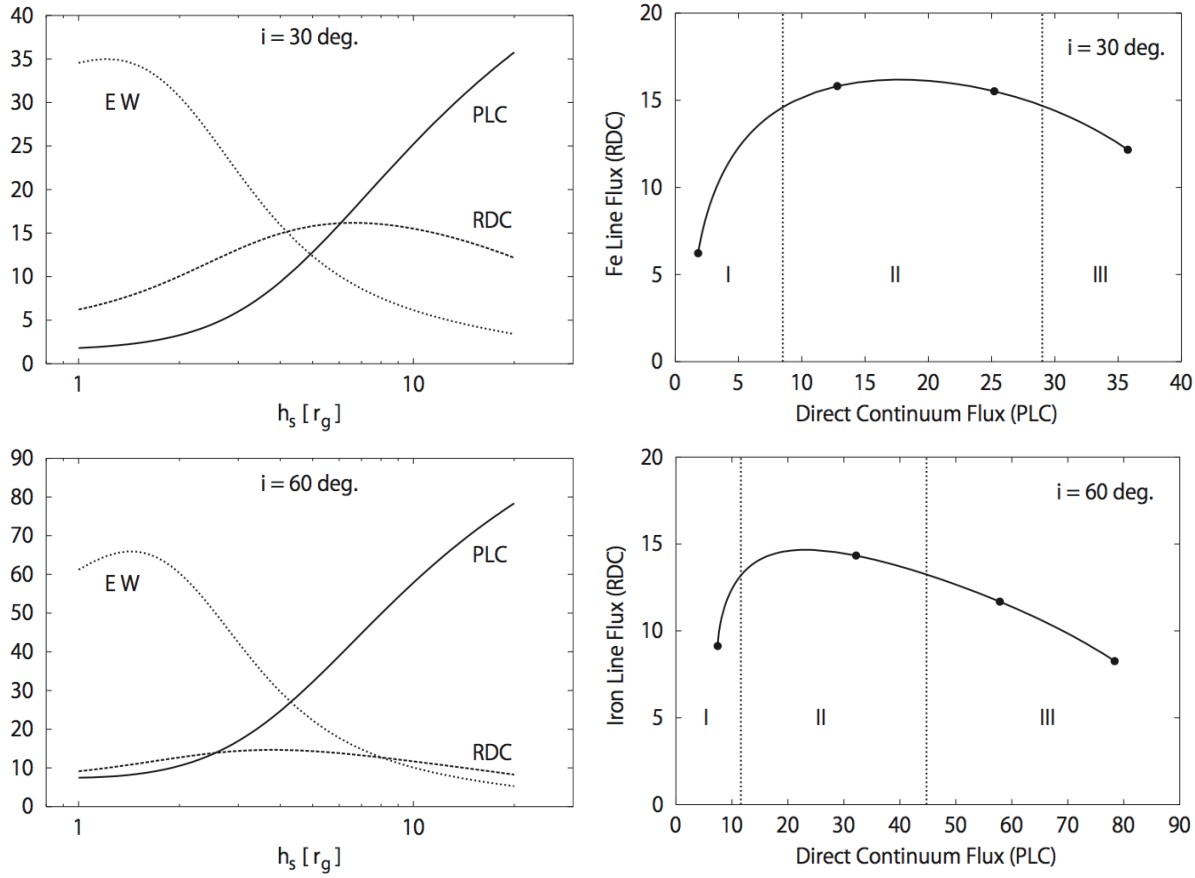

Figure 2.17: Simulated results of the "light bending" model proposed by Miniutti & Fabian (2004). (Left) Intensities of the Power-Law Component (PLC) and Reflection-Dominated Component (RDC), and the equivalent width (EW) of the broad iron line, all shown against the distance between the primary emitter with constant luminosity and the black hole. (Right) The equivalent width of the broad iron line against the intensity of PLC.

(2007), respectively. Here, the 6–6.5 keV and 15–45 keV ranges of MCG–6-30-15 are found to exhibit relatively low time variability. However, accordingly to the interpretation by Tanaka et al. (1995) and Miniutti et al. (2007), these energy bands in MCG–6-30-15 are dominated by the relativistic reflection component with the relativistic broad iron line and the strong Compton hump, and hence they must have high variability, because the relativistic reflection, generated near the BH, should follow the variable primary emission down to short timescales. This naive idea disagrees with Fig. 2.16.

To solve the above self-contradiction, Miniutti & Fabian (2004) proposed a sophisticated scenario invoking general-relativistic "light bending" effects. They consider a point-like primary emitter with a constant luminosity, which moves in position along the axis through the black hole perpendicular to the disk. When the primary source gets closer to the black hole, a larger fraction of photons will be "bent" toward the disk and the black hole, while the primary intensity arriving to a distant observer will decrease. Futhremore, as shown in Fig. 2.17, the number of photons illuminating the disk will not change very much, and so will be the strength of the reflection component. Therefore,

the primary continuum (PLC in Fig. 2.17) can vary while keeping the reflection strength and the Fe-K line flux both approximately constant. However, this scenario, often called "Light-post model with light bending", requires very special geometry with fine parameter tuning. The primary source must be at a height of several to ten R_S above the black hole, without significant lateral extent. It is totally unexplained how the high luminosity of typical AGNs can be emitted from such a compact source region, and how it can move vertically without changing the luminosity. The only possibility could be the base of some jets, but Seyfert galaxies, including MCG–6-30-15, are generally radio quiet, with little evidence for a significant jet activity.

2.3.6 Partial covering absorption by ionized absorbers

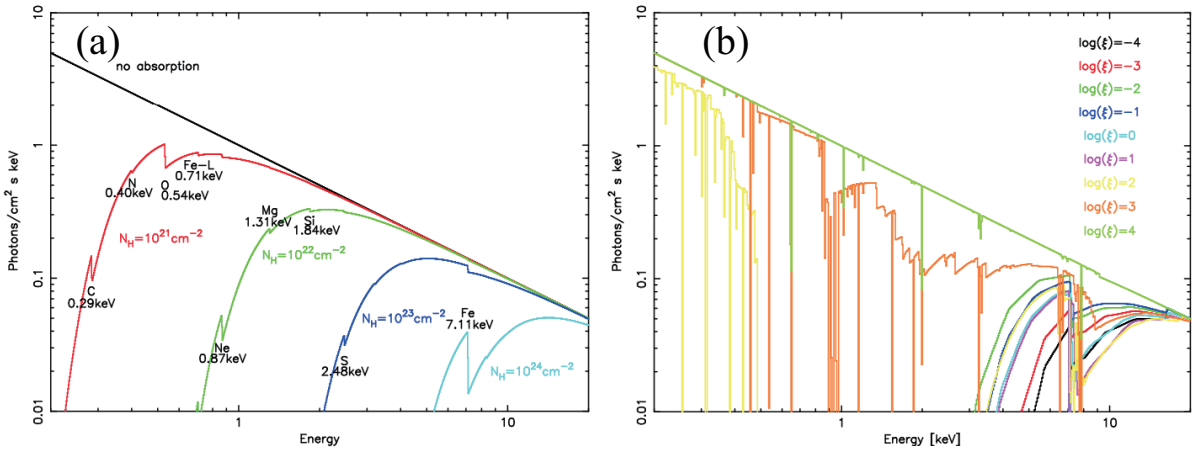

Figure 2.18: (a) Spectral shapes of the $\Gamma = 2.0$ PL model seen through a neutral absorber with a column density of 0 (black), 10^{21} (red), 10^{22} (green), 10^{23} (blue), and 10^{24} cm^{-2} (cyan). (b) The same as panel (a), but with a fixed column density of 10^{24} cm^{-2} and the ionization parameter is varied as 10^{-4} (black), 10^{-3} (red), 10^{-2} (green), 10^{-1} (blue), 1 (cyan), 10 (purple), 10^2 (yellow), 10^3 (orange), and 10^4 (light green). These figures are from Ebisawa (2006).

The shape of spectra from accreting black holes can be affected not only by the addition of the secondary (reflection) signals possibly with relativistic smearing, but also due to photo-absorption by materials of various physical parameters. Besides the metal abundance which may be usually assumed 1 Solar, such absorbers have two main physical parameters; the column density and the ionization parameter ξ (§2.3.3). When the former increases, the X-ray spectrum is evidently more significantly affected with a deeper absorption edges, as shown in Fig. 2.18 (a). If the latter increases, the spectral shape becomes generally softer, and energies of the absorption edges get higher, due to lack of the number of electrons bound in outer shells of atoms from C up to Fe. The behavior is the same as that in the ionized reflection component in Fig. 2.13. Then, the spectral shape finally becomes as shown in Fig. 2.18 (b). At $\xi \gtrsim 10^3$, the Fe ions become mostly He-like (Fe XXV), and at $\xi \gtrsim 10^4$, they will be mostly fully ionized, thus significantly reducing the absorption effects.

When patchy absorbers cover the radiating source, some of the primary continuum is absorbed,

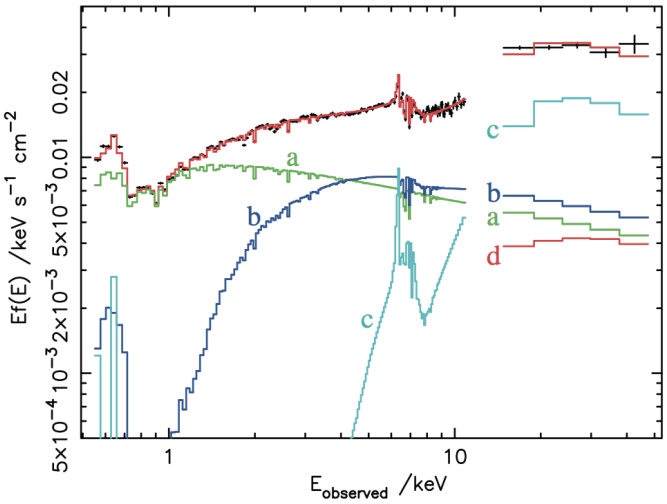

Figure 2.19: The *Suzaku* spectrum of MCG–6-30-15 (black data points), fitted with a model (red) invoking partially covering ionized absorption. In the model, green, blue, cyan, and orange represent a direct primary continuum, an absorbed primary continuum, a distant reflection component, and the cosmic X-ray background, respectively (Miller et al. 2008).

while the rest not. This condition is called "partial absorption", and makes several spectral components which have a common slope and different absorption. Employing this model with ionized absorbers, Miller et al. (2008) successfully explained the *Suzaku* spectrum of MCG–6-30-15 without invoking the relativistically-blurred reflection component. As shown in Fig 2.19, the ionized partial absorption produces an additional hard component (blue), of which hte spectral shape is similar to that of the relativistic reflection (cyan in Fig. 2.15b). It also predicts a soft-excess-like features below $\sim$ 1 keV (Fig 2.19). Furthermore, Miyakawa et al. (2012) successfully explained the RMS spectra of MCG–6-30-15 and other AGNs assuming changes only in the partial covering factor. However, this interpretation requires several zones (more than two) of absorbers with different column densities and ionization parameters, and their geometry needs some sort of fine tuning. In addition, it is yet to be confirmed whether changes in the partial-covering parameters can be unambiguously distinguished from those in the intrinsic emission.

2.3.7 Ambiguity in X-ray studies and the objective of the present thesis

As described so far, the X-ray spectra from AGN central regions, wherein the primary and the reprocessed or absorbed signals are mixed up, allow several different interpretations; major two of them are the relativistically-blurred reflection, and the partially covering ionized absorptions interpretation. They often degenerate in actual data analysis, and yield similar fit goodness to the same X-ray data like Fig. 2.15 and Fig 2.19. Furthermore, they both require a very limited or special geometry that cannot be examined by other means, thus leaving plenty room for other interpretations. Thus, the X-ray studies of AGNs are still in a deep confusion.

The interpretations quoted above are commonly based on an assumption that the spectral shape of

a primary continuum is a single Power Law (PL). This physically means that an AGN central engine, namely a Compton corona, has a single zone with a uniform electron temperature and a single optical depth. However, an AGN, with its steeply deepening gravitational potential must involve strong gradients in physical conditions of the matter accreting onto it. Therefore, the simplified assumption of a single-zone corona may not be warranted. If so, significant revisions would be needed in the existing views of the AGN X-ray emission, including the popular disk reflection and partial covering interpretations in particular. To solve the ambiguity of the AGN X-ray interpretation, it is therefore essential to clarify the true nature of the primary X-rays from the central engine.

In the present thesis, we try to discard any preconceived views, and "listen to" what data are telling us. By utilizing time variations of each spectral component in the overall X-ray emission from AGNs, we expect to determine its true spectral shape. Thus, combining X-ray timing studies with rigorous X-ray spectroscopic means will allow us to much more strongly constrain, than before, the picture of the AGN central engine. This approach is completely different from the previous ones which assume the single-PL primary component.

Chapter 3

INSTRUMENTATION

3.1 Overview of the *Suzaku* satellite

Suzaku (*ASTRO-E2*) is the Japanese fifth X-ray astronomical satellite, following *Hakucyo* (launched in 1979), *Temma* (1983), *Ginga* (1987), and *ASCA* (1993). Among them, the size of *Suzaku* is second to none, with the entire length of 6.5 m, the width of 5.4 m, and the weight of 1680 kg, as shown in Fig. 3.1. In 2005 July, it was launched from the Uchinoura space center, by the M-V-6 rocket of Institute of Space and Astronomical Science/Japan Aerospace Exploration Agency (ISAS/JAXA). As illustrated in Fig. 3.2, it was finally put into an approximate circular orbit with the orbital inclination of 31 degree and the altitude of $\sim$ 550 km. *Suzaku*'s attitude is controlled by triaxial wheels to orient a normal vector of its solar paddles at the direction of the Sun within 30 degree.

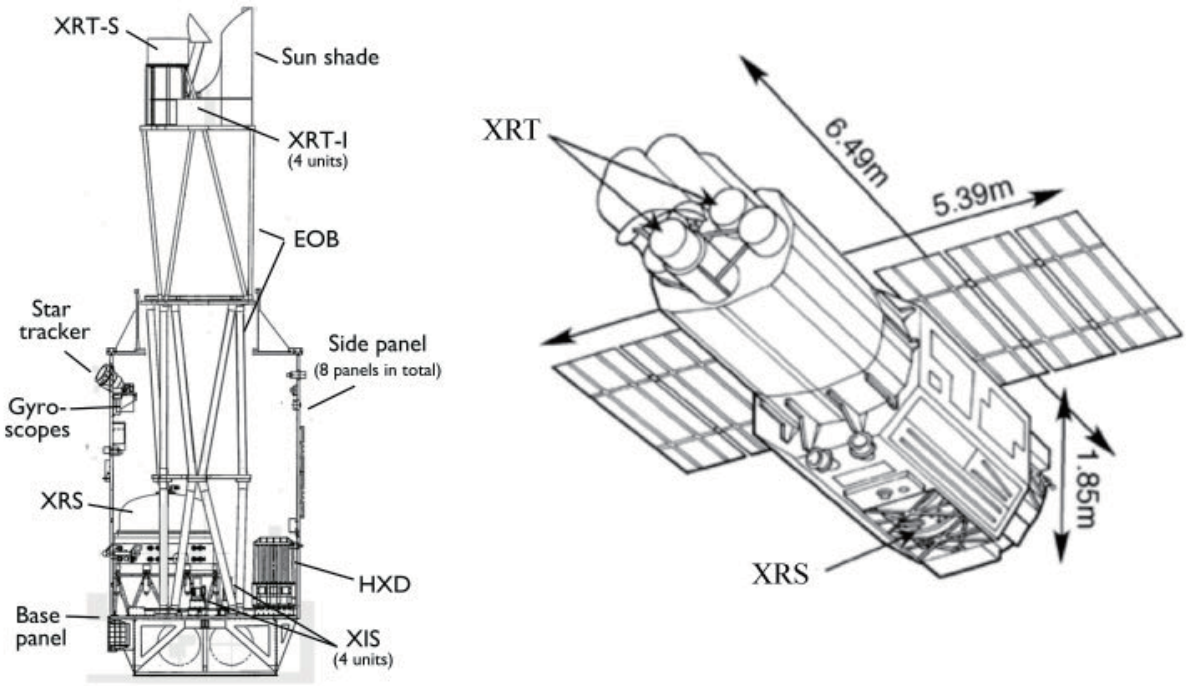

Figure 3.1: A cross section (left) and an outer view (right) of the *Suzaku* satellite. There figures are from Mitsuda et al. (2007).

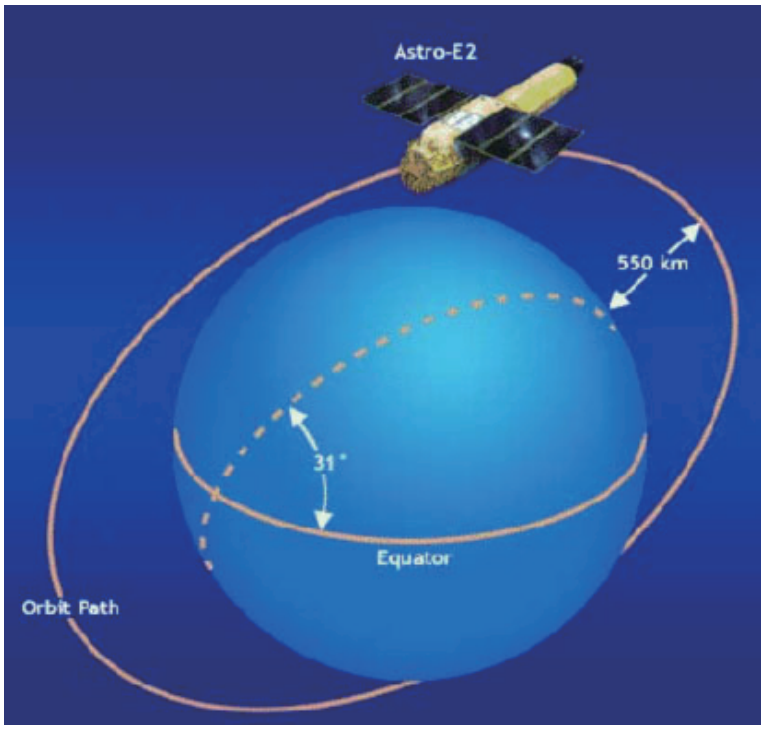

Figure 3.2: The orbit of *Suzaku*. This figure is from the technical description in the *Suzaku* homepage (URL: http://www.astro.isas.ac.jp/suzaku/doc/suzaku_td/node6.html).

Major capabilities of *Suzaku* include a 0.3–600 keV broad-band simultaneous coverage and high sensitivity in the whole band. The former is realized by two instruments. One is the X-ray Imaging Spectrometer (XIS; Koyama et al. 2007) working in a soft X-ray band of 0.3–10 keV, placed at focal planes of four units of the X-ray Telescope (XRT; Serlermitsos et al. 2007). The other is a non-imaging high-energy instrument, the Hard X-ray Detector (HXD; Takahashi et al. 2007), covering a hard X-ray band of 10–600 keV. Its pointing direction is coordinated with the optical axis of the XRT, and it acquires the data simultaneously with the XIS, although the HXD has a wider field-of-view ($32' \times 32'$ in 10–80 keV and $4^\circ \times 4^\circ$ in > 80 keV) than the XIS ($17' \times 17'$). Besides them, the X-ray spectrometer (XRS; Kelley et al. 2007) is mounted at the focal position of one unit of the XRT, but unfortunately, it did not work in orbit because of loss of its liquid helium coolant. Positions of these instruments on *Suzaku* are shown in Fig. 3.1, and more detailed descriptions of the XRS, the XIS and the HXD are given in §3.2, §3.3, and §3.4, respectively.

The high sensitivity, as the other specialty of *Suzaku*, is realized by the low-altitude orbit, where the effects of cosmic rays, including both primary particles from the Sun and outside the solar system, and secondary ones such as neutrons, become weak due to the earth magnetism. In addition, the HXD is designed to minimize the Cosmic X-ray background, residual cosmic-ray signals, and internal radio-activation and radio-isotopic background. Together with the wide-band coverage, the high sensitivity of *Suzaku* make it ideally suited to the studies of faint X-ray sources, such as active galactic nuclei.

3.2 The X-ray Telescope (XRT)

Because X-rays have index of refraction which is slightly less than unity, they could be focused by concave lenses, but the absorption would be unavoidable. Instead, they can be focused by total reflection (or the Bragg reflection), when they make "grazing" incidence onto a smooth reflector which is made of materials (mostly metals) with a high plasma frequency. Specifically, the incident angle from a reflector is limited to be less than 1 degree for a few keV X-ray, and the angle becomes smaller when the energy of X-ray higher.

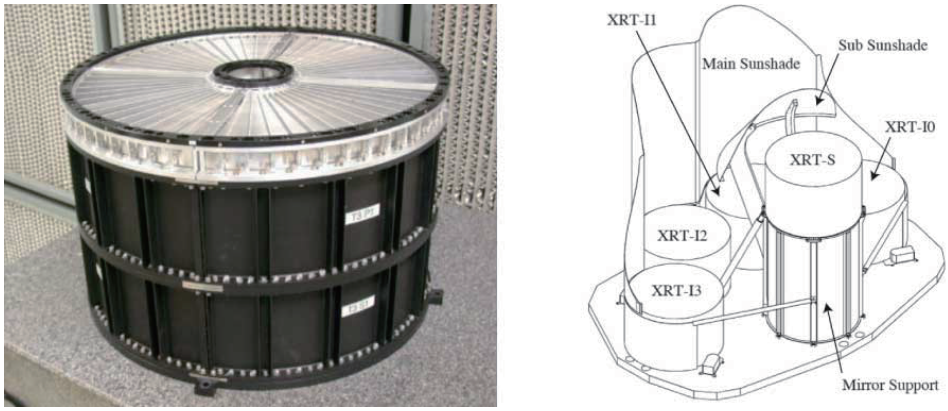

Figure 3.3: (Left) A photogragh of the XRT. (Right) Positions of the five XRT units at the top of the spacecraft. These figures are from Serlemitsos et al. (2007).

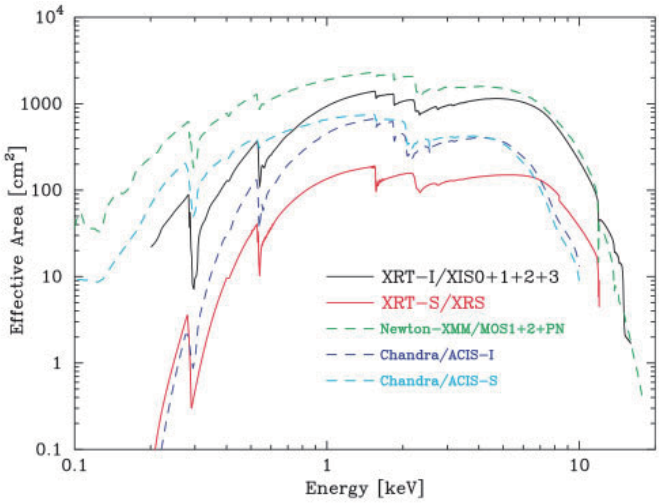

Figure 3.4: Black and red show a total effective area of the four XRT-I units and that of XRT-S, respectively. Green, blue and cyan represent those of *XMM-Newton*, the ACIS-I and the ACIS-S of *Chandra*, respectively (Serlemitsos et al. 2007). Transmissions of the thermal shield and the optical blocking filter, and the quantum efficiency of the CCD are all take into account.

Each XRT unit (Serlemitsos et al. 2007), shown in Fig. 3.3, has two-section cylindrical structures, approximating the type I Wolter optical system which consists of a hyperboloid and a paraboloid

reflectors. The diameter of a tubular structure is 40 cm, and focal lengths of the four XRT units for the XIS (called XRT-Is) and that for the XRS (XRT-S) are 4.75 m and 4.5 m, respectively. Thin aluminum replica mirrors were produced by replication technique (Serlemitsos, Soong 1996), and 175 pieces of them were concentrically nested for each XRT-I and 168 pieces for XRT-S. This afforded light X-ray telescopes with large effective areas as shown in Fig. 3.4.

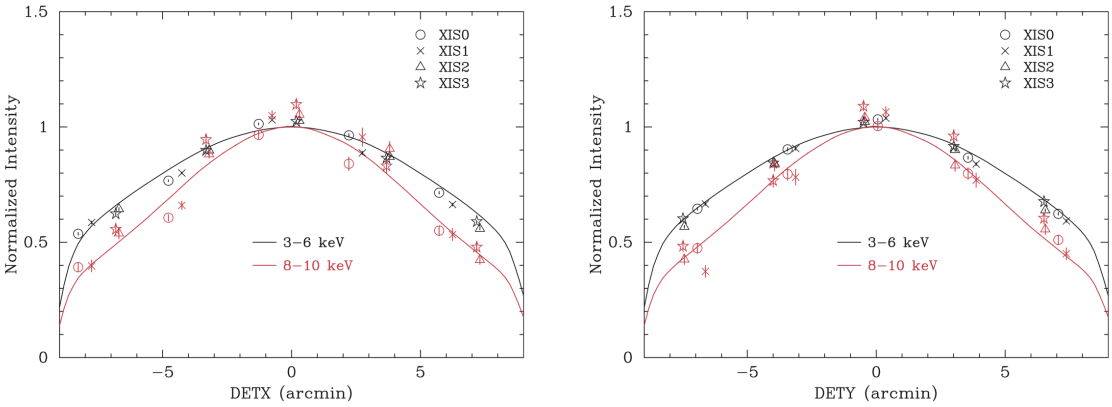

Figure 3.5: Vignetting of XRT-I, measured with 3–6 keV (black) and 8–10 keV (red) signals of the Crab Nebula on 2005 August 22–27 (Serlemitsos et al. 2007). The model curves were calculated with spectral parameters of $N_{\rm H} = 0.33 \times 10^{22}$ cm^{-2}, a photon index of 2.09, and a normalization of 9.85 photons cm^{-2} s^{-1} keV^{-1}. Sudden drops of the calculated curves shown in Fig. 3.5 at 8′ are due to the detector edge, rather than the XRT vignetting.

Important telescope capabilities include the effective area and the angular resolution. As shown in Fig. 3.4, the total effective area of the XRT is smaller in low energies than that of *XMM-Newton*. However, the *Suzaku* XRT retains a large effective area towards high energies up to 10 keV, and can be comparable with *XMM-Newton* in 6–10 keV, where the Fe-K line and edge structures appear, and high sensitivity is required to study them. This is a strong advantage of *Suzaku* in AGN studies. As to the angular resolution, the *Suzaku* XRT is characterized by a typical value of $\sim 2'.0$ in terms of half-power diameter, almost independent of the X-ray energy. This resolution is limited by the replication technique and by the conical approximation, and is about twice finer than that of the previous japanese X-ray satellite, *ASCA*.

Vignetting is another important characteristic of telescopes. As shown in Fig. 3.5, the effective area of the XRT decreases by ∼20% at $\sim 5'$ in 3–6 keV and at $\sim 3.5'$ in 8–10 keV. Because higher-energy photons have smaller reflection angles, they are more sensitive to vignetting than lower-energy ones. Thus, when an attitude of the satellite is shifted from the main target, count rates obtained in the higher energy bands are more affected than the those in the lower.

3.3 The X-ray Imaging Spectrometer (XIS)

The XIS utilized Charge Coupled Device (CCD), a two-dimensional semiconductor pixel array, for measuring the energy and two-dimensional position of individual X-ray photons. When a photon with an energy E enters a CCD, it is photo-absorbed with a certain probability (i.e., quantum efficiency), and a photoelectron is produced. The photoelectron collides against Si atoms, and generates electron-hole pairs. The number of the pairs are proportional to the incident energy, as $E/W_{\rm Si}$, where $W_{\rm Si} \sim 3.65$ eV is the averaged ionization energy of Si. Thus, counting the number of the pairs (equivalently, measuring their total charge), we can accurately measure the energy of the incident single photon.

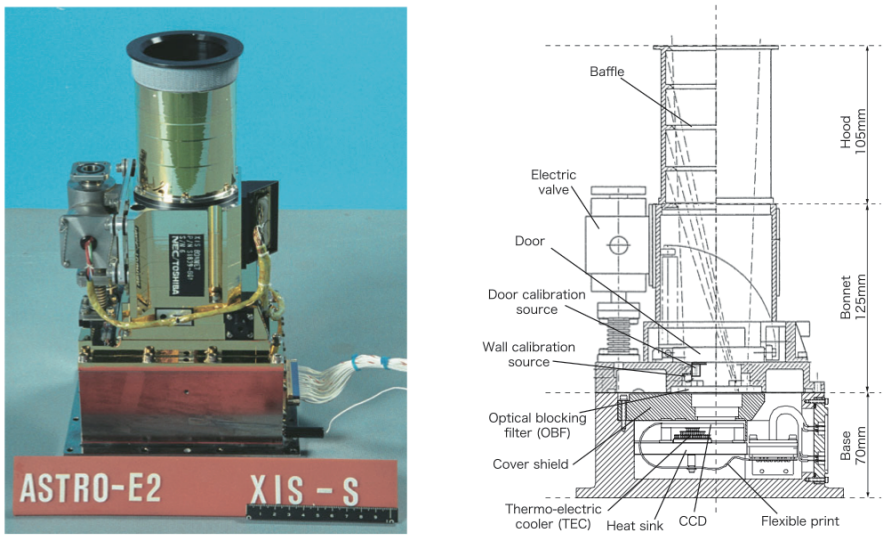

Figure 3.6: The picture (left) and a cross-sectional view (right) of the XIS onboard *Suzaku*. These figures are from Koyama et al. (2007).

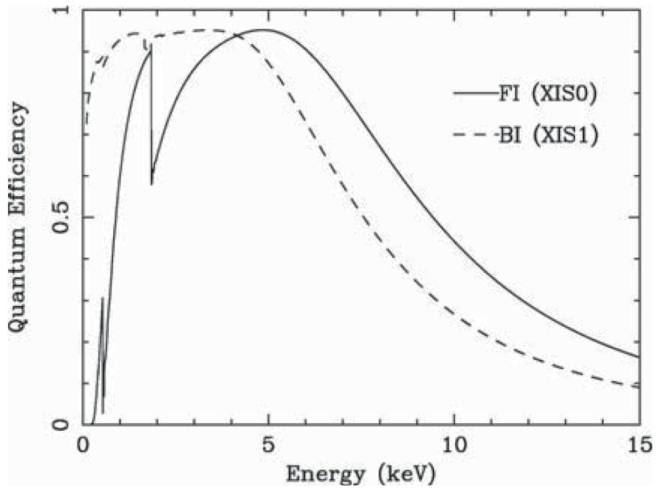

Figure 3.7: The quantum efficiency of XIS FI/BI (Koyama et al. 2007).

The XIS consists of four CCD cameras, operated independently in a photon-counting mode. They are named XIS0, 1, 2, and 3, and located on the focal plane of the corresponding XRT. XIS0, 2, and 3 utilized front-side illuminated (FI) CCDs, while XIS1 back-side illuminated (BI) one. Each CCD camera has a field of view of $17'.8 \times 17'.8$, as defined by the physical CCD size (25 mm$\times$ 25 mm) and the XRT focal length (4.75 m). Each of them has a time resolution in Normal mode of 8 sec, and an energy resolution of $\sim$ 130 eV at 6 keV. The effective area per camera at 1.5 keV is 330 (FI)/370 (BI) cm^{-2}, while that at 8 keV is 160 (FI)/110 (BI) cm^{-2}. Figure 3.6 shows the appearance of one of them. As shown in Fig. 3.7, quantum efficiency of the FI CCDs is lower and higher than that of the BI CCD at low and high energy, respectively. This is because photons enter from the electrode-side surface into an FI CCD, and low-energy photons are likely to be absorbed by the electrodes or the insulation layers.

In 2006 November 9, XIS2 suddenly stopped working, presumably due to a collision by a micro-meteorite. Furthermore, after launch, the low-energy effective area and the energy resolution have gradually been degrading, because of contamination by out gases from the satellite onto optical blocking filters of the cameras, and an increase of the charge transfer inefficiency, respectively. However, the energy resolution has been recovered nearly to its initial value, by artificially injecting charges to fill in lattice defects, which is called the spaced-row charge injection.

3.4 The Hard X-ray Detector (HXD)

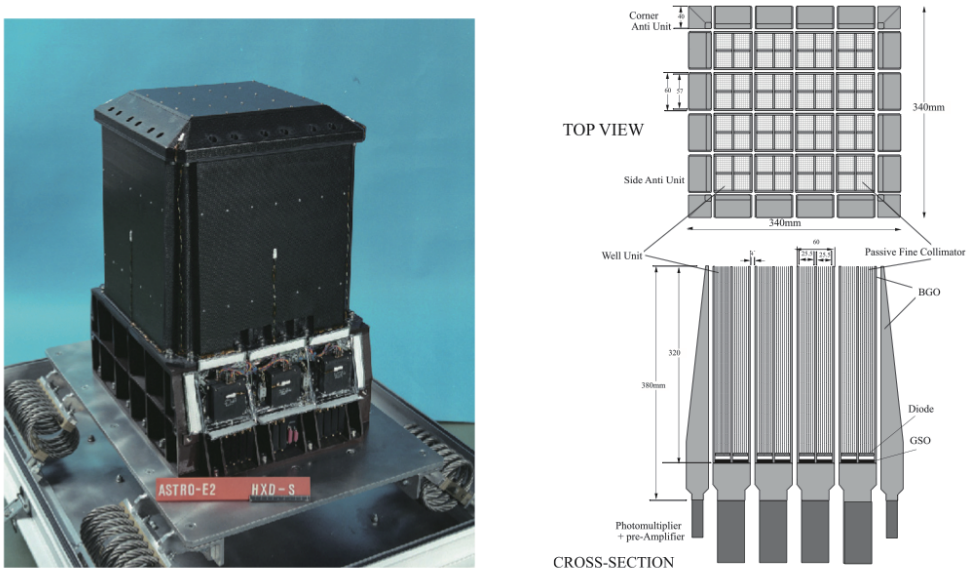

Figure 3.8: The appearance (left) and the cross-sectional view (right) of the HXD. These figures are from Takahashi et al. (2007).

The Hard X-ray Detector (HXD) covers the 10–600 keV broad band with an unprecedented sensitivity, and has an appearance as shown in Fig 3.8. In a hard X-ray band, signals from typical celestial

objects decrease rapidly toward higher energies, while the background signal does not. In the harder energy bands, the background elimination is therefore highly important. The background signals are composed of those entering through the field of view, those entering from outside the field of view and detector-intrinsic ones. The first component, dominated by the Cosmic X-ray background, can be reduced by a tightly collimated field of view of the HXD, which is shown in Fig. 3.8 (right). The second is cut by various anti-coincidence schemes, among 16 "Well-type" detector units, within each well type detector using phoswich technique, and between these 16 and surrounding 20 "Anti" detector units. The last component is eliminated using materials with least amount of natural radio-isotopes, and those which are not strongly radio-activated in orbit under bombardments with magnetically-trapped protons.

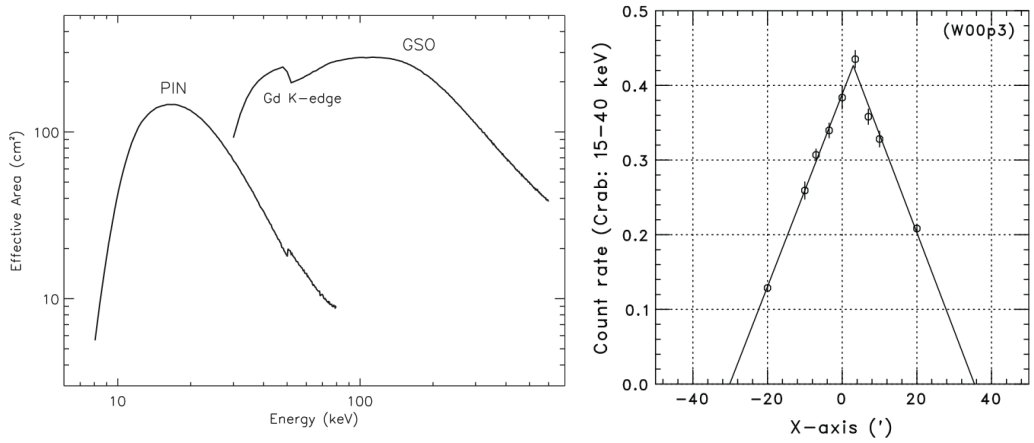

Figure 3.9: (left) The effective area HXD PIN/GSO (Takahashi et al. 2007). (right) The angular response of a file collimator along the satellite X-axis (Kokubun et al. 2007).

Each Well-type unit, serving as a main detector, has a stocked 2-layer detection part; 2 mm-thick silicon PIN diodes in front, and 5 mm-thick GSO scintillators behind. The former detects photons with energy of 10–70 keV, while those with higher-energy of 40–700 keV can pass through it and detected by the latter. The PIN and GSO elements are placed in a deep "well" formed by BGO scintillators, which act as an active shield. Scintillation light photons from the two types of inorganic scintillators, GSO and BGO, are read by a common phototube. The difference of fluorescence decay times between BGO ($\sim$ 300 ns) and GSO ($\sim$ 60 ns) together with pulse shape discrimination enables us to distinguish signals from the main detectors (GSO) and the shields. The BGO shields narrow down the field of view of the main detector as $4.^\circ5 \times 4.^\circ5$ in the PIN+GSO band ($\gtrsim$ 100 keV), and a passive fine collimator put in a well part of the unit makes it even narrower to $34' \times 34'$ in the lower-energy PIN band ($\lesssim$80 keV; the right of Fig. 3.9). Finally, the 20 Anti-detectors (Fig. 3.8 right) are also made by BGO crystals, and are individually read by a phototube.

Chapter 4

OBSERVATION AND DATA REDUCTION

4.1 Basic Strategy of the Research

The main theme of the present thesis is to study primary X-ray emission from the central engine of AGNs. For this purpose, we should focus on type I AGNs (type 1–1.9 in sub classification in §2.1.2). This is because they have absorption with a column density of $\lesssim 10^{21-22}$ cm^{-2} on their primary X-ray emission, which is generally much lower than those of type II objects with $\gtrsim 10^{23}$ cm^{-2}. As reviewed in Chapter 3, *Suzaku* is clearly the most appropriate satellite for this study, because of its simultaneous coverage of the $\sim$ 0.5–45 keV broad band of type I AGNs, where primary X-ray emission extends. Thus, the present thesis begins with searching the *Suzaku* archive for suitable AGNs.

Suzaku has been operated for $\sim$ 8 years, and observed many AGNs in the performance verification phase ($\sim$ 1 year after the launch) and the AO-1–7 cycles. All data sets include XIS and HXD data which were obtained simultaneously, and become public as the *Suzaku* archival data, 1 year after their observations. By 2013 March, $\sim$ 300 AGNs were observed ($\sim$ 350 datasets were obtained), and $\sim$ 100 of them are type I AGNs. However, these observations have been proposed and conducted by a large number of Principal Investigators under different objectives. As a result, the obtained data sets are quite inhomogeneous; the net exposure ($\sim$ 0.45 times gross pointing duration) varies form $\sim$ 10 ksec to $\sim$ 450 ksec, and the actual source intensity and variability were various. Some objects were observed many times, with a variety of intervals, while others were only once. Thus, the AGNs available in the *Suzaku* archive cannot be regarded as as a complete (e.g., flux-limited) sample defined in an objective way. Hence, we do not aim to make our research statistically complete in any sense. Instead, we survey the archive for a limited number of AGNs usable in the present thesis.

Along the above guideline, we produced light curves and spectra of all the $\sim$ 100 type I AGNs in the *Suzaku* archive, and selected 13 objects which are basically relatively bright and variable, with a sufficiently long exposure. More detailed selection criteria are given in §5.2 for soft-band study, and in §6.3 for hard-band investigation. Table 4.1 give a list (joint from Chapter 5 and 6) of AGNs to be analyzed in the present thesis.

Table 4.1: Information of the *Suzaku* data sets of AGNs analyzed in the present thesis.

Target name	Type	Obs. ID	Start time	Exposure	Nominal	ver.
MCG–6-30-15 #1	Sy1	100004010	2005/08/17 16:09:53	46698.7	XIS	2.0
NGC 3516 #1	Sy1	100031010	2005/10/12 13:57:09	134469.6	XIS	2.0
NGC 4051 #1	NLSy1	700004010	2005/11/10 19:14:14	119578.0	HXD	2.0
MCG–6-30-15 #2	Sy1	700007010	2006/01/09 03:20:12	143196.5	XIS	2.0
MCG–6-30-15 #3	Sy1	700007020	2006/01/23 12:0904	98483.4	XIS	2.0
MCG–6-30-15 #4	Sy1	700007030	2006/01/27 22:16:43	96691.9	XIS	2.0
Markarian 841 #1	Sy1	701084010	2007/01/22 08:45:44	51752.8	HXD	2.1
Markarian 841 #2	Sy1	701084020	2007/07/23 16:43:49	50925.3	HXD	2.1
Markarian 509 #1	Sy1	701093010	2006/04/25 18:47:44	24575.6	HXD	2.0
Markarian 509 #2	Sy1	701093020	2006/10/14 07:50:00	25929.8	XIS	2.0
Markarian 509 #3	Sy1	701093030	2006/11/15 09:00:13	24446.6	XIS	2.0
Markarian 509 #4	Sy1	701093040	2006/11/27 03:54:07	33094.4	XIS	2.0
NGC 5548 #1	Sy1	702042010	2007/06/18 22:28:15	31118.8	XIS	2.0
NGC 5548 #2	Sy1	702042020	2007/06/24 21:53:31	35915.2	XIS	2.0
NGC 5548 #3	Sy1	702042040	2007/07/08 10:02:55	30699.6	XIS	2.0
NGC 5548 #4	Sy1	702042050	2007/07/15 13:57:39	30019.7	XIS	2.0
NGC 5548 #5	Sy1	702042060	2007/07/22 10:40:25	28917.8	XIS	2.0
NGC 5548 #6	Sy1	702042070	2007/07/29 04:20:44	31809.9	XIS	2.0
NGC 5548 #7	Sy1	702042080	2007/08/05 00:37:46	38775.7	XIS	2.0
Fairall 9 #1	Sy1	7020430810	2007/06/07 03:43:52	167798.3	XIS	2.1
4C+74.26	RLQ	702057010	2007/10/28 10:21:17	91583.0	HXD	2.1
IC4329A #1	Sy1	702113010	2007/08/01 10:21:17	25453.4	XIS	2.1
IC4329A #2	Sy1	702113020	2007/08/06 00:41:45	30623.3	XIS	2.1
IC4329A #3	Sy1	702113030	2007/08/11 11:00:23	26895.9	XIS	2.1
IC4329A #4	Sy1	702113040	2007/08/16 11:48:47	24219.4	XIS	2.1
IC4329A #5	Sy1	702113050	2007/08/20 23:26:16	24026.2	XIS	2.1
3C382	BLRG	702125010	2007/04/27 23:05:29	130580.0	XIS	2.1
NGC 3227 #1	Sy1	703022010	2008/10/28 08:12:52	58917.2	XIS	2.2
NGC 3227 #2	Sy1	703022020	2008/11/04 03:36:31	53699.5	XIS	2.2
NGC 3227 #3	Sy1	703022030	2008/11/12 02:48:55	56577.2	XIS	2.2
NGC 3227 #4	Sy1	703022040	2008/11/20 17:00:00	64567.9	XIS	2.2
NGC 3227 #5	Sy1	703022050	2008/11/27 21:29:20	79429.8	XIS	2.2
NGC 3227 #6	Sy1	703022060	2008/12/02 14:28:03	51410.5	XIS	2.2
NGC 4051 #2	NLSy1	703023010	2008/11/06 07:39:03	274530.5	XIS	2.2
NGC 4051 #3	NLSy1	703023020	2008/11/23 16:47:60	78385.5	XIS	2.2
MCG-2-58-22	Sy1	704032010	2009/12/02 22:36:33	138968.8	XIS	2.4
MR2251-178	RQQ	704055010	2009/05/07 03:28:24	136924.0	XIS	2.3
NGC 3516 #2	Sy1	704062010	2009/10/28 05:35:15	251355.5	HXD	2.4

Table 4.1: Information of the *Suzaku* data sets of AGNs analyzed in the present thesis.

Markarian 509 #5	Sy1	705025010	2010/11/21 14:17:42	102120.5	XIS	2.5
Fairall 9 #2	Sy1	705063010	2010/05/19 03:00:49	229296.3	HXD	2.5
Markarian 841 #3	Sy1	706029010	2012/01/05 20:45:03	244351.8	XIS	2.7
Markarian 841 #4	Sy1	706029020	2012/01/18 18:18:03	110289.0	XIS	2.7

4.2 Data Reduction

For all the AGNs listed on Table 4.1, we retrieved the XIS (§3.3) and HXD (§3.4) data from the *Suzaku* archive. In the present thesis, the data of XIS 0, 2 and 3 (after 2006 November, XIS 0 and 3 only), which use FI CCD chips (§3.3), were added and used as XIS FI data. The data from XIS 1 were not analyzed, since it uses a BI CCD (§3.3), and has a relatively high and unstable background. On-source events of the three or two XIS FI cameras were extracted from a circular region of $120''$ radius centered on each source. Background events were accumulated on a surrounding annular region of the same camera, with the inner and outer radii of $180''$ and $270''$, respectively. The response matrices and ancillary response files were produced by `xisrmfgen` and `xissimarfgen` (Ishisaki et al. 2007), respectively.

In a similar way, we prepared events of HXD-PIN which covers a 10–70 keV range (§3.4). Non X-ray Background (NXB) contained in the data was estimated by analyzing a set of fake events which were created by a standard NXB model (Fukazawa et al. 2009). The on-source events and the NXB events were analyzed in the same manner, and the latter was subtracted from the former. In addition, the contribution from Cosmic X-ray Background (CXB; Boldt et al. 1987) was estimated and also subtracted from the on-source data. This was conducted using the HXD-PIN response to diffuse sources, assuming the spectral CXB surface brightness model determined by HEAO 1 (Gruber et al. 1999): $9.0 \times 10^{-9} (E/3 \text{ keV})^{-0.29} \exp(-E/40 \text{ keV})$ erg cm^{-2} s^{-1} str $^{-1}$ keV^{-1}, where E is the photon energy. The estimated CXB count rate amounts to 5% of the NXB signals, in agreement with Kokubun et al. (2007).

Although a higher energy range above $\gtrsim$ 70 keV is covered by HXD-GSO (§3.4), we do not use these data here for the following two reasons. One is that the AGN signals are very weak in this high energy region. The other is that the GSO background is significantly more variable (Fukazawa et al. 2009; Kokubun et al. 2007) than that of HXD-PIN, and such artificial variations make our analysis rather difficult.

Chapter 5

SOFT X-RAY ANALYSIS

The central objective of the present thesis is to decompose the AGN X-ray emission into its constituent components, in as model-independent and general manner as possible. As already touched on in §2.3.7, many such attempts have been made in "static" ways, by theoretically modeling the spectal shapes of these components and combining them to explain observed X-ray spectra. However, many different interpretations degenerate, due to insufficient data statistics and due to our limited knowledge in such spectral modeling. An alternative approach has been to utilize time variations, including the difference spectrum method and the RMS variation methods (§2.3.5). However, it has been difficult to obtain a complete spectral decomposition with these methods. In this Chapter, we hence develop a novel method of "dynamical" spectroscopy that fully combines the spectrum and timing information, and apply it to a soft X-ray energy band below ~ 3 keV of several AGNs. The analysis is meant to understand the nature of so-called soft excess phenomena which have long remained as a mystery.

5.1 Analysis of the Bright Type I Seyfert Markarian 509

Markarian 509 (hereafter Mrk 509) is a bright and typical Seyfert galaxy that exhibits a strong soft X-ray excess structure (Cerruti et al. 2011). In order to understand prototypical behavior of the soft excess, and to establish a novel timing method to analyze it, we first focus on this AGN. It has a redshift of z=0.034, and located at a Galactic latitude of 42° with a relatively low line-of-sight Galactic absorption of $N_{\rm H} = 4.4 \times 10^{20}$ cm^{-2} (Stark et al. 1987). Its estimated BH mass, $\sim 1.4 \times 10^8$ $M_\odot$ (Peterson et al. 2004), and a typical 0.5–2 keV luminosity of 1.0×10^{44} erg s^{-1}, indicate an Eddington ratio of 0.1 (Vasudevan & Fabian 2009).

5.1.1 Light curves

To grasp variation characteristics (with possible energy dependence) of Mrk 509, we made background-subtracted light curves in three bands; 0.5–3 keV (soft band) and 3–10 keV (middle band) using XIS FI, and 15–45 keV (hard band) using HXD-PIN. As shown in Fig. 5.1, the source thus exhibited more than $\sim 10\%$ variations in the softer two energy bands, with apparently tight correlations between them. The 0.5–3 keV variation tend to exhibit slightly larger relative amplitudes than the 3–10 keV

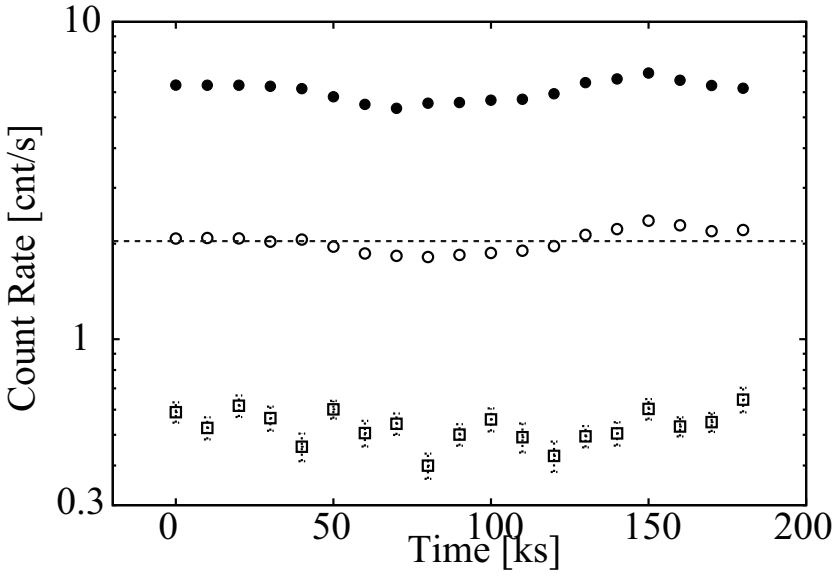

Figure 5.1: Background-subtracted and dead-time corrected light curves of Mrk 509, with 10 ks binning in the 0.5–3 keV (filled circles), 3–10 keV (open circles), the 15–45 keV band (open squares), with the last one multiplied by a factor of 5. 1σ errors of the XIS data points are all less than 0.04 cnt s^{-1}, and smaller than the plotting symbols. Dotted lines show the average 3–10 keV count rates.

one, while any time lag between them is within ~ 1 ksec. On the other hand, the hard-band light curve do not show clear correlations with those in the softer bands, possibly involving rather uncorrelated variations. The behavior of the HXD signals is investigated in Chapter 6.

5.1.2 Difference spectrum analysis

What is spectral shape of the component which produced the soft-band variations in Fig. 5.1? For this purpose, we divide the data into High and Low phases, in which the data are above and below the dotted line in Fig. 5.1, respectively. Then, we accumulate High- and Low-phase spectra, and subtract the latter from the former, to extract a difference spectrum. This method is called "difference spectrum analysis", and has often been utilized to identify the main variable component in AGNs (e.g., Miniutti et al. 2007), as well as in black-hole binaries (Makishima et al. 2008) and accreting neutron stars (Mitsuda et al. 1984).

Figure 5.2 shows the difference spectrum of Mrk 509. In order to approximately remove the instrumental responses (§3.3-3.4; particularly energy-dependent detection efficiencies) of the XIS and the HXD, the result is presented in the form of ratios to a common simulated spectrum, which is generated assuming an input power-law (PL) spectrum with a photon index of $\Gamma = 2.0$. There, the time-averaged spectra (black) are also shown in the same style. These spectral presentations are identical to the νF_ν form, except that the effects of finite energy resolutions of the detectors still remain. The derived difference spectrum looks like a single PL with $\Gamma < 2$, without strong spectral features such as Fe-K lines which can be clearly seen in the time-averaged spectrum. In addition,

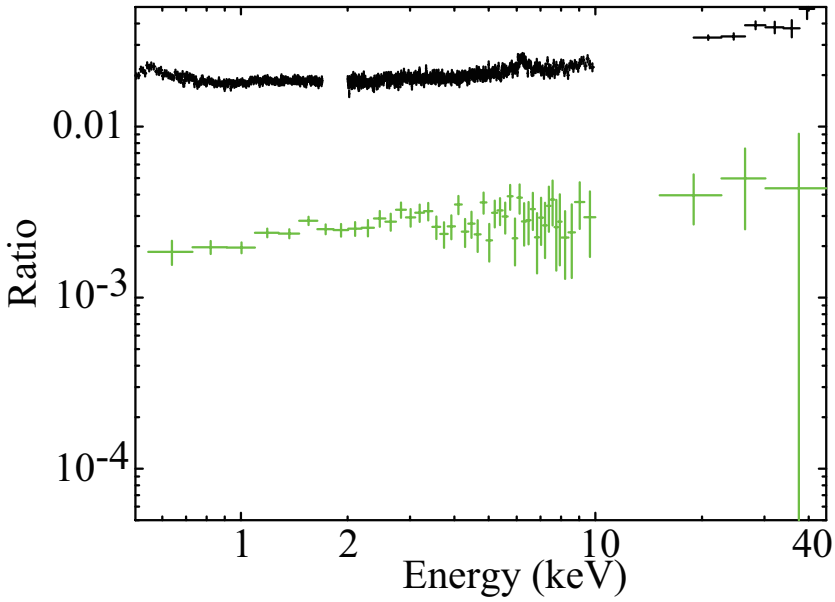

Figure 5.2: The difference spectrum of Mrk 509 (green) in a form of the $\Gamma = 2.0$ PL ratio, obtained by subtracting Low- from High-phase spectra. Black data points show the time-averaged spectrum in the same form. Here and hereafter, the data points below and above ~ 10 keV are from the XIS and the HXD, respectively.

the difference spectrum lacks the upturn in $\lesssim 1$ keV seen in the other spectrum. In other words, the difference spectrum is considered to lack the soft excess structure that is observed in the average spectrum.

To quantify the spectral shape of the difference component, we utilize the process called spectral fitting. Specifically, an assumed spectral model, with a certain number of free parameters, is convolved through the instrumental responses (§3.3), and the obtained simulated data (or model prediction) are compared with the actual data through chi-square tests. Then, the optimal values of the free parameters are searched to minimize the chi-square value, and it is examined whether the model can be accepted or ruled out. Hereafter, we employ an acceptance level to be the null hypothesis probability $N_{\rm P} = 1\%$ in the chi-square test.

We assumed an absorbed-PL model, `Phabs*PL` where `Phabs` represents a photoelectric absorption factor due to neutral matter of cosmic abundance (Morrison & McCammon 1983), and `PL` a PL model, and fitted the difference spectrum with the model. This particular model has three free parameters; the equivalent hydrogen column density $N_{\rm H}$ of `Phabs`, as well as the normalization and the photon index Γ of PL. (See Appendix A for details of XSPEC12 models utilized in the present thesis.) The XIS and HXD data were fitted with the same model with a common parameter set, and the chi-square was calculated over the entire XIS and HXD data points. This is a process called "simultaneous fitting". Figure 5.3 shows the result of the fit in a νF_ν form, wherein ordinate is in a unit of keV^2(Photons cm^{-2} s^{-1} keV^{-1}). Like in the ratio to the $\Gamma = 2.0$ PL, the XIS and HXD responses have been removed in this representation. Furthermore, the results are approximately corrected for the effects of the

finite energy resolution (called deconvolution). The νF_ν results, however, depend on the employed model (so-called obliging effects). Hereafter, we show fitting results in this presentation, while spectra without fitted by a model in the $\Gamma = 2.0$ PL ratio.

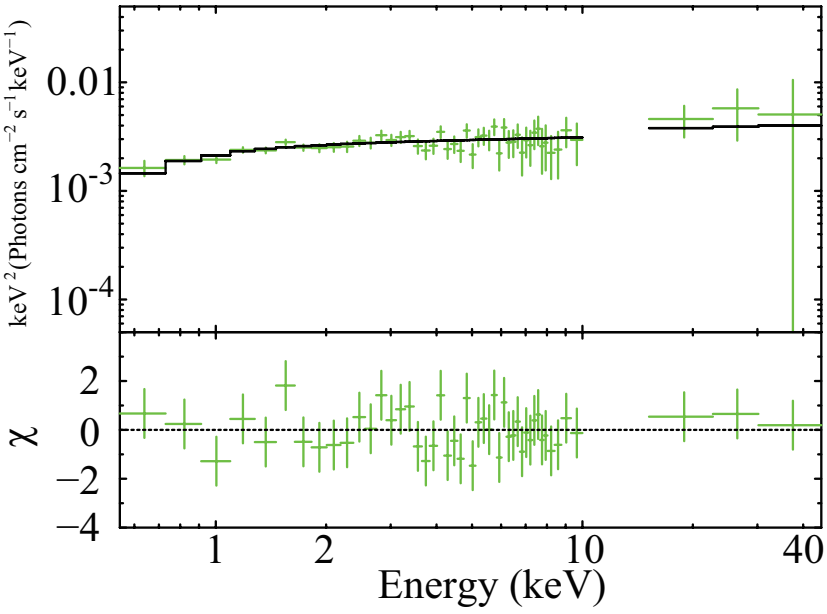

Figure 5.3: (Top) The difference spectrum of Mrk 509 (green) in a νF_ν form, fitted with the `Phabs*PL` model (black). (Bottom) Fit residuals obtained by subtracting the model from the data.

As shown in Fig. 5.3 and Table 5.1, the fit was acceptable with χ^2/d.o.f. $= 31.46/45$. Thus, the varying component in Mrk 509 has been successfully reproduced with a weakly-absorbed PL model. Because the absorption makes the model to have a convex shape, the varying component cannot fully explain the concave shape of the time-averaged spectrum in the soft X-ray band (Fig. 5.3), and another signal component should be necessary. In principle, we could then assume an absorbed PL with $\Gamma = 1.52$ having a free normalization, and introduce another softer model component, so that their sum can reproduce the overall spectrum. However, the undetermined normalization of the $\Gamma = 1.52$ PL leaves large freedom in the fitting.

Table 5.1: Results in the fits to the difference and variable spectra of Mrk 509.

Model	Parameter	Difference (§5.1.2)	Variable (§5.1.5)
`Phabs`	$N_{\rm H}^{*}$	0.08 ± 0.05	< 0.21
`PL`	Γ	$1.92^{+0.09}_{-0.08}$	$1.91^{+0.41}_{-0.29}$
	$E_{\rm cut}$ (keV)	200 (fix)	
	$N_{\rm PL}^{\dagger}$	$2.60^{+0.30}_{-0.26}$	$1.64^{+0.66}_{-0.34}$
χ^2/d.o.f.		31.46/45	3.51/4

* Equivalent hydrogen column density in 10^{22} cm^{-2}.

† The cutoff power-law normalization at 1 keV, in units of 10^{-3} photons keV^{-1} cm^{-2} s^{-1}.

5.1.3 Count-count plot

In order to more thoroughly identify different X-ray emission components of Mrk 509, we focus on the energy-dependent variations shown in Fig. 5.1. To quantify the correlations in the softer two energy bands therein, we made a Count-Count Plot (CCP), in which abscissa, denoted x, is the 3–10 keV band XIS FI count rate, and ordinate, denoted y, is that in the 0.5–3 keV, with a bin size of 10 ksec. This bin with was chosen to be short enough to resolve the variations seen in Fig. 5.1, and long enough to achieve sufficient photon statistics. The reference band, 3–10 keV, was chosen because the soft excess phenomenon usually vanish in $\gtrsim 2.5$ keV (e.g., Risaliti & Elvis 2004). Later in §7.1.3, we show that the spectral decomposition remains unaffected even if we use 2–3 keV for the reference band.

In the derived CCP, shown in Fig. 5.4, x and y are indeed correlated tightly, and in addition, rather linearly. To examine the correlation in a more quantitative way, we fitted the data in the CCP with one straight line, expressed as

$$y = Ax + B, \tag{5.1}$$

in which the two parameters, A and B, were both left free. The reason why we here employ a linear correlation assumption rather than a curved function like an exponential is threefold. One is that typical weakly-absorbed Seyfert galaxies were reported to exhibit CCPs with a straight distribution (e.g., Taylor et al. 2003; Noda et al. 2013b). Actually, later in Chapter 6, we show that CCPs of more variable Seyferts exhibit linear data distributions. Secondly, assuming a straight line in the fit to the CCP has a simple physical meaning, that the main variable component varies only in its normalization without any spectral shape change, and there is no other variable components, although this might not be always true. Finally, there is no clearly justifiable non-linear function to fit the distribution.

Here, a systematic error of 1% was included to the 0.5–3 keV XIS FI count rate, to consider uncertainties in the CCD contamination (§3.3) which varies as the source moves on the focal plane by attitude jittering. The fit goodness was evaluated by the chi-square test, in which we combined both x and y errors as $\sigma = \sqrt{\sigma_y^2 + (a\sigma_x)^2}$ where σ_x and σ_y are 1-sigma statistical errors associated with x and y, respectively.

As a result, with χ^2/d.o.f. $= 32.0/17$, the data distribution in the CCP has been reproduced successfully with eq. (1). This property can be explained assuming that Mrk 509 has a single spectral component which varies in its intensity, but not in its spectral shape. The derived slope and offset are $A = 2.60 \pm 0.19$ and $B = 0.87 \pm 0.37$ cnt s^{-1}, respectively; They are significantly positive (at more than 90% confidence level). To examine how the results are affected by a bin size in the CCP, we repeated the same fits employing bin widths of 5 ksec, 20 ksec, and 25 ksec. As a consequence, these fits gave slopes and offsets which are consistent, within 1σ errors, with those in the case of 10 ksec. Since we thus confirmed that the results are not affected strongly by the bin size in the CCP, we conduct the subsequent analyses with a bin size of 10 ksec.

To be rigorous, the fit goodness of 34.7/17 is somewhat poor, with a null-hypothesis probability

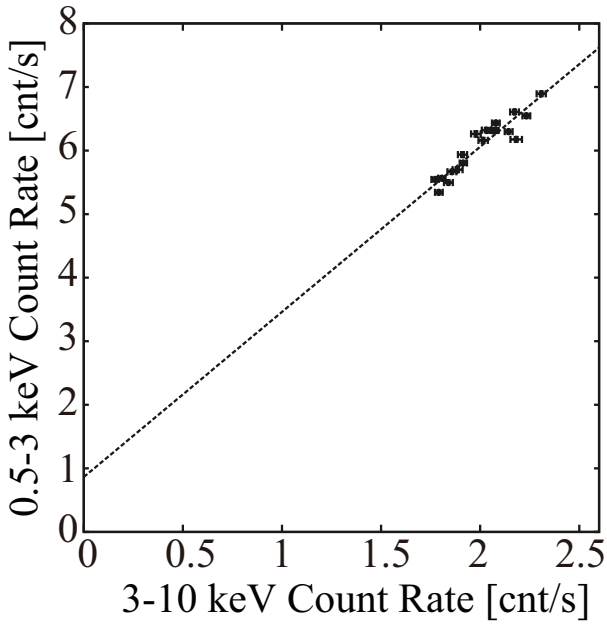

Figure 5.4: The CCP of Mrk 509, in which abscissa gives NXB-subtracted XIS FI count rate in 3–10 keV, while ordinate gives that in 0.5–3 keV. All data are binned into 10 ksec. The error bars represent statistical $\pm 1\sigma$ range. The dotted straight line refers to eq. (1).

of 0.7%. This is mainly due to 3 deviating data points, which are likely affected by changes in the warm absorber. Excluding them gives χ^2/d.o.f.= 19.9/14, while the values of A and B are still same as before within errors.

5.1.4 Count-count correlation with positive offset (C3PO) method

The two parameters, A and B, of eq. (1) reflect energy dependence of the observed variability. Since the 0.5–3 keV count statistics are high enough, we may divide it into multiple energy bands, and study this issue in further details. Thus, we divided the 0.5–3 keV band into seven finer bands, 0.5–0.8 keV, 0.8–1 keV, 1–1.2 keV, 1.2–1.4 keV, 1.4–1.7 keV, 1.7–2 keV, and 2–3 keV, and made seven additional CCPs. In the derived CCPs shown in Fig. 5.5, abscissa is again the 3–10 keV count rate, while ordinate is those in the seven finer soft X-ray bands. In the same way as in Fig. 5.4, we fitted these CCPs with eq. (1), and obtained Table 5.2. The CCPs exhibit strong correlations, and the fits with eq. (1) are successful. All CCPs exhibit positive slopes ($A > 0$) and offsets ($B > 0$). Furthermore, as seen in Table 5.2, the values of A and B, when summed over the 7 bands, becomes consistent with those in the originate 0.5–3 keV band. As described in §5.1.5 and §5.1.6 below, the values of A and B in Table 5.2 allows us to decompose data into a variable and a stationary components. Hereafter, we call this spectrum-decomposing method the Count-Count Correlation with Positive Offset (C3PO) method.

This method was first introduced by Churazov et al. (2001) to analyze the data of the leading black-hole binary, Cyg X-1. It was then applied to AGNs by Taylor et al. (2003). The method has

Table 5.2: Parameters obtained by fitting 7 CCPs in Fig. 5.5 with eq. (1).*

Energy range (keV)	A	B (counts s^{-1})	χ^2/d.o.f.
0.5–0.8	0.15 ± 0.03	0.14 ± 0.05	32.1/17
0.8–1	0.27 ± 0.03	0.17 ± 0.05	30.3/17
1–1.2	0.37 ± 0.04	0.19 ± 0.06	27.9/17
1.2–1.4	0.41 ± 0.04	0.11 ± 0.07	30.4/17
1.4–1.7	0.56 ± 0.04	0.03 ± 0.07	22.2/17
1.7–2	0.31 ± 0.03	0.07 ± 0.06	34.7/17
2–3	0.55 ± 0.04	0.02 ± 0.06	20.1/17
Sum	2.60 ± 0.19	0.87 ± 0.37	–

* Errors refer to 1σ confidence limits.

been then significantly developed by Noda et al. (2011b, 2013a, and 2013b), to a level where it can be used to accurately qualify the decomposed spectra. Below, we follow the latest method by Noda et al. (2013b).

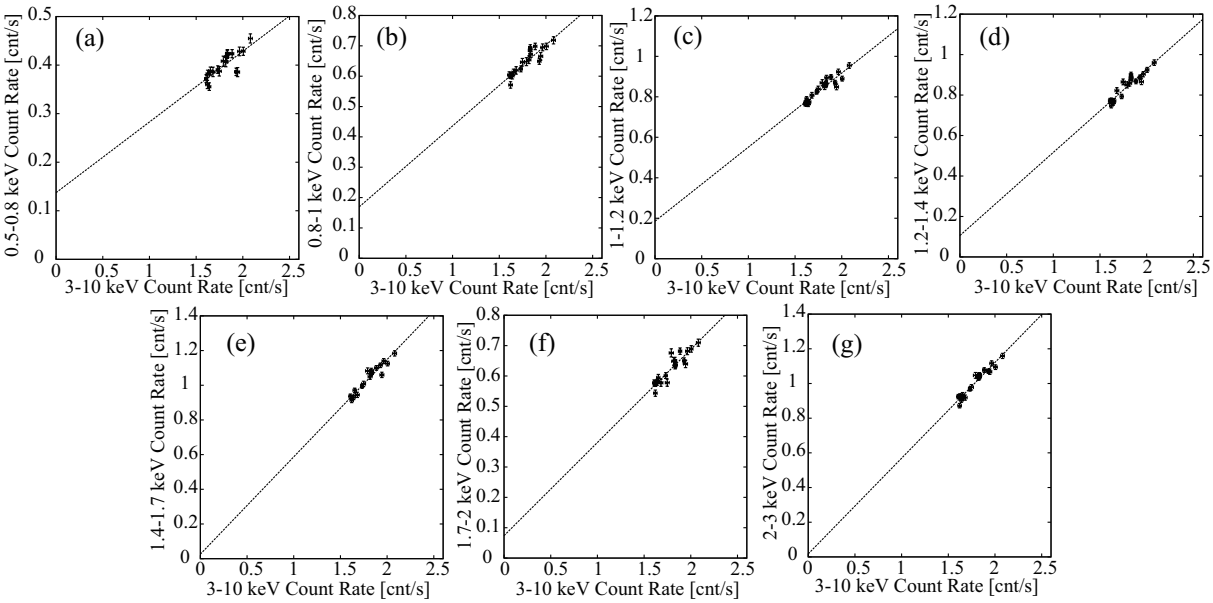

Figure 5.5: The CCPs of Mrk 509 in the seven finer soft X-ray bands. In all panels, abscissa is the 3–10 keV count rate like in Fig. 5.4, while ordinate gives NXB-subtracted XIS FI count rate in (a) 0.5–0.8 keV, (b) 0.8–1 keV, (c) 1–1.2 keV, (d) 1.2–1.4 keV, (e) 1.4–1.7 keV, (f) 1.7–2 keV, and (g) 2-3 keV.

5.1.5 Variable component

We have obtained seven values of A (Table 5.2) which cover the 0.5–3 keV energy range. Since this parameter represents the data-distribution slope in each CCP, a larger/smaller value of A would mean that this particular energy band is more/less sensitive to the time variation, in a sense relative to the higher 3–10 keV band. Therefore, we can construct a 0.5–3 keV "spectrum" by collecting the 7 values of A, dividing them by the corresponding energy intervals, and then multiplying the average count

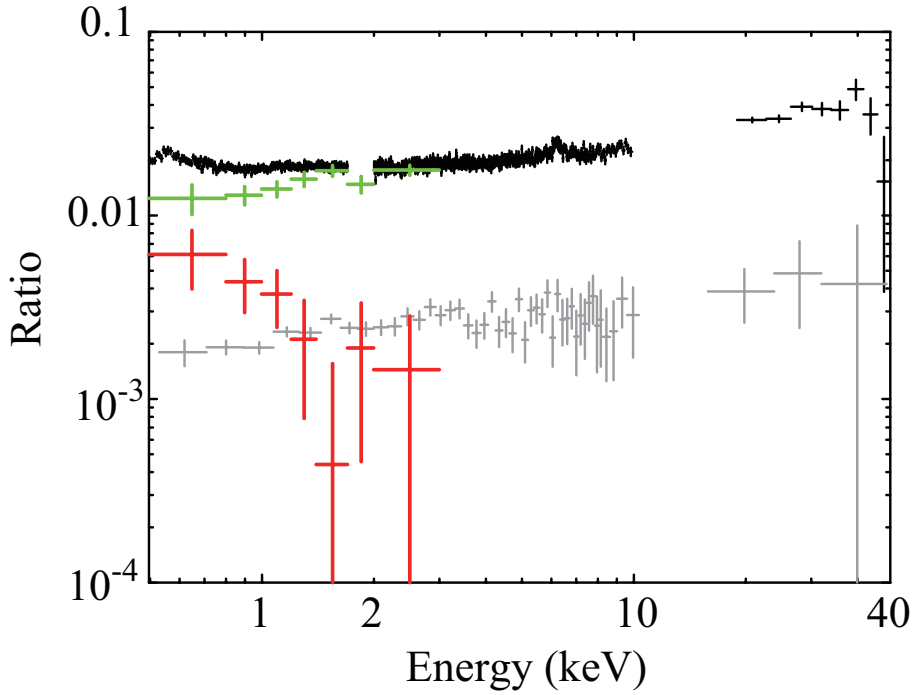

Figure 5.6: Time-averaged (black), difference (grey; the same as Fig. 5.2), variable (green), and stationary spectra (red) of Mrk 509, in a form of ratios to a common $\Gamma = 2$ PL.

rate x_0 in the reference 3–10 keV band. As seen in Fig. 5.1, the value of x_0 is ~ 1.90 cnt s^{-1}. The results, which we hereafter call a "variable component" or "variable spectrum", is plotted in Fig. 5.6 in green, after divided by the same $\Gamma = 2.0$ PL used to normalize the difference spectrum in Fig. 5.2.

As observed in Fig. 5.6, the variable spectrum is featureless, and exhibits, at least up to 3 keV which is the upper energy band, nearly the same shape as the difference spectrum which is reproduced in grey. Accordingly, we fitted the variable spectrum with the same `Phabs*PL` model. The results, given in Table 5.1, confirms that the values of $N_{\rm H}$ and Γ are consistent, within errors, with those derived from the difference spectrum (already given in the same table). Thus, the reliability of the C3PO method has been confirmed by the traditional timing analysis. Furthermore, the normalization of the variable component is meaningful in its absolute value, while that of the difference spectrum is not. This means that the C3PO method can take over the traditional difference spectrum method.

5.1.6 Stationary component

Offsets B of eq. (1), divided by the corresponding energy intervals, define a stationary spectrum in the 0.5–3 keV band. In Fig. 5.6, we show it in red, as a ratio to the same $\Gamma = 2$ PL as the difference and the variable spectra. As expected from the CCPs which show larger offsets B in lower energy bands, the stationary component has a soft spectral shape. Then, what kind of physical process is responsible for this soft spectrum? To examine this, we fitted it with five possible models which are often used to describe the soft excess structures (§2.3.2);

1. power law function (`PL`), which is a phenomenological model to represent the general spectral slope,

2. multi-color disk emission (`Diskbb`), emitted by an optically-thick accretion disk as a superposition of black body components with different temperature,

3. thin-thermal plasma emission (`TTP`), generated by a hot gas filling a rather large (often non-AGN) region of the host galaxy,

4. relativistically-blurred ionized reflection (`RBR`), generated via reflection of the primary emission by an inner region of the accretion disk, where the gravitational effects of the central black hole is significant

5. thermal Comptonization (`Compton`), generated in a coronal region that is independent of that emits the variable component.

All these fits incorporated the neutral absorption factor, `Phabs`, with the column density again fixed at a value of 4.4×10^{22} cm^{-2} which represents the Galactic line-of-sight column density (§5.1). Furthermore, the redshift was fixed at 0.034. In the fit with `PL`, the photon index and the normalization were both left free. The `Diskbb` model was fitted with the disk temperature and the normalization left free. When `TTP` is employed, the abundance was fixed at 0.5 Solar, while the plasma temperature and the normalization were left free. In the fit with `RBR`, the photo index of the incident power law continuum was fixed at 2, the emissivity index at 3, the inclination at 30°, the Fe abundance at 1 Solar, and the inner and outer disk radii of a disk were at 1.24 $R_{\rm g}$ and 400 $R_{\rm g}$, respectively, while the ionization parameter and the normalization were left free. Finally, to perform the `Compton` fit, the seed photon temperature was fixed at 20 eV to simulate typical disk emission, and the geometry of the electron cloud was assumed to be plane like, while the electron temperature, the optical depth, and the normalization were left free.

The five models all yielded acceptable fits to the stationary spectrum, and gave the parameters summarized in Table 5.3. The photon index turned out to be ~ 4, which is much softer than that of the variable component (~ 1.9), and the typical slope, ~ 1.7, of many AGNs. Alternatively, the data were reproduced by thin-thermal emission with a temperature of $\sim$ 1 keV. The relativistically-smeared reflection model was successful on the condition that the reflection is generated by an extremely-relativistic and moderately-ionized accretion disk. When we employ the thermal Comptonization model, `Compton`, the additional coronal region was required to have an electron temperature of $\lesssim 0.5$ keV, and the optical depth of $\gtrsim 16$. Although `Diskbb` can explain the stationary emission, hereafter we do not consider this alternative, since the obtained disk temperatures of ~ 0.2 keV are an order of magnitude higher than the expected temperature of an inner edge of the accretion disk, calculated by eq.(2.5) to be $\sim$ 20 eV for a black hole mass of 10^8 $M_\odot$ and an accretion rate of 10% of the Eddington limit. The power-law modeling may not be considered either, since this phenomenological model was employed only to evaluate the approximate spectral softness, and has no particular physical

meanings. Thus, the remaining interpretations for the soft stationary component are a thin-thermal plasma emission, a relativistically-smeared reflection, and a thermal Comptonization.

Table 5.3: Parameters, with 90%-confidence errors, obtained by fitting the soft stationary spectrum of Mrk 509.

Model	Parameter	Value
`PL`	Γ	$3.96^{+1.15}_{-1.03}$
	$N^{*}_{\rm PL}$	$4.00^{+1.22}_{-1.24}$
	χ^2/d.o.f.	2.03/5
`Diskbb`	$T_{\rm disk}$ (keV)	$0.21^{+0.11}_{-0.06}$
	$N^{\dagger}_{\rm disk}$	
	χ^2/d.o.f.	2.52/5
`TTP`	A ($Z_{\odot}$)	0.5 (fix)
	kT (keV)	$0.6^{+0.7}_{-0.2}$
	$N^{\ddagger}_{\rm TTP}$	$5.38^{+4.52}_{-2.18}$
	χ^2/d.o.f.	3.89/5
`RBR`	$q^{\#}$	3 (fix)
	$R_{\rm in}$ ($R_{\rm g}$)	1.24 (fix)
	$R_{\rm out}$ ($R_{\rm g}$)	400 (fix)
	$A_{\rm Fe}$ ($Z_{\odot}$)	1 (fix)
	$\xi^{\S}$	< 620
	z	0.0344 (fix)
	$N^{||}_{\rm RBR}$	0.13 ± 0.04
	χ^2/d.o.f.	1.89/4
`Compton`	z	0.0344 (fix)
	$T_{\rm e}$ (keV)	$0.45^{+45.57}_{-0.31}$
	τ	$16.5(> 4.6)$
	$N^{\#}_{\rm Compton}$	4.68 ± 1.42
	χ^2/d.o.f.	2.19/4
	L^{**}	$5.1^{+2.1}_{-2.5}$

* The cutoff power-law normalization at 1 keV, in units of 10^{-3} photons keV^{-1} cm^{-2} s^{-1} at 1 keV.

† The `diskbb` normalization, in $((R_{\rm in}/{\rm km})/(D/10\ {\rm kpc}))^2 \cos\theta$, where $R_{\rm in}$ is the inner disk radius, D the distance to the source, and θ the angle of the disk.

‡ The `TTP` normalization, in units of $(10^{-17}/4\pi(D_{\rm A}(1+z))^2) \int n_{\rm e} n_{\rm H} dV$, where $D_{\rm A}$ is the angular size distance to the source (cm), $n_{\rm e}$ and $n_{\rm H}$ are the electron and H densities (cm^{-3}).

§ The ionization parameter, in units of erg cm s^{-1}.

|| The `RBR` normalization, in units of 10^{-5} photons keV^{-1} cm^{-2} s^{-1} at 1keV.

The `Compton` normalization, in units of photons keV^{-1} cm^{-2} s^{-1} at 1 keV.

** The 0.5–3 keV luminosity of the extracted soft stationary emissions, in units of 10^{43} erg s^{-1}.

5.1.7 Overall spectral fitting

Our final step of the analysis of the 2010 Mrk 509 data (Noda et al. 2011b) is a procedure to be called "simultaneous model fitting to the spectrum triplet", where "triplet" means the C3PO-derived variable and stationary spectra, plus the time-averaged 0.5–45 keV data. Specifically, we select a typical two-

component spectral model, requiring the first component to reproduce the variable spectrum, the second one to successfully describe the stationary signals, and their sum to give an acceptable fit to the time-averaged spectrum. Considering the triplet in this way has dual advantages. One of them is that the time-averaged data may be reproduced by many different two-component models, but this degeneracy is expected to be reduced because some of these models may fail to express (either one or both of) the C3PO-derived spectra.

Let us explain the other merit of the simultaneous triplet fitting. The slope A and the offset B derived with the C3PO method have large errors when the source variation is small. As long as we individually analyze the variable and the stationary components, the large errors permit many different models to be acceptable, and make it difficult for us to distinguish them. Actually, in §5.1.7, we were not able to arrive at a unique interpretation of the stationary component. However, we expect the C3PO-extracted two spectra to add up to become identical to the time-averaged spectrum, because taking the time average (denoted by $<\ >$) of eq. (5.1) gives

$$< y >= A < x > +B. \tag{5.2}$$

Since the errors associated with A and B tend to cancel out in this summation, we can make the use of high statistics of the time-averaged signals via the simultaneous fitting. In particular, we may be able to exclude some of the summed-up models, because they become discrepant with the time-averaged signals in > 3 keV where the C3PO-derived spectra are no longer defined.

Given these, we fitted the 0.5–45 keV time-averaged spectrum with a model of `Phabs*Ioabs*(PL + Refl + Fe-K + SE)`. Here, `Phabs` and `Ioabs` represent the Galactic/intrinsic neutral absorption and an ionized absorption, respectively; The former is the same model as that used in the previous subsection, and the latter, which is not essential, is described later. `PL` represents a cutoff PL model, `Refl` a reflection continuum without any relativistic or ionization effects, and `Fe-K` a gaussian to represent the Fe-Kα line. The cutoff energy in `PL` and `Refl` was fixed at 200 keV, and the redshift in `Ioabs`, `Refl` and `Fe-K` at 0.00885, while the other parameters were left free. Finally, `SE` represents the soft excess component, which is clearly seen in Fig. 5.7.

First, we examined the case that `SE` is a thin-thermal plasma emission (`TTP`) from the Mrk 509 host galaxy. Its plasma temperature, abundance, and the normalization were left free, while the redshift was fixed at 0.00885. As shown in Fig. 5.7 and Table 5.4, the fit was unsuccessful with χ^2/d.o.f.=590.29/515. The main reason of this fit failure is that the `PL` and the `SE` terms disagree with the C3PO-derived variable and stationary component, with χ^2/d.o.f. $= 25.33/7$ and $17.41/7$, respectively. In addition, the metal abundance (Table 5.4) turned out to be much lower than the Solar value, which makes the fit physically unrealistic, because galactic center regions around the AGN must be metal-richer. Thus, the TTP can be ruled out.

Second, we expressed the SE component by a relativistically-blurred reflection (`RBR`) component model with the emissivity index q, the inner radius $R_{\rm in}$, the ionization parameter ξ, and the normalization left free, while the outer radius $R_{\rm out}$ and the inclination fixed at 400 $R_{\rm g}$ and 30°, respectively.

Table 5.4: Results of the simultaneous fitting to spectrum triplet (the time-averaged, the variable, and the stationary spectrum) of Mrk 509, wherein the soft excess is represented by the TTP, BRB, or Compton model.

Model	Parameter	TTP	RBR	Compton
Absorption to all				
`Phabs`	$N_{\rm H}^{\dagger}$		0.044 (fix)	
`Ioabs`	$N_{\rm i}^{\dagger}$	22.7	0.13	0.13
	logξ	2.6	2.3	2.2
	Cvr frac.	0.05	1	1
	z		0.0344	
Broad-Band Primary component*				
`PL`	$\Gamma_{\rm PL}$	2.04	2.05	1.96
	$E_{\rm cut}$ (keV)		200 (fix)	
	$N_{\rm PL}^{\ddagger}$	2.03	1.81	1.82
Neutral reflection component				
`Refl`	$\Gamma_{\rm ref}$		$=\Gamma_{\rm PL}$	
	$E_{\rm cut}$ (keV)		200 (fix)	
	$f_{\rm ref}$	1.7	1.7	1.2
	A ($Z_{\odot}$)		1 (fix)	
	$A_{\rm Fe}$ ($Z_{\rm Fe,\odot}$)		1 (fix)	
	i (degree)		60 (fix)	
	$N_{\rm ref}$		$=N_{\rm PL}$	
`Fe-K`	$E_{\rm c}^{\S}$	6.34	6.34	6.34
	σ (keV)	0.11	0.08	0.11
	$N_{\rm Fe}^{\#}$	2.82	2.46	3.04
	EW (eV)	46	41	
Thin-thermal plasma component				
`TTP`	z	0.0344 (fix)	–	–
	kT (keV)	0.17	–	–
	A ($Z_{\odot}$)	0.01	–	–
	$N_{\rm apec}^{**}$	0.26	–	–
Relativistic reflection component				
`RBR`	$q^{\|\|}$	–	3.4	–
	$R_{\rm in}$ ($R_{\rm g}$)	–	1.24	–
	$R_{\rm out}$ ($R_{\rm g}$)	–	400 (fix)	–
	$A_{\rm Fe}$ ($Z_{\odot}$)	–	1 (fix)	–
	$\xi^{\dagger\dagger}$	–	216.6	–
	z	–	0.0344 (fix)	–
	$N_{\rm RBR}^{\ddagger\ddagger}$	–	1.10	–
Soft Primary component*				
`Compton`	z	–	–	0.0344 (fix)
	T_0 (keV)	–	–	0.02 (fix)
	kT (keV)	–	–	0.25
	τ	–	–	$13.4^{+0.4}_{-0.1}$
	$N_{\rm Comp}^{\S\S}$	–	–	293.3
χ^2/d.o.f.		590.29/501	626.71/500	550.55/501

* Later to be identified in §7.1.1.

† Equivalent hydrogen column density in 10^{22} cm^{-2} for the Galactic or the intrinsic line-of-sight absorption.

‡ The power-law normalization at 1 keV, in units of 10^{-2} photons keV^{-1} cm^{-2} s^{-1} at 1 keV.

§ Center energy in keV in the rest frame.

The Gaussian normalization in units of 10^{-5} photons cm s^{-1}.

|| The emissivity index (scales as R^{-q}).

** The `TTP` normalization, in units of $(10^{-17}/4\pi(D_{\rm A}(1+z))^2)\int n_{\rm e}n_{\rm H}dV$, where $D_{\rm A}$ is the angular size distance to the source (cm), $n_{\rm e}$ and $n_{\rm H}$ are the electron and H densities (cm^{-3}).

†† The ionization parameter, in units of erg cm^{-2} s^{-1}.

‡‡ The `reflionx` normalization, in units of 10^{-6} photons keV^{-1} cm^{-2} s^{-1} at 1 keV.

§§ The `Compton` normalization, in units of photons keV^{-1} cm^{-2} s^{-1} at 1 keV.

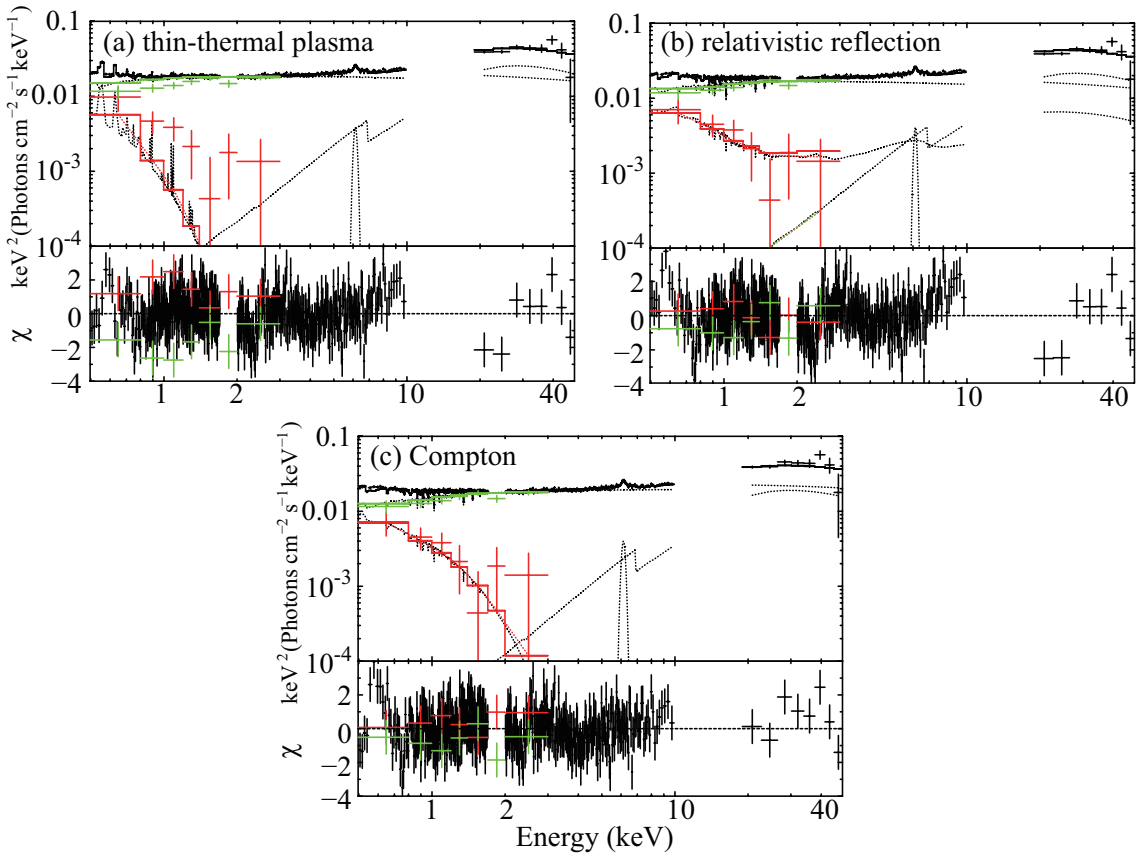

Figure 5.7: Results of the simultaneous triplet fitting of Mrk 509. The time-averaged spectrum was fitted with a model of `Phabs * Ioabs * (PL + Refl + Fe-K + SE)`, where `SE` is (a) TTP, (b) RBR, and (c) Compton. Simultaneously, the variable and the stationary components were fitted with `Phabs * Ioabs * PL` and `wabs * zxipcf * SE`, respectively. In panel (c), the `PL` and `Compton` emission are identified to be the Broad-Band and Soft Primary component in §7.1 and 7.2, respectively.

The photon index of the incident continuum for SE was tied to that of `PL`. As shown in Fig. 5.7, the fit became worse than the previous fit with the `TTP` model, and gave parameters shown in Table 5.4. In this case, the variable and the stationary spectra were both successfully reproduced with χ^2/d.o.f.=5.99/7 and 2.71/7, respectively. On the other hand, the RBR model, which can explain the C3PO-derived components with strong relativistic ($R_{\rm in} \sim 1.2 R_{\rm g}$) and ionized effects ($\xi \sim 200$), failed to explain the time-averaged spectrum in the hard X-ray band, and left large residuals especially in 7–10 keV. Thus, RBR interpretation is considered to be inappropriate for the `SE` model, either.

Finally, we examined the remaining possibility, that is, the thermal Compton component modeling for the `SE` signal. The electron temperature, the optical depth, and the normalization of `Compton` were left free, while the seed photon temperature was fixed at 0.02 keV as estimated in §2.2.3, and the geometry was assumed to be spherical. As shown in Fig. 5.7, the fit drastically improved from the TTP and RBR interpretations, and became acceptable with χ^2/d.o.f.=550.53/515, 6.77/7, and 2.91/7 for the time-averaged, the variable, and the stationary spectrum, respectively. (Line-like positive residuals which can be seen at $\sim$ 0.56 keV are considered due to an $O_{\rm VII}$ emission line as already

reported by e.g., Cerruti et al. 2011). As summarized in Table 5.4, the photon index of the PL, ~ 1.95, which agree with well with the value of ~ 1.92 (Table 5.1) obtained by analyzing the variable component alone. The reflection fraction is ~ 1.2; namely, the solid angle of cold reflectors against the primary emitter is $\sim 2.4\pi$, which is moderate and reasonable for a plane-like accretion disk and a dust torus. Similarly, the soft Comptonization parameters, including the electron temperature of ~ 0.25 keV and the optical depth of $\tau \sim 13$ are consistent, within errors, with those derived by analyzing the stationary component (Table 5.3). In this way, the thermal Comptonization modeling of the soft excess signal has given a successful and fully self-consistent explanation to the soft excess phenomenon of Mrk 509.

Let us explain the meaning and motivation of the ionized absorption `Ioabs`, which was introduced in the above fits but not described therein. Ionized absorbers which affect the continuum shape especially below 2 keV, and make the spectral interpretation more complex. Mrk 509 is one of the prototypical examples of such warm absorbers, (e.g., Kaastra et al. 2011) Thus, to describe the individual continuum shapes correctly, we introduced the warm absorber model, and obtained a similar result to the previous studies with $N_{\rm i} \sim 10^{21}$ cm^{-2} and $\log \xi \sim 2$ (e.g., Cerruti et al. 2011).

A potential problem here is that the errors in the variable and stationary components are (anti-) correlated rather than being independent. Usually, we need particular caution in simultaneously fitting such data sets, because the number of independent data bins would be over-estimated (double-counted) and hence, the degree of freedom would be over-estimated. However, this is considered to work in more conservative sense, because the reduced chi-square would be under-estimated, and hence we can avoid a risk of wrongly rejecting models that are in fact acceptable. Furthermore, in the present triplet fitting, the overall degree of freedom (~ 500) is dominated by those of the time-averaged spectrum, while those of the C3PO-derived components (~ 14) are negligible. Therefore, the effect of double-counting is considered negligible.

Finally, the triplet analysis may raise yet another suspect partially related to the above issue, that the C3PO-derived spectra with relatively large errors contribute little to the quantification of the soft excess, and the method gives no more information than is available from the traditional "static" analysis of the time-averaged spectrum alone. In order to examine this issue, we removed the C3PO-derived components from the previous fit, and fitted only the time-averaged spectrum with the model of `Phabs*Ioabs*(PL + Refl + Fe-K + SE)`, where `SE` is the Compton model. As a result, an error range of e.g. the optical depth spread to 12.7–13.9, which is more than twice as the fit with C3PO components of 13.3–13.8 (Table 5.4). Therefore, our dynamical analysis (combined with the static one) provides a much more powerful tool of the soft-excess study.

5.1.8 Comparison with the 2006 *Suzaku* spectra

Prior to the 2010 observation analyzed so far, Mrk 509 was observed by *Suzaku* four times in 2006. These observations started on 2006 April 25, October 14, November 15 and November 27, with a typical net exposure of 25 ksec. Although these data sets are too short for the C3PO method, we can

Table 5.5: The same as table Fig. 5.4, but obtained from the 2006 *Suzaku* spectra of Mrk 509.

Component	Parameter	2006/4/25	2006/10/14	2006/11/15	2006/11/27
Absorption to all					
`Phabs`	$N_{\rm H}$		0.044 (fix)		
`Ioabs`	log $N_{\rm H}$	$0.34^{+0.15}_{-0.17}$	$0.27^{+0.11}_{-0.19}$	$0.26^{+0.10}_{-0.18}$	$0.27^{+0.12}_{-0.22}$
	log (ξ [erg cm s^{-1}])	$2.03^{+0.08}_{-0.03}$	$2.08^{+0.04}_{-0.02}$	$2.03^{+0.03}_{-0.05}$	$2.03^{+0.06}_{-0.03}$
	Cvr frac.	$0.34^{+0.15}_{-0.17}$	$0.27^{+0.11}_{-0.19}$	$0.26^{+0.10}_{-0.18}$	$0.27^{+0.12}_{-0.22}$
	z		0.0344 (fix)		
Broad-Band Primary component*					
`PL`	Γ	$1.79^{+0.04}_{-0.05}$	$1.80^{+0.04}_{-0.05}$	$1.82^{+0.06}_{-0.04}$	$1.81^{+0.03}_{-0.04}$
	$E_{\rm cut}$ (keV)		200 (fix)		
	$N_{\rm PL}$	$1.25^{+0.09}_{-0.09}$	$1.34^{+0.09}_{-0.09}$	$1.30^{+0.12}_{-0.12}$	$1.20^{+0.09}_{-0.05}$
Reflection component					
`Refl`	$\Gamma_{\rm ref}$		$= \Gamma_{\rm PL}$		
	$E_{\rm cut}$ (keV)		200 (fix)		
	$f_{\rm ref}$	0.6	0.8	0.7	0.8
	A ($Z_\odot$)		1 (fix)		
	$A_{\rm Fe}$ ($Z_{\rm Fe,\odot}$)		1 (fix)		
	i (degree)		60 (fix)		
	$N_{\rm ref}$		$= N_{\rm PL}$		
`Fe-K`α	$E_{\rm c}$ (keV)	$6.43^{+0.05}_{-0.04}$	$6.43^{+0.05}_{-0.04}$	$6.40^{+0.08}_{-0.09}$	$6.51^{+0.07}_{-0.09}$
	σ (keV)	$0.10^{+0.09}_{-0.06}$	$0.10^{+0.14}_{-0.08}$	$0.15^{+0.13}_{-0.08}$	$0.23^{+0.12}_{-0.14}$
	$N_{\rm Fe}$	$2.89^{+1.00}_{-0.93}$	$2.95^{+1.25}_{-0.92}$	$3.02^{+1.66}_{-1.52}$	$4.89^{+2.34}_{-2.23}$
	EW (eV)	57^{+45}_{-30}	54^{+42}_{-32}	59^{+54}_{-30}	105^{+60}_{-79}
Soft Primary component*					
`Compton`	z		0.0344 (fix)		
	T_0 (keV)		0.02 (fix)		
	kT (keV)	0.33	0.35	0.30	0.29
	τ	$12.0^{+1.6}_{-1.0}$	$13.6^{+0.8}_{-0.7}$	$11.2^{+0.7}_{-0.4}$	$12.3^{+0.8}_{-0.6}$
	$N_{\rm Comp}$	$2.28^{+0.68}_{-0.42}$	$2.41^{+0.49}_{-0.41}$	$2.84^{+0.48}_{-0.40}$	$1.90^{+0.40}_{-0.37}$
	$F_{\rm Comp}$ (erg s^{-1} cm^{-2})	2.3	2.4	2.8	1.9
χ^2/d.o.f.		561.52/575	647.61/655	528.92/557	706.26/616

* Later to be identified in §7.1.1.

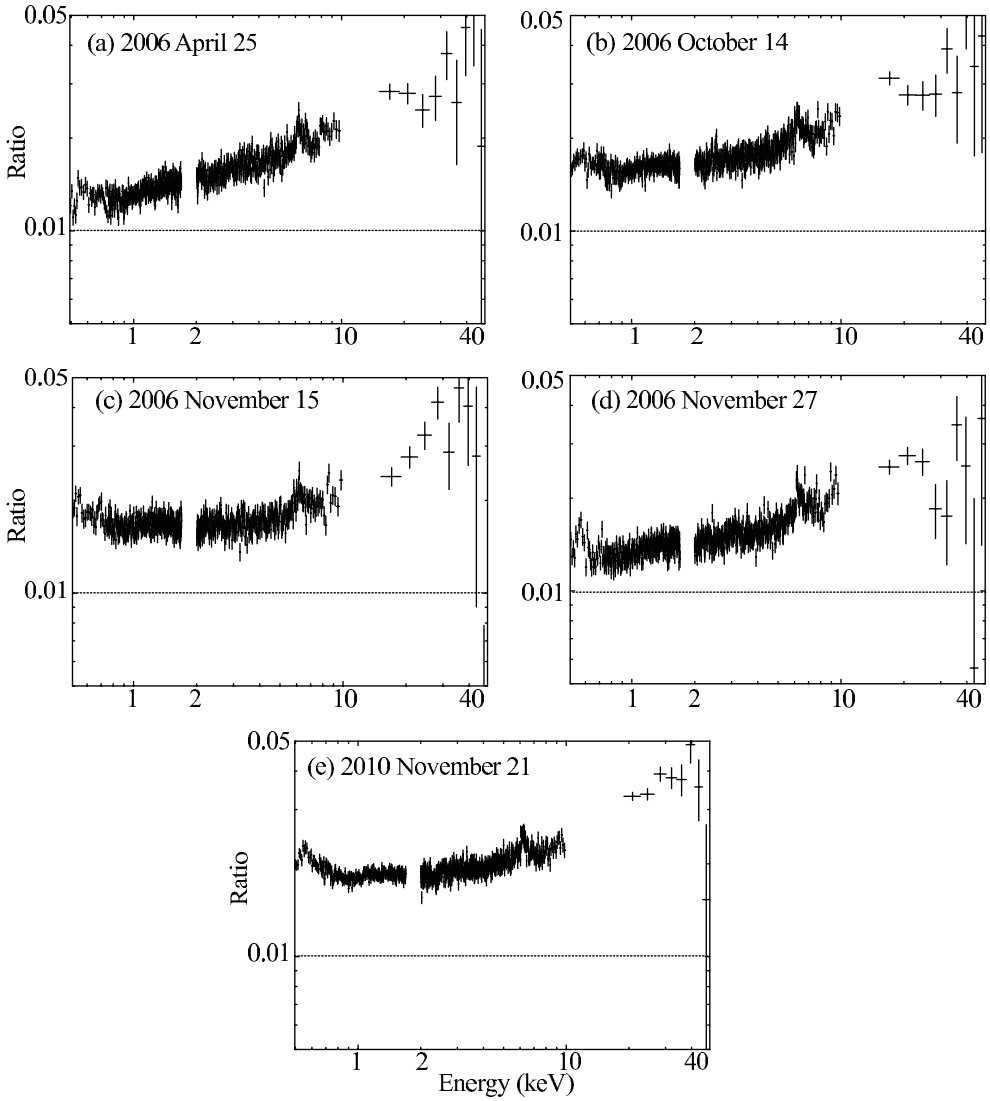

Figure 5.8: Time-averaged spectra of the 2006 *Suzaku* datasets of Mrk 509, and that of 2010 which is the same as in Fig. 5.2, all shown in the form of ratios to the same $\Gamma = 2.0$ PL ratio.

compare time-averaged spectra among the total 5 observations. The results, presented in Fig. 5.8, shows that the source was brightest in 2010, while dimmest in 2006 November 27, with a factor of ~ 1.5 difference. The spectral shape in 2006 April is hardest and flat, while the other spectra are softer and concave below ~ 3 keV. These differences of the spectral shape are considered mainly due to changes in the soft band intensity.

To quantify these spectral shape differences, we made four spectral ratios among the five spectra, using the hardest one (2006 April) as the denominator. The derived 0.5–45 keV spectral ratios shown in Fig. 5.9, are relatively flat in the 3–10 keV band, while they show upturn toward the lower energy band below 3 keV, with a clear break at ~ 3 keV. This means that the 3–45 keV intensity remained constant within $\lesssim 10\%$, whereas that in the 0.5–3 keV band is at most $\gtrsim 50\%$ different among the 5 observations. Thus, a soft component is considered to have varied in the 0.5–3 keV band, independently of a 0.5–45 keV broad-band continuum, with their spectral shape kept approximately the same.

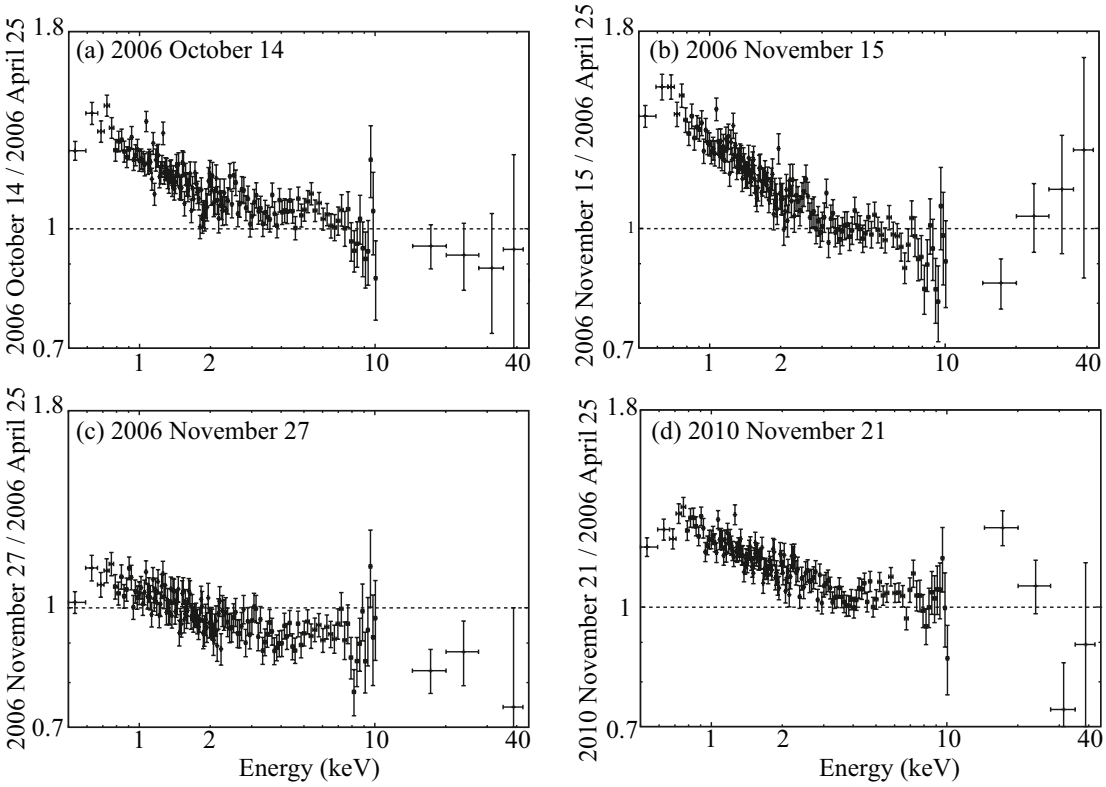

Figure 5.9: The spectra acquired on (a) 2006 Ocotber 14, (b) 2006 November 15, (c) 2006 November 27, and (d) 2010 November 21, all divided by that obtained in 2006 April 25 (Noda et al. 2011b).

To verify the above prospect, we fitted the time-averaged spectra in 2006 with the same model, based on the thermal Comptonization interpretation, as that in the fit to the 2010 spectrum (§5.1.8), `Phabs*Ioabs*(PL + Refl + Fe-K + SE)`, where `SE` is the Compton model. The parameter conditions were the same as those in §5.1.8, except that we have not incorporated the variable and stationary components into the fits since they cannot be obtained in the 2006 datasets. As shown in Fig. 5.10 and Table 5.5, all the time-averaged spectra were successfully reproduced with the model which explains the soft component in terms of thermal Comptonization. The obtained fit parameters are summarized in Table 5.5. The photon indices of the main variable Comptonization component modeled by `PL` are all ~ 1.80, and all the same within errors among the five observations. Furthermore, the PL normalization stayed constant within errors. The reflection fractions of the `Refl` model are all ~ 0.7, and the same within errors. Thus, the flat spectral ratios of the 3–45 keV band in Fig. 5.9 can be explained naturally by the conservation of spectral shapes of these hard continua.

Like in the 2010 case, the thermal Comptonization model has successfully explained the soft excess in the 2006 data sets. The derived electron temperature is always low, ~ 0.3 keV, and the optical depth is high, ~ 10 (FIg. 5.10, Table 5.5). In other wards, the soft excess component retained approximately constant slope. However, its normalization changed significantly by an overall factor of ~ 1.5. Thus, the long-term spectral changes of Mrk 509 (Fig. 5.8, Fig. 5.9) can be attributed to intensity variations (with insignificant shape changes) in the soft Comptonization component. Because

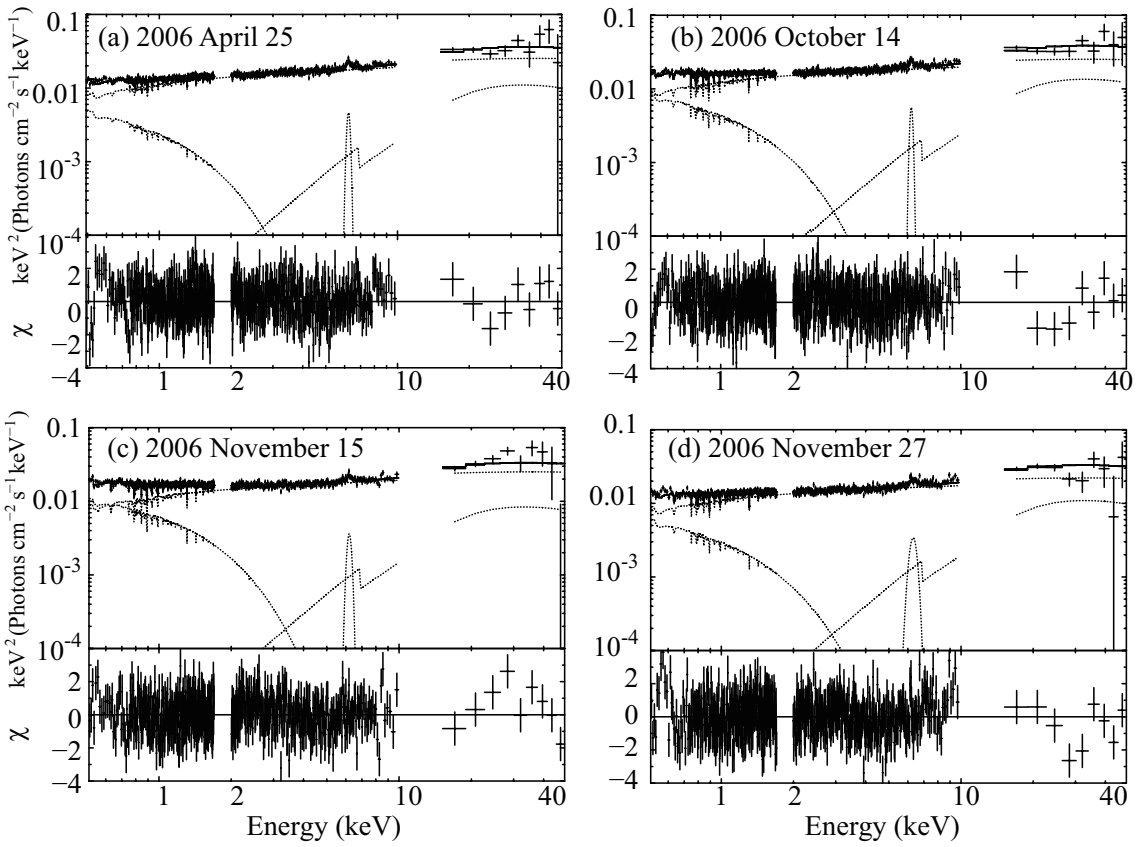

Figure 5.10: Same as Fig. 5.7, but of the 2006 *Suzaku* spectra, without the variable or stationary components. The `PL` and `Compton` signal are identified to be the Broad-Band and Soft Primary continuum in §7.1.1, respectively (Noda et al. 2011b).

the interval between 2006 November 15 and 27 is about two weeks, the soft Comptonization component is considered to be variable on a timescale of less than two weeks, but longer than a few days.

5.2 Target Selection for Further Analysis

In §5.1, we have succeeded in establishing the novel method called C3PO, to dynamically extract the soft excess component of Mrk 509, and identifying its nature. Our next task is to apply it to other AGN datasets obtained by *Suzaku*, and to examine whether we can derive similar results. Then, which of the *Suzaku*-observed AGNs are suitable for this study? Since timing information is crucial in our attempt, we must select AGNs which were observed continuously for a sufficient period longer than ~ 100 ksec, and exhibited 0.5–10 keV peak-to-peak variations of at least $\sim 10\%$. In order to investigate soft X-ray emission from the central engine, jet-dominated systems like Blazars should be excluded. Strongly-absorbed objects like type II AGNs are also unfavorable, due to their obvious lack of statistics in the soft X-ray band. In addition, in order for the soft X-ray signals not to be contaminated significantly by non-AGN soft X-rays (hot plasma emission and integrated discrete sources) from the host galaxy, we need to select AGNs with a 0.5–3 keV luminosity higher than $\sim 10^{43}$ erg s^{-1}, which is a maximum soft

X-ray luminosity of elliptical galaxies without nuclear activity (e.g, Vikhlinin et al. 1999; O'Sullivan et al. 2001; Fukazawa et al. 2006).

Based on the above considerations, we employ the following criteria in searching the *Suzaku* archive for those AGNs which are appropriate for our soft X-ray analysis.

1. The *Suzaku* dataset must have a net exposure of $\gtrsim$ 100 ksec, with a 0.5–10 keV peak-to-peak variation of $\gtrsim$ 10%.
2. The object must exhibit a Seyfert-like X-ray spectrum without dominated by a jet component.
3. The object should not be affected by a strong ($\gtrsim 10^{23}$ cm^{-2}) Galactic/intrinsic absorption.
4. The 0.5–3 keV luminosity must be higher than $\sim 10^{43}$ erg s^{-1}.

Table 5.6: Summary of the 12 observations of the 9 AGNs to be studied in §5.3.

Object name	Type	Obs. date	redshift	$N_{\rm H}$(Gal)*	previous Suzaku study
Fairall 9#1	Sy1	2007 Jun. 7	0.047	0.03	Patrick et al. (2011)
Fairall 9#2	Sy1	2010 May 19	0.047	0.03	Lohfink et al. (2012)
CBS126	Sy1	2010 Oct. 18	0.079	0.014	Chiang et al. (2012)
Ark120	Sy1	2007 Apr. 1	0.033	0.10	Zhou et al. (2011)
1H0419-577#1	Sy1	2007 Jul. 7	0.104	0.02	Turner et al. (2009)
1H0419-577#2	Sy1	2010 Jan. 16	0.104	0.02	–
MCG-2-58-22	Sy1.5	2009 Dec. 2	0.047	0.027	Rivers et al. (2011)
3C120#1	BLRG	2012 Feb. 9	0.033	0.17	Lohfink et al. (2013)
3C120#2	BLRG	2012 Feb. 14	0.033	0.17	Lohfink et al. (2013)
3C382	BLRG	2007 Apr. 27	0.058	0.074	Sambruna et al. (2011)
4C+74.26	RLQ	2007 Oct. 25	0.104	0.119	Larsson et al. (2008)
MR2251-178	RQQ	2009 May 7	0.064	0.024	Gofford et al. (2011)

* Equivalent hydrogen column density in 10^{22} cm^{-2} for the Galactic or the intrinsic line-of-sight absorption.

From the launch in 2005 July, some $\sim$ 100 type I AGNs have been observed with *Suzaku*, amounting to a total of $\sim$ 130 observations. By examining all those datasets, we have found 9 AGNs (12 observations) that survive the above criteria (Noda et al. 2013a); Fairall 9 (Seyfert 1), Ark 120 (Seyfert 1), 1H0419-577 (Seyfert 1), CBS126 (Seyfert 1), MCG–2-58-22 (Seyfert 1.5), 3C120 (broad line radio galaxy), 3C382 (broad line radio galaxy), 4C+74.26 (radio-loud quasar), and MR2251-178 (radio-quiet quasar). Table 5.6 summarizes basic information on these objects.

In the same way as Fig. 5.1 for Mrk 509, we produced background-subtracted light curves of each of the selected 12 data sets all in three bands; 0.5–3 keV (soft band) and 3–10 keV (middle band) using XIS FI, and 15–45 keV (hard band) using HXD-PIN. Among them, five (to be finally selected in §5.3.1) are shown in Fig. 5.11, while the others are shown in Appendix. As already required by the 1st observation criterion, all of them exhibit more than $\sim$ 10% variations in the soft and middle

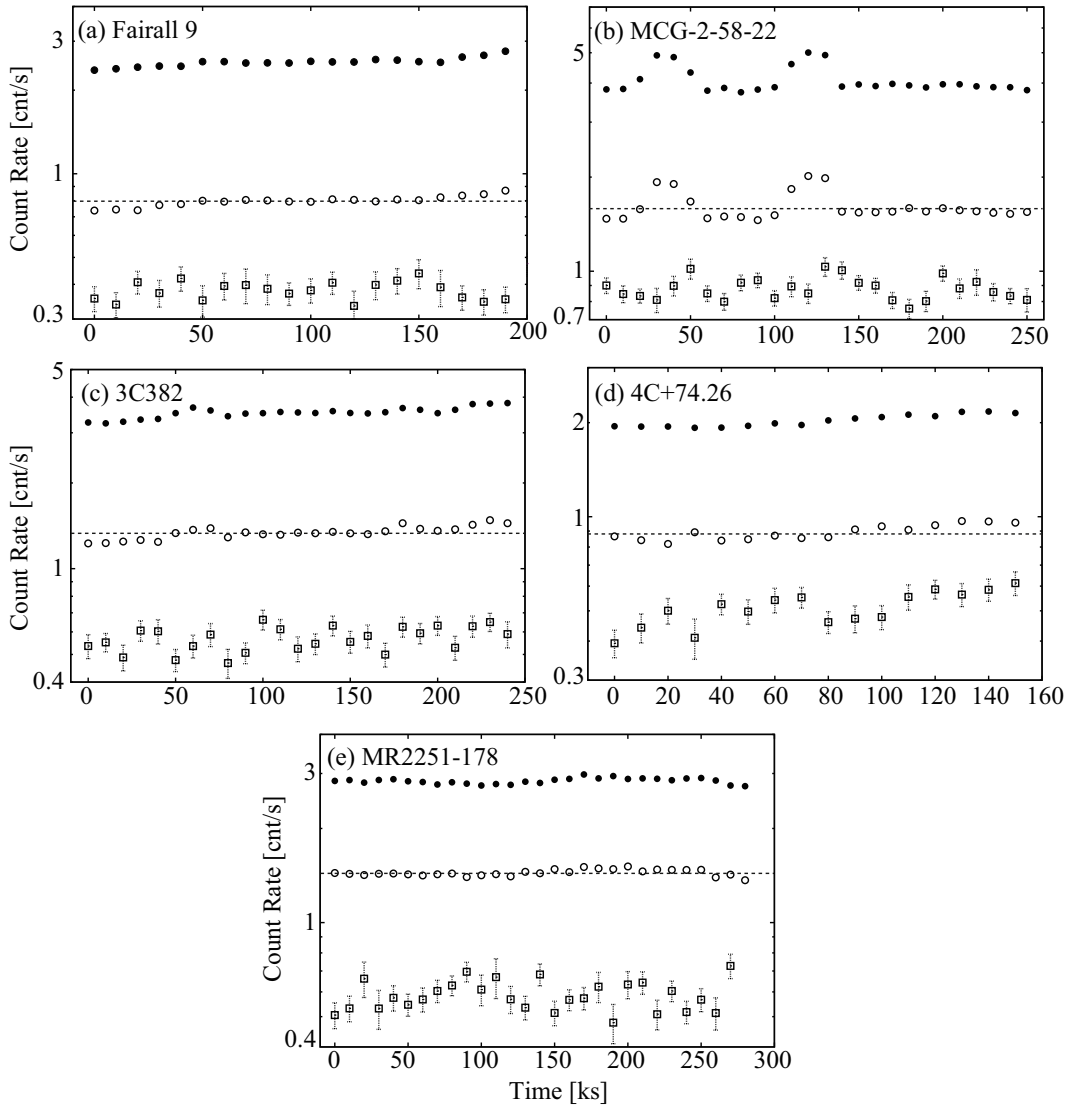

Figure 5.11: Same as Fig. 5.1, but of five AGNs out of the 12 data sets selected in §5.2. The name of AGNs is shown in each panel (Noda et al. 2013a).

bands. Like in the case of Mrk 509 (Fig. 5.1), the softer two bands exhibit a tight correlation at first glance, with possibly larger variation amplitudes in the softest band. Although independent variations apparently exist in their hard band, these may be mostly due to uncertainties in estimating the NXB (§3.4). The analysis of harder energy bands, including the HXD data, is described in §6.

5.3 Applying the C3PO Method to Several Other AGNs

In §5.2, we have selected 12 data sets of 9 AGNs that are suitable for our study. In this section, we apply the C3PO method to them, following the same routine as established in §5.1 for Mrk 509.

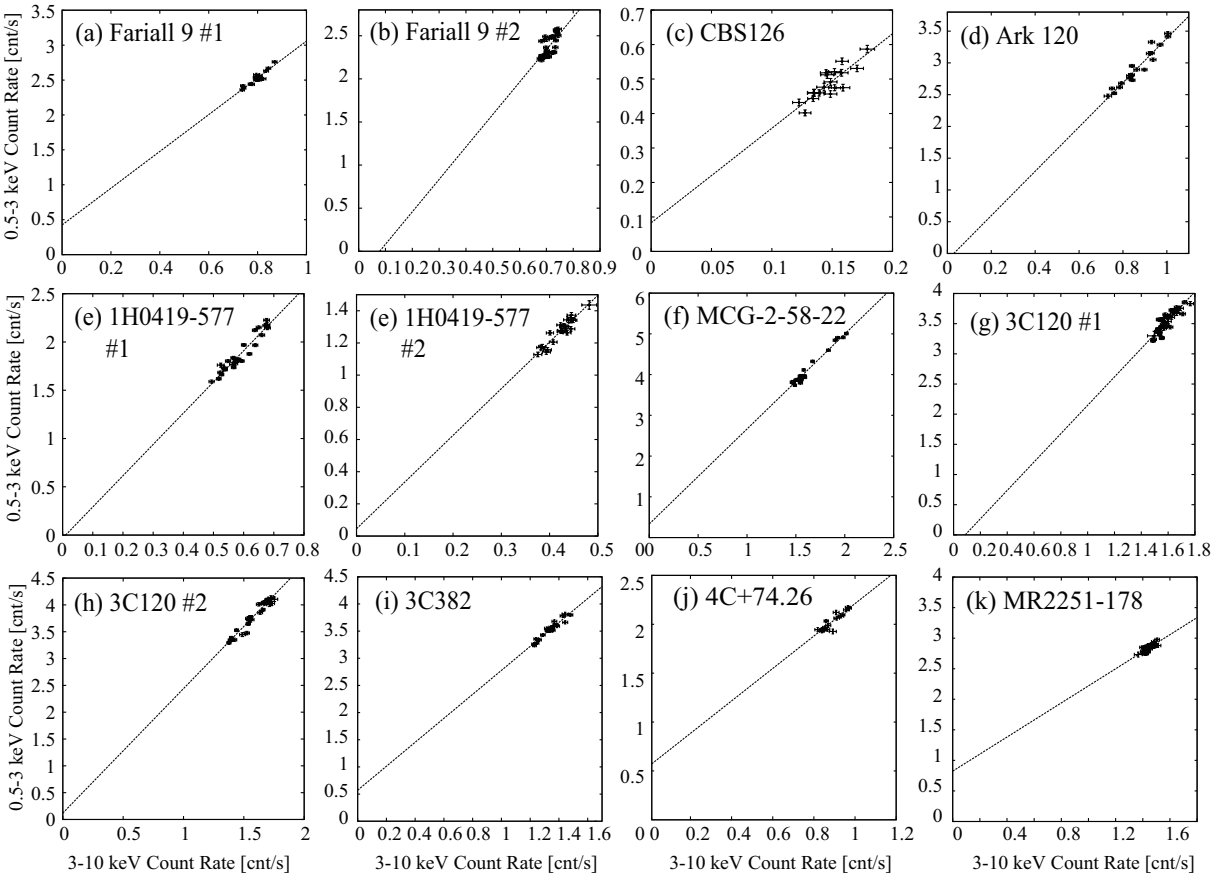

Figure 5.12: CCPs of the 12 data sets, presented in the same way as Fig. 5.4.

5.3.1 CCPs and C3PO decomposition

To quantify correlation between the soft (0.5–3 keV) and middle (3–10 keV) bands, CCPs (one for each observation) were produced from the 12 sets of light curves (§5.2) in the same manner as in §5.1.4 and Fig. 5.4. The CCPs, shown in Fig. 5.12, generally reveal tight correlation between the two energy bands. We produced linear fits with eq. (5.1), where the slope A and the offset B were again left free. Statistical and systematic errors are included in the same way as §5.1.4.

As shown in Table 5.7 and Fig. 5.12, data distributions in the CCPs have been reproduced successfully (beyond the confidence level of $N_{\rm p}$ =1%) with eq. (1), except the second observation of Fairall 9, the first observation of 1H0419-577, and the first observation of 3C120. The failure of these three linear fits could mean shape changes in the main variable component, or the presence of more than one variable components. Because it is difficult to exclude these additional variations, and because the values of A and B, as well as their errors, are unreliable in these cases, we do not use these data sets in the subsequent study. The other 9 data sets are consistent with the view that the main continuum varied without any spectral shape change.

Among the 9 observations, the offset B was consistent with 0 in four data sets; CBS126, Ark 120, the second observation of 1H0419-577, and the second observation of 3C120. These data sets

Table 5.7: Parameters obtained by fitting the twelve CCPs in Fig. 5.12 with eq. (1).*

Object	A	B (counts s^{-1})	χ^2/d.o.f.	note
Fairall 9#1	4.36 ± 0.10	0.51 ± 0.21	19.2/18	†
Fairall 9#2	3.76 ± 0.70	-0.29 ± 0.49	84.1/27	not linear
CBS126	2.74 ± 0.43	0.08 ± 0.06	31.1/16	$B \sim 0$
Ark120	3.49 ± 0.23	-0.10 ± 0.20	32.8/17	$B \sim 0$
1H0419-577#1	3.24 ± 0.20	-0.03 ± 0.12	52.3/23	not linear
1H0419-577#2	2.90 ± 0.27	0.05 ± 0.11	17.3/19	$B \sim 0$
MCG-2-58-22	2.33 ± 0.08	0.33 ± 0.13	31.5/24	†
3C120#1	2.35 ± 0.23	-0.20 ± 0.36	75.5/37	not linear
3C120#2	2.32 ± 0.12	0.12 ± 0.19	27.2/25	$B \sim 0$
3C382	3.78 ± 0.26	0.65 ± 0.23	21.6/23	†
4C+74.26	3.22 ± 0.30	0.48 ± 0.17	12.0/14	†
MR2251-178	1.39 ± 0.22	0.83 ± 0.31	31.4/26	†

* Errors refer to 1σ confidence limits.

† Finally selected.

are unusable in the present study, since they would not yield, within the data statistics, significant stationary signals at least in the XIS energy range. The remaining 5 data sets, in contrast, showed significantly positive offsets. This means that a certain signal should remain in the 0.5–3 keV bands, even when the intensity of the variable component becomes zero. They are considered to be suited to the C3PO method, hence we hereafter focus on the 5 observations of the 5 objects: the first observation of Fairall 9, MCG-2-58-22, 3C382, 4C+74.26, and MR2251-178.

After the procedure in §5.1.5, we divided the 0.5–3 keV band of the individual 5 AGNs into the finer 7 bands and made additional 7 CCPs. The total 35 CCPs (5 objects times 7 energy bands) are shown in Fig. C.10–B.6 in Appendix. Fitting them with a straight line in the same condition as in §5.1.5 gave the slope A and offset B from each AGN, as summarized in Table 5.8. Most of the CCPs thus exhibit strong correlations, and the fits with eq. (1) were successful. Furthermore, the CCPs have generally given positive slopes ($A > 0$) and positive offsets ($B > 0$). Thus, the C3PO can allow us to decompose the soft-band data of the 5 AGNs into a variable and a stationary part, like in the 0.5–3 keV band of Mrk 509.

Before we proceed to detailed studies of the 5 object with positive B, let us briefly examine whether they systematically differ from the 4 objects in which B is consistent with zero. For this purpose we produced Fig. 5.13, in which we plotted all the 12 observations on the plane of $B/A < x >$ representing relative strengths of the soft excess and the average 3–10 keV flux. (The three data sets with unacceptable linear fits were also included for reference.) It gives us two inferences. One is that the 5 positive-B objects tend to have higher X-ray intensities than the others. The other is that the horizontal error ranges do not appear to differ distinctly between the two classes, except for Ark 120 which has a rather tight upper limit in $B/A < x >$. These suggest that the 4 objects of which B is consistent with 0 do not differ fundamentally from the 5 positive-B objects; simply they were too faint,

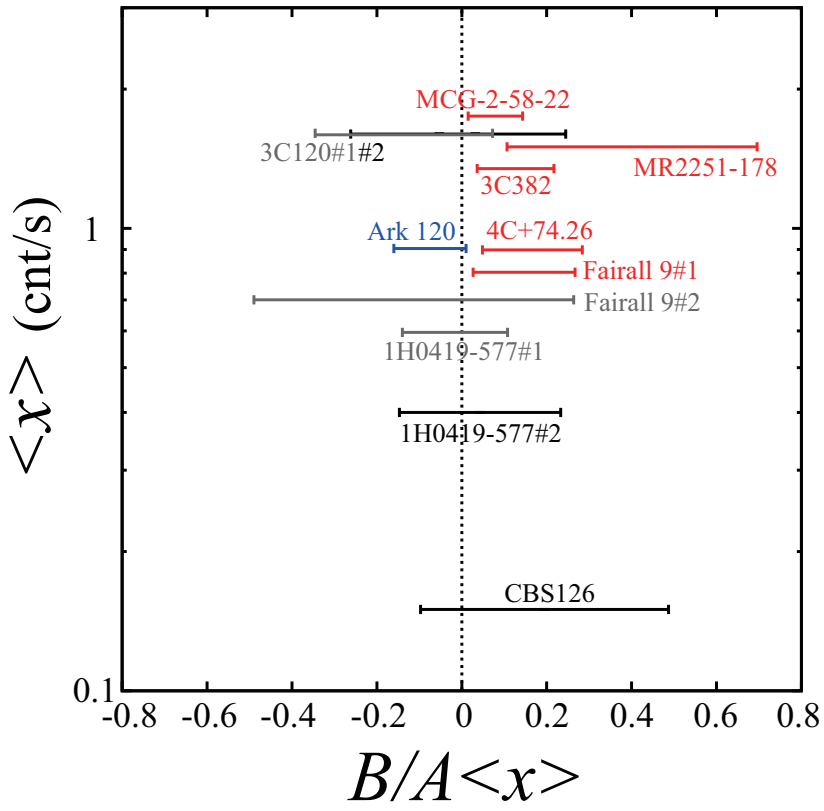

Figure 5.13: A scatter plot between a 3–10 keV average count rate $< x >$ and a relative strength of soft excess $B/A < x >$ of each AGN in table 5.7. Red shows objects of which the CCPs have linear distributions and significantly positive offsets, while black and grey show ones of which the CCPs have 0-consistent offsets and non-linear distributions, respectively. Blue is a plot of Ark 120, which exhibits a soft excess strength inconsistent with red.

or they happened to have somewhat smaller soft excess than the average. Thus, our results on the 5 objects to be derived below are considered applicable to general AGNs, rather than a limited/special subclass of them.

5.3.2 Variable and difference spectra

Following the Mrk 509 case (§5.1.4), the slopes A obtained in the finer 7 bands in each AGN was multiplied by the average 3–10 keV count rate, x_0, and divided by the corresponding energy intervals. As seen in Fig. 5.11, the value of x_0 is ~ 0.84 cnt s^{-1} in Fairall 9, ~ 1.68 cnt s^{-1} in MCG-2-58-22, ~ 1.40 cnt s^{-1} in 3C382, ~ 0.95 cnt s^{-1} in 4C+74.26, and ~ 1.50 cnt s^{-1} in MR2251-178. The variable component of each AGN, obtained by assembling the 7 values of A, is shown in Fig. 5.14 in green in a form of a ratio to a $\Gamma = 2.0$ PL.

Like in Mrk 509, is the variable component similar to the difference spectrum in each AGN? To examine this, we made a High- and a Low-phase spectra, and subtracted the latter form the former to extract a difference spectrum in each AGN (cf. §5.1.4). The obtained difference spectra, shown

Table 5.8: Parameters obtained by fitting 35 CCPs (seven energy bands times the five AGNs) in Fig. C.10–B.6 with eq. (1).*

Object	Energy range (keV)	A	B (counts s^{-1})	χ^2/d.o.f.
Fairall 9	0.5–0.8	0.23 ± 0.04	0.05 ± 0.03	21.1/18
	0.8–1	0.31 ± 0.04	0.10 ± 0.03	13.5/18
	1–1.2	0.44 ± 0.05	0.06 ± 0.21	16.0/18
	1.2–1.4	0.37 ± 0.06	0.09 ± 0.05	22.4/18
	1.4–1.7	0.55 ± 0.07	0.02 ± 0.06	23.9/18
	1.7–2	0.29 ± 0.04	0.05 ± 0.03	13.8/18
	2–3	0.48 ± 0.07	0.06 ± 0.05	24.6/18
MCG-2-58-22	0.5–0.8	0.17 ± 0.01	0.01 ± 0.02	40.8/24
	0.8–1	0.25 ± 0.02	0.08 ± 0.03	39.3/24
	1–1.2	0.34 ± 0.02	0.08 ± 0.03	44.2/24
	1.2–1.4	0.37 ± 0.02	0.04 ± 0.03	33.2/24
	1.4–1.7	0.46 ± 0.02	0.05 ± 0.03	41.2/24
	1.7–2	0.29 ± 0.01	0.03 ± 0.02	20.8/24
	2–3	0.49 ± 0.02	0.04 ± 0.03	29.3/24
3C382	0.5–0.8	0.14 ± 0.02	0.08 ± 0.03	25.4/23
	0.8–1	0.25 ± 0.02	0.08 ± 0.03	9.3/23
	1–1.2	0.27 ± 0.03	0.17 ± 0.04	18.7/23
	1.2–1.4	0.38 ± 0.03	0.04 ± 0.04	14.1/23
	1.4–1.7	0.37 ± 0.06	0.18 ± 0.08	48.8/23
	1.7–2	0.27 ± 0.03	0.06 ± 0.04	22.7/23
	2–3	0.53 ± 0.05	0 ± 0.06	23.7/23
4C+74.26	0.5–0.8	0.05 ± 0.03	0.04 ± 0.02	25.6/14
	0.8–1	0.06 ± 0.03	0.13 ± 0.03	16.6/14
	1–1.2	0.20 ± 0.04	0.10 ± 0.04	14.8/14
	1.2–1.4	0.32 ± 0.03	0.04 ± 0.03	8.0/14
	1.4–1.7	0.40 ± 0.07	0.08 ± 0.06	21.5/14
	1.7–2	0.19 ± 0.05	0.11 ± 0.05	26.2/14
	2–3	0.50 ± 0.05	0.04 ± 0.05	11.5/14
MR2251-178	0.5–0.8	0.08 ± 0.03	0.07 ± 0.05	19.8/26
	0.8–1	0.07 ± 0.06	0.17 ± 0.09	42.9/26
	1–1.2	0.16 ± 0.06	0.15 ± 0.09	27.7/26
	1.2–1.4	0.22 ± 0.07	0.11 ± 0.10	30.2/26
	1.4–1.7	0.36 ± 0.05	0.05 ± 0.08	12.7/26
	1.7–2	0.27 ± 0.06	-0.01 ± 0.09	27.4/26
	2–3	0.26 ± 0.10	0.30 ± 0.14	40.8/26

* Errors refer to 1σ confidence limits.

in Fig. 5.14 in grey, are apparently PL-like without prominent features such as a Fe-Kα line, and resemble the variable spectra (in green) at least in the 0.5–3 keV band where the latter is defined. For quantitative comparison, the variable and the difference spectra, were both fitted with `Phabs*PL`, where the column density of `Phabs` and the photon index of `PL` were left free, and the parameters summarized in Table 5.9 were obtained. As expected from Fig. 5.14, the variable spectrum of each object thus agree, within errors, with the corresponding difference spectrum, except for the obvious normalization difference. Thus, in the same way as Mrk 509, the variable spectrum is considered to be the same component as the difference spectrum in each AGN.

As shown in Table 5.9, the varying components of the 5 AGNs, as well as (that of) Mrk 509, commonly have photon indices of 1.7–2, which are typical for the main variable Comptonization signal in type I AGNs (§2.3.1). In addition, the derived column density of the absorption is consistent, within errors, with the Galactic line-of-sight absorption summarized in Table 5.6, except 4C+74.26

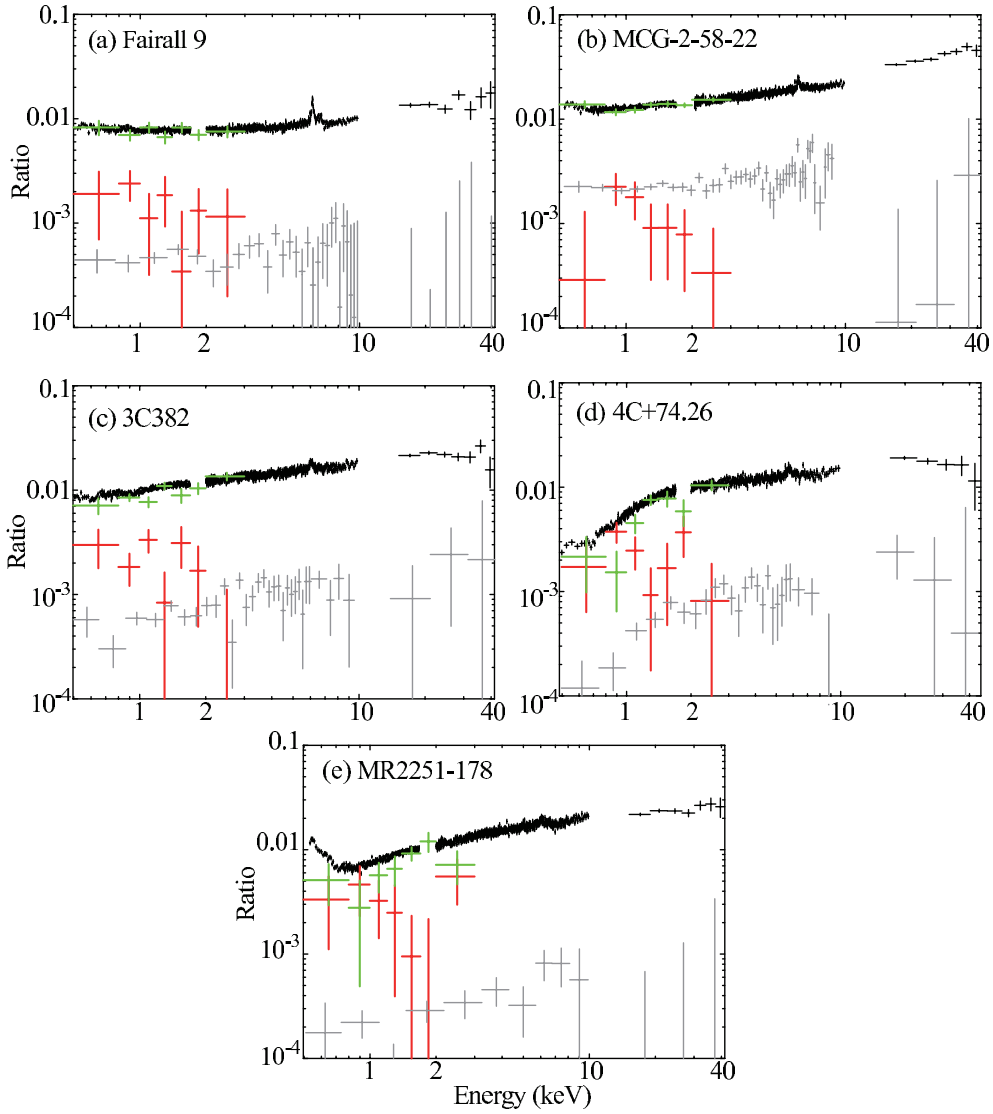

Figure 5.14: Time-averaged (black), difference(grey), variable (green), and red stationary spectra of the 5 AGNs, in a form of ratios to a $\Gamma = 2$ PL. The PL is common among the 5 panels, as well as within each.

which has a significantly larger absorption than the Galactic one. This means that 4C+74.26 has a strong intrinsic neutral absorption (both in the variable and the difference spectra), while the others do not. For further confirmation, we fitted simultaneously the variable and the difference spectra, using the same (but free) photon index and the same (but free) absorption, but with separate normalization. The fit has been successful (Table 5.9) in all the 5 objects; thus, the above inference has been reinforced.

5.3.3 Stationary components

By dividing the offsets B in the finer soft energy bands by the corresponding energy intervals, the stationary components of the 5 AGNs has been extracted, and are shown in Fig. 5.14 in red as a ratio to the same $\Gamma = 2$ PL, as used to normalize the time-averaged, variable and the difference spectra.

Table 5.9: Results of the fits to the variable and difference spectra of the 5 AGNs.

		Fairall 9	MCG-2-58-22	3C382	4C+74.26	MR2251-178
				Variable spectra		
`Phabs`	$N_{\rm H}^{*}$	< 0.13	< 0.03	< 0.11	$0.63^{+0.51}_{-0.40}$	< 1.85
`PL`	Γ	$2.02^{+0.49}_{-0.21}$	$1.82^{+0.12}_{-0.09}$	$1.52^{+0.39}_{-0.17}$	$2.34^{+1.06}_{-0.92}$	$2.43^{+2.74}_{-1.38}$
	$E_{\rm cut}$ (keV)			200 (fix)		
	$N_{\rm PL}^{\dagger}$	$0.75^{+0.32}_{-0.08}$	$1.27^{+0.12}_{-0.06}$	$0.85^{+0.29}_{-0.07}$	$1.57^{+2.52}_{-0.89}$	$1.52^{+3.65}_{-1.03}$
χ^2/d.o.f.		3.27/4	7.06/4	6.82/4	7.97/4	4.52/4
				Difference spectra		
`Phabs`	$N_{\rm H}^{*}$	< 0.15	< 0.02	< 0.20	$0.51^{+0.30}_{-0.24}$	< 0.64
`PL`	Γ	$1.96^{+0.25}_{-0.17}$	$1.84^{+0.06}_{-0.05}$	$1.65^{+0.17}_{-0.16}$	$1.94^{+0.30}_{-0.24}$	$1.44^{+0.32}_{-0.26}$
	$E_{\rm cut}$ (keV)			200 (fix)		
	$N_{\rm PL}^{\dagger}$	$0.49^{+0.16}_{-0.08}$	$2.13^{+0.15}_{-0.10}$	$0.64^{+0.17}_{-0.12}$	$0.94^{+0.48}_{-0.28}$	$0.18^{+0.20}_{-0.06}$
χ^2/d.o.f.		21.97/33	66.78/44	30.77/31	17.04/25	10.95/10
				Simultaneous fit		
`Phabs`	$N_{\rm H}^{*}$	< 0.15	< 0.02	< 0.20	$0.51^{+0.30}_{-0.24}$	< 0.64
`PL`	Γ	$1.96^{+0.25}_{-0.17}$	$1.84^{+0.06}_{-0.05}$	$1.65^{+0.17}_{-0.16}$	$1.94^{+0.30}_{-0.24}$	$1.44^{+0.32}_{-0.26}$
	$E_{\rm cut}$ (keV)			200 (fix)		
	$N_{\rm PL}^{\dagger}$	$0.49^{+0.16}_{-0.08}$	$2.13^{+0.15}_{-0.10}$	$0.64^{+0.17}_{-0.12}$	$0.94^{+0.48}_{-0.28}$	$0.18^{+0.20}_{-0.06}$
χ^2/d.o.f.		21.97/33	66.78/44	30.77/31	17.04/25	10.95/10

* Equivalent hydrogen column density in 10^{22} cm^{-2}.

† The cutoff power-law normalization at 1 keV, in units of 10^{-2} photons keV^{-1} cm^{-2} s^{-1}.

All of the stationary spectra are apparently soft like that of Mrk 509. To evaluate the spectral shapes of the stationary components, we fitted them again with the five possible models introduced in §5.1.7, under the same parameter conditions as before. The Galactic absorption was included into the fits with the column density fixed at the values summarized in Table 5.6. As a result, the fits were all successful, and gave the results in Table 5.10.

The photon indices of `PL` became ~ 3, which is slightly harder than that of the stationary component of Mrk 509. This is still much softer than the mainly varying component with $\Gamma \lesssim 2$. We no longer consider this `PL` modeling which is purely empirical, or the `Diskbb` representation which again gave too high temperatures. In contrast, the TTP model with a plasma temperature of ~ 1 keV, or the RBR model with an extremely relativistic effects, can reproduce the stationary components of all of the 5 AGNs, as well as that of Mrk 509. The `Compton` model is also able to explain them by an optically-thick corona with the electron temperature of $\lesssim 0.5$ and the optical depth of $\gtrsim 15$. In this way, properties of the varying signals from the 5 AGNs, which are of somewhat different types, follow those of Mrk 509.

Table 5.10: Same as Table 5.3, but obtained in the fits to the stationary components of the 5 AGNs.

Model	Parameter	Fairall 9	MCG-2-58-22	3C382	4C+74.26	MR2251-178
PL	Γ	$2.89^{+1.29}_{-1.14}$	$2.92^{+1.00}_{-0.98}$	$3.16^{+1.16}_{-0.93}$	$3.24^{+0.98}_{-0.91}$	$2.93^{+1.75}_{-2.05}$
	$N^{*}_{\rm PL}$	$1.92^{+0.71}_{-0.73}$	$1.41^{+0.60}_{-0.61}$	$2.61^{+0.74}_{-0.75}$	3.20 ± 0.92	$3.13^{+1.55}_{-1.80}$
	χ^2/d.o.f.	2.28/5	4.09/5	6.88/5	7.36/5	4.50/5
diskbb	$T_{\rm disk}$ (keV)	$0.35^{+0.42}_{-0.18}$	$0.34^{+0.23}_{-0.11}$	$0.33^{+0.21}_{-0.13}$	$0.26^{+0.20}_{-0.08}$	$0.27^{+0.27}_{-0.11}$
	$N^{\dagger}_{\rm disk}$	21.7 ± 8.2	19.5 ± 7.3	35.9 ± 10.3	157 ± 45	140 ± 69
	χ^2/d.o.f.	3.23/5	2.74/5	6.97/5	7.91/5	4.88/5
TTP	A ($Z_{\odot}$)			1 (fix)		
	z	0.0471 (fix)	0.0469 (fix)	0.0579 (fix)	0.1040 (fix)	0.0640 (fix)
	kT (keV)	$1.2^{+4.8}_{-0.7}$	$1.1^{+0.5}_{-0.3}$	$1.7^{+1.0}_{-0.4}$	$1.3^{+0.4}_{-0.6}$	$1.3^{+1.3}_{-0.8}$
	$N^{\ddagger}_{\rm apec}$	$3.29^{+2.72}_{-1.73}$	$2.78^{+1.35}_{-1.07}$	$7.11^{+2.29}_{-2.76}$	$7.37^{+3.24}_{-2.97}$	$7.14^{+5.43}_{-4.25}$
	χ^2/d.o.f.	3.49/5	0.25/5	7.29/5	4.48/5	4.65/5
RBR	q			3 (fix)		
	$R_{\rm in}$ ($R_{\rm g}$)			1.235 (fix)		
	$R_{\rm out}$ ($R_{\rm g}$)			400		
	i (degree)			60 (fix)		
	$A_{\rm Fe}$ ($Z_{\rm Fe,\odot}$)			1 (fix)		
	$\Gamma_{\rm ref}$			2 (fix)		
	$\xi^{\S}$	$50.0^{+4.9}_{-16.6}$	$50.1^{+5.9}_{-17.5}$	$60.3^{+9.0}_{-7.8}$	$36.3^{+9.1}_{-7.3}$	$22.8^{+4.1}_{-6.1}$
	$N^{||}_{\rm RBR}$	0.62 ± 0.23	0.42 ± 0.17	0.61 ± 0.18	1.97 ± 0.47	5.09 ± 1.90
	χ^2/d.o.f.	2.37/4	7.38/4	7.29/4	4.48/4	4.65/4
Compton	z	0.0471 (fix)	0.0469 (fix)	0.0579 (fix)	0.1040 (fix)	0.0640 (fix)
	kT (keV)	$0.80^{+1.23}_{-0.38}$	$0.26^{+0.11}_{-0.07}$	$0.46^{+0.27}_{-0.17}$	$0.77^{+0.60}_{-0.28}$	$0.86^{+0.09}_{-0.13}$
	τ	$16.2^{+11.1}_{-5.6}$	$94.1^{+28.1}_{-21.0}$	$23.9^{+17.3}_{-8.3}$	$14.9^{+6.9}_{-4.0}$	$15.2^{+179.2}_{-10.2}$
	$N^{\#}_{\rm comp}$	0.21 ± 0.08	0.03 ± 0.01	0.41 ± 0.12	0.83 ± 0.24	0.42 ± 0.14
	χ^2/d.o.f.	2.39/4	2.59/4	6.63/4	7.35/4	4.57/4
	L^{**}	$1.9^{+0.4}_{-0.5}$	0.4 ± 0.1	$3.7^{+0.7}_{-0.5}$	$10.2^{+1.6}_{-1.9}$	$6.5^{+2.1}_{-1.3}$

* The PL normalization at 1 keV, in units of 10^{-3} photons keV^{-1} cm^{-2} s^{-1} at 1 keV.

† The diskbb normalization, in $((R_{\rm in}/{\rm km})/(D/10\ {\rm kpc}))^2 \cos\theta$, where $R_{\rm in}$ is the inner disk radius, D the distance to the source, and θ the angle of the disk.

‡ The TTP normalization, in units of $(10^{-17}/4\pi(D_{\rm A}(1+z))^2) \int n_{\rm e} n_{\rm H} dV$, where $D_{\rm A}$ is the angular size distance to the source (cm), $n_{\rm e}$ and $n_{\rm H}$ are the electron and H densities (cm^{-3}).

§ The ionization parameter, in units of erg cm^{-2} s^{-1}.

|| The RBR normalization, in units of 10^{-5} photons keV^{-1} cm^{-2} s^{-1} at 1keV.

The Compton normalization, in units of photons keV^{-1} cm^{-2} s^{-1} at 1 keV.

** The 0.5–3 keV luminosity of the extracted soft stationary emissions, in units of 10^{43} erg s^{-1}.

Table 5.11: Results of the fits to the time-averaged spectra of 5 AGNs with `Phabs*Ioabs*(PL + Refl + Fe-K + SE)` where `SE` = Compton.

		Fairall 9	MCG-2-58-22	3C382	4C+74.26	MR2251-175
				Case without `SE`		
	Γ	2.10	1.90	1.81	1.88	1.69
χ^2/d.o.f.		1105.61/651	1099.49/832	1070.05/842	666.18/601	1581.01/865
				Case with `SE` = TTP		
	kT	$0.32^{+0.02}_{-0.04}$	$0.18^{+0.02}_{-0.03}$	$0.25^{+0.03}_{-0.04}$	$0.68^{+0.08}_{-0.07}$	$0.31^{+1.47}_{0.87}$
TTP	A ($Z_\odot$)	< 0.005	< 0.007	< 0.004	< 0.005	< 0.002
χ^2/d.o.f.		728.62/651	846.70/832	883.80/842	612.45/601	983.20/865
				Case with `SE` = RBR		
χ^2/d.o.f.		785.06/651	945.79/832	886.26/842	660.51/601	1145.17/865
				Case with `SE` = Compton		
Absorption to all						
`Phabs`	$N_{\rm H}$	0.032(fix)	0.035(fix)	0.074(fix)	$0.24^{+0.02}_{-0.02}$	0.028(fix)
`Ioabs`	$N_{\rm H}$	–	$0.36^{+0.24}_{-0.27}$	$0.41^{+0.32}_{-0.27}$	$1.08^{+0.39}_{-0.35}$	0.91 ± 0.05
	logξ	–	$0.36^{+0.84}_{-0.25}$	$3.20^{+0.16}_{-0.13}$	$0.57^{+0.18}_{-0.22}$	$0.30^{+0.04}_{-0.03}$
	Cvr frac.	–	$0.13^{+0.21}_{-0.08}$	$0.71^{+0.17}_{-0.48}$	$0.54^{+0.08}_{-0.06}$	$0.83^{+0.03}_{-0.02}$
	z	0.0471 (fix)	0.0469 (fix)	0.0579 (fix)	0.1040 (fix)	0.0640 (fix)
Broad-Band Primary component*						
`PL`	Γ	$1.87^{+0.04}_{-0.03}$	$1.84^{+0.04}_{-0.02}$	1.75 ± 0.01	1.84 ± 0.06	1.66 ± 0.01
	$E_{\rm cut}$ (keV)		200 (fix)			100 (fix)
	$N_{\rm PL}$	$0.68^{+0.03}_{-0.01}$	1.33 ± 0.01	1.03 ± 0.01	0.99 ± 0.09	$1.04^{+0.01}_{-0.03}$
Reflection component						
`Refl`	$\Gamma_{\rm ref}$			$= \Gamma_{\rm PL}$		
	$E_{\rm cut}$ (keV)		200 (fix)			100 (fix)
	$f_{\rm ref}$	$0.9^{+0.3}_{-0.4}$	1.6 ± 0.2	< 0.3	$0.4^{+0.4}_{-0.2}$	< 0.1
	A ($Z_\odot$)			1 (fix)		
	$A_{\rm Fe}$ ($Z_{\rm Fe,\odot}$)			1 (fix)		
	i (degree)			60 (fix)		
	$N_{\rm ref}$			$= N_{\rm PL}$		
`Fe-K`	$E_{\rm c}$	$6.37^{+0.05}_{-0.04}$	$6.26^{+0.08}_{-0.09}$	6.43 ± 0.03	6.41 ± 0.04	6.40 ± 0.04
	σ (keV)	10^{-4}(fix)	10^{-4}(fix)	$0.099^{+0.032}_{-0.031}$	10^{-4}(fix)	10^{-4}(fix)
	$N_{\rm Fe}$	$2.30^{+0.21}_{-0.11}$	1.89 ± 0.32	$2.18^{+0.41}_{-0.42}$	$1.46^{+0.34}_{-0.35}$	$1.12^{+0.29}_{-0.30}$
	EW (eV)	84^{+12}_{-15}	34^{+54}_{-32}	48^{+32}_{-44}	34^{+20}_{-10}	21^{+15}_{-21}
Soft primary component*						
Compton	z	0.0471 (fix)	0.0469 (fix)	0.0579 (fix)	0.1040 (fix)	0.0640 (fix)
	T_0 (keV)			0.02 (fix)		
	kT (keV)			0.5 (fix)		
	τ	$13.7^{+0.79}_{-0.95}$	$16.2^{+1.4}_{-1.5}$	$15.6^{+0.44}_{-0.31}$	$18.5^{+2.07}_{-1.30}$	$13.7^{+0.42}_{-0.54}$
	$N_{\rm Comp}$	$0.39^{+0.08}_{-0.09}$	$0.66^{+0.15}_{-0.12}$	$2.27^{+0.34}_{-0.57}$	$3.25^{+2.35}_{-2.17}$	$42.2^{+26.7}_{-12.3}$
χ^2/d.o.f.		721.33/652	825.32/833	894.07/843	624.26/602	929.15/866

* Later to be identified in §7.1.1.

5.3.4 The triplet analysis

Before attempting our final step, i.e., the spectrum triplet analysis (§5.1.7), let us examine whether the time-averaged spectra of the 5 AGNs suggest the soft-excess structure via the conventional "static" analysis. We fitted the the time-averaged spectra with `Phabs*Ioabs*(PL + Refl + Fe-K)`, without including any `SE` model. The individual components and their parameter conditions in these fits are the same as those utilized in §5.1.7, except for the cutoff energy of MR 2251-178 fixed at 100 keV according to Gofford (2011). Like in §5.1.7, the `Ioabs` factor is explained in the last paragraph. Except for 4C+74.26, the fits failed with χ^2/d.o.f. values shown in Table 5.11, mainly because of positive residuals in the soft X-ray bands. Thus, at least the 4 AGN spectra exhibit soft-excess signals above the "static" power-law fit. In order to examine these signals coincide with the stationary component extracted in §5.3.4, let us proceed to the analysis of the spectrum triplet.

As the soft excess signal, we first consider the TTP emission (presumably from the host galaxy) like in the Mrk 509 case, and fitted the time-averaged spectra of the 5 AGNs with `Phabs*Ioabs*(PL + Refl + Fe-K + SE)`, where `SE` is represented by the TTP model. Simultaneously, the variable and the stationary spectra were fitted with `Phabs*Ioabs*PL` and `Phabs*Ioabs*SE`, respectively. The parameter conditions in these models were the same as those in §5.1.7. As a result, the fits were successful, except for MR 2251-178 shown in Fig. 5.15 (a), giving χ^2/d.o.f. values in Table 5.11. (The obtained parameters are summarized in Appendix.) However, as shown in Table 5.11, the obtained abundance in the TTP model were all less than 1% of the Solar value, and are hence physically unrealistic. Therefore, the TTP model can be generally ruled out, just like in the Mrk 509 case.

Next, we employed the RBR interpretation, again with the parameter conditions as in §5.1.7. Then, the fit was unacceptable ($\chi^2/\nu > 1.10$ for $\nu \sim 700$, $N_{\rm P} < 1\%$) for 3C382 and 4C+74.26, which acceptable ($\chi^2/\nu < 1.10$) for the others. (The obtained parameters are summarized in Appendix.) Shown in Fig. 5.15 (b), the RBR model can reproduce the variable and the stationary component, while cannot successfully explain the hard X-ray band. Thus, the RBR interpretation is inappropriate

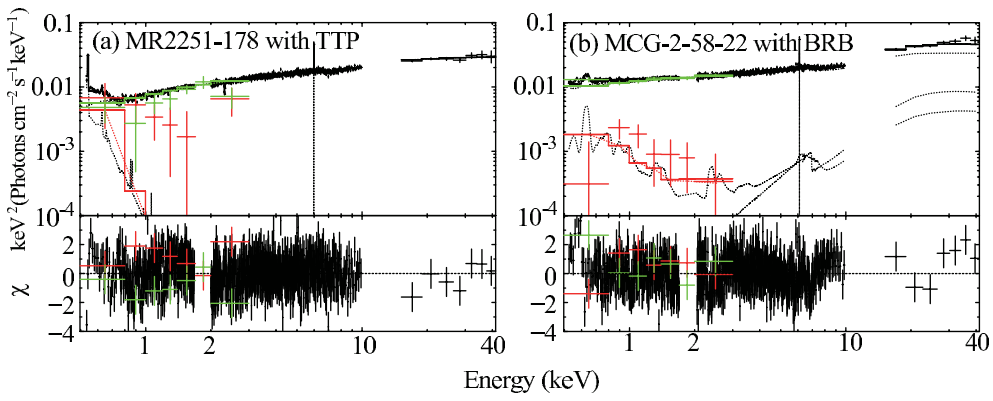

Figure 5.15: Fits to the time-averaged spectra of (a) MR 2251-178 and (b) MCG-2-58-22 with `Phabs*Ioabs*(PL + Refl + Fe-K + SE)`, where `SE` refers to TTP and RBR, respectively.

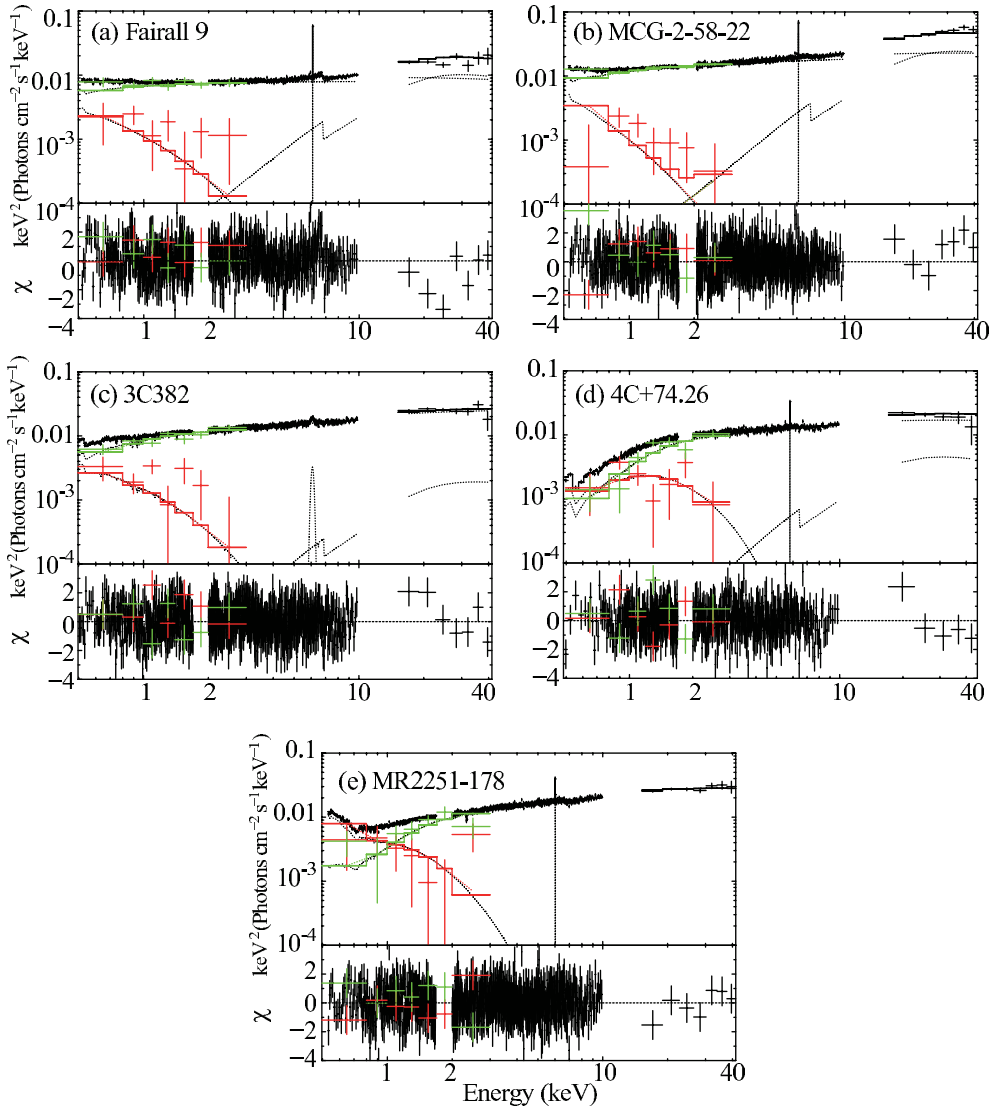

Figure 5.16: Same as Fig. 5.15, but of the 5 AGNs, and with `SE` = Compton. The `PL` and `Compton` model are found to be the Broad-Band and Soft Primary component in §7.1.1, respectively.

for the origin the soft excess in the 5 AGNs, as well as Mrk 509.

Finally, we considered the Compton process, and set `SE` = Compton, again with the same parameter conditions as in §5.1.7. Then, as shown in Fig.5.16 and summarized in Table 5.11, the time-averaged spectra of the 5 AGNs have all been successfully explained. In addition to the ovarial fit goodness, the variable and the stationary components have simultaneously been reproduced with χ^2/d.o.f. = 6.89/7 and 4.01/7 for Fairall 9, 15.69/7 and 10.02/7 for MCG-2-58-22, 8.83/7 and 9.52/7 for 3C382, 13.10/7 and 9.51/7 for 4C+74.26, and 8.30/7 and 5.97/7 for MR 2251-178. Thus, like in Mrk 509, in all the 5 AGNs, the "dynamic" analyses are considered to be fully consistent with the "static" analyses. Together with the first-cut results on Mrk 509 (§5.1), we now conclude that a Compton corona with a relatively low electron temperature and a relatively lager optical depth is commonly found in some, if not all, disk-dominated AGNs.

In these fits, an ionized absorption model, `Ioabs`, was introduced except for Fairall 9, because Weaver et al. (1995), Sambruna et al. (2011), Kaspi et al. (2004), and Gofford et al. (2011) reported such effects in MCG-2-58-22, 3C382, 4C+74.26, and MR 2251-178, respectively. In the fits of Fairall 9, we set `Ioabs`=none, because the object was reported to have a bare-nucleus (e.g., Schmoll et al. 2008; Patrick et al. 2011). Since Gofford et al. (2011) reported several absorption features by outflows in MR 2251-178, we included three `zgaussian` models with free σ and negative normalization, representing $\mathrm{Fe_{I-XVI}}$ M-shell unresolved transition forest (at a center energy of $E_\mathrm{c} = 0.77$ keV), $\mathrm{Fe_{XXIV}}$ L-shell ($E_\mathrm{c} = 1.29$ keV), and $\mathrm{Fe_{XXV-XXVI}}$ K-shell ($E_\mathrm{c} = 7.57$ keV). The obtained parameters in the `Ioabs` model, shown in Table 5.11 or Appendix, are almost consistent the previous *Suzaku* studies, within errors.

Chapter 6

HARD X-RAY ANALYSIS

To fully understand composition of the overall AGN X-ray emission, the hard X-ray bands above 3 keV are even more important than the soft X-ray energies where our study (in Chapter 5) has been successful. This is because the hard X-ray emission of AGNs is considered to consist, in still more complex ways than in the soft X-ray range, of several components overlapping with one another: a variable PL continuum, a reflection continuum accompanied by a prominent Fe-K line, an absorbed PL caused by partially-covering ionized absorbers, and often a relativistically-blurred reflection component. Because their spectral shapes are often similar to one another (§2.3.7), many different interpretations of the hard X-ray spectra of AGNs degenerate, and hence the correct composition has not yet been identified. To overcome this big difficulty in the X-ray studies, our C3PO method is considered to provide a powerful tool in the hard X-ray energies as well. In the present Chapter, we search for more reliable and robust decomposition of the hard X-ray spectra of type I AGNs than performed before, using the "dynamical" analysis with our C3PO method, as well as the traditional "static" approach.

6.1 The Highly Variable Type I Seyfert NGC 3516

NGC 3516 is a bright and highly variable type I Seyfert galaxy, located in northern sky (α=11h 06m 47.5s, δ+72d 34m 07s) at a redshift of $z = 0.00885$. Its X-ray spectrum is known to exhibit large time variations on time scales of years (Turner et al. 2011). Its hard X-ray spectrum has been explained by some authors with the relativistically-smeared reflection (Markowitz et al. 2006), and by others with partial ionized absorptions (Turner et al. 2008, 2011). Thus, the interpretation of hard X-ray spectrum of this object is still controversial. It has a line-of-sight Galactic absorption of $N_{\rm H} = 3.4 \times 10^{20}$ cm^{-1}, and an estimated BH mass of 2×10^7 $M_\odot$ (e.g., Peterson et al. 2004). Compared to the objects studied in Chapter 5, NGC 3516 has a somewhat lower 0.5–2 keV luminosity of 2–8$\times 10^{39}$ erg s^{-1} (George et al. 2002), which translates to an Eddington ratio of ~ 0.006. In the present section, we utilize two *Suzaku* datasets of NGC 3516, obtained on 2005 October and 2009 October (Chapter 4), and analyze the energy range above 2 keV to avoid the reported contamination by thermal emission from the host galaxy (George et al. 2002).

6.1.1 Light curves

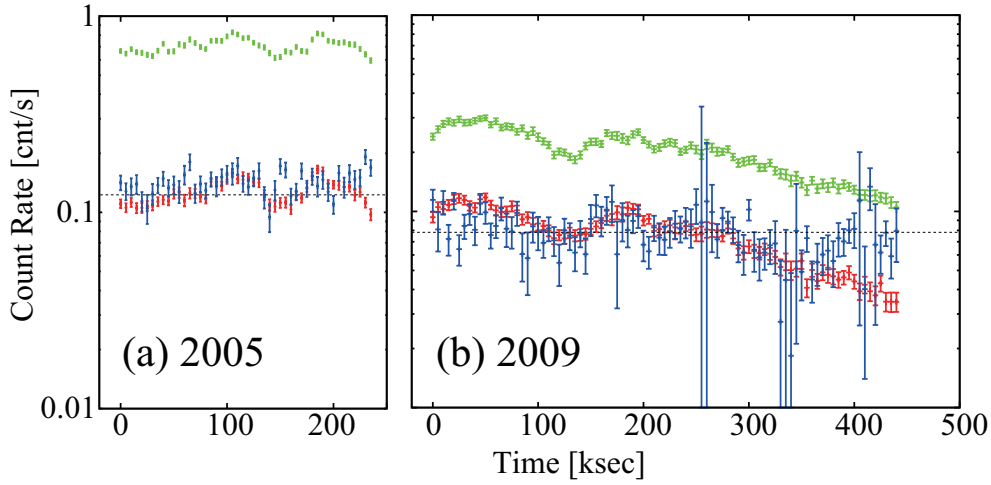

Figure 6.1: Background-subtracted and dead-time corrected light curves of NGC 3516, with 5 ks binning in the 2–3 keV (red), 3–10 keV (green), and 15–45 keV (blue) bands, respectively. The 2005 XIS count rates are multiplied by a factor of 0.5 to absorb differences in the observing conditions between the two data sets (see text). Dotted lines show the average 3–10 keV count rates.

Figure 6.1 shows 2–3 keV, 3–10 keV (XIS FI) and 15–45 keV (HXD-PIN) light curves of NGC 3516 produced from the 2005 and 2009 *Suzaku* datasets. There, the 2009 XIS data are shown as a sum of two cameras (XIS 0, XIS 3), while those of 2005 are summed over three FI cameras (includes XIS2 which was still alive at that time; §3.3), and then multiplied by a factor of $0.5 = 2/3 \times 0.75$, where the additional factor 0.75 represents the differences in pointing positions between the two observations (§3.4). The 2009 HXD count rate was multiplied by a different factor of ~ 0.9, to compensate for the pointing-position difference. Therefore, the source intensity in the two observations can be directly compared.

In Fig. 6.1, the 2–3 keV and the 15–45 keV signals in 2005 are twice stronger than those in 2009, while the 3–10 keV signal in 2005 is about four times higher than that in 2009. Therefore, the 2–45 keV spectral shape in 2005 is expected to be more convex than that in 2009. In terms of variation characteristics, the 2005 light curves fluctuate around the averaged level, while those of 2009 exhibit a more monotonic decrease. The 2–3 keV variation amplitude in 2005 and 2009 is about 50% and a factor of ~ 4, respectively, while those in the higher two energy ranges are slightly smaller. Thus, the source showed different behavior on the two occasions, in terms of both the spectrum and the variability.

6.1.2 Difference spectrum analysis

In order to investigate the principal varying component in the 2–45 keV band of NGC 3516, we performed the difference spectrum analysis (cf. §5.1.2, §5.3.2), dividing the data into a High and Low phase with respect to the average count rate (a dotted line in Fig. 6.1). The accumulated High-

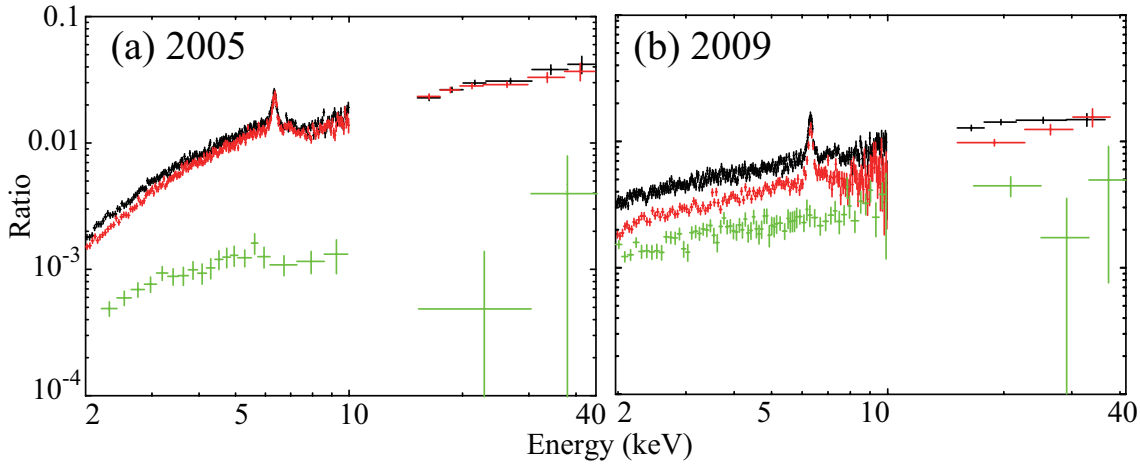

Figure 6.2: The High-phase (black), Low-phase (red), and difference spectrum (green) of NGC 3516 in 2005 (panel a) and 2009 (panel b), in the from of ratios to a common $\Gamma = 2.0$ PL.

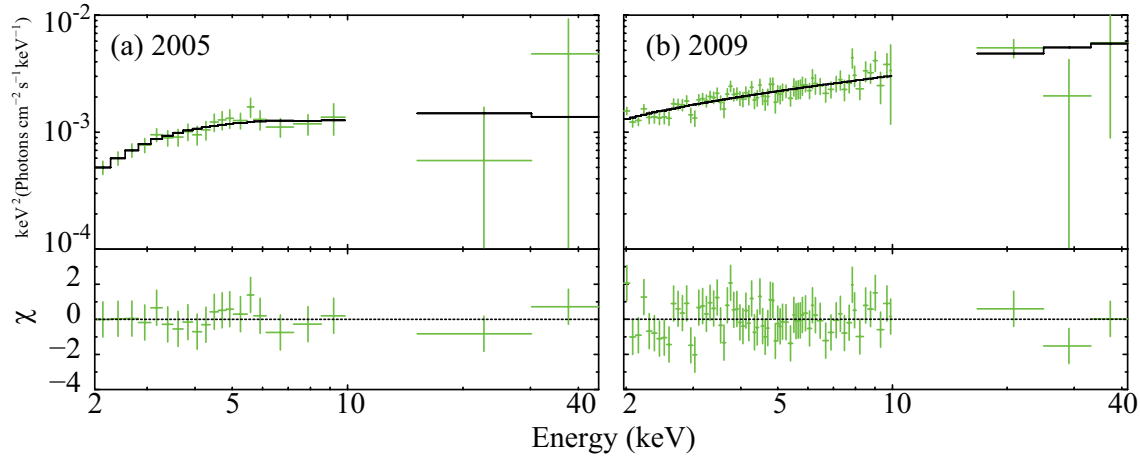

Figure 6.3: Difference spectra of NGC 3516 in 2005 (panel a) and 2009 (panel b), in a νF_ν form, fitted with `Phabs*PL`.

and Low-phase spectra of the two observations are shown in Fig. 6.2 in a form of the $\Gamma = 2.0$ PL ratio. Because the 2009 light curves show larger variations (Fig. 6.1) than those in 2005, the separation between the High- and Low-phase spectra in 2009 is larger than that in 2005. Furthermore, as inferred in §6.1.2, the spectra in 2005 are indeed more convex than those in 2009.

The difference spectra, obtained by subtracting the Low-phase from the High-phase spectra, are shown in Fig. 6.2 (green). Apparently, they are softer than the High- and Low-phase spectra, and are featureless without noticeable emission lines (e.g., at ~ 6.4 keV). In addition, the 2005 result is softer and more absorbed than that of 2009. We fitted them with an absorbed PL continuum with a free column density $N_{\rm H}$ and a free slope Γ, with $z = 0.00885$ fixed. As shown in Fig. 6.3 and Table 6.1, the fits are successful, and confirm that the difference spectrum in 2005 is softer by $\Delta\Gamma \sim 0.5$ and more absorbed by $\Delta N_{\rm H} \sim 3 \times 10^{22}$ cm^{-2}. Thus, the slope and the absorption of the mainly varying

Table 6.1: Results of the fits to the variable and difference spectra of NGC 3516.

Model	Parameter	Difference (§6.1.2)		Variable (§6.1.5)	
		2005	2009	2005	2009
`Phabs`	$N_{\rm H}^{*}$	$3.6^{+1.7}_{-1.5}$	$0.44^{+0.45}_{-0.43}$	$4.5^{+4.4}_{-4.0}$	< 1.9
`PL`	Γ	$2.06^{+0.40}_{-0.34}$	$1.58^{+0.11}_{-0.12}$	$2.19^{+0.56}_{-0.48}$	$1.71^{+0.14}_{-0.13}$
	$E_{\rm cut}$ (keV)	200 (fix)			
	$N_{\rm PL}^{\dagger}$	$0.15^{+0.15}_{-0.07}$	$0.12^{+0.03}_{-0.02}$	$0.91^{+1.87}_{-0.55}$	$0.31^{+0.07}_{-0.10}$
χ^2/d.o.f.		26.84/34	106.16/109	11.18/13	15.90/13

* Equivalent hydrogen column density in 10^{22} cm^{-2}.

† The cutoff power-law normalization at 1 keV, in units of 10^{-2} photons keV^{-1} cm^{-2} s^{-1}.

continuum have both changed significantly in four years.

6.1.3 Count-count plots

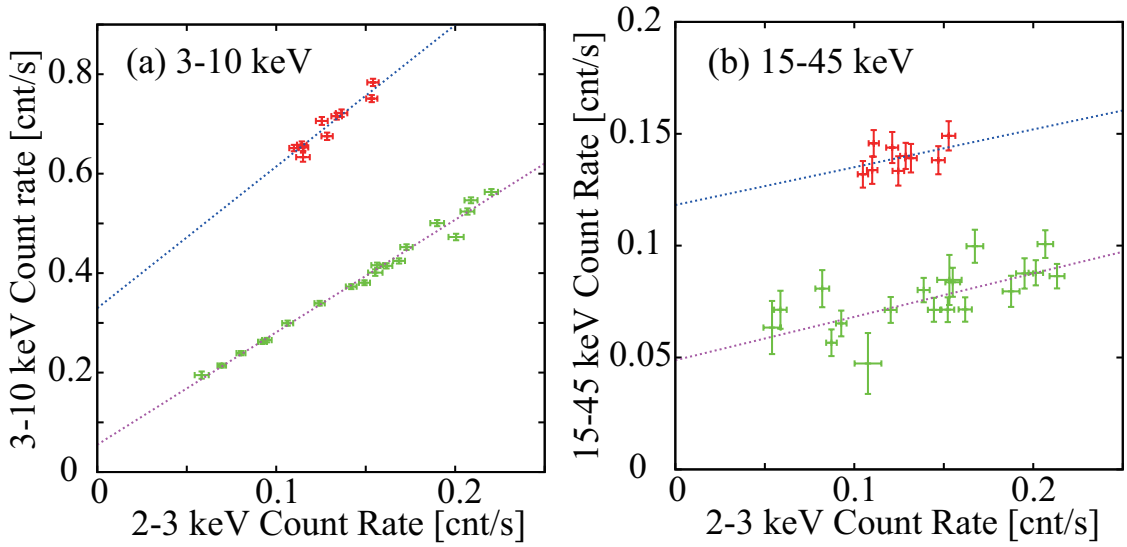

Figure 6.4: The CCPs of NGC 3516 in 2005 (red) and 2009 (green), in which abscissas gives NXB-subtracted XIS FI count rate in 2–3 keV, while ordinate gives that in 3–10 keV (panel a) and 15–45 keV (panel b). All data are binned into 25 ksec. The error bars represent statistical $\pm 1\sigma$ range, and the dotted straight lines refer to eq. (5.1).

Like in §5.1.3, we made CCPs, where abscissa is the count rate in the 2–3 keV data, while ordinate is that in the 3–10 keV or 15–45 keV energy ranges, with a bin size of 25 ksec. The result, shown in Fig. 6.4 clearly reconfirms the long-term spectral changes suggested by Fig. 6.1 and Fig. 6.3. Hereafter, we analyze the 2005 and 2009 data sets in parallel, but separately. We have included 1% systematic errors in the 2–3 keV band, while not to the 3–10 keV and 15–45 keV bands, where statistical errors dominate any systematic error. With χ^2/ d.o.f. = 20.1/8 in 2005 and 19.5/17 in 2009, the CCPs between the 2–3 keV and the 3–10 keV band were successfully fitted with eq. (5.1),

and gave $A = 2.89 \pm 0.31$ and $B = 0.65 \pm 0.08$ in 2005, while $A = 2.26 \pm 0.05$ and $B = 0.056 \pm 0.007$ in 2009. In the CCPs between the 2–3 keV and the 15–45 keV ranges, the fits were also successful with χ^2/d.o.f. $= 5.5/7$ in 2005 and 28.1/17 in 2009; we obtained $A = 0.09 \pm 0.06$ and $B = 0.118 \pm 0.015$ in 2005, while $A = 0.19 \pm 0.04$ and $B = 0.049 \pm 0.007$ in 2009. Because the obtained slopes and offsets are all significantly positive, we can apply the C3PO method to the 3–45 keV energies of both data sets.

To confirm that the C3PO parameters thus derived in the higher energy bands are relatively insensitive to the bin size (like in the soft X-ray result; §5.1.3,), we examined the bin widths of 5 ksec, 10 ksec, 20 ksec, 30 ksec. From those in the case of 25 ksec, these parameters were confirmed change by no more than 5%, which is less than 1σ errors. Thus, in subsequent analyses of the hard X-ray band, we employ the bin size of 25 ksec.

6.1.4 The C3PO analysis

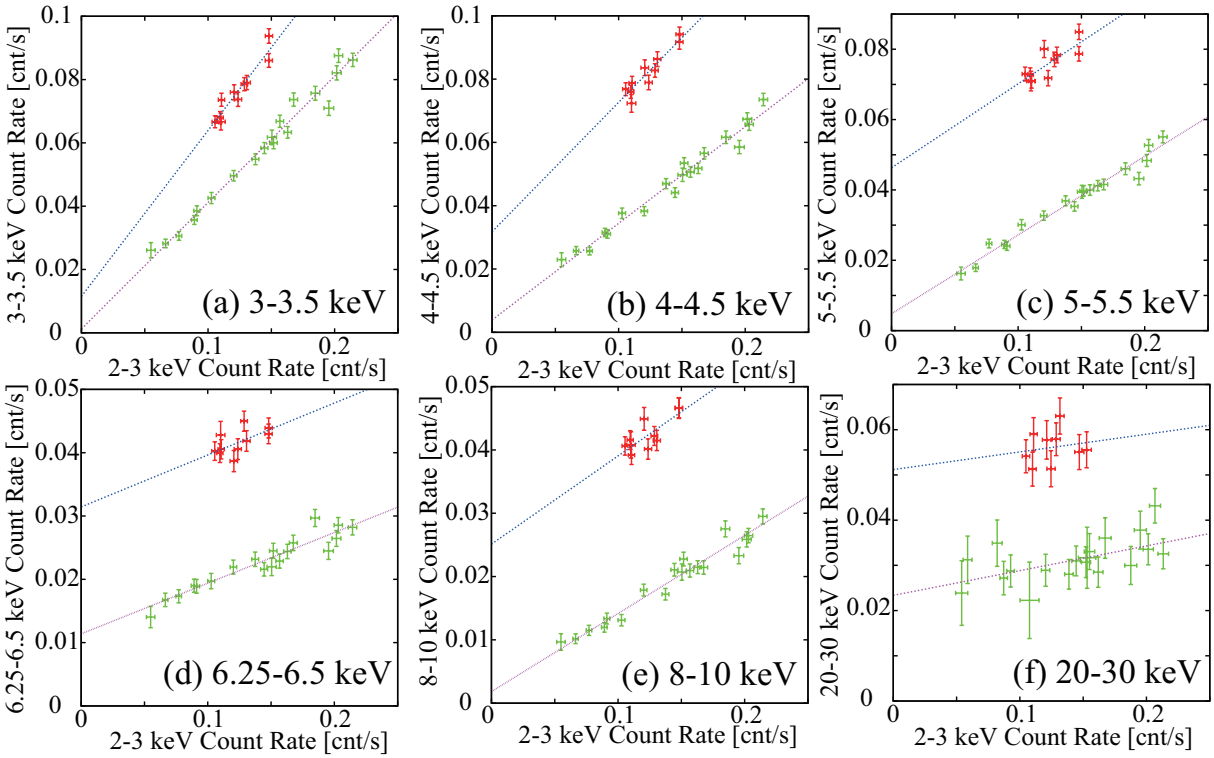

Figure 6.5: The same as Fig. 6.4, but ordinate gives NXB-subtracted XIS FI count rate in (a) 3–3.5 keV, (b) 4–4.5 keV, (c) 5–5.5 keV, (d) 6.25-6.5 keV, (e) 8–10 keV, and (f) 20–30 keV.

Like in §5.1.4, we divided the 3–10 keV energy range of the two data sets into 13 finer bands, with boundaries at 3, 3.5, 4, 4.5, 5, 5.5, 6, 6.25, 6.5, 6.75, 7, 7.5, 8, and 10 keV. Because we aim to analyze the HXD-PIN data as well, the 15–45 keV broadband was similarly subdivided into three; 15-20, 20-30, and 30–45 keV. Then, we made 16 CCPs using again 2–3 keV as the reference. In Fig. 6.5, six of the 16 CCPs are shown, where the two observations again form two distinct branches. By fitting

Table 6.2: Parameters obtained by fitting the CCPs with eq. (5.1).

Observation	Range (keV)	Slopes*	Offsets†	χ^2/d.o.f.
2005	3–3.5	0.52 ± 0.06	0.22 ± 0.14	18.2/8
	3.5–4	0.46 ± 0.06	0.49 ± 0.14	17.5/8
	4–4.5	0.41 ± 0.05	0.62 ± 0.12	13.9/8
	4.5–5	0.38 ± 0.05	0.66 ± 0.11	11.8/8
	5–5.5	0.24 ± 0.06	0.91 ± 0.15	24.2/8
	5.5–6	0.29 ± 0.04	0.64 ± 0.10	13.1/8
	6–6.25	0.08 ± 0.04	0.47 ± 0.09	19.5/8
	6.25–6.5	0.08 ± 0.03	0.62 ± 0.08	15.0/8
	6.5–6.75	0.06 ± 0.02	0.32 ± 0.06	12.9/8
	6.75–7	0.04 ± 0.02	0.32 ± 0.04	6.8/8
	7–7.5	0.10 ± 0.03	0.37 ± 0.06	12.4/8
	7.5–8	0.09 ± 0.01	0.21 ± 0.04	5.7/8
	8–10	0.15 ± 0.04	0.51 ± 0.09	16.6/8
	15–20	0.03 ± 0.14	0.68 ± 0.11	13.9/8
	20–30	0.05 ± 0.21	0.53 ± 0.17	14.7/8
	30–45	0.15 ± 0.08	0.06 ± 0.07	7.4/8
2009	3–3.5	0.40 ± 0.01	0.12 ± 0.18	26.1/17
	3.5–4	0.36 ± 0.01	0.26 ± 0.14	17.2/17
	4–4.5	0.31 ± 0.01	0.39 ± 0.16	26.0/17
	4.5–5	0.26 ± 0.01	0.39 ± 0.15	25.3/17
	5–5.5	0.22 ± 0.01	0.48 ± 0.13	24.4/17
	5.5–6	0.19 ± 0.01	0.38 ± 0.07	8.5/17
	6–6.25	0.08 ± 0.01	0.51 ± 0.08	22.9/17
	6.25–6.5	0.08 ± 0.01	1.13 ± 0.09	18.2/17
	6.5–6.75	0.05 ± 0.00	0.40 ± 0.05	13.4/17
	6.75–7	0.05 ± 0.00	0.34 ± 0.06	22.5/17
	7–7.5	0.09 ± 0.01	0.36 ± 0.06	11.9/17
	7.5–8	0.06 ± 0.01	0.10 ± 0.05	17.9/17
	8–10	0.12 ± 0.01	0.18 ± 0.09	26.9/17
	15–20	0.18 ± 0.05	2.23 ± 0.51	37.4/17
	20–30	0.06 ± 0.03	2.53 ± 0.29	14.4/17
	30–45	0.01 ± 0.00	0.58 ± 0.24	24.4/17

Notes.

* Slopes, a in units of 1.

† Offsets, b, for 2005 in units of 10^{-1} and 2009 in units of 10^{-2}.

the data in the 16 CCPs (separately for 2005 and 2009) with eq. (5.1), the parameters summarized in Table 6.2 were obtained. Since the obtained values of A and B are mostly positive, we can decompose the 3–45 keV data into a variable and a stationary components.

In Chapter 5, we have identified the soft excess (= the stationary) component as those signals which remain even when the 3–10 keV (the reference band) intensity vanishes. In this Chapter, the reference band has been changed to 2–3 keV, so that the C3PO method can be applied to a harder/broader energy range (3–45 keV). However, this raises a technical problem: the 2–3 keV reference band can contain the hardest end of the soft excess component which is considered to lack fast variations (Chapter 5), or any other AGN emission that remains constant during typical `Suzaku` observations (1–3 days). In other words, the reference-band intensity x in eq. (5.1) can have a non-zero and

generally unknown intensity floor, C. Then, eq. (5.1) should be rewritten as

$$y = A(x - C) + B + AC = A(x - C) + B' \quad \text{where } B' = B + AC. \tag{6.1}$$

In this case, the variable spectrum must be constructed by assembling $A(x_0 - C)$, instead of Ax_0, resulting in a systematic decrease in the spectral normalization (with the same slope). The stationary component would be more seriously affected by the choice of C, because the assembly of B' is expected to have a different spectral shape from that of B. However, as already discussed in detail in Noda et al. (2013b), the newly obtained stationary component, constructed from B', is mathematically a summation of the stationary component (for $C = 0$) made from B and the variable component AC. When $C \neq 0$, the variable component is therefore reduced by a certain fraction, and that signal is simply added on top of the original stationary component. Because the essence of the signal decomposition is thus the same regardless of the value of C, we hereafter consider, for simplicity, only the case with $C = 0$. Further discussion on this point is given in §7.1.4.

6.1.5 Variable Components

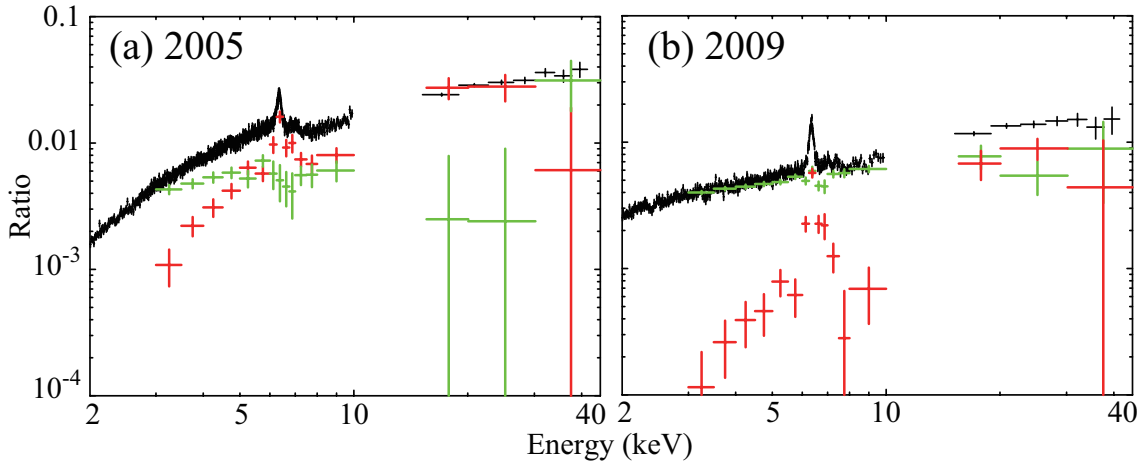

Figure 6.6: The time-averaged (black), the variable (green), and the stationary (red) spectra of NGC 3516 in 2005 (panel a) and 2009 (panel b), in a form of the $\Gamma = 2.0$ PL ratio.

In the 3–45 keV broad energy range, 16 values of the slope A (Table 6.2) were obtained via the C3PO technique. Multiplying them by the average count rate in the 2–3 keV band, $x_0 \sim 0.14$ cnt s^{-1} in 2005 and ~ 0.8 cnt s^{-1} in 2009, and dividing them by the corresponding energy intervals, the variable component has been constructed as shown in Fig. 6.6 in green. It is similar in shape to the difference spectrum (Fig. 6.3), without prominent spectral features.

To quantify the shape of the variable spectra, we fitted them with `Phabs*PL`, where the column density of `Phabs` and the photon index of `PL` were left free, like in the fits to the difference spectra. The fits were successful, and gave the results as summarized in Table 6.1. The obtained parameters are consistent, within errors, with those of the difference spectra, except the normalizations which

are meaningless in the difference spectra. Like in the soft X-ray band analyses, the variable and the difference spectra are thus considered to be essentially identical.

6.1.6 Stationary Components

By dividing the offsets B obtained in the fits to the 16 CCPs by the corresponding energy intervals, the stationary components have been obtained as shown in Fig. 6.6 in red. They are much harder than the corresponding variable spectra, and notably, exhibit prominent Fe-Kα lines. These properties are direct consequence of the large offsets seen in Fig. 6.5 at the Fe-K (panel d) and HXD-PIN (panel f) energies. Especially in 2009, it looks like a reflection component generated at a distant and cold material. However, the two stationary spectra are considerably different, especially in the 3–45 keV continuum intensity and intensity ratio of the Fe-Kα line to the continuum.

To investigate physical processes producing the stationary components, we proceed to the spectral fitting (cf. §5.1.6, §5.3.3). In the hard X-ray region, the following models are possible (§5.1.6, §5.3.3):

- A cold reflection continuum generated at a neutral accretion disk or dust torus, accompanied by a sharp Fe-K edge at ~ 7.1 keV and a narrow Fe-Kα emission line at ~ 6.4 keV. It is modeled by `ReflFe`.
- An ionized reflection component produced by an ionized accretion disk. Its edge depth and edge energy, as well as the emission-line intensity, depend on the ionization parameter ξ. It is modeled by `Iorefl`.
- A relativistically-blurred and ionized reflection continuum, created at regions close to the central black hole, e.g., on an ionized accretion disk. The model for this component is denoted here `RBR` (its XSPEC model name is `kdblur*reflionx`). It differs from the 2nd model (a simple ionized reflection) in that the edges and lines are smeared by relativistic effects, including the longitudinal and transverse Doppler effects, and the gravitational redshift, all working at a range of radii from the BH. As a result, the model looks somewhat like a hard featureless continuum.
- An absorbed PL continuum, which represents another primary continuum independent of the variable PL. It is modeled by `Phabs'*PL'`.

These models, from top to bottom, progressively become featureless. Because the narrow Fe-Kα structures can be clearly seen in the stationary spectra, at least the `ReflFe` model should be included, but it is not obvious at this stage whether any other component(s) must also be included or not.

First, we fitted the stationary components with `Phabs*ReflFe` alone. The column density of `Phabs`, and the photon index Γ of the incident PL continuum for `ReflFe`, were fixed at the values obtained in the fits to the difference spectrum in Table 6.1. (The results depend only weakly on the value of Γ.) The abundance and the inclination of `ReflFe` were fixed at 1 Solar and 60°, respectively, while the other parameters were left free. As a result, the stationary component in 2009 has been successfully reproduced only by `ReflFe` as shown in Fig. 6.7 (e), and yielded the parameters summarized in

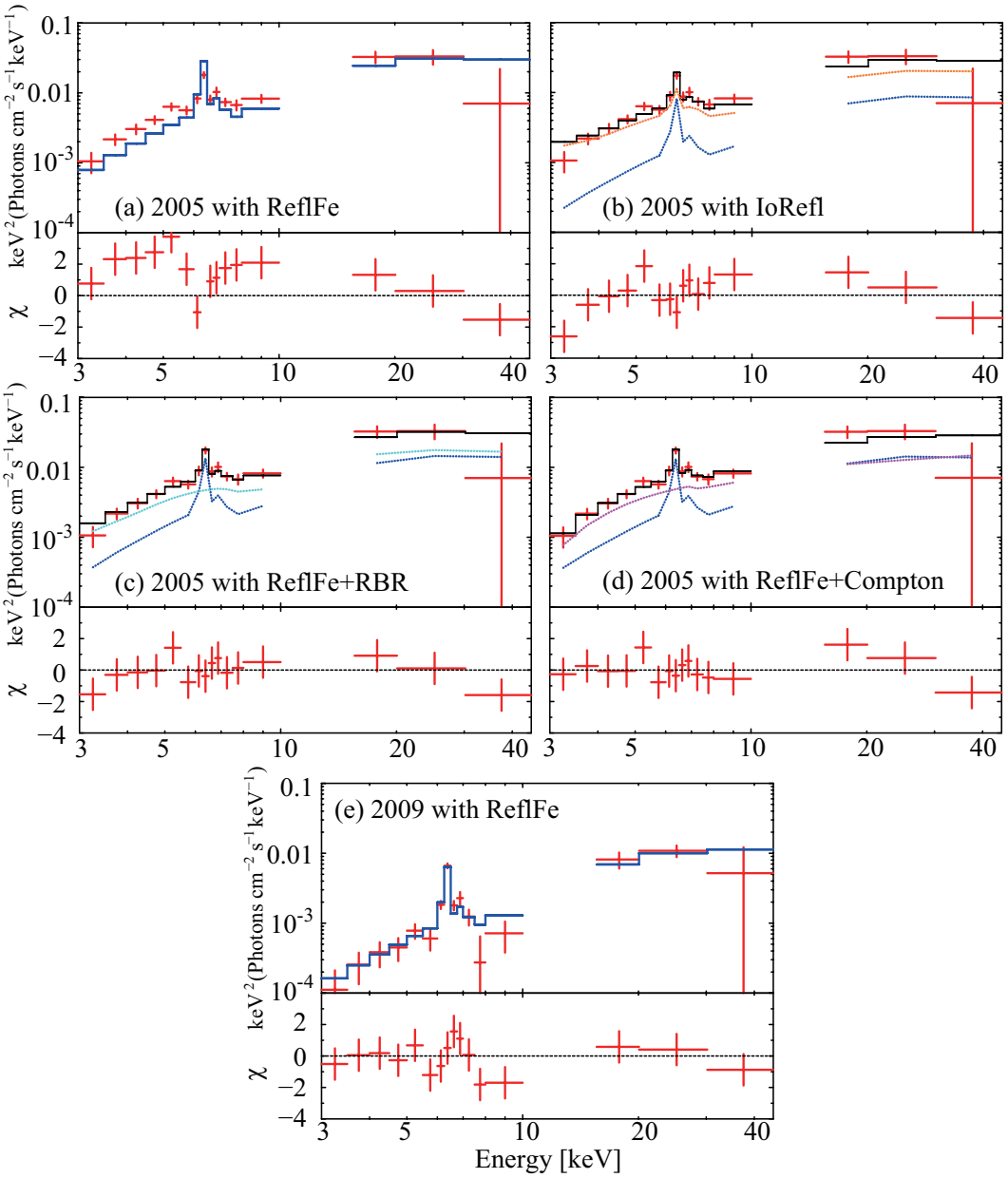

Figure 6.7: The stationary component in 2005 (panel a-d) and 2009 (panel e), fitted with several hard X-ray models. Blue represents a cold reflection model `ReflFe`, purple an absorbed PL `Phabs * PL`, orange an ionized disk reflection `Iorefl`, and cyan a relativistically-blurred and ionized reflection model `RBR`.

Table 6.3: Results of the spectral fits to the C3PO-derived stable spectra in 2005 and 2009.

Component	Parameter	2005	2009
Absorption to all			
`Phabs`	$N_{\rm H0}^{\dagger}$	3.6 (fix)	0.9 (fix)
Neutral reflection component			
`Refl`	$\Gamma_{\rm ref}$	2.12 (fix)	1.75 (fix)
	$E_{\rm cut}$ (keV)	200 (fix)	
	$f_{\rm ref}$ $(\Omega/2\pi)$	1 (fix)	
	A $(Z_{\odot})$	1 (fix)	
	$A_{\rm Fe}$ $(Z_{\rm Fe,\odot})$	1 (fix)	
	i (degree)	60 (fix)	
	$N_{\rm ref}^{\ddagger}$	0.70	$0.67^{+0.05}_{-0.06}$
χ^2/d.o.f.		90.24/15	18.99/15
Absorption to all			
`phabs`	$N_{\rm H}^{*}$	3.6 (fix)	–
Neutral reflection component			
`Refl`	$\Gamma_{\rm ref}$	2.12 (fix)	–
	$E_{\rm cut}$ (keV)	200 (fix)	
	$f_{\rm ref}$ $(\Omega/2\pi)$	1 (fix)	
	A $(Z_{\odot})$	1 (fix)	
	$A_{\rm Fe}$ $(Z_{\rm Fe,\odot})$	1 (fix)	
	i (degree)	60 (fix)	
	$N_{\rm ref}^{\ddagger}$	2.00	–
Ionized reflection component			
`Iorefl`	$A_{\rm Fe}$ $(Z_{\rm Fe,\odot})$	1 (fix)	
	$\Gamma_{\rm ref}$	2.12 (fix)	–
	ξ (erg cm s^{-1})	97.0	–
	$N_{\rm ref}^{\S}$	0.65	–
χ^2/d.o.f.		20.11/13	–
Absorption to all			
`Phabs`	$N_{\rm H0}^{*}$	3.6 (fix)	–
Neutral reflection component			
`Refl`	$\Gamma_{\rm ref}$	2.12 (fix)	–
	$E_{\rm cut}$ (keV)	200 (fix)	
	$f_{\rm ref}$ $(\Omega/2\pi)$	1 (fix)	
	A $(Z_{\odot})$	1 (fix)	
	$A_{\rm Fe}$ $(Z_{\rm Fe,\odot})$	1 (fix)	
	i (degree)	60 (fix)	
	$N_{\rm ref}^{\ddagger}$	$3.31^{+1.19}_{-1.42}$	–
Relativistic reflection component			
`RBR`	q	5.6	–
	$R_{\rm in}$ $(R_{\rm g})$	1.6	–
	$R_{\rm out}$ $(R_{\rm g})$	400 (fix)	–
	A $(Z_{\odot})$	1 (fix)	
	$\Gamma_{\rm ref}$	2.12 (fix)	–
	ξ (erg cm s^{-1})	49.4	–
	$N_{\rm ref}^{\S}$	$1.32^{+0.19}_{-0.36}$	–
χ^2/d.o.f.		9.69/11	–

Table 6.3: (Continue) Results of the spectral fits to the C3PO-derived stable spectra in 2005 and 2009.

Component	Parameter	2005	2009
Absorption to all			
`Phabs`	$N_{\rm H0}^{\dagger}$	3.6 (fix)	–
Neutral reflection component			
`ReflFe`	$\Gamma_{\rm ref}$	2.12 (fix)	–
	$E_{\rm cut}$ (keV)	200 (fix)	
	$f_{\rm ref}$ $(\Omega/2\pi)$	1 (fix)	
	A $(Z_{\odot})$	1 (fix)	
	$A_{\rm Fe}$ $(Z_{\rm Fe,\odot})$	1 (fix)	
	i (degree)	60 (fix)	
	$N_{\rm ref}^{\ddagger}$	0.33 ± 0.50	–
Hard Primary component*			
`Phabs'`	$N_{\rm H1}^{*}$	$11.6^{+5.5}_{-5.2}$	–
`PL'`	Γ_1	$1.51^{+0.74}_{-0.49}$	–
	$E_{\rm cut}$ (keV)	200 (fix)	
	$N_{\rm PL}^{\#}$	$2.61^{+0.88}_{-0.37}$	–
χ^2/d.o.f.		9.22/12	–

* Later to be identified in §7.1.2.

† Equivalent hydrogen column density in 10^{22} cm^{-2}.

‡ The `ReflfFe` normalization at 1 keV, in units of 10^{-2} photons keV^{-1} cm^{-2} s^{-1} at 1 keV.

§ The `RBR` or `Iorefl` normalization, in units of 10^{-6}.

The `PL` normalization at 1 keV, in units of 10^{-2} photons keV^{-1} cm^{-2} s^{-1} at 1 keV.

Table 6.3. Thus, our C3PO method has allowed to extract the refection signals in nearly model-independent ways. Before the present work, such a pure reflection spectrum was observed only in very limited cases (e.g., Reynolds et al. 1996), and its spectral shape was usually assumed based on model calculations (e.g., George & Fabian 2002). In contrast, the `ReflFe` model failed on the 2005 stationary spectrum (Fig. 6.7 a), because it over-predicts the Fe-Kα line and under-predicts the observed 3–10 keV continuum. It would be unrealistic to try improving the fit by reducing the Fe abundance, because a nuclear region of the host galaxy would be sufficiently metal enriched, and 1-Solar abundance reflection has already given a very satisfactory explanation of the 2009 stationary component. This means that an additional continuum (without the Fe-K features), which is softer than the cold reflection continuum, must be introduced in the fitting model to the 2005 stationary component. Thus, we tried two component fits to the 2005 stationary spectrum.

Considering the need for a somewhat softer continuum than the cold reflection, an ionized reflection component (§2.3.3), `Iorefl`, was added, with the photon index of the incident PL and the Fe abundance fixed at 2.1 and 1 Solar, respectively, while the other parameters left free. Thus, we fitted the stationary spectrum in 2005 with `Phabs*(ReflFe + Iorefl)`. As shown in Fig. 6.7 (b) and Table 6.3, the fit drastically improved to χ^2/d.o.f.=20.11/13. Further incorporating relativistic effects into

the ionized reflection, and hence utilizing the model as `Phabs*(ReflFe + RBR)`, the fit became still better, and fully acceptable with χ^2/d.o.f.=9.69/11 (Fig. 6.7 c and Table 6.3). Thus, the combination of the cold reflection and the relativistically-blurred reflection can reproduce the stationary component in 2005.

An absorbed PL can be an alternative candidate for the additional softer continuum. In the above successful fit, we therefore replace the `RBR` model by `Phabs'*PL'`, and fitted the 2005 stationary emission with `Phabs*(ReflFe + Phabs'*PL')`, where `Phabs'` and `PL'` are meant to be distinct from `Phabs` and `PL`, which were to fit the variable component (Table 6.1), respectively. The parameter of `Phabs` and `ReflFe` were the same as those in the previous fit, while the other parameters (including those of `Phabs'*PL'`) were left free. As shown in Fig. 6.7 (d), the fit was successful as well, and the parameters are summarized in Table 6.3.

In summary, the C3PO-derived stationary spectrum in 2009 can be explained in terms of pure cold reflection, while that of 2005 additionally requires either RBR or an absorbed PL in addition.

6.1.7 Triplet spectrum analyses

As the final confirmation of the C3PO decomposition of the 2009 spectrum, we followed the procedure in §5.1.7 and §5.3.4, and simultaneously fitted the triplet spectra. Specifically, the 2009 variable spectrum was fitted with `model_v` = `Phabs*Ioabs*PL` (found in §6.1.5), its stationary counterpart with `model_s0` = `Phabs*Ioabs*ReflFe` (after §6.1.6), and the 2009 time-averaged data simultaneously with `model_v + model_s0`. The parameter conditions were the same as those in §6.1.5 and §6.1.6, except that the column density of `Phabs` and the incident photon index of `ReflFe` were tied to those in `model_v`. In addition, `model_v` was multiplied by an ionized absorption factor `Ioabs`, of which the meaning and motivation are explained in the last paragraph. As shown in Fig. 6.8 (a) and Table 6.4, the fit to the 2009 spectral tripled has been successful. What happens when an ionized reflection component is considered alternatively to the neutral reflection component? This issue was difficult to examine by only the fit to the stationary component in §6.1.6, because the stationary spectrum does not cover $\lesssim 3$ keV, where the ionized reflection includes many emission lines as shown in Fig. 2.13, giving a large difference from a neutral one. To examine this, we replaced `ReflFe` in `model_s0` by `Iorefl`, and fitted again the spectral triplet. The result became still successful with χ^2/d.o.f.=548.9/484, but gave a rather stringent upper limit of ionization parameter as $\xi < 12.3$. Thus, the reflection component is required to be almost neutral in the 2009 data of NGC 3516. In short, the wide-band 2009 spectrum of NGC 3516 have been decomposed successfully into a variable PL with $\Gamma \sim 1.7$ and a reflection from a (nearly-) neutral material.

When the same analysis was applied to the 2005 spectral triplet, the simultaneous fit naturally failed with χ^2/d.o.f.=1472.89/744: as expected (§6.1.6), the model underpredicts the 3-10 keV continuum of the stationary spectrum, and of the time-averaged data as well. Accordingly, we changed `model_s0` into `model_s1 = Phabs * Ioabs * (ReflFe + RBR)`, by adding the `RBR` component which is one of the two surviving interpretations in §6.1.6. The ionization parameter and the normalization

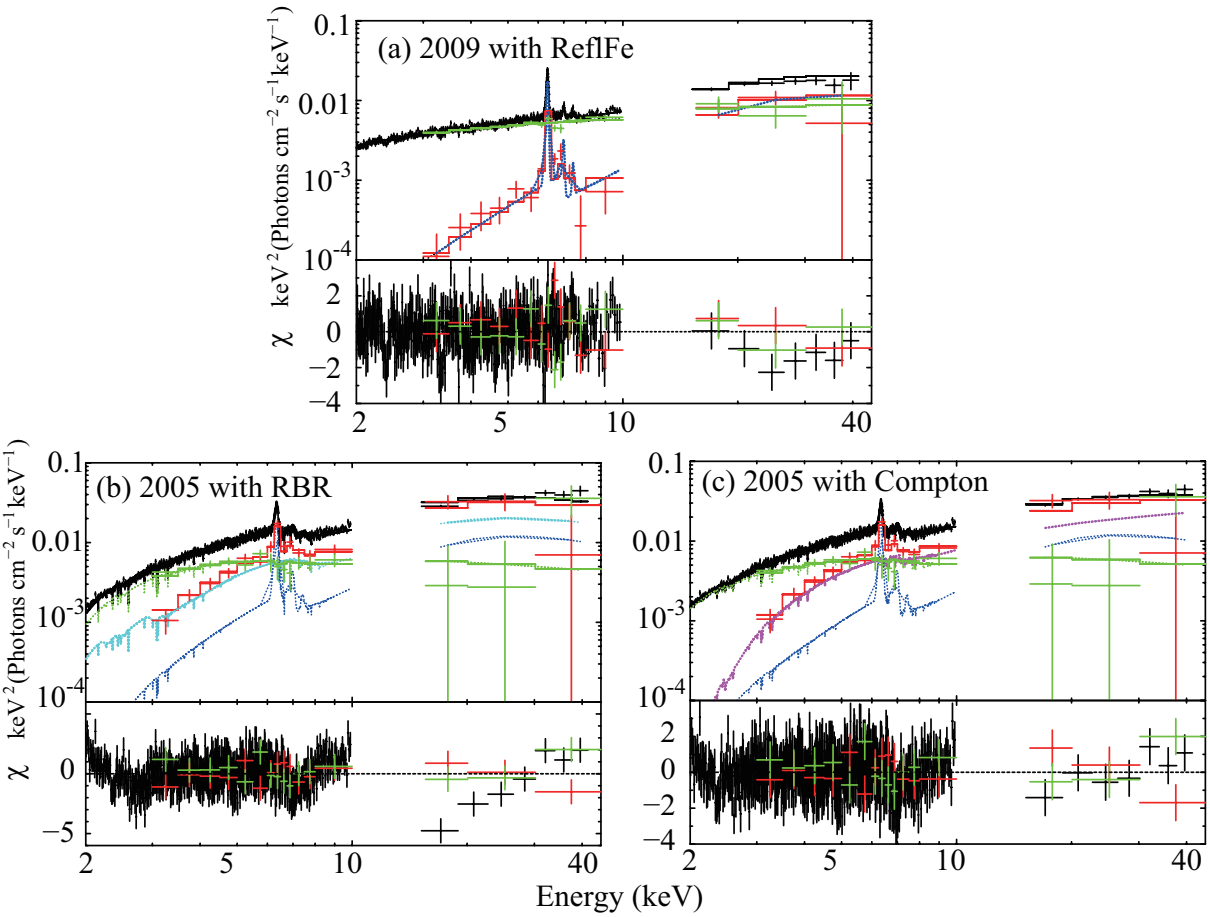

Figure 6.8: Simultaneous fits to the time-averaged (black), the variable (green), and the stationary spectra (red) of NGC 3516 in 2009 (panel a) and 2005 (panels b and c). Blue line represents the `ReflFe` model, cyan the `RBR` model, while purple the additional Comptonization model. In panel (a and c), the `PL` model in green is found as the Broad-Band Primary continuum, while the `Phabs' * PL'` signal in purple as the Hard Primary component in §7.1.2.

of the the `RBR` model were left free, its Fe abundance was fixed at 1 Solar, and its incident photon index was tied to that of the PL component. The other parameters were treated in the same way as in the 2009 triplet fitting, Then, as shown in Fig. 6.8 (b) and Table 6.4, the fit to the 2005 spectral triplet drastically improved, and the two C3PO-derived spectra were well reproduced. Nevertheless, the overall fit still remained unacceptable with χ^2/d.o.f.=998.54/741, because the model does not agree in shape with the time-averaged spectrum, particularly in the 7–10 and 15–45 keV ranges. In short, the BRB interpretation of the stationary signals is inappropriate as an explanation of the 2005 *Suzaku* data.

To examine the additional absorbed PL model which is the other candidate allowed by the 2005 stationary spectrum, we changed `model_s1` to `model_s2 = Phabs*Ioabs*(ReflFe + Phabs'*PL')`, allowing all the parameters of `Phabs'*PL'` to be free. Then, as shown in Fig. 6.8 (c) and Table 6.4, the fits to the 2005 triplet has become fully successful. Furthermore, not only the overall chi-square, but also those of the individual components became acceptable; χ^2/d.o.f.=777.31/709, 11.34/16, and

Table 6.4: Parameters obtained by fitting simultaneously the time-averaged spectrum of NGC 3516, together with the variable and stationary spectra derived by the C3PO method.

Component	Parameter	2005	2009
Absorption to all			
`Phabs`	$N_{\rm H0}^{\dagger}$	2.4	$0.9^{+0.2}_{-0.4}$
`Ioabs`	$N_{\rm i}^{\dagger}$	13.5	< 2.4
	$\log \xi$	3.07 ± 0.06	> 4.89
	Cvr frac.	1 (fix)	
	z	0.0086 (fix)	
Broad-Band Primary component			
`PL`	Γ_0	1.88	$1.70^{+0.08}_{-0.12}$
	$E_{\rm cut}$ (keV)	200 (fix)	
	$N_{\rm PL}^{\ddagger}$	11.4	$3.13^{+0.49}_{-0.57}$
Reflection component			
`ReflFe`	$\Gamma_{\rm ref}$	$= \Gamma_{\rm PL}$	
	$E_{\rm cut}$ (keV)	200 (fix)	
	$f_{\rm ref}$ $(\Omega/2\pi)$	2.0	2.0 ± 0.5
	A $(Z_{\odot})$	1 (fix)	
	$A_{\rm Fe}$ $(Z_{\rm Fe,\odot})$	1 (fix)	
	i (degree)	60 (fix)	
	$N_{\rm ref}$	$= N_{\rm PL}$	
χ^2/d.o.f.		1472.89/744	508.61/484
Absorption to all			
`Phabs`	$N_{\rm H0}^{*}$	4.8 ± 0.4	–
`Ioabs`	$N_{\rm i}^{*}$	$5.1^{+0.7}_{-0.6}$	–
	$\log \xi$	3.11 ± 0.06	–
	Cvr frac.	1 (fix)	
	z	0.0086 (fix)	
Broad-Band Primary component			
`PL`	Γ_0	2.20 ± 0.15	–
	$E_{\rm cut}$ (keV)	200 (fix)	
	$N_{\rm PL}^{\ddagger}$	$0.98^{+0.28}_{-0.32}$	–
Reflection components			
`ReflFe`	$\Gamma_{\rm ref}$	$= \Gamma_{\rm PL}$	
	$E_{\rm cut}$ (keV)	200 (fix)	
	$f_{\rm ref}$ $(\Omega/2\pi)$	$2.8^{+0.7}_{-0.4}$	–
	A $(Z_{\odot})$	1 (fix)	
	$A_{\rm Fe}$ $(Z_{\rm Fe,\odot})$	1 (fix)	
	i (degree)	60 (fix)	
	$N_{\rm ref}$	$= N_{\rm PL}$	
`RBR`	q	> 4.3	–
	$R_{\rm in}$ $(R_{\rm g})$	< 1.8	–
	$R_{\rm in}$ $(R_{\rm g})$	400	–
	i (degree)	60 (fix)	
	$A_{\rm Fe}$ $(Z_{\rm Fe,\odot})$	1 (fix)	
	$\Gamma_{\rm ref}$	$= \Gamma_{\rm PL}$	
	ξ (erg cm s^{-1})	< 73.6	–
	$N_{\rm ref}^{\S}$	$2.63^{+0.19}_{-0.36}$	–
χ^2/d.o.f.		998.54/741	–

Table 6.4: (Continue) Parameters obtained by fitting simultaneously the time-averaged spectrum of NGC 3516, together with the variable and stationary spectra derived by the C3PO method.

Component	Parameter	2005	2009
Absorption to all			
`Phabs`	$N_{\rm H0}^{\dagger}$	3.6 ± 0.4	–
`Ioabs`	$N_{\rm i}^{\dagger}$	$43.8^{+0.7}_{-0.6}$	–
	$\log \xi$	3.11 ± 0.06	–
	Cvr frac.	1 (fix)	
	z	0.0086 (fix)	
Broad-Band Primary component*			
`PL`	Γ_0	2.17 ± 0.15	–
	$E_{\rm cut}$ (keV)	200 (fix)	
	$N_{\rm PL}^{\S}$	$0.99^{+0.28}_{-0.32}$	–
Reflection component			
`ReflFe`	$\Gamma_{\rm ref}$	$= \Gamma_{\rm PL}$	
	$E_{\rm cut}$ (keV)	200 (fix)	
	$f_{\rm ref}$ $(\Omega/2\pi)$	$2.5^{+0.7}_{-0.4}$	–
	A $(Z_{\odot})$	1 (fix)	
	$A_{\rm Fe}$ $(Z_{\rm Fe,\odot})$	1 (fix)	
	i (degree)	60 (fix)	
	$N_{\rm ref}$	$= N_{\rm PL}$	
Hard Primary component*			
`Phabs'`	$N_{\rm H1}^{*\dagger}$	$8.9^{+1.2}_{-1.9}$	–
`PL'`	Γ_1	1.42 ± 0.06	–
	$E_{\rm cut}$ (keV)	200 (fix)	
	$N_{\rm PL}^{\ddagger}$	$0.99^{+0.28}_{-0.24}$	–
χ^2/d.o.f.		799.28/741	–

* Later to be identified in §7.1.2.

*† Equivalent hydrogen column density in 10^{22} cm^{-2}.

‡ The power-law normalization at 1 keV, in units of 10^{-2} photons keV^{-1} cm^{-2} s^{-1} at 1 keV.

§ The `reflionx` normalization in units of 10^{-6}.

10.62/16, for the time-averaged, the variable, and the stationary spectra, respectively. The obtained photon index of the main variable `PL` (`model_v`) is consistent, within errors, with that obtained by fitting the variable component only (§6.1.5). The photon index of `PL'` is ~ 1.4, and the column density of `Phabs'` is $\sim 9 \times 10^{22}$ cm^{-2} (totally $\sim 1.2 \times 10^{23}$ cm^{-2} for `Phabs*Phabs'`). They are all consistent, within errors, with those obtained in the fit to the 2005 stationary emission, and are significantly different from those of `model_v`.

Like in §5.1.7, the triplet analysis has thus successfully brought our "dynamical" C3PO decomposition into full agreement with the traditional "static" model fitting analysis. Furthermore, it successfully solved the degeneracy of the two models (`RBR` and `Phabs' * PL'`), where the latter remained feasible in §6.1.6 to express the 2005 stationary spectrum. The 2009 data can be decomposed

into; (i) a variable PL component with a canonical slope ($\Gamma_0 = 1.6$) and a relatively weak absorption ($N_{\rm H0} \sim 1 \times 10^{22}$ cm^{-2}), expressed by `model_v`, and (ii) a reflection component (with a narrow Fe-K line), namely, `model_s0`, produced in approximately Solar-abundance materials located far away from the central BH. This reconfirms one of the simplest views of the AGN emission (§2.3.1). The 2005 data has been successfully decomposed as well, but into *three* components; (i) the same `model_v` as seen in 2009, but with a steeper slope ($\Gamma_0 \sim 2.2$) and a higher absorption ($N_{\rm H0} \sim 1 \times 10^{22}$ cm^{-2}), (ii) the reflection component, `model_s0`, which has an approximately the same intensity as that in 2009, and (iii) a strongly absorbed ($N_{\rm H1} \sim 9 \times 10^{22}$ cm^{-2}), flatter ($\Gamma_1 \sim 1.4$) PL. The sum of (ii) and (iii) makes up `model_s2`. Although these results all assume zero intensity floor ($C = 0$) in the reference energy band (2–3 keV), cases with $C \neq 0$ can be readily explained by assuming that a certain fraction of `model_v` remained unchanged, and was included into the stationary signals. In other words, our spectral decompositions in 2009 and 2005 both remain valid even if $C \neq 0$ in the 2–3 keV reference band.

In these fits, the ionized absorption modeled by `Ioabs` was introduced, whereas Turner et al. (2011) found several zones of ionized absorbers in NGC 3516, from the same *Suzaku* data. Although they considered multiple ionized absorption models, we used only one `Ioabs` model, and succeeded in deriving the acceptable results on both data sets.

6.1.8 A brief discussion on the origin of the "strongly-absorbed PL component"

Evidently, the most important result from the present study on NGC 3516 is the discovery of (iii), namely, the strongly-absorbed PL contributing to the stationary signal in 2005. Its presence and absence account for the main difference between the 2005 and 2009 data. In 2005, it was indeed 5–10 times more intense than the neutral reflection, and dominated the HXD-PIN range. In many studies, this component has been interpreted to be due to "partial absorption", in the other words, regarded as some of the primary emission passing though absorbers (§2.3.6). However, this popular interpretation cannot explain the results obtained with the C3PO method, because the origin of the partially-absorbed components is the primary emission, and they should show the identical variation properties and spectral shapes in the hard X-ray band to the non-absorbed part of the primary continuum in `model_v`. The partially-absorbed primary component thus would not significantly appear in the stationary emission obtained with the C3PO method.

Then, how is the strongly-absorbed and stationary PL component, which was derived with C3PO, is produced? We first consider the secondary components, which are produced by reprocesses including photo-absorption and Compton down-scattering (reflection) by some materials around the central BH. If the secondary components are generated at distant locations from the central region emitting primary X-ray, they have low time variability, which may explain the lack of variability of the C3PO-derived stationary emission. In addition, when the geometry and ionization degree of the materials are finely tuned, its hard spectral shape might be successfully explained as well. However, the secondary components must include a certain flux of Fe-K line, depending on the Fe abundance of the materials.

When we force the models of the secondary components to reproduce the stationary component, in addition to the model of the distance reflection, the Fe abundance became required to be unrealistically low. Furthermore, the solid angle of the materials generating the distant reflection against the primary region got required to be $\gtrsim 4\pi$ as shown in Table 6.4 in 2005, which is unrealistically large.

To make the solid angle of the distant reflectors moderate to be $\sim 2\pi$ for an infinite plane, the amount of illuminating primary X-ray emission needs to be increased. Then, we naturally interpreted the strongly-absorbed and stationary PL as an additional primary component to the variable PL. When we consider the two kinds of primary PL components, the solid angle of the distant reflectors became $\sim 2.5\pi$ as shown in Table 6.4, which is much more reasonable than the previous value. Such interpretations including multiple primary components were already reported in a black hole binary Cyg X-1 (e.g., Makishima et al. 2008; Yamada et al. 2013), and applied to several types of AGNs to explain the soft excess in Chaper 5. These correspond to a novel picture that the AGN central engine presumable includes several coronae with different electron temperatures and optical depths generating distinct hard primary continua. This issue is discussed again in §7.5.

6.2 The Type I Seyfert NGC 3227

In NGC 3516 (§6.1), the strongly-absorbed PL emission (§6.1.7) changed in its intensity from 2005 to 2009, independently of that of the main variable PL. However, we have not caught a moment in which the strongly-absorbed PL component just varied. To catch that moment, we should investigate another AGN which was observed by *Suzaku* more frequently. Therefore, we next focus on the typical and bright Seyfert galaxy NGC 3227, which was observed 6 times with *Suzaku* for a gross exposure of ~ 50 ksec each (§4.1). Intervals between adjacent observations were commonly two weeks. This AGN has a redshift of $z = 0.0039$ and a column density of the Galactic absorption $N_{\rm H} \sim 2 \times 10^{20}$ cm^{-2}. Its black hole mass and typical 0.5–2 keV luminosity are $\sim 4 \times 10^7$ $M_\odot$ (e.g., Peterson et al. 2004) and $\sim 5 \times 10^{41}$ erg s^{-1} (George et al. 1998), which implies an Eddington ratio of ~ 0.001.

6.2.1 Spectra obtained from six individual observations

Figure 6.9 shows six time-averaged 2–45 keV spectra of NGC 3227, visualizing how the spectral shape changed among the six observations. The spectra commonly exhibit a prominent Fe-Kα line at ~ 6.35 keV (6.4 keV at the rest frame), of which the intensity is apparently similar among the six data sets. A clear Ni-Kα emission line at $\sim$7.15 keV and a deep Fe-K absorption edge at $\sim$7.1 keV can be seen in the 4th spectrum, while they are less prominent in the others.

The six spectra have rather different continuum shapes as well. The spectrum in the 1st observation, when the source was brightest, has a much softer shape than the other data sets, while that in the 4th observation is the faintest and hardest. Thus, the intensity differences among the 6 observations are much larger in softer X-rays than in the range above ~ 10 keV. In the 2–10 keV band, the spectral shape is concave in the 4th observation, while rather convex in the others. Because NGC 3227

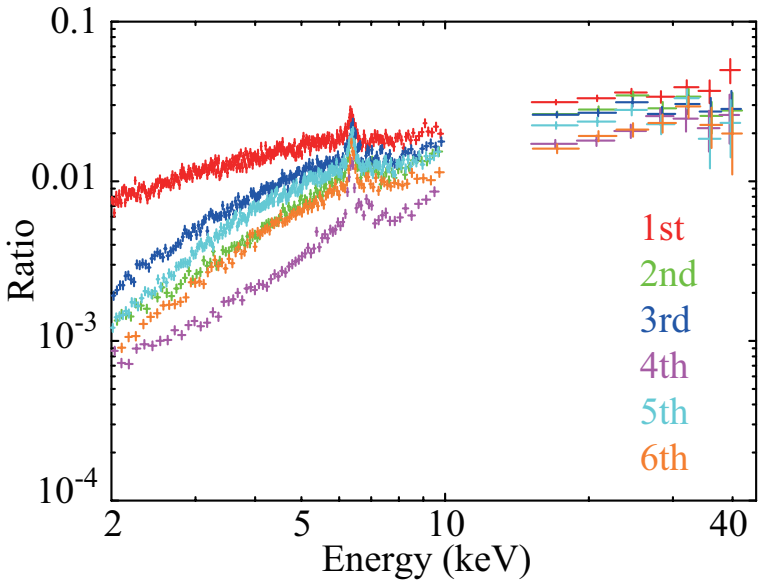

Figure 6.9: Background-subtracted *Suzaku* spectra of NGC 3227 obtained in the 1st (red), 2nd (green), 3rd (blue), 4th (purple), 5th (cyan), and 6th observations (orange). They are normalized to a common $\Gamma = 2.0$ PL.

thus exhibited even larger spectral shape changes than the previous source, NGC 3516, this AGN is considered to deserve detailed studies.

6.2.2 Light curves

To study time variations of NGC 3227, we show, in Fig. 6.10 (a), an overall 2–3 and 3–10 keV light curves combining all the six data sets. Panels (b), (c), and (d) of the same figure give those of the 1st, 2nd, and 4th observations, respectively, in three energy bands. At least on the 1st occasion (Fig. 6.10 b), the variation amplitudes were larger in the XIS signals than those of HXD-PIN.

As shown in Fig. 6.10 (a), the source was more variable in the 1st and the 3rd observations than in the others. Particularly in the first observation, the count rate varied by an order of magnitude within only ~ 100 ksec, and the shortest timescale of the variation was ~ 20 ksec ($\lesssim 10\ R_{\rm g}/c$). In contrast, the 2nd, 4th, and 5th observations individually recorded variations by no more than 20%. (The variations seen in the HXD-PIN light curves in Fig. 6.10 could be due to residual NXB variability.) Thus, the source exhibited interesting short- and long-term variations, together with complex spectral changes (Fig. 6.9).

A comparison between the spectra (Fig. 6.9) and the light curves (Fig. 6.10) suggests that the source is more soft-X-ray variable as the HXD vs. XIS hardness ratio decreases. To examine this property, we made a scatter plot between the hardness ratio obtained by dividing the 15–45 keV time-averaged count rate by the 2–3 keV one, against the RMS variability calculated using the entire light curve with 10 ksec binning in each observation. The results, shown in Fig. 6.11, clearly confirm the suggested negative correlation. This phenomenon cannot be easily explained by changes of a single

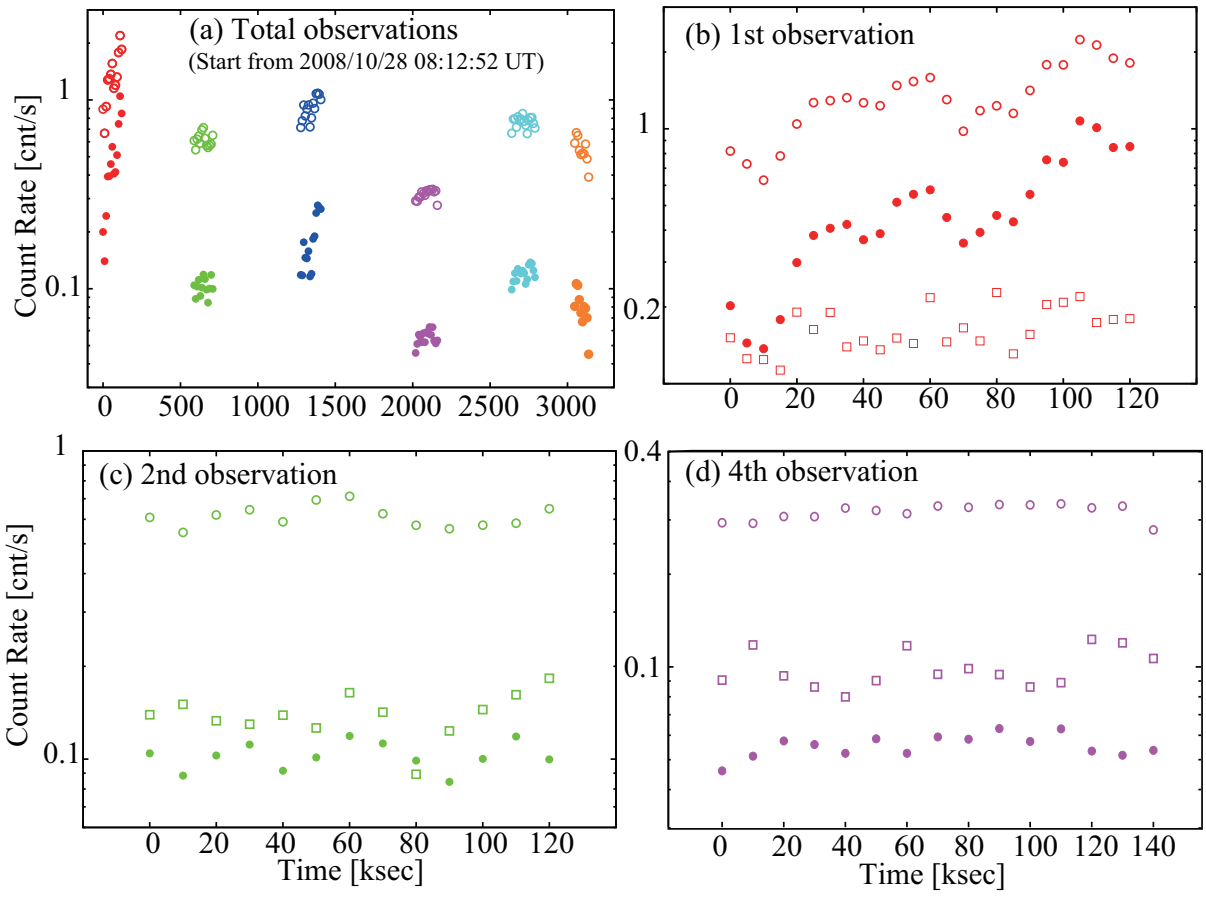

Figure 6.10: (a) Background-subtracted and dead-time corrected 2–3 keV (filled) and 3–10 keV (open) light curves of the six *Suzaku* data sets of NGC 3227 with 10 ks binning. The observations are specified by colors in the same way as in Fig. 6.9. Panels (b), (c), and (d) show expanded light curves in the 1st, 2nd and the 4th observations, respectively, in the 2–3 keV (filled circle), 3–10 keV (open circle), and the 15–45 keV (open square) bands with 10 ks binning. Errors in the XIS data points are all less than ~ 0.02 cnt s^{-1}, and omitted. The HXD-PIN data points have typically $\sim 1.4\%$ systematic errors (Fukazawa et al. 2009).

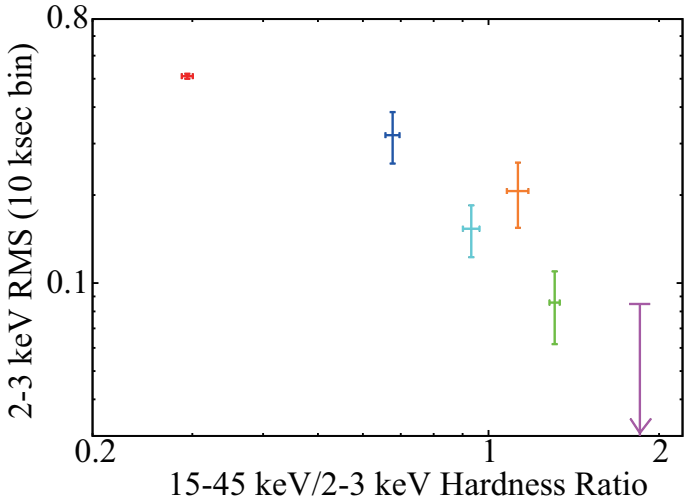

Figure 6.11: A scatter plot between the hardness (15–45 vs. 2–3 keV) and the 2–3 keV RMS variation of NGC 3227. Colors of the data plots are the same as in Fig. 6.9 and Fig. 6.10, indicating the six observations.

variable spectrum (unless assuming an artificial fine tuning), and suggests the presence of a highly variable soft emission and a less variable hard component.

6.2.3 Count-count plot

To investigate characteristics of the variability, we produced, in Fig. 6.12, a 2–3 keV vs 3-10 keV CCP incorporating all the six observations. Surprisingly, data points in the CCP distribute along a single broken line with a clear break point at a 2–3 keV count rate of $x \sim 0.16$ cnt s^{-1}. Hereafter, the distributions above and below the break are called Bright and Faint branches, respectively. The data points from the 1st (red) and the 3rd (blue) observations, when the source was bright and variable, mostly follow the Bright branch, while those from the other data sets (cyan, green, orange, and purple) define the Faint branch. We fitted the data in the two branches separately with eq. (5.1), in the same way as in §6.1.3. As a result, the Bright-branch data were expressed reasonably well with a slope $A = 1.48 \pm 0.08$ and an offset $B = 0.62 \pm 0.03$, with χ^2/d.o.f. =30.0/17. In contrast, the fit to the Faint branch was unsuccessful with χ^2/d.o.f. =99.5/44 because of a larger data scatter. Particularly, the 5th data set (cyan), which is somewhat in between the two branches, showed large deviations. Excluding the 5th data (cyan), and further increasing the systematic error to 7%, the fit in the Faint branch became successful with χ^2/d.o.f. =53.2/44, giving $A = 4.55 \pm 0.36$ and $B = 0.18 \pm 0.04$. Clearly, the two branches have significantly different parameters.

As seen in the light curves, the Bright-branch data exhibit fast variations on a timescale of < 1 day (Fig. 6.10b), while those in the Faint branch are dominated by slower ($\sim$ 2 weeks) variations as represented by the behavior of the 2nd, 4th, 5th, and 6th data sets in Fig. 6.10(a). The break at $x \sim 0.16$ cnt s^{-1} is a point where the short-term variability disappears, and the long-term one starts dominating. In other words, this CCP data distribution provides evidence for the presence of

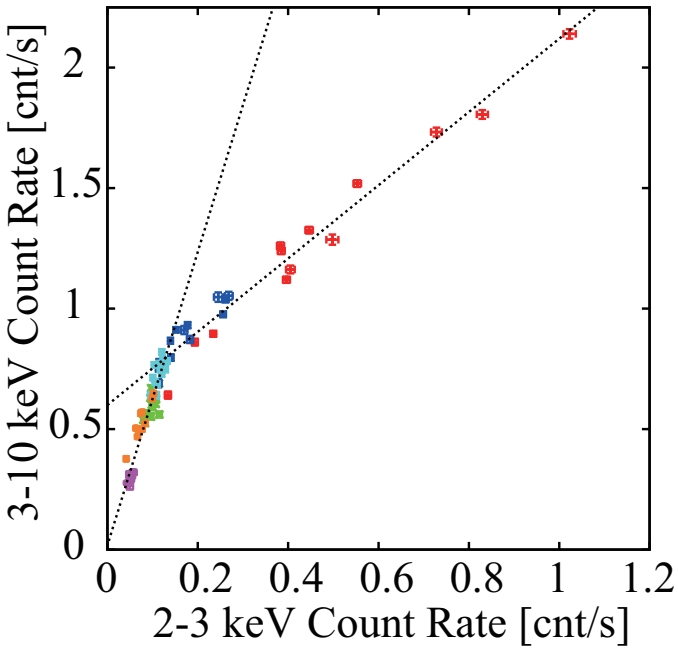

Figure 6.12: A 2–3 keV vs 3–10 keV CCP of NGC 3227, in which the six observations are indicated with the same colors as in Fig. 6.10. All data are binned into 10 ksec. The error bars represent statistical $\pm 1\sigma$ range.

independent short- and long-term variations, each caused presumably by intensity (but not shape) changes of a certain spectral component.

6.2.4 The C3PO application to the short-term variation

To quantify the spectral variability, we apply the C3PO method to the entire assembly of the six data sets of NGC 3227. Selecting again the 2–3 keV as the reference, the 3–10 keV XIS and 15–45 keV HXD-PIN ranges were divided into the 13 and 3 finer bands, respectively, with the same boundaries as those in §6.1.3. Then, as shown in Fig. 6.13, all the 16 finer-band CCPs were found to exhibit the same break point at $x \sim 0.16$ cnt s^{-1} as Fig. 6.12. Hence, we divided the data into the Bright and Faint branches in the same way, and separately fitted the two branches with eq. (5.1) in each CCP. The systematic error of 3% was incorporated into fits to the Bright branch, while 7% to the Faint one. The fit results summarized in Table 6.5 show that the short-term variation has significantly positive values of A and B in all the CCPs, while the long-term variation has $B < 0$ in lower energies. In higher energies, the offsets of both branches become more significantly positive relative to the average intensity in that energy band. Thus, the stationary spectrum from either branch is expected to be hard.

Like in §6.1.3, we decomposed the Bright-branch data (the 1st and 3rd data sets) into variable and stationary components by the C3PO method. For simplicity, we again assumed $C = 0$, and employed the multiplicative factor of $x \sim 0.55$ cnt s^{-1} (the average rate in 2–3 keV in the two observations) to calculate the variable component. (Although we could alternatively choose $C = 0.16$, the break point,

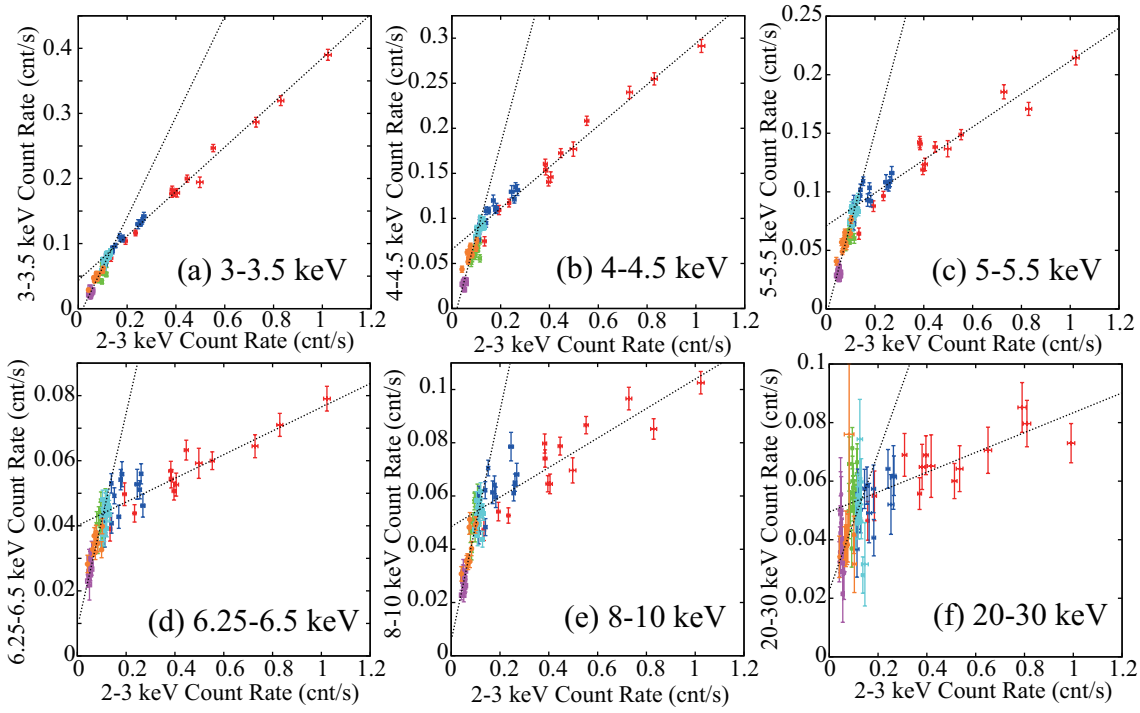

Figure 6.13: The finer-band CCPs of NGC 3227, in which all the 6 data sets are merged together, and the 2–3 keV band is used as reference. All data are binned into 10 ksec, and the error bars represent statistical $\pm 1\sigma$ range. The two dotted straight line represent the fits with eq. (5.1) to the two separate branches.

Table 6.5: Parameters obtained by fitting to the short- and long-term variations in the 16 CCPs.

	Short-term (Bright)			Long-term (Faint)		
Range (keV)	Slopes	Offsets$\times 10^2$	χ^2/d.o.f.	Slopes	Offsets$\times 10^2$	χ^2/d.o.f.
3–3.5	0.34 ± 0.01	4.60 ± 0.32	17.8/17	0.63 ± 0.05	-0.54 ± 0.33	51.3/36
3.5–4	0.27 ± 0.01	6.24 ± 0.26	13.0/17	0.66 ± 0.05	-0.29 ± 0.36	50.2/36
4–4.5	0.22 ± 0.01	6.92 ± 0.41	31.7/17	0.73 ± 0.07	-0.54 ± 0.44	68.6/36
4.5–5	0.17 ± 0.01	7.30 ± 0.33	26.1/17	0.78 ± 0.06	-0.76 ± 0.40	51.1/36
5–5.5	0.14 ± 0.01	7.05 ± 0.41	31.1/17	0.69 ± 0.06	-0.19 ± 0.39	54.5/36
5.5–6	0.10 ± 0.01	6.58 ± 0.40	35.4/17	0.63 ± 0.05	0.15 ± 0.33	42.6/36
6–6.25	0.04 ± 0.01	3.43 ± 0.18	20.4/17	0.29 ± 0.03	0.27 ± 0.18	42.7/36
6.25–6.5	0.03 ± 0.01	4.20 ± 0.21	23.1/17	0.27 ± 0.02	1.35 ± 0.17	26.2/36
6.5–6.75	0.03 ± 0.01	2.61 ± 0.17	25.8/17	0.22 ± 0.02	0.39 ± 0.15	40.5/36
6.75–7	0.02 ± 0.01	2.13 ± 0.20	45.0/17	0.18 ± 0.02	0.47 ± 0.13	33.5/36
7–7.5	0.04 ± 0.01	3.58 ± 0.20	23.5/17	0.32 ± 0.03	0.30 ± 0.19	40.4/36
7.5–8	0.04 ± 0.01	2.17 ± 0.21	40.0/17	0.23 ± 0.02	0.18 ± 0.15	42.9/36
8–10	0.05 ± 0.01	4.99 ± 0.32	43.7/17	0.47 ± 0.03	0.43 ± 0.23	32.0/36
15–20	0.04 ± 0.01	6.79 ± 0.42	12.9/17	0.27 ± 0.09	3.56 ± 0.67	57.4/36
20–30	0.04 ± 0.01	4.80 ± 0.35	12.4/17	0.23 ± 0.08	2.72 ± 0.57	43.8/36
30–45	0.00 ± 0.01	1.60 ± 0.27	26.6/17	0.09 ± 0.06	0.58 ± 0.42	67.1/36

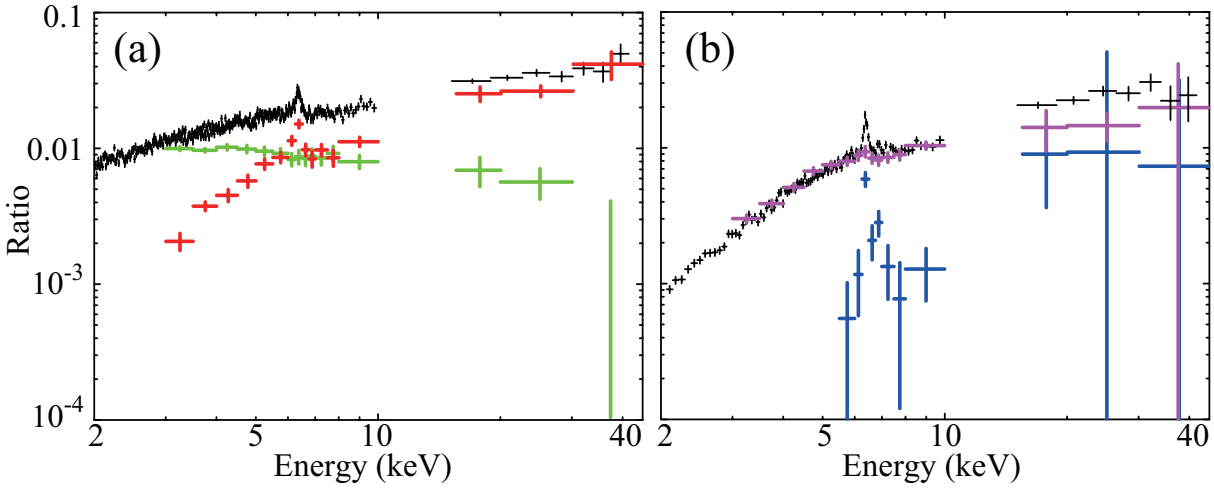

Figure 6.14: The C3PO results on NGC3227 in the Bright (or short-term; panel a) and the Faint (or long-term; panel b) branch, produced by the 1st+3rd and 2nd+4th+6th data sets, respectively. Green and red in (a) show the Bright-branch variable and stationary spectrum, respectively, while purple and blue in (b) the Faint-branch variable and stationary ones, respectively. All are in the case of $C = 0$. Black is the averaged spectrum over the 1st and 3rd data sets (panel a), while that over the 2nd, 4th, and the 6th observations (panel b).

subsequent results do not differ significantly from the case with $C = 0$.) As shown in Fig. 6.14 (a), the variable component derived in this way is again featureless with a rather steep slope, while the stationary component has a hard shape and exhibits a prominent Fe-Kα emission line at ~ 6.4 keV. These characteristics of the short-term C3PO components are apparently similar to those of NGC 3516 extracted in §6.1.3.

6.2.5 The long-term variation

What kinds of components are responsible for the long-term variation that distinguishes the CCPs of this AGN from those of NGC 3516? To examine this, we next applied the C3PO method to the Faint branch. The variable component was constructed using a 2–3 keV count rate of $x_0 \sim 0.1$ cnt s^{-1}, which is the average over the 2nd, 4th and 6th data sets. Figure 6.14 (b) shows the long-term variable and stationary components derived in this way. The variable component (varying on long time scales) is very similar in shape to the stationary component in the Bright branch, except the lack of the Fe-K line. Instead, the Fe-K line appears in the Faint-branch stationary component. The hard X-ray signals that were in the Bright-branch stationary spectrum were approximately halved into the Faint-branch C3PO components. Hereafter, the derived four components, the Bright-branch variable and stationary, the Faint-branch variable and stationary are called BV, BS, and FV, FS, respectively.

In Fig. 6.14 (b), FS declines too steeply below ~ 6 keV, lacking signals in the 3–5.5 keV range. This is obviously because of the negative values of offset B (Table 6.5), which make FV and FS over- and under-estimated, respectively. Thus, the case with $C = 0$ is physically unrealistic, and we must

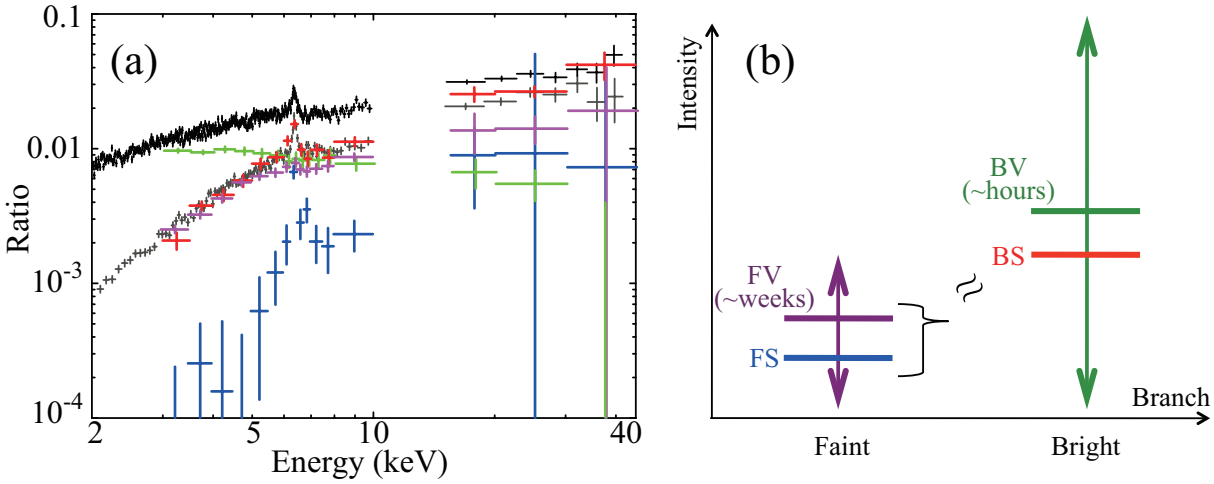

Figure 6.15: (a) The same as a superposition of Fig. 6.14 (a) and (b), but the Faint-branch components (purple and blue) were re-calculated using $C = 0.01$ cnt s^{-1}. Grey shows the spectrum averaged over the faint-branch observations. (b)A schematic diagram of the relation and variations of the four C3PO components found in NGC 3227.

consider a positive intensity floor C in eq. (5.1), but too large a value of C is meaningless (§6.1.3). We therefore chose an intensity floor of $C = 0.01$ cnt s^{-1} which is the minimum that makes all the offset values in the 3–45 keV band positive. The corrected FV and FS components for the long-term variation are shown in Fig. 6.15. Thus, FV and FS decreased and increased, respectively. As a result, FS (blue) has become very similar in shape to a cold reflection component, including the Fe-Kα emission line at ~ 6.4 keV and the hard X-ray hump. Below, we utilize these corrected FV and FS derived with $C = 0.01$ cnt s^{-1} as the Faint-branch components.

In Fig. 6.15, the Bright-branch spectra (the same as Fig. 6.14 a; BV in green, BS in red, the total in black) are superposed for comparison. We can reconfirm the resemblance of BS (red) and FV (purple) except the Fe line, and the clear spectral shape difference between the variable emissions in the Bright and Faint branch. There, the time-averaged spectrum in the Faint branch (black in Fig. 6.14b) is also reproduced in grey. Surprisingly, BS is nearly identical, both in shape and normalization, to the Faint-branch time-averaged spectrum, including the Fe-K emission line and the Compton hump. From these, we arrive at the following view of the spectral intensity variations of NGC 3227; BV varies on short time scales (within ~ 1 day) in the Bright branch, without spectral shape changes. When BV disappears, BS which is equal to FV+FS becomes dominant, and the state changes into the Faint branch. During the Faint-branch state, FV varies on long time scales (~ 2 weeks), while FS remains stable for $\gtrsim 2$ months. Intensity variations and relations of the four spectral components in the two branches are schematically summarized in Fig. 6.15 (b).

The striking agreement of the red (BS) spectrum in Fig. 6.15 (a) with the grey one is considered physically meaningful, rather than a mere chance coincidence. This gives an a posteriori justification to our Bright-branch C3PO analysis, wherein $C = 0$ was assumed.

6.2.6 Overall spectral fitting

Table 6.6: Parameters obtained in the fits to the six NGC 3227 datasets.

		1st	2nd	3rd	4th	5th	6th
Absorption to all							
`Phabs`	$N_{\rm H}^{*\dagger}$	$1.6^{+0.3}_{-0.2}$	1.6 ± 0.5	3.2 ± 0.4	2.9	< 2.2	$2.4^{+0.6}_{-0.8}$
`Ioabs`	$N_{\rm H}^{\dagger}$	$23.2^{+27.9}_{-12.1}$	–	$3.0^{+23.9}_{-2.5}$	–	–	–
	logξ	$4.3^{+0.3}_{-0.2}$	–	$3.9^{+0.8}_{-0.6}$	–	–	–
	Cvr frac.	1 (fix)	–	1 (fix)	–	–	–
	z			0.0039 (fix)			
Broad-Band Primary component*							
`PL`	Γ_0	2.34 ± 0.09	–	$2.49^{+0.12}_{-0.11}$	–	–	–
	$E_{\rm cut}$ (keV)			200 (fix)			
	$N_{\rm PL}^{\ddagger}$	$1.84^{+0.26}_{-0.24}$	–	$1.05^{+0.23}_{-0.18}$	–	–	–
Reflection component							
`ReflFe`	$\Gamma_{\rm ref}$	$= \Gamma_{\rm PL}$	2 (fix)	$= \Gamma_{\rm PL}$	2 (fix)	2 (fix)	2 (fix)
	$E_{\rm cut}$ (keV)			200 (fix)			
	$f_{\rm ref}$	0.9 ± 0.2	1 (fix)	1.1 ± 0.1	1 (fix)	1 (fix)	1 (fix)
	z			0.0039 (fix)			
	A ($Z_\odot$)			1 (fix)			
	$A_{\rm Fe}$ ($Z_{\rm Fe,\odot}$)			1 (fix)			
	i (degree)			60 (fix)			
	$N_{\rm ref}^{\S}$	$= N_{\rm PL}$	1.50 ± 0.13	$= N_{\rm PL}$	1.35	1.38 ± 0.11	1.22 ± 0.12
Hard primary component*							
`PhabsC'`	$N_{\rm H}^{\dagger}$	$9.7^{+2.9}_{-1.8}$	$21.1^{+4.2}_{-3.6}$	$11.4^{+1.1}_{-1.0}$	27.8	$9.8^{+1.3}_{-0.8}$	$15.3^{+2.9}_{-2.4}$
	Cvr frac.	> 0.64	$0.63^{+0.08}_{-0.03}$	> 0.57	0.64	0.80 ± 0.03	$0.69^{+0.02}_{-0.04}$
`PL'`	Γ_1	$1.48^{+0.04}_{-0.05}$	$1.41^{+0.07}_{-0.06}$	$1.66^{+0.05}_{-0.04}$	1.25	1.67 ± 0.06	1.66 ± 0.08
	$E_{\rm cut}$ (keV)			200 (fix)			
	$N_{\rm PL}^{\#}$	0.42 ± 0.06	$0.26^{+0.06}_{-0.04}$	$0.63^{\pm}0.06$	0.14	0.56 ± 0.07	$0.38^{+0.06}_{-0.05}$
χ^2/d.o.f.		419.45/355	180.70/155	252.35/221	184.35/108	243.21/249	142.04/136

* Later to be identified in §7.1.2.

† Equivalent hydrogen column density in 10^{22} cm^{-2}.

‡ The `PL` normalization at 1 keV, in units of 10^{-2} photons keV^{-1} cm^{-2} s^{-1} at 1 keV.

§ The `ReflFe` normalization at 1 keV, in units of 10^{-2} photons keV^{-1} cm^{-2} s^{-1} at 1 keV.

\# The `PL'` normalization at 1 keV, in units of 10^{-2} photons keV^{-1} cm^{-2} s^{-1} at 1 keV.

In order to confirm the spectral decomposition and the time variability characterization made in §6.2.5, we move on to simultaneous fits to the triplet spectra like in §6.1.7. Because the 1st and 3rd observations are considered to include BV and BS (which is roughly the same as FV+FS), while the others only FV and FS, these two cases are handled in different ways.

First, we examine the 1st and the 3rd (Bright branch) data sets. Following the analysis of NGC 3516 (§6.1), we again employ the interpretation that invokes the additional primary component (modeled as an absorbed hard PL). Hence, we prepared `model_bv` = `Phabs*Ioabs*PL` and `model_bs` = `Phabs*Ioabs*(ReflFe + PhabsC'*PL')`, and fitted the triplet spectra in the Bright branch data sets with them under the same parameter conditions as in §6.1.7. Here, `PhabsC'` appears for the first time; it is basically the same as `Phabs'`, but includes an additional free parameter describing the fraction

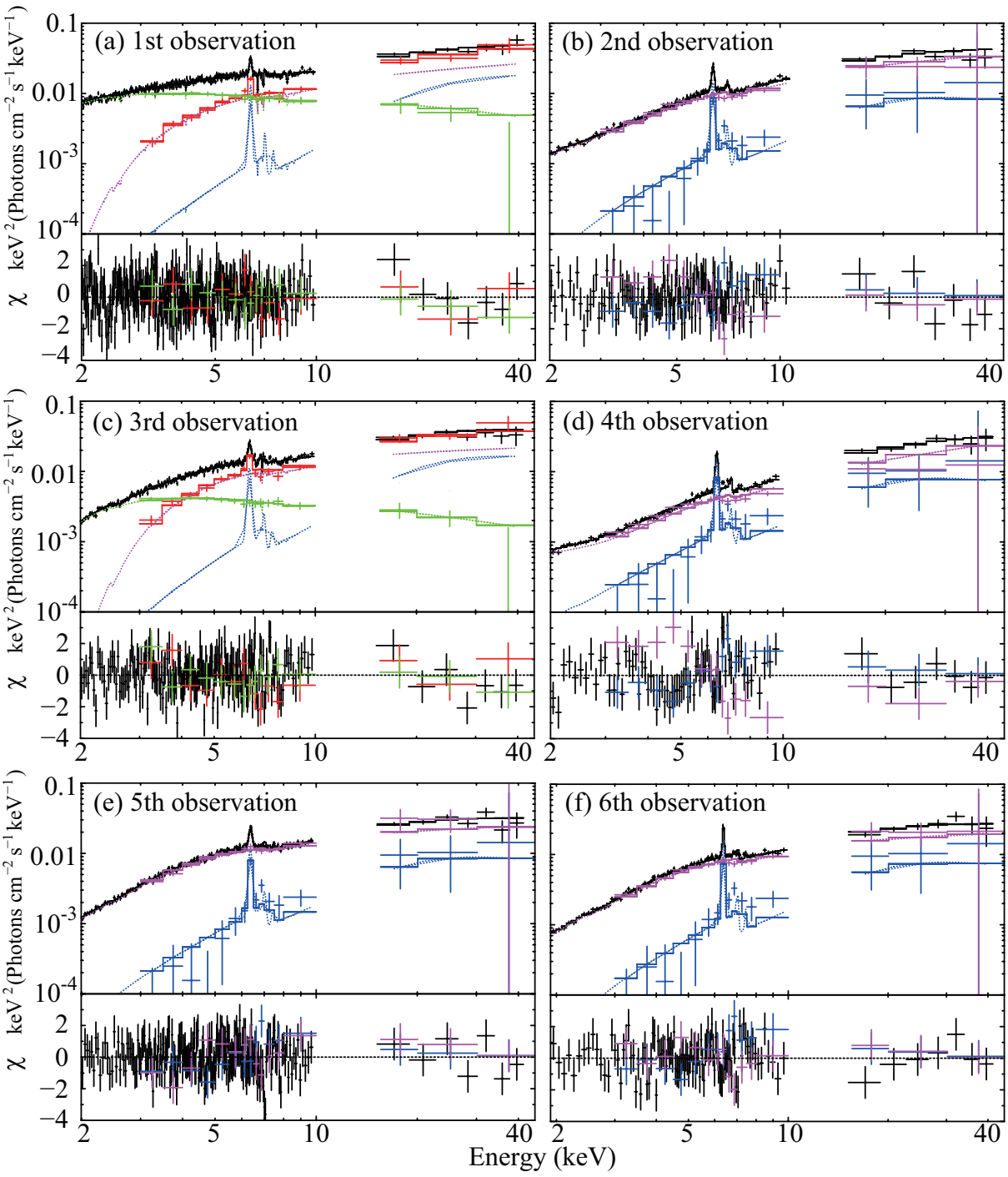

Figure 6.16: Simultaneous fits to the time-averaged (black), BV (green), BS (red), FV (purple), and FS (blue) spectra. The 1st (panel a) and 3rd (panel c) spectra are fitted with `model_bv` and `model_bs`, while the 2nd (panel b), 4th (panel d), 5th (panel e), and the 6th (panel f) spectra with `model_fv` and `model_fs`. The `PL` model in green and the `Phabs' * PL'` model in purple are identified to be the Broad-Band and Hard Primary component, respectively, in §7.1.2.

covered by the absorber with $N'_{\rm H}$. (The introduction of the particle covering model is to explain the spectra in the Bright branch by the same model as that for the Faint branch, which is explained in the next paragraph.) As shown in Fig. 6.16 (a,c), the fits were successful both in the 1st and 3rd data sets, giving parameters in Table 6.6. The photon index of BV became $\Gamma_0 \sim 2.3$, while that of the additional PL, which is part of BS and later becomes equivalent to FV, turned out to be significantly harder with $\Gamma_1 \sim 1.5$. These slopes of the individual primary continua are similar to those of NGC 3516. In addition, the absorption working on the additional PL became significantly higher ($\sim 10^{23}$ cm^{-2}) than that on BV, like in NGC 3516. The covering fraction of `PhabsC'` was consistent, within errors, with 1 in both observations. Thus, the additional PL in NGC 3227 is presumably the same component as that in NGC 3516. The change in the time-averaged spectrum from the 1st to the 3rd data sets can be explained only by an intensity decrease of BV.

Next, we simultaneously fitted the triplet spectra, individually in the 2nd, 4th, 5th, and 6th data sets (Faint branch). The utilized models are `model_fv` = `Phabs*PhabsC'*PL'` and `model_fs` = `Phabs*ReflFe`, of which sum is equal to `model_bs` utilized in the fits to the Bright-branch data sets. Obviously, this model composition is motivated by the close resemblance between the red and grey spectra in Fig. 6.15 (a). The employed parameter conditions were the same as those of `mode_bs`, except that the photon index, the reflection fraction and the normalization in `ReflFe` were fixed at 2, 1, and left free, respectively. As shown in Fig. 6.16 and Table 6.6, the fits were successful, except for the 4th data set. The slowly variable components, namely FV, were successfully reproduced by a partially-absorbed PL with the column density of $\sim 10^{23}$ cm^{-2}, the covering fraction of ~ 0.8, and the photon index of ~ 1.5. The stable component, namely FS, was explained by a neutral and distant reflection model. This justified our choice of $C = 0.01$ cnt s^{-1} in the Faint-branch C3PO analysis (§6.2.5). The difference among the 2nd, 5th, and 6th time-averaged spectra can be attributed to intensity changes of FV alone.

6.2.7 Possibility of other interpretations

Because NGC 3227 has periods when the rapidly variable PL (i.e., BV) disappears, we can utilize such Faint-branch data to test other models for FV, under higher statistics than in NGC 3516. In the present subsection, let us utilize the 2nd data set for this purpose. The FV component, which was successfully modeled by a (partially) absorbed PL model, may allow at least two alternative interpretations; a relativistically-blurred refection (BRB), and a thermal Comptonization with high-temperature seed photons. The former may be considered again, even though it failed to explain the triplet spectra of NGC 3516 (§6.1.7); so we first tried this interpretation. Replacing the `PhabsC'*PL'` by `RBR`, the triplet fitting was repeated with `model_fv1 = Phabs*RBR`, where the photon index of the incident PL and the iron abundance were fixed at 2.3 and 1 Solar, respectively, while the other parameters were fixed at the same values as in §6.2.6. As shown in Fig. 6.17 (a) and Table 6.7, the triplet fit became unsuccessful, with χ^2/d.o.f.=299.2/156 (cf. 180.7/155 previously), mainly due to large positive residuals in the 7–10 keV band. After all, the RBR interpretation fails to explain the

Table 6.7: Same as Table 6.6, but with `model_fv1 = Phabs*(ReflFe + RBR)` and `model_fv2 = Phabs*(ReflFe + Compton + Compton)`.

		2nd
Absorption to all		
`Phabs`	$N_{\rm H}^{*}$	3.1
Neutral and relativistic reflection		
`ReflFe`	$\Gamma_{\rm ref}$	2 (fix)
	$E_{\rm cut}$ (keV)	200 (fix)
	$f_{\rm ref}$	1 (fix)
	z	0.0039 (fix)
	A ($Z_{\odot}$)	1 (fix)
	$A_{\rm Fe}$ ($Z_{\rm Fe,\odot}$)	1 (fix)
	i (degree)	60 (fix)
	$N_{\rm ref}^{\dagger}$	1.6
`RBR`	q	5.4
	$R_{\rm in}$ ($R_{\rm g}$)	1.4
	$R_{\rm out}$ ($R_{\rm g}$)	400
	i (degree)	60 (fix)
	$A_{\rm Fe}$ ($Z_{\odot}$)	1 (fix)
	Γ (keV)	2.3 (fix)
	ξ (erg cm s^{-1})	25.5
	$N_{\rm RBR}^{\ddagger}$	6.8
χ^2/d.o.f.		299.2/156
Absorption to all		
`Phabs`	$N_{\rm H}^{*}$	0.17
Reflection		
`ReflFe`	$\Gamma_{\rm ref}$	2 (fix)
	$E_{\rm cut}$ (keV)	200 (fix)
	$f_{\rm ref}$	1 (fix)
	z	0.0039 (fix)
	A ($Z_{\odot}$)	1 (fix)
	$A_{\rm Fe}$ ($Z_{\rm Fe,\odot}$)	1 (fix)
	i (degree)	60 (fix)
	$N_{\rm ref}^{\dagger}$	1.6
Double Compton		
`Compton`	z	0.0039 (fix)
	T_0 (keV)	0.02 (fix)
	$T_{\rm e}$ (keV)	200 (fix)
	τ	1.4
	$N_{\rm Comp}^{\S}$	0.26
`Compton`	z	0.0039 (fix)
	T_0 (keV)	1.6
	$T_{\rm e}$ (keV)	84
	τ	3.4
	$N_{\rm Comp}^{\S}$	6.2
χ^2/d.o.f.		246.7/153

* Equivalent hydrogen column density in 10^{22} cm^{-2}.

† The `ReflFe` normalization at 1 keV, in units of 10^{-2} photons keV^{-1} cm^{-2} s^{-1} at 1 keV.

‡ The `RBR` normalization in units of 10^{-6}.

§ The thermal Comptonization component normalization, in units of 10^{-5} photons keV^{-1} cm^{-2} s^{-1} at 1 keV.

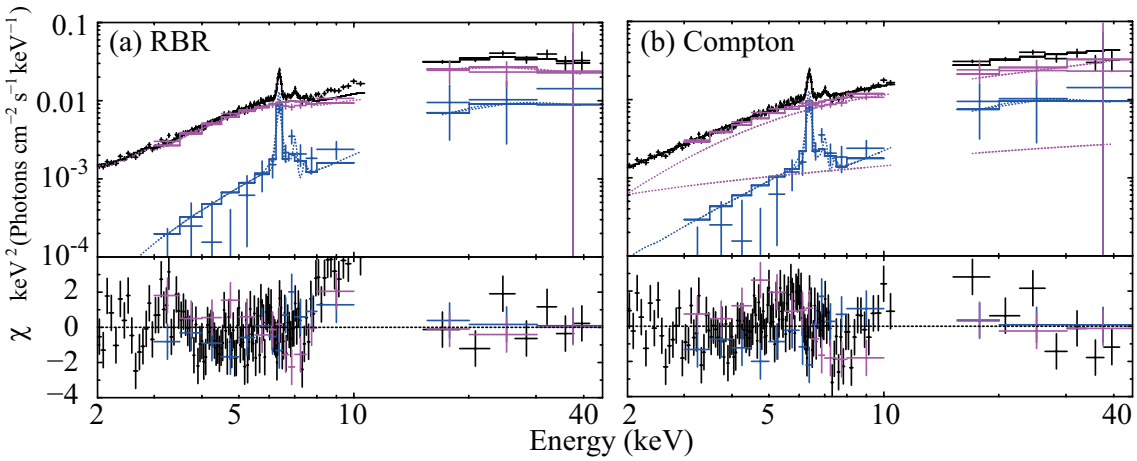

Figure 6.17: Same as Fig. 6.16 (b), but fitted with `model_fv1 = Phabs*(ReflFe + RBR)` and with `model_fv2 = Phabs*(ReflFe + Compton + Compton)`.

stationary additional spectral component, like the NGC 3516 case.

Next, we examined the interpretation invoking a thermal Comptonization component with a high seed photon temperature of several keV. We replaced the `PhabsC'` model by `Compton + Compton`, and fitted the triplet spectra with `model_fv2 = Phabs*(Compton + Compton)`. The use of two Comptonization components is to mimic the partially absorbed PL comprising `model_fv`, because a Comptonized emission would drop steeply toward lower energies if the seed photon has a rather high temperature. The electron and seed photon temperatures of one `Compton` were fixed at 200 keV and 0.02 keV, respectively, while those for the other Compton were left free. Optical depths were left free in both `Compton` models. As shown in Fig.6.17 (b) and Table 6.7, the fit was unsuccessful with χ^2/d.o.f.=246.7/153, mainly because of negative residuals around $\sim$ 7.1 keV. This structure is considered to correspond to a neutral Fe-K absorption edge produced by a neutral absorber, and the failure of this double Compton model is caused by its lack of the Fe-K edge seen in the actual data. In other words, the FV component is best reproduced by a strongly (and partially) absorbed PL, and its low energy cutoff is actually due to photoelectric absorption by nearly neutral matter.

6.3 Target Selection for Further Analysis

In NGC 3516 (§6.1) and NGC 3227 (§6.2), we discovered the new hard X-ray component, characterized by a hard slope, a high absorption, and relatively slow variations. In order to examine whether this component is a general phenomenon, we need to apply, like in §5.2, the C3PO method to hard X-ray bands of other *Suzaku* AGN data sets. As already learned from NGC 3516 and NGC 3227, a successful C3PO analysis requires a long exposure and large variations. In addition, we would like to examine whether or not the relevant hard X-ray component varied, e.g., on long time scales. Thus, suitable AGN targets may be selected from the *Suzaku* archive, based on the following criteria:

- The object must have been observed with *Suzaku* more than twice.

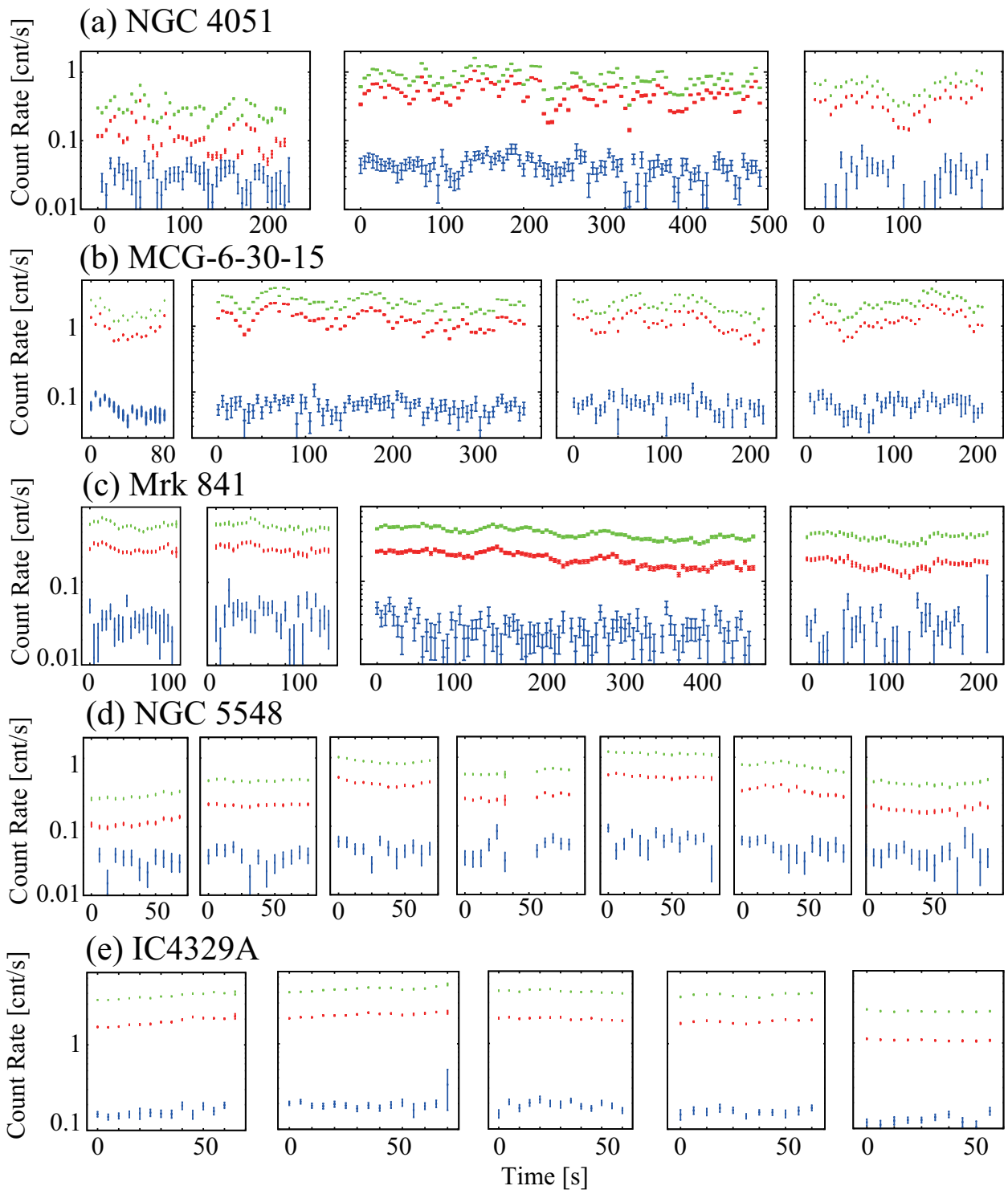

Figure 6.18: Light curves of all observations of the selected five AGNs, presented in the same way as Fig. 6.1. The name of AGNs are shown above each panel.

Table 6.8: Summary of information on the 5 AGNs to be studied in §6.4.

Object name	No. of Obs.	Type	Redshift	$M_{\rm BH}{}^{*}$	$N_{\rm H}({\rm Gal})^{\dagger}$	Previous *Suzaku* study
NGC 4051	3	Sy1	0.0033	0.2	1.3	Terashima et al. (2009)
MCG–6-30-15	4	Sy1	0.00775	0.3	1.4	Miniutti et al. (2007)
Mrk 841	4	Sy1	0.047	10	2.3	Cerruti et al. (2010)
NGC5548	7	Sy1	0.047	100	1.7	Turner et al. (2009)
IC4329A	5	Sy1	0.016	1	46.1	–

* Black hole mass in an unit of 10^7 $M_\odot$.

† Equivalent hydrogen column density in 10^{23} cm^{-2} for the Galactic or the intrinsic line-of-sight absorption.

- The net total exposure after summing all the observations must be longer than 200 ksec.
- The object must have exhibited peak-to-peak variations by more than a factor of two.

These criteria are objectively defined, like the initial selection criteria in Chpater 5: a main difference is that we here require a larger variation amplitude (10% vs. factor 2), because the HXD-PIN data have much larger measurement errors than those of the XIS. After filtering the entire *Suzaku* archive of type I AGNs ($\sim$ 100 objects, $\sim$130 total observations) with these criteria, 5 AGNs (23 observations) remained; NGC 4051, MCG–6-30-15, Mrk 841, NGC 5548, and IC4329A, which are all type I Seyfert galaxies. The data sets of NGC 5548 and IC4329A were obtained within 2–3 months, while the others were observed with intervals of several weeks–several years. The longest interval is about four years between the 2nd and the 3rd observations of Mrk 841. Table 6.8 is a summary of the information about these 5 AGNs.

In the same way as Fig. 6.1, we made background-subtracted light curves of the selected 5 AGNs, and show the results in Fig. 6.18. These 2–3 keV light curves all satisfied the above criteria, exhibiting peak-to-peak variations by a factor of $\gtrsim 2$. In particular, the 2–3 keV variation amplitude of NGC 4051 is large enough to reach about an order of magnitude. On the other hand, all the 15–45 keV light curves commonly have lower variability than the other bands. This suggests the presence of stable signals in the harder energy band, which may be effectively extracted by the C3PO method.

Table 6.9: Parameters obtained by fitting the 5 CCPs in Fig. 6.19 with eq. (5.1).*

Object	A	B (counts s^{-1})	χ^2/d.o.f.
NGC 4051	1.36 ± 0.02	0.14 ± 0.01	56.3/33
MCG–6-30-15	1.51 ± 0.04	0.41 ± 0.05	45.4/35
Mrk 841	1.59 ± 0.06	0.07 ± 0.01	23.3/34
NGC 5548	2.03 ± 0.03	0.05 ± 0.01	19.1/20
IC4329A	1.84 ± 0.05	0.36 ± 0.09	10.2/12

* A systematic error of 2% is included in the 3-10 keV bands.

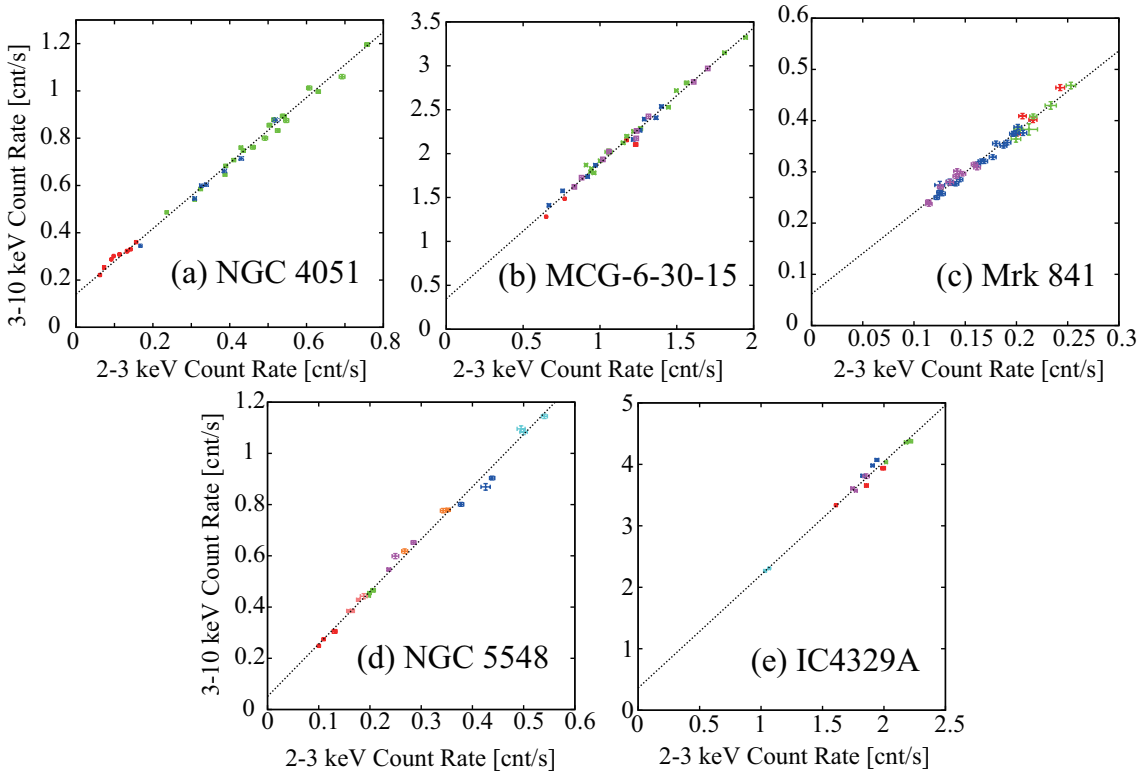

Figure 6.19: The CCPs of the selected five AGNs, produced between the 2–3 keV and 3–10 keV bands. Different data sets of the same object are distinguished by colors.

6.4 Application of the C3PO analysis to Other AGNs

6.4.1 Extractions of variable and stationary spectra

Following the recipe of the C3PO method, we produced 3–10 keV vs. 2–3 keV CCPs of the five AGNs, as shown in Fig. 6.19. Multiple data sets of the same object were merged into a single CCP. Surprisingly, all the five CCPs reveal a tight linear correlation, in spite of the various intervals up to four years. This makes a contrast to the case of NGC 3516 in which the 2005 and 2009 data followed different branches, and to that of NGC 3227 where the data points drew a broken line. Especially in the NGC 4051 and MCG–6-30-15 CCPs which have the longest total exposure of $\sim$ 400 ksec, almost all the points distribute on a single straight line. Actually, as shown in Table 6.9, fittings of the five CCPs with eq. (5.1) are all successful, giving significantly positive slopes and offsets. Thus, we can apply again the C3PO method to the total datasets of each AGN. This makes our study simpler than in Chapter 5, where we had to discard 7 observations out of the 12 initially-selected ones, to make the C3PO method work.

With the same energy boundaries as in §6.1, we divided the 3–45 keV range into finer energy bands, made 16 CCPs for each AGN (totally 80 CCPs), and fitted all of them with eq. (5.1). (These CCPs and the fitting results are shown in Appendix.) Then, the variable and stationary components shown in Fig. 6.20 were obtained. The C3PO-derived variable spectra are all featureless, and are generally

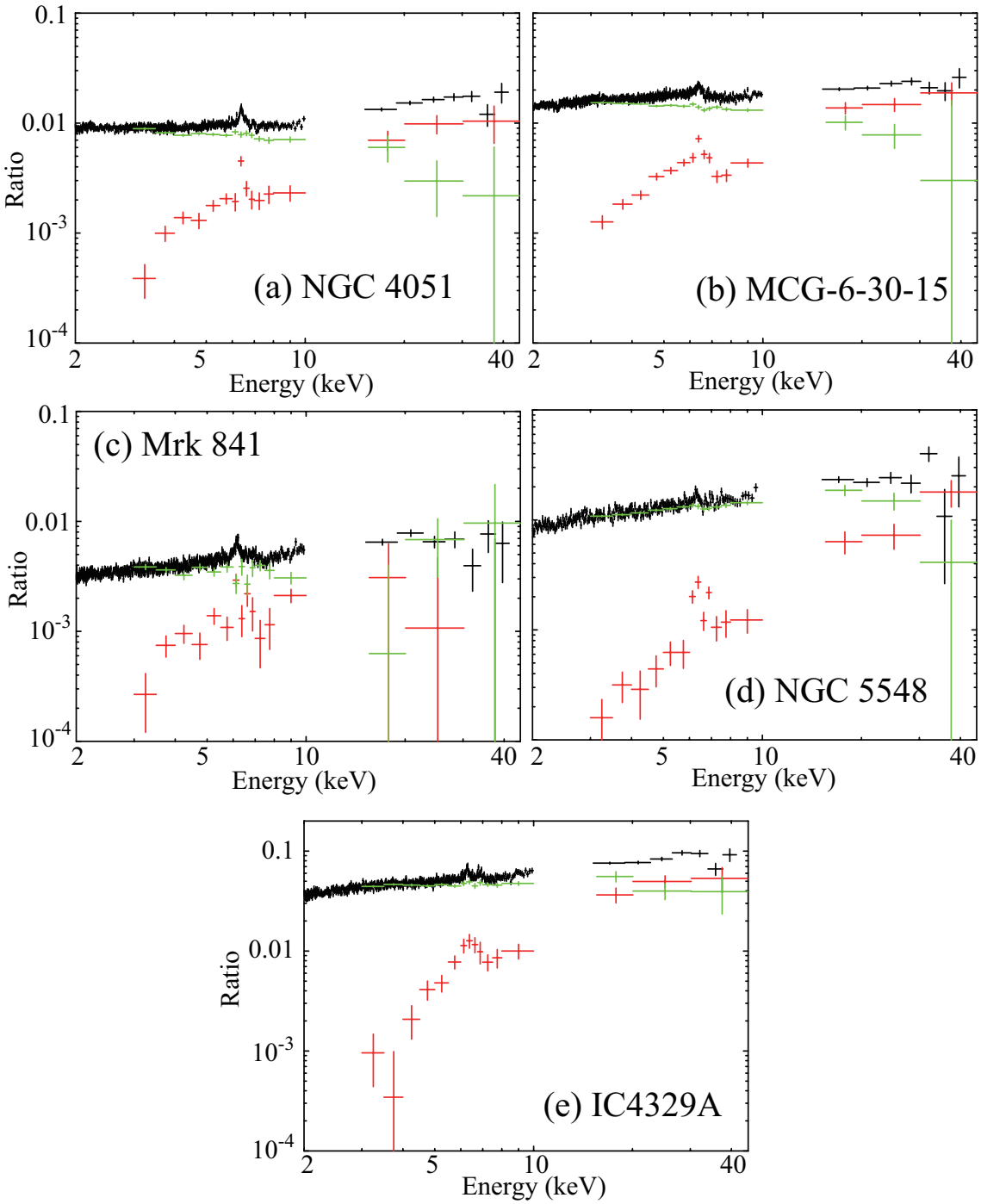

Figure 6.20: The same as Fig. 6.6, but of the selected five AGNs.

softer than the time-averaged spectrum in each AGN. The stationary components commonly exhibits an Fe-Kα emission line, and the Fe-K absorption edge at $\sim$ 7.1 keV can be clearly seen particularly in those of MCG–6-30-15 and IC4329A. Intensity ratios between the extracted Fe-Kα emission line and the stationary continuum (i.e., the line equivalent width) are smaller than that expected in the cold neutral reflection, except for NGC 5548. Therefore, the variable components are all similar to those obtained in the 2005 and 2009 data sets of NGC 3516; the stationary component of NGC 5548 is similar to the 2009 results of NGC 3516, while those of the other four AGNs to the 2005 case of NGC 3516.

6.4.2 Spectral analysis

To verify the expectation in the previous subsection, we jump to the triplet spectral analysis, because it can take over the preliminary analysis of the variable and constant component. In the same way as in §6.1 and §6.2, we employ the additional primary continuum interpretation, and utilize `model_v = Phabs*Ioabs*PL` and `model_s = Phabe*Ioabs*(ReflFe + Phabs'*PL')`, where NGC 5548 required only `model_s = Phabe*Ioabs*ReflFe`. Among the multiple observations of each AGN, the brightest data set was utilized for the time-averaged spectrum, and the x_0 value, which determines the normalization of the variable component, was selected to be the average 2–3 keV count rate in the brightest data set.

As shown in Fig. 6.21 and Table 6.10, the fits were successful except for MCG–6-30-15. The result of MCG–6-30-15 is discussed in the final part of the present section. As expected, an acceptable result was obtained in NGC 5548 without including the additional absorbed PL. This is similar to the 2009 result of NGC 3516 shown in Fig. 6.8 (a); the seven observations of NGC 5548 can all be understood as combinations of the variable PL and the stable reflection component. On the other hand, results on the other objects are similar to that of the 2005 data set of NGC 3516, which is characterized by the prominent presence of the additional PL. In all these cases, the additional PL has a significantly harder slope than that of the main variable PL, and is absorbed by an optically-thick material with a column density of $\sim 10^{23}$ cm^{-2}, just in the same way as the 2005 observation of NGC 3516 and NGC 3227. Thus, the additional hard components in these AGNs, including NGC 3516, NGC 3227, NGC 4051, MCG–6-30-15, Mrk 841, and IC4329A, are considered to be generated by a common physical process.

Among the selected five AGNs, only the fit for MCG–6-30-15 failed (Table 6.10), mainly because of positive residuals in 5–7 keV and negative ones in 7–10 keV. In addition, the C3PO-derived stationary component was not explained successfully in the 7–10 keV band. This suggests that the absorbed-PL modeling of the additional hard continuum needs to be improved to better reproduce the time-averaged and the C3PO-derived stationary spectra of this particular object. Then, we invoked the partial covering absorptions for the additional component like the NGC 3227 Faint-branch cases, and replaced `Phabs'` by `PhabsC'`. However, the triplet spectral fitting with `model_s = Phabs*Ioabs*(ReflFe + PhabsC'*PL')` was not significantly better, with χ^2/d.o.f.=960.0/822. Then, we further invoked ion-

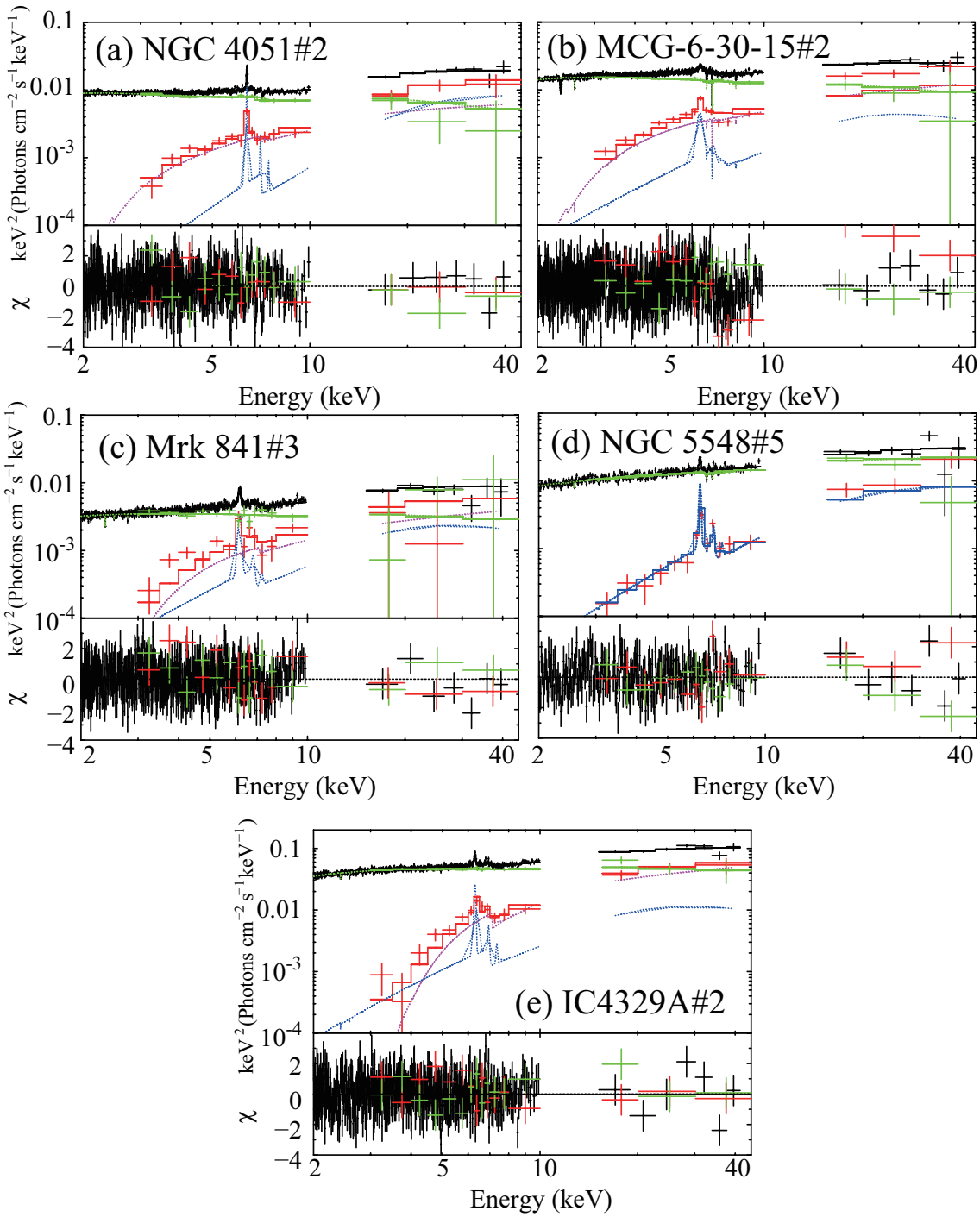

Figure 6.21: Fitting results of the triplet spectral analyses in the selected 5 AGNs. The green `PL` and purple `Phabs' * PL'` model are found to be the Broad-Band and Hard Primary continuum in §7.1.2, respectively.

Table 6.10: Results of the triplet spectral fits of the selected five AGNs.

		NGC 4051	MCG–6-30-15	Mrk 841	NGC 5548	IC 4329A
Absorption to all						
`Phabs`	$N_{\rm H}^{*\dagger}$	$0.51^{+0.11}_{-0.09}$	0.67	$0.42^{+0.12}_{-0.35}$	$0.39^{+0.13}_{-0.12}$	$1.03^{+0.04}_{-0.55}$
`Ioabs`	$N_{\rm H0}\dagger$	$74.2^{+22.4}_{-11.6}$	6.1	$0.3^{+2.7}_{-0.3}$	$2.7^{+27.7}_{-2.1}$	$64.6^{+28.2}_{-15.4}$
	logξ	$1.9^{+0.1}_{-0.5}$	4.3	$2.7^{+0.6}_{-0.8}$	$3.3^{+1.2}_{-0.3}$	$0.8^{+0.5}_{-0.7}$
	Cvr frac.	$0.36^{+0.06}_{-0.04}$	1	> 0.36	> 0.27	0.25 ± 0.1
	z	0.0023 (fix)	0.0078 (fix)	0.0364 (fix)	0.0172 (fix)	0.0161 (fix)
Broad-Band Primary component*						
`PL`	Γ_0	$2.40^{+0.08}_{-0.07}$	2.23	$2.09^{+0.05}_{-0.11}$	1.71 ± 0.03	$2.15^{+0.08}_{-0.06}$
	$E_{\rm cut}$ (keV)			200 (fix)		
	$N_{\rm PL}^{\ddagger}$	$2.32^{+0.34}_{-0.66}$	2.21	$0.42^{+0.08}_{-0.03}$	0.82 ± 0.05	$8.09^{+2.07}_{-1.82}$
Reflection component						
`ReflFe`	$\Gamma_{\rm ref}$			$= \Gamma_0$		
	z	0.0023 (fix)	0.0078 (fix)	0.0364 (fix)	0.0172 (fix)	0.0161 (fix)
	A ($Z_\odot$)			1 (fix)		
	$A_{\rm Fe}$ ($Z_{\rm Fe,\odot}$)			1 (fix)		
	$f_{\rm ref}$	$1.9^{+0.4}_{-0.3}$	0.7	1.2 ± 0.2	0.5 ± 0.1	0.4 ± 0.1
	i (degree)			60 (fix)		
	$N_{\rm ref}$			$= N_{\rm PL}$		
Hard Primary component*						
`Phabs'`	$N_{\rm H1}^{\dagger}$	$9.3^{+2.4}_{-3.2}$	10.1	$19.3^{+10.0}_{-5.8}$	–	$25.0^{+10.5}_{-10.0}$
`PL'`	Γ_1	1.62 ± 0.13	1.40	$1.41^{+0.21}_{-0.18}$	–	1.32 ± 0.19
	$E_{\rm cut}$ (keV)			200 (fix)		
	$N_{\rm PL}^{\ddagger}$	$0.15^{+0.06}_{-0.04}$	0.14	0.05 ± 0.01	–	$0.38^{+0.30}_{-0.17}$
χ^2/d.o.f.		645.88/592	980.4/824	568.7/600	313.8/277	550.4/574

* Later to be identified in §7.1.2.

† Equivalent hydrogen column density in 10^{22} cm^{-2}.

‡ The `PL` normalization at 1 keV, in units of 10^{-2} photons keV^{-1} cm^{-2} s^{-1} at 1 keV.

ization effects in the partial absorption, replacing `PhabsC` by `Ioabs`, and fitted the triplet spectra of MCG–6-30-15 with `model_s = Phabs*Ioabs*(ReflFe + Ioabs'*PL')`. As shown in Fig. 6.22 and Table C.4, the fit significantly improved, and became acceptable with χ^2/d.o.f.=899.9/819. According to this model, the stationary component is implied to have a partial ionized absorption with a covering fraction of ~ 0.9, and the spectral shape of its additional PL is similar to those in the Faint-branch data sets of NGC 3227.

In the fits of the present section, the ionized absorption modeled by `Ioabs` was generally applied to the overall model as well, because MCG–6-30-15, NGC 4051, Mrk 841, NGC 5548, and IC4329A were all reported to bear ionized absorption features by Miller et al. (2008), King et al. (2012), Longinotti et al. (2010), Andrade-Velázquez et al. (2011), and Steenbrugge et al. (2005), respectively. In MCG–6-30-15 and NGC 4051, several ionized absorption features by outflows were also reported.

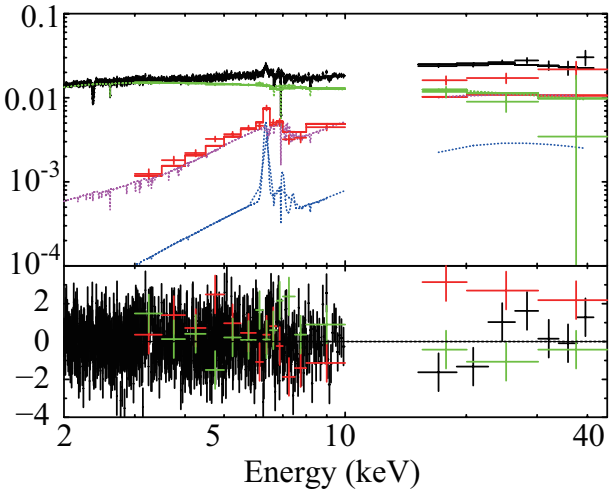

Figure 6.22: Same as Fig. 6.21(b), but with `model_s = Phabs*Ioabs*(ReflFe + Ioabs'*PL')`. That is the simple absorption on the purple model was replaced by an ionized partial absorption. The `PL` model in green and purple represent the Broad-Band and Hard Primary component, respectively, which are identified in §7.1.2.

Thus, we additionally introduced three negative gaussians at $\sim$ 2.4 keV, $\sim$ 6.67 keV, and $\sim$ 6.97 keV, which correspond to S XV Heα (e.g., Rodes-Roca et al. 2011), Fe XXV, and Fe XXVI absorption, respectively.

Table 6.11: A result of MCG–6-30-15 with `model_s = Phabs*Ioabs*(RefFe+Ioabs'*PL')`.

		MCG–6-30-15
Absorption to all		
`Phabs`	$N_{\rm H}^{\dagger}$	0.73 ± 0.06
`Ioabs`	$N_{\rm H}^{\dagger}$	$9.7^{+22.0}_{-4.6}$
	logξ	$4.7^{+0.6}_{-1.8}$
	Cvr frac.	1 (fix)
	z	0.0078 (fix)
Broad-Band Primary component*		
`PL`	Γ_0	2.22 ± 0.03
	$E_{\rm cut}$ (keV)	200 (fix)
	$N_{\rm PL}^{\ddagger}$	$2.17^{+0.10}_{-0.09}$
Reflection component		
`ReflFe`	$\Gamma_{\rm ref}$	$= \Gamma_0$
	$E_{\rm cut}$ (keV)	200 (fix)
	$f_{\rm ref}$	0.5 ± 0.1
	z	0.0078 (fix)
	A ($Z_{\odot}$)	1 (fix)
	$A_{\rm Fe}$ ($Z_{\rm Fe,\odot}$)	1 (fix)
	i (degree)	60
	$N_{\rm ref}$	$= N_{\rm PL}$
Hard Primary component*		
`Ioabs'`	$N_{\rm H}^{\dagger}$	$47.6^{+15.6}_{-8.8}$
	logξ	2.1 ± 0.1
	z	0.0078 (fix)
	Cvr frac.	$0.92^{+0.03}_{-0.04}$
`PL'`	Γ_1	$1.75^{+0.11}_{-0.12}$
	$E_{\rm cut}$ (keV)	200 (fix)
	$N_{\rm PL}^{\ddagger}$	$0.52^{+0.28}_{-0.22}$
χ^2/d.o.f.		899.9/819

* Later to be identified in §7.1.2.

† Equivalent hydrogen column density in 10^{22} cm^{-2}.

‡ The `PL` normalization at 1 keV, in units of 10^{-2} photons keV^{-1} cm^{-2} s^{-1} at 1 keV.

Chapter 7

Disscussion

With the C3PO method, we succeeded in the model-independent spectral decomposition, in the soft and hard X-ray energies of the selected type I AGNs. In the present Chapter, we summarize the obtained results, examine properties of the extracted spectral components, and discuss their nature.

7.1 Summary of the Result

We mainly divided the *Suzaku* 0.5–45 keV band into two energy ranges; the soft X-ray (0.5–3 keV) band and the hard X-ray (3–45 keV) band, and applied the C3PO method to them in Chapter 5 and Chapter 6, respectively. Below, the obtained results are summarized individually.

7.1.1 Soft X-ray results

Analyzing the *Suzaku* data sets of Mrk 509 and the five AGNs in §5.1–5.3 with the C3PO method, and further employing the technique of simultaneously fitting spectral "triplets", we succeeded in extracting two spectral components which generally exist in the 0.5–3 keV band of these objects:

1. A PL-like continuum with a photon index of ~ 1.8, which is highly variable on a timescale of several hours, namely $\sim \ 10 R_{\rm g}/c$. It is dominant not only in the soft X-ray band, but also in the hard X-ray band above 3 keV. Therefore, we hereafter call it the *Broad-Band Primary component*.

2. A soft component, to be identified with the long-known issue of "soft X-ray excess" feature. It exhibits a long-term variations on a timescale of $\sim$ 3–10 days, namely $\sim 1000\ R_{\rm g}/c$, which is independent of that of the Broad-Band Primary component above. It has a typical 0.5–3 keV luminosity of $\sim 10^{44}$ erg s^{-1}, while its spectral shape is represented by a color temperature of ~ 0.2 keV, or an equivalent photon index of 3–4. In the triplet analysis in Chapter 5, it has been reproduced successfully by neither a thin-thermal plasma emission (possibly in the host galaxy), nor a relativistically-blurred ionized reflection component that is produced as secondary emission. Instead, it can be regarded as a primary emission. Given this, we therefore call it

the *Soft Primary component*. The nature of this component and its physical interpretation is discussed in §7.4.

7.1.2 Hard X-ray results

With the application of the C3PO method to the hard X-ray region of NGC 3516 (§6.1), NGC 3227 (§6.2), and the selected five AGNs (§6.4), we revealed the presence of the following three spectral components in the 3–45 keV energy range.

1. A single cutoff PL-like continuum with a photon index of $\sim$ 1.7–2.3, suffering relatively low absorption with a column density $\lesssim 10^{22}$ cm^{-2}. It is highly variable on a timescale of several hundreds ksec or less, namely $\sim 10\ R_{\rm g}/c$, except for some objects like NGC 3516 in 2009 and NGC 5548, which exhibited relatively monotonic variations. It does not change its spectral shape when its flux varies, making CCP distributions linear. It is colored in green throughout, and considered to be identical to *Broad-Band Primary component* identified in §7.1.1.

2. A reflection component from cold and neutral materials without relativistic effects. It is accompanied by a narrow Fe-Kα emission line, which has an intensity consistent with an Fe abundance of $\sim$ 1 Solar. It remained unchanged during the individual observations of NGC 3516. In the other six AGNs selected for the hard-band study, it also remained almost constant through multiple observations, with intervals up to $\sim$ 5 years. It is expressed in blue in the present figures.

3. A hard PL component (in purple) with a photon index of 1.3–1.8, strongly absorbed with a column density of $\sim 10^{23}$ cm^{-2}. While this component is much less variable than the Broad-Band Primary component, it varied significantly between the 2005 and the 2009 observations of NGC 3516, and in the Faint branch of NGC 3227. Unlike the reflection component, it lacks any narrow spectral features, such as an Fe-Kα emission line, and can be reproduced by neither a neutral nor ionized reflection spectral model. Furthermore, the triplet analysis ruled out its interpretation as a relativistically-smeared reflection component. More generally, this component cannot be a secondary one, since it varied quite independently of the Broad-Band Primary component that makes up a major part of the primary emission in many AGNs. It cannot be the partially absorbed primary signal, either, since its spectral slopes are considerably harder, and the underlying CCPs are quite linear. This is indeed a new component that has not been noticed before, and we devote §7.5 to its discussion. In addition to the former two primary components, it is hereafter called *Hard Primary component.*

7.1.3 Relation between the soft-band and hard-band results

In Chapter 5, the 0.5–3 keV photon variations were examined against the 3–10 keV reference signals, while the analysis in Chapter 6 decomposed the 3–45 keV spectra using the 2–3 keV intensity as the

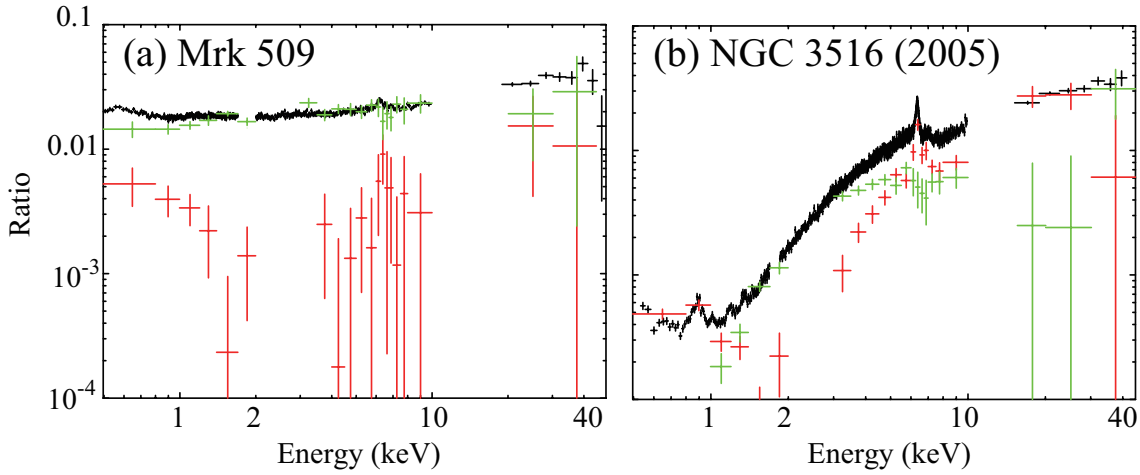

Figure 7.1: Triplet spectra of Mrk 509 in 2010 (panel a) and NGC 3516 in 2005 (panel b), decomposed with the C3PO method using the 2–3 keV signals as the reference. Black, green and red show the time-averaged, the variable, and the stationary spectra, respectively.

reference. Then, is it possible to decompose both soft and hard X-ray spectra simultaneously? To examine this, we applied the C3PO method simultaneously to the 0.5–2 keV and the 3–45 keV regions of Mrk 509 in 2010 and NGC 3516 in 2005, taking the 2–3 keV band as the common reference.

The results of this analysis on Mrk 509 are given in Fig. 7.1 (a). Using the 2–3 keV counts as the reference, the 0.5–2 keV signals have been decomposed again into Soft Primary component (red) and Broad-Band Primary component (green), of which the intensities and spectral shapes agree, within errors, with those when the 3–10 keV counts were used as the reference (Fig. 5.6 in §5.1.4). Thus, the soft X-ray decomposition of Mrk 509 is relatively insensitive to the choice of the reference band. Furthermore, Fig. 7.1 (a) shows a hint of a stationary hard component including a Fe-Kα emission line at $\sim$ 6.4 keV and a hard X-ray hump in the 15–45 keV range (by reflection component maybe with the Hard Primary component), suggesting that the method is applicable in principle to the entire energy range. However, the C3PO-derived stable hard X-ray signals of Mrk 509 have much poorer statistics than those of the AGNs studied in Chapter 6, simply because of much lower variability of Mrk 509. The same limitation applies to the the other AGNs selected in Chapter 5, which also have rather lower variability.

Figure 7.1 (b) shows the broad-band C3PO results on NGC 3516 (in 2005) when the 2–3 keV signals are used as the reference. (The results above 3 keV should be exactly identical to Fig.6.6 a.) Thus, the stationery signals of NGC 3516, which have been very strongly detected in energies above 3 keV, are also found in the soft X-ray band below 2 keV, with a spectral shape similar to that of Mrk 509. However, this soft-excess luminosity of NGC 3516 is $\sim 2 \times 10^{41}$ erg s^{-1} (in 0.5–2 keV), which is comparable to that of typical soft X-ray emission from the host galaxy. Therefore, we cannot conclude for sure whether NGC 3516 hosts the Soft Primary component or not. The other AGNs selected in Chapter 6 are subject to the same problem.

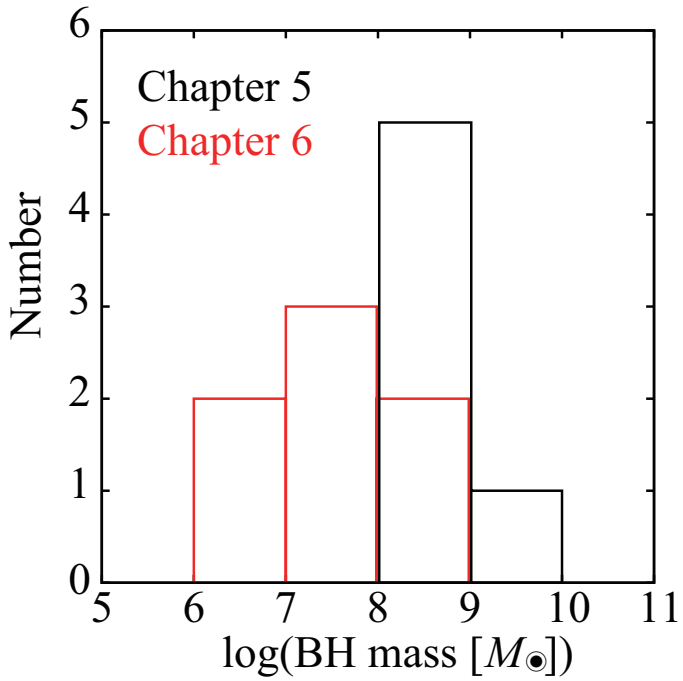

Figure 7.2: The number distributions of BH masses in Chapter 5 (black) and 6 (red).

As we have seen above, the C3PO method can in principle be applied to wide-band data, and can be used to decompose broad-band spectra into a variable and a stationary components. However, AGNs suited to the soft band analysis are not necessarily appropriate for the hard X-ray studies, and vice versa. This is the reason why we had to conduct separately the studies in Chapter 5 and Chapter 6. Generally speaking, the hard-band decomposition requires highly variable AGNs with relatively low BH masses, while the soft-band study favors higher-luminosity AGNs (to avoid the host-galaxy contamination) which are intrinsically less variable. Actually, as shown in Fig. 7.2, the BH masses of the AGNs analyzed in the two Chapters exhibit distinct distributions.

7.1.4 Problems and limitations of the C3PO method

Problems

Although the C3PO method has been proven to provide a very powerful mean of decomposing AGN spectra, it is of course subject to several intrinsic problems and limitations. Here, let us examine these issues. The most straightforward one is how to choose the reference band. However, as already shown to some extent in §7.1.3, the C3PO results will not be very sensitive to this choice, as long as intensity variations at different energies are correlated linearly with one another. We may then choose an energy band where the stationary component becomes minimum. In fact, the 2–3 keV range used in Chapter 6 and §7.1.3 satisfies this condition (e.g., Markowitz et al. 2003; Noda et al. 2013b); the soft excess signals decrease rapidly above $\sim$ 2 keV, while the hard-band stationary components generally have

considerably harder spectra than the averaged spectrum. Then, the problem reduces to the issue of how to deal with a finite offset that may remain even in the optimally chosen reference band.

Let us hence consider the more fundamental problem with the C3PO method, i.e., its inherent uncertainty in the offset count rate included in the reference band, or "intensity floor" (§6.1.3). In Chapter 6, we assumed for simplicity that this intensity floor, C in eq. (5.1), to be zero, and gave some justification in §6.1.3 and §6.2.5. However, this assumption is not necessarily warranted, and there is no way to estimate C from the data themselves. Thus, after Noda et al. (2013b), we examined in a more concrete manner how the spectral shapes of the C3PO-derived variable and stationary components depend on the assumed values of C. The result of this attempt on the 2009 data of NGC 3516 is shown in Fig. 7.3, where we changed C from 0 (the same as in Chapter 6) to the maximum allowed by the data (=the minimum intensity observed in the reference band of 2–3 keV). The variable component (the Broad-Band Primary in §7.1.2) thus keeps its spectral shape independently of C, and only its intensity decreases as C gets larger. On the other hand, as expected from §6.1.3, the stationary components change in both its spectral shape and intensity as we assume different values of C.

As already described in §6.1.6, the C3PO-derived stationary component of NGC 3516 in 2009 can be reproduced by a neutral and distant reflection (the 2nd component in §7.1.2) when $C = 0$. When $C > 0$, a PL-like component formed by the AC term in eq. (6.1) is added on top of the neutral reflection component, making the spectral shape more concave. The same phenomenon happens in the other AGNs as well. The concave spectral shapes with $C > 0$ may be explained in the following two ways. One is adding a new PL, and the other is changing the spectral shape of the reflection component (or of the Hard Primary component if it is present). Mathematically, the former option is much simpler and more reasonable, because the normalization decrease in the variable component towards higher C must be compensated exactly by an increase in the stationary component. Actually, as studied in detail in Noda et al. (2013b), the flatter shapes of the stationary component for $C > 0$ in Fig. 7.3 (c) can be readily explained by presuming that the variable PL did not completely vanish during our observation. This is the most preferred treatment of the intrinsic uncertainty in C, and the effects are at most some changes in the relative strengths of the Broad-Band and Hard Primaries (§7.1.2). In Chapter 6, we implicitly adopted this stand point. Importantly, the Faint-branch data of NGC 3227 (Fig. 6.14) actually fulfilled this condition.

When we alternatively choose to modify the spectral shape of the reflection component, ionized refection process (Fig. 2.13) may be invoked to explain the flatter spectral shapes in Fig. 7.3 towards larger C. However, the ionized reflection component includes many emission lines at $\lesssim 3$ keV as shown in Fig. 2.13. We in fact considered such a possibility already in §6.1.7 in our analysis of the triplet spectrum of NGC 3516, and found that strong ionization of the reflector can be ruled out ($\xi < 12.3$). Of course, an ionized reflection model would give a better fit to the stationary component with $C \neq 0$, but such a modeling is disfavored by the time-averaged spectrum which has a much higher statistics and is capable of utilizing the full energy resolution of the XIS.

Yet another possibility to explain the stationary spectrum extracted with $C \neq 0$ is to assume that

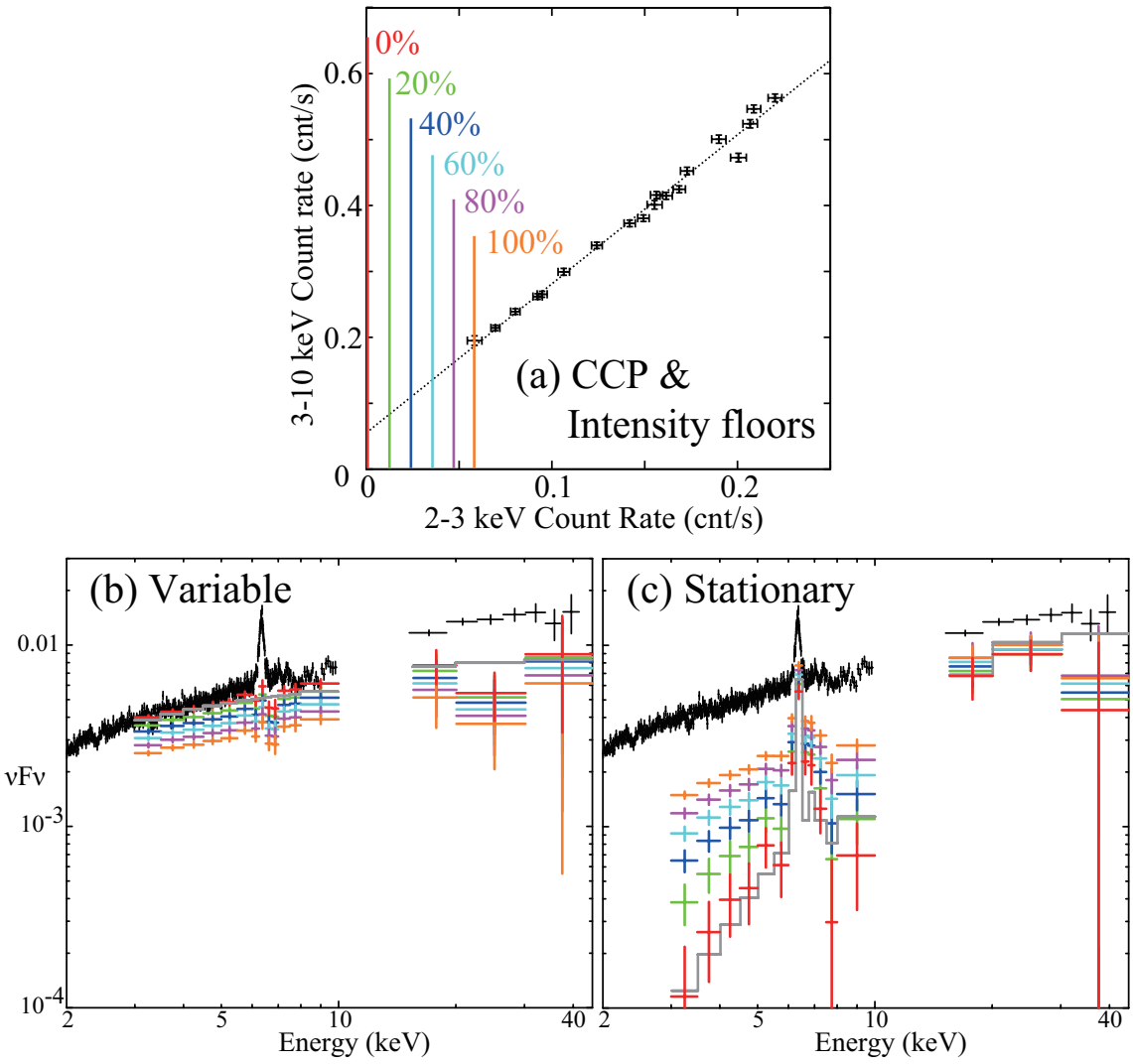

Figure 7.3: Effects of different intensity floors on the NGC 3516 data in 2009. (a) Same as Fig. 6.4(a), but with colored lines showing different intensity floors to be chosen in the 2–3 keV reference band. (b) The time-averaged spectrum (black; the same as Fig.6.8 a), compared with the C3PO-extracted variable component assuming six different values of C between 0 and the maximum allowed by the data. Colors correspond to those in panel (a). (c) The same as panel (b), but for the stationary signals.

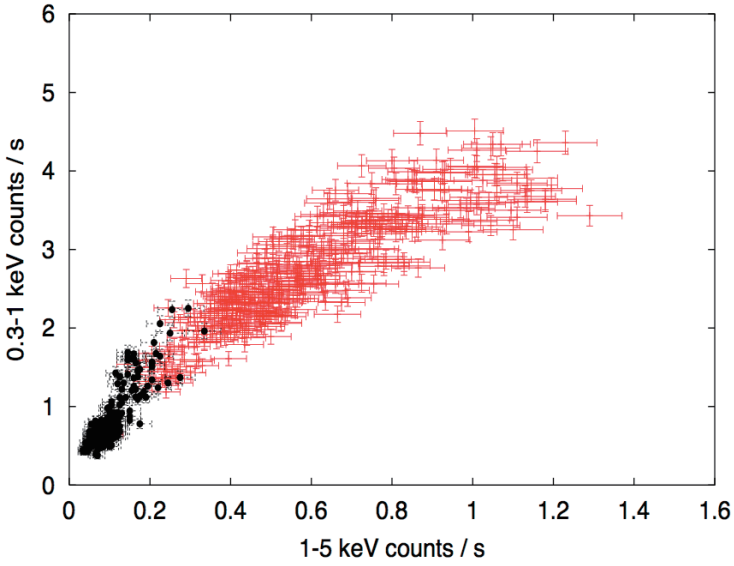

Figure 7.4: A CCP of the narrow line type I Seyfert galaxy 1H0707-495 (Fabian & Miniutti 2005). Black and red data points are from different observations.

the Hard Primary component (§7.1.2) has a flatter shape toward lower energies, instead of decreasing rapidly as represented by the strong absorption. This condition may be realized by physical processes such as partial and/or ionized absorption, which we already invoked in §6.2.6 when analyzing the data of NGC 3227. Since this possibility cannot be ruled out, we must be cautious about the values of $N_{\rm H}$ attributable to the Hard Primary component; it may decrease by several times if higher values of C are chosen. Nevertheless, the higher energy part of the stationary component is much less ($< 10\%$) affected by the uncertainty in C. Therefore, the very hard nature of the Hard Primary component is considered more robust. In particular, as argued in §6.2.5, the Faint Branch spectrum of NGC 3227, with significant absorption, is important, because it becomes almost solely the Hard Primary component after subtracting the distant reflection.

Limitations

Let us also consider limitation of the C3PO analysis. This method, needless to say, cannot be utilized if the object is not variable. In addition, it can be applied only to those AGNs of which the CCPs are characterized by linear data distributions, like those studied in the present thesis. However, some objects show non-linear CCPs as presented in Fig. 7.4. Such behavior may take place if, e.g., two or more components are varying independently on similar time scales, or when the intensity changes are mainly caused by those in the absorption, or when a single component varies both in intensity and spectral shape. Since this kind of CCPs cannot be reproduced by a straight line, the C3PO method cannot be applied to those AGNs. They are beyond the scope of the present thesis.

By the C3PO method, we succeeded in obtaining two spectral components (variable and stationary), from both the soft and hard X-ray bands, hence, $2 \times 2 = 4$ components in total. Because the

variable component in the soft X-ray band is considered to be the same as that in the hard X-ray band, namely the Broad-Band Primary, one variable and two stationary components were, in reality, extracted. However, each of these components can be a composite of multiple sub-components which vary on similar time scale. Thus, the number of the obtained components must be a lower limit. In fact, the stationary component in the hard X-ray band can be divided into the Hard Primary component and the neutral disk reflection component, by a spectral fitting which is independent of the C3PO method, or utilizing long-term variations (in NGC 3227; §6.2.5).

7.2 A Novel Picture of AGN X-ray Spectra

Our results summarized in §7.1 may be illustrated in Fig. 7.5, which gives a novel picture of AGN X-ray spectra, to replace the previous one shown in Fig. 2.11. In this view, the Soft Primary component in red and the Hard Primary component in purple are primary components, as well as the fast variable Broad-Band Primary component in green that was previously regarded as the only primary emission. The largest difference from the previous view appears in the interpretation of the hard X-ray signals. A part of the hard X-ray (15–45 keV) hump, which was so far interpreted solely as secondary components such as relativistically-blurred reflection and/or a partially-absorbed Broad-Band Primary, is in reality contributed significantly by the slowly-varying Hard Primary component (the 3rd in §7.1.2) discovered in the present thesis.

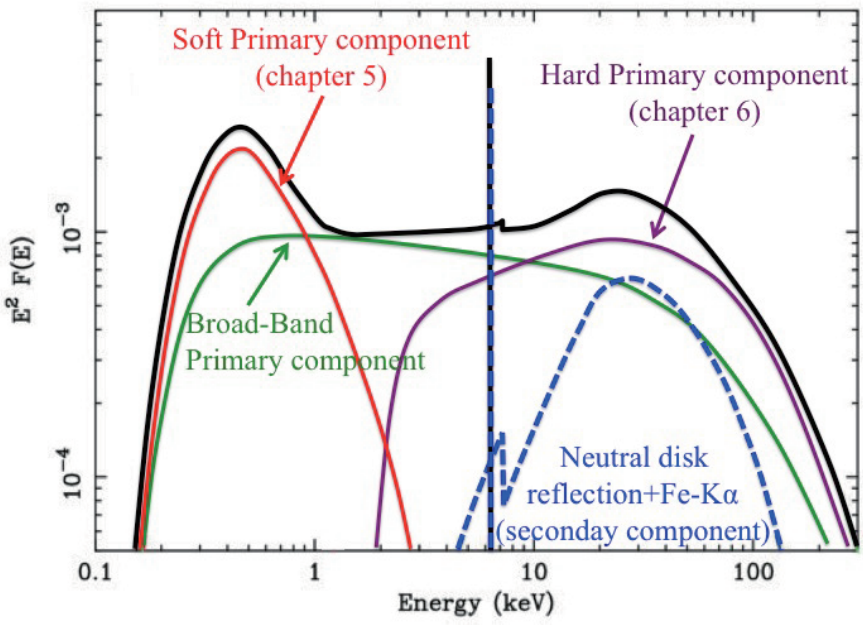

Figure 7.5: A novel schematic picture of AGN X-ray spectra. Green, red, purple, and blue lines represent the rapidly variable Broad-Band Primary component, the slowly variable Soft Primary component (Chapter 5), the strongly-absorbed Hard Primary component without rapid variation (Chapter 6), and the neutral disk reflection component, respectively.

Our novel picture evidently has important implications for the central engine. In this view, the spectral shape of the primary continuum is concave as a sum of the three components (the Soft, Broad-Band, and Hard Primaries), in contrast to the previous picture (Fig. 2.11) where the primary emission was assumed as a single PL. Furthermore, these primary three components are all explained most reasonably in terms of inverse-Comptonization of some seed photons, as they are reproduced by `Compton` or `PL` (§5.3.4, §6.4.2). This means that the central engine of AGNs are composed of multiple primary coronal regions with different electron temperatures and/or different optical depths, presumably reflecting complex geometry of the overall primary emission region. Below, from §7.3 through §7.5, we discuss, one by one, the four characters of Fig. 7.5, and consider a possible geometry of the central engine in §7.6.

7.3 Neutral disk reflection component

According to our new picture presented in §7.2, the neutral disk reflection component (represented by a blue broken line) is the only genuine secondary component, produced presumably in outer accretion-disk regions or molecular torus (§2.1.4). Of course, this is component has long been known, but our new method allows us to much better constrain the reflection parameters, including the Fe abundance $A_{\rm Fe}$ and the reflector solid angle Ω. To see this, we repeated the fitting to the 2009 spectrum of NGC 3516, but this time, without fixing $A_{\rm Fe}$ to 1 Solar (cf. §6.1.7). Figure 7.6 shows how the data constrain $A_{\rm Fe}$ and Ω, when only the time-averaged spectrum is fitted (panel a) as performed in many previous works, and when the C3PO-derived two components are simultaneously incorporated (panel b) as in Chapter 6. Without the C3PO-derived components, the two parameters degenerate as shown in Fig. 7.6(a), imposing very large errors on both parameters. In this case, we would not be able to discuss physical condition of the reflecting materials surrounding the central BH. Previous studies of the X-ray emission form AGNs always suffered this kind of spectral degeneracy (§2.3.7). On the other hand, the inclusion of the C3PO-derived components have drastically reduced the errors on the two parameters (panel b). Thus, we have revealed almost model-independently that the scattering materials which generated the reflection component of NGC 3516 in 2009 have $A_{\rm Fe} \sim 1.2$ Solar value and $\Omega \sim 3.8\pi$, within errors of several tens percent. This great improvement occurs in the following way. In Fig. 7.6 (a), the Fe-Kα line flux is accurately constrained by the time-averaged spectrum, but the secondary continuum is not, due to its confusion with the primary continuum. If Ω is decreased, the reflection in the hard secondary continuum would be compensated by adjusting the other (primary) components, while $A_{\rm Fe}$ would increase to explain the line photon flux. This produces the strong anti-correlation between the two parameters. This kind of degeneracy is solved by our C3PO method (particularly in this case where the absorbed Hard Primary component is absent), because the stationary component accurately constrains both the Fe line flux and continuum of the reflection signals.

In the fit to NGC 3516 in 2009 in §6.1.7, the Fe-Kα line width was fixed at $\sigma = 0.035$ keV. To examine the distance of the reflector, we repeated the triplet fits with σ left free, and obtained an

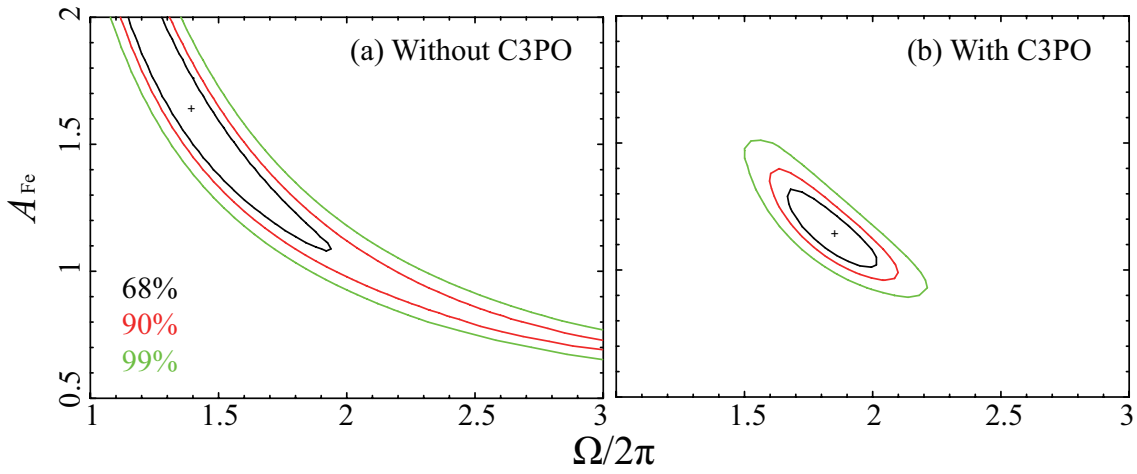

Figure 7.6: Confidence contours of the Fe abundance and the solid angle of the reflection, obtained in the fit to the time-averaged spectrum of NGC 3516 in 2009, without considering (panel a) and simultaneously incorporating (panel b) the C3PO-derived variable and stationary components. Black, red, and green contours represent 68%, 90%, 99% confidence levels, respectively.

upper limit as $\sigma < 0.05$ keV. If we identify the reprocessor with an optically-thick accretion disk in Keplerian rotation, its typical distance is hence constrained as $\gtrsim 2500\ R_{\rm S}$, where $R_{\rm S} \sim 6 \times 10^{12}$ cm for a BH mass of $2 \times 10^7\ M_\odot$ in NGC 3516. In addition, we can independently estimate the distance of the reprocessor because the reflection component of NGC 3516 in 2009 was extracted as emission that was constant during the observation period of ~ 500 ksec. This means that the reprocessor must be extended over a linear dimension larger than ~ 500 ksec $\times\ c\ \sim\ 1.5 \times 10^{16}$ cm $\sim 5000\ R_{\rm S}$, in good agreement with the estimation from the Fe-Kα line width. Thus, in the triplet fit of NGC 3516 in 2009, we succeeded in constraining, much better than before, the distance to the repocessor which generated the secondary X-rays, as well as its $A_{\rm Fe}$ and Ω.

The estimated Ω (Fig. 7.6 b) of NGC 3516 in 2009 is much larger than the value of 2π, expected for an infinite plane of an accretion disk. How about the other AGNs? Figure 7.7 summarizes the values of Ω of the analyzed AGNs obtained in the triplet fits, as a function of their 3–10 keV flux. As best represented by the behavior of NGC 5548, all the AGNs exhibit negative correlation in Fig. 7.7. Some data points including the faintest occasion of NGC 5548, NGC 3516, and NGC 4051 show very large values of Ω to reach an unphysical vale of $\sim 4\pi$. This discrepancy can be solved, when we take it into account that the primary source was rather faint in these observations, while the reflected emission, generated at $\gtrsim 5000\ R_{\rm S}/c$, should represent a longer-term average luminosity. Actually, if we consider the average 3–10 keV flux of NGC 5548 to be $\sim 1.5 \times 10^{-11}$ erg s^{-1} cm^{-2}, the solid angle becomes reasonable at $\Omega \sim 2\pi$.

Although the unusually large values of Ω can be thus explained in some cases, the puzzle still remains for the 2005 observation of NGC 3516 and the bright occasions of NGC 4051, because these data were taken in a relatively bright phase. These cases can be solved by a different idea: the

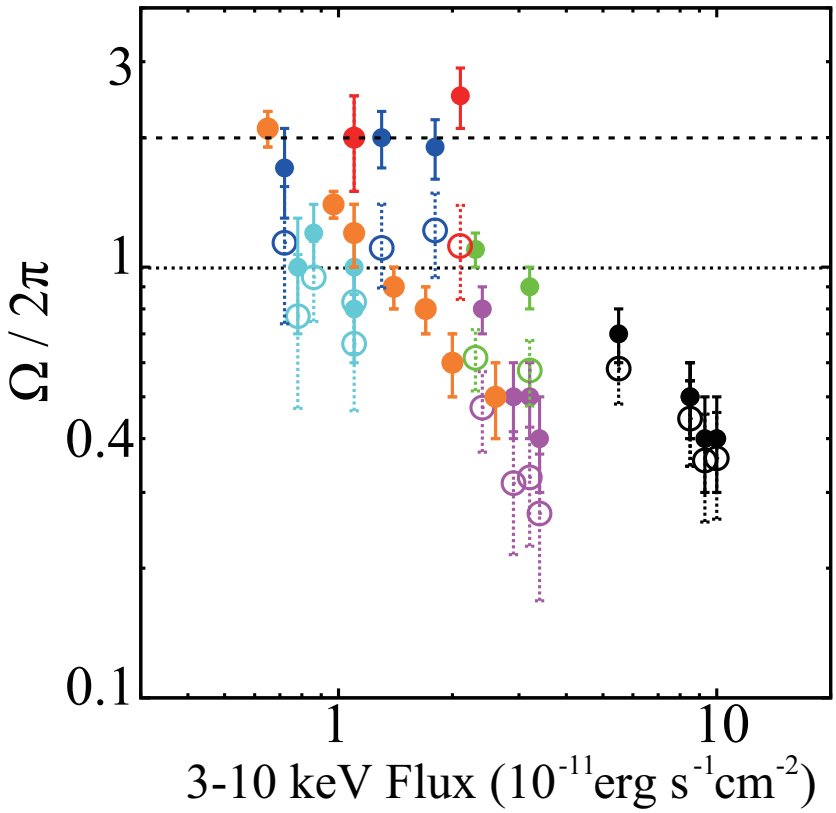

Figure 7.7: The solid angle of reflection (divided by 2π) against illumination by the Broad-Band Primary component (the 1st in §7.1.2), shown as a function of the 3–10 keV flux in all the *Suzaku* observations utilized in the present thesis; NGC 3516 (red), NGC 3227(green), NGC 4051 (blue), MCG–6-30-15 (purple), Mrk 841 (cyan), NGC 5548 (orange), and IC4329A (black). A dashed line and a dotted line indicate solid angles of 2π and 4π, respectively. Filled circles show the results summarized in Table 6.4, 6.6, and 6.10, while open circles give revised values when the solid angle is calculated against the Broad-Band and Hard Primary continua in §7.1.2.

values of $\Omega/2\pi$ in Fig. 7.7 (filled circles) were calculated assuming that the illuminating primary signals come only from the Broad-Band Primary (green in our spectra), while the reality is that the Hard Primary (purple), regarded as another primary emission, must be contributing as well. In other words, the value of Ω should be shared by the two PL components. Open circles in Fig. 7.7 show the solid angles re-calculated by taking into account the illuminating primary X-rays from the harder PL. All of them, including NGC 3516 and NGC 4051, become consistent with $\Omega \sim 2\pi$ or less, which is physically natural for an infinite plane. Thus, the presence of the Hard Primary component is essential in obtaining correct understanding of the reflector.

7.4 Optically-thick Compton Interpretation of Soft Primary

The largest significance of our results obtained in Chapter 5 is that the long-known soft X-ray feature, which was so far identified in "static" ways through spectral fitting as an excess above an assumed PL,

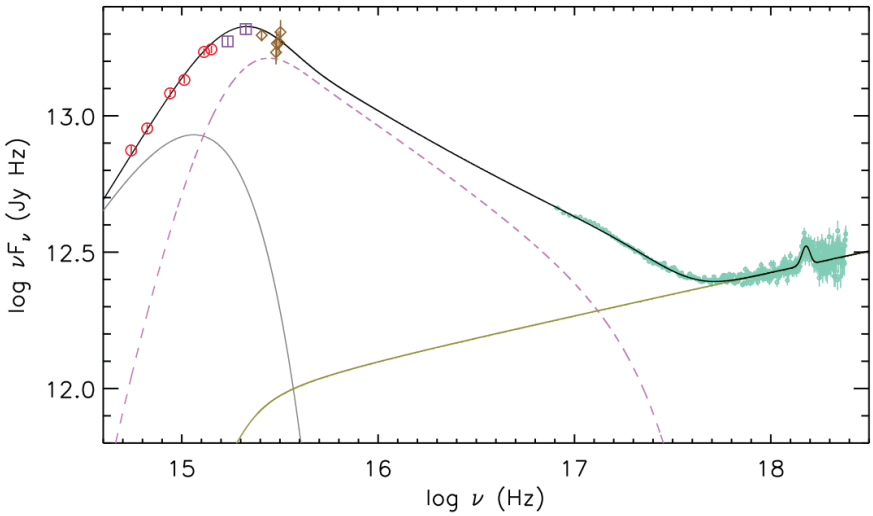

Figure 7.8: Multi-wavelength spectral fitting of Mrk 509 (Mehdipour et al. 2011). Red shows the data of OM onboard *XMM-Newton*, purple the *HST*/COS, brown the *FUSE*, and green the EPIC-pn onboard *XMM-Newton*. Grey solid line represents the blackbody emission, dark green solid line the Broad-Band Primary emission, while the dashed purple line the stationary Soft Primary component.

has been extracted in dynamical ways without assuming any continuum model. In §5.3, we selected several types of AGNs which left a significantly positive y-intercept in the CCPs between 0.5–3 keV and 3–10 keV band, and systematically applied the C3PO method to obtain the stationary soft component. This component was confirmed to be responsible for the soft excess phenomenon, and to be common to different types of AGNs, including even the more strongly absorbed one. Although the C3PO decomposition did not work in §5.3, in 7 out of 12 AGNs, these 7 objects, as already argued therein, do not appear to be qualitatively different from the successful 5 objects; simply they were somewhat fainter, or had smaller soft-excess strengths. Therefore, our results derived in §5.3 are considered to be general enough.

Another scientific importance of the results in Chapter 5 is that the soft excess signals in our sample AGNs have been confirmed to be primary photons, rather than some secondary ones (e.g., ionized relativistic reflection). This is mainly because the soft component has been extracted as an independent emission that has different variability characteristics from those of the main PL. Furthermore, in §5.1.7, the C3PO-extracted soft excess component of Mrk 509 was successfully reproduced by a thermal Comptonization component with a low electron temperature of ~ 0.4 keV and a high optical depth of ~ 15. Recently, Mehdipour et al. (2011) conducted simultaneous mutli-wavelength observations of Mrk 509 with XMM-*Newton*, *Hubble*, *FUSE* and *Swift*. As shown in Fig. 7.8, they detected a steep continuum ranging from the optical to the soft X-ray frequencies, and interpreted it as a soft Comptonization component with an electron temperature of ~ 0.2 keV and an optical depth of ~ 17, which are very similar to the Compton parameters we derived (§5.1.7). This means that the independent two analyses, our timing analysis and their multi-wavelength spectral fitting, revealed the

presence of the same soft Comptonization emission. As described in §5.3.4, the same interpretation applies to the soft excess components from the 5 AGNs in addition to Mrk 509.

In what kind of coronae are these Soft Primary signals produced? Their time variability is much lower than that of the Broad-Band Primary component, and occurs on time scales of several days to weeks which correspond to $\gtrsim 10^3\ R_{\rm S}$ in Mrk 509. Considering these spectral and variability characteristics, one possible location of the corona may be surface of the accretion disk. Although the temperature of a standard accretion disk in AGNs cannot theoretically reach such a high temperature as ~ 0.5 keV (§2.2.3), its surface might harbor a considerably hotter atmosphere when illuminated by the main hard X-ray emission (the two harder primaries) with a high luminosity of $\sim 10^{44}$ erg s^{-1}, or when heated by magnetic mechanism (§2.3.1). As described in §7.7, simultaneous X-ray and optical observations of selected objects could be useful to reveal the origin of the Soft Primary component.

7.5 The Hard Primary Component

7.5.1 Photon index vs. absorption

In Chapter 6, we succeeded in obtaining two variable hard X-ray continuum components with different properties; one is a weakly absorbed softer PL with faster variability, called the Broad-Band Primary component, and the other a more strongly absorbed harder PL with slower variations (Hard Primary; §7.1.2). To characterize them, we produce, in Fig. 7.9, a scatter plot between $N_{\rm H}$ and Γ of these components after Table 6.4, 6.6, and 6.10. There, we employed only $N_{\rm H}$ of the neutral absorption, while the ionized absorption was ignored. Because the absorption to the Hard Primary in the Faint branch of NGC 3227 was partial, each spectrum defines a pair of data points, with and without the absorption by $N_{\rm H} \sim 10^{23}$ cm^{-2} (connected by red lines). A vacancy seen at (Γ, $N_{\rm H}$)=($\gtrsim 2$, $\gtrsim 5 \times 10^{22}$ cm^{-2}) is considered due to the selection effect, because we chose type I AGNs with a total absorption of $N_{\rm H} \lesssim 10^{23}$ cm^{-2}.

In Fig. 7.9, the overall data points appear separated into two groups, a steeper-slope group and a flatter-slope one, separated by a gap at $\Gamma \sim 1.9$. The Hard Primary components all belong to the flatter-slope group. The Broad-Band Primaries mostly belong to the steeper-slope group, but with two exceptions, namely NGC 3516 in 2009 and NGC 5548 (all 7 data sets combined together). Thus, some caution is needed when we examine these two particular cases.

7.5.2 Estimation of Comptonization parameters

Let us interpret Fig. 7.9 in terms of thermal Comptonization (§2.3.1). The photon index of ~ 1.6 representing the flatter-slope group is consistent with those reported in the past studies (e.g., Tucker et al. 1973; Mushotzky 1974), and those of black hole binaries in the low/hard state (e.g., Remillard & Mcclintock 2006). In addition, it is relatively similar to theoretical predictions (e.g., Haardt et al. 1993, 1994), and presumably well explained as thermal Comptonization continua (§2.3.1). Utilizing eq. (2.7, 2.8), the Compton y-parameter can be estimated as ~ 1.4, and the optical depth becomes

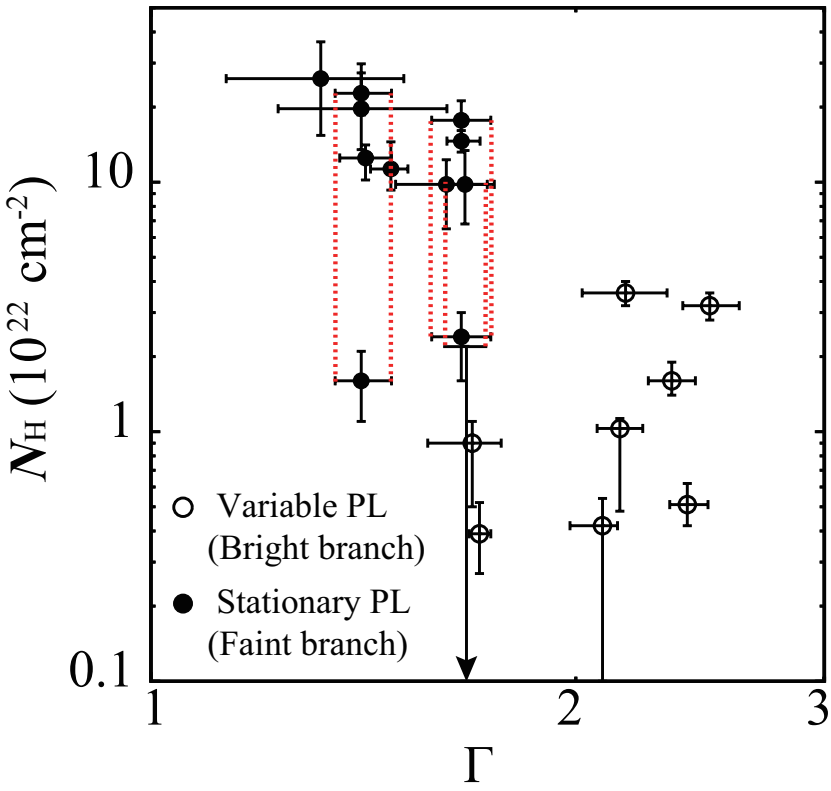

Figure 7.9: Column densities against photon indices of the variable (open circle) and stationary (filled circle) PL components, which have been identified with the Broad-Band and Hard Primaries, respectively, taken from Table 6.4, 6.6, and 6.10. The partially-absorbed Hard Primaries in the 2nd, 5th, and 6th observations of NGC 3227 are plotted twice; one is strongly absorbed, while the other weakly, which are connected together by red dotted lines.

0.8, when assuming an electron temperature of $kT_{\rm e} = 200$ keV.

The photon index of ~ 2.3, representing the steeper-slope group in Fig. 7.9, is slightly larger than the theoretically preferred value. Such a steeper PL continuum has often been observed in many highly accreting AGNs such as Narrow Line Seyfert I galaxies (e.g., Laor et al. 1994; Boller et al. 1996). The y-parameter is estimated as ~ 0.8, and the optical depth becomes 0.4, when we assume the same $kT_{\rm e} = 200$ keV as before.

As above, the flatter- and steeper-slope groups differ, interestingly, by a factor of ~ 2 in their Compton optical depth τ, assuming a common $kT_{\rm e}$. To examine whether this property depends on the assumed value of $kT_{\rm e}$, we produce Fig. 7.10 from eq. (2.7, 2.8), where the expected photon index Γ is displayed on a ($kT_{\rm e}$, τ) plane. With any value of $kT_{\rm e}$ between 10 and 1000 keV, the flatter-slope group is concluded to have about twice higher τ than the steeper-slope group.

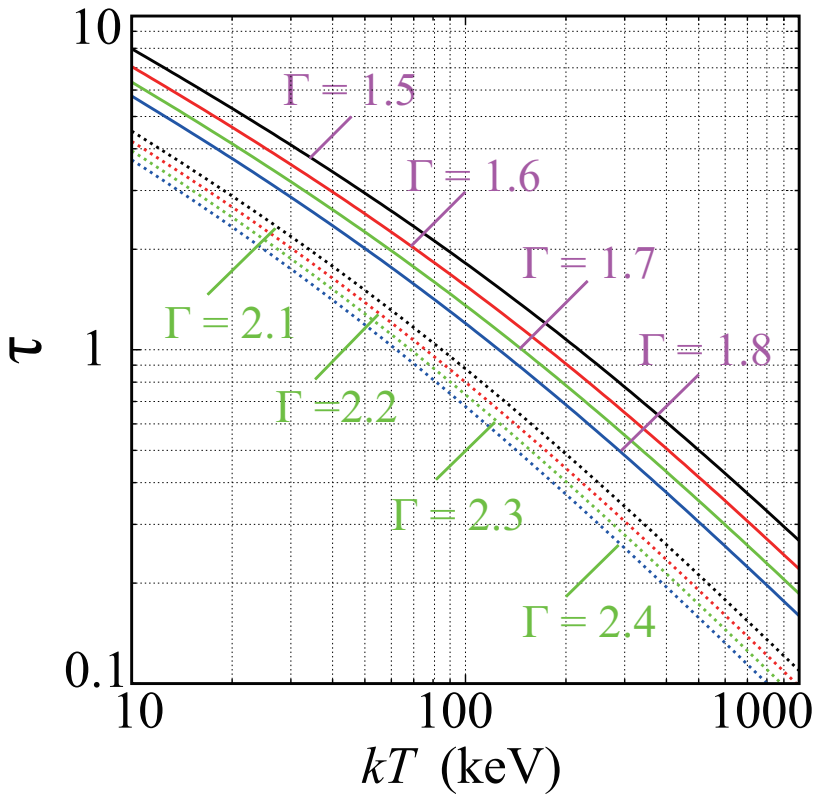

Figure 7.10: Equivalent photon index Γ of thermal Comptonization from eq. (2.7, 2.8). Loci of constant Γ are plotted on the plane of electron temperature kT_e vs. optical depth τ.

7.5.3 Dependence on the Eddington ratio

Apart from a few exceptions, the present AGNs generally host two hard X-ray continua, the variable and the stationary ones, which have been identified with Broad-Band and Hard Primary components, respectively. (Although this division is not completely identical to that of Fig. 7.9, we come back to this issue later in §7.5.4.) Then, which parameter determines the relative dominance of the two continua? Let us tentatively employ the Eddington ratio η as the parameter, because this is the most fundamental parameter that controls the accretion physics. For this purpose, Fig. 7.11 displays flux ratios of the Hard vs. Broad-Band Primaris, calculated in the 6–10 keV range, as a function of η. The 6–10 keV band was chosen because it is not affected by the absorption so strongly, and not much contributed by the distant reflection (Fig. 7.5). The value of η was estimated from eq. (2.1) and the black hole masses in §6.1, §6.2, and Table 6.8; the bolometric luminosities were calculated by multiplying the observed 3–10 keV fluxes by a common bolometric scaling factor of 10, and then scaling for the redshift. In Fig. 7.11, each AGN appears twice; the brightest and faintest observations among all, connected by a line. Because the intensity changes of an object among its multiple observations is mostly attributed to variations of the Broad-Band Primary (except for NGC 3516), with the Hard Primary component showing smaller or no changes, the connecting line always have a negative slope. Since NGC 3516 in 2009 and NGC 5548 exhibited no Hard Primary component (the stationary signals

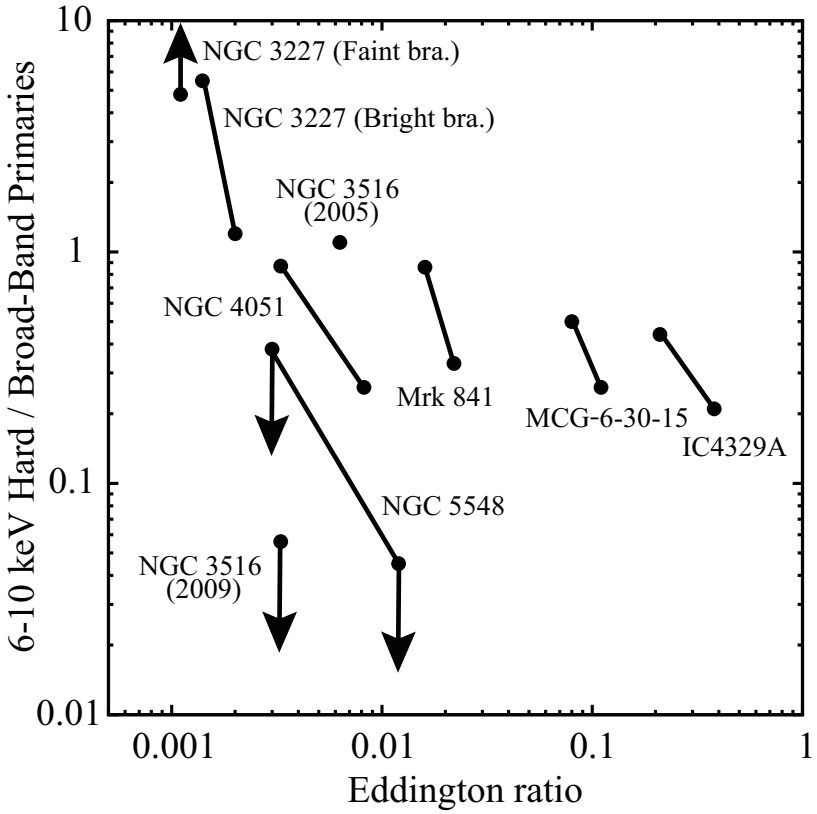

Figure 7.11: Ratios of the Hard and Broad-Band Primary components calculated in the 6–10 keV range, shown against the Eddington ratio calculated by multiplying the 3–10 keV flux by a bolometric scaling factor of 10. Except for NGC 3516 in 2009 and the Faint branch of NGC 3227, each AGN (branch) has two plots connected by a line, representing the brightest and faintest epochs among the present data sets.

are explained solely by the distant reflection), only upper limits are shown. In contrast, the Faint branch of NGC 3227 showed no Broad-Band Primary component, and it is expressed as a lower limit.

Figure 7.11 reveals a clear dependence of the Hard/Broad-Band Primary ratio on η. While this spectral ratio is approximately constant at 0.3–1 for $\eta \gtrsim 0.01$, it increases drastically as the object becomes less luminous. In other words, η can be indeed regarded as the controlling parameter. However, NGC 5548 and NGC 3516 are seen to violate this general trend. This issue is considered in the next subsection.

7.5.4 Re-classifying the two hard X-ray components

In Fig. 7.11, NGC 3516 in 2009 and NGC 5548 exceptionally deviate from the general spectral dependence on the Eddington ratio. This may be related to the fact that the dominant hard X-ray continua in these two cases, though obtained with the C3PO analysis as the variable PL components, are classified in Fig. 7.8 into the flatter-slope (to be identified with the Hard Primary) group. This suggests that we should employ the classification of Fig. 7.9, rather than the ways (either "variable"

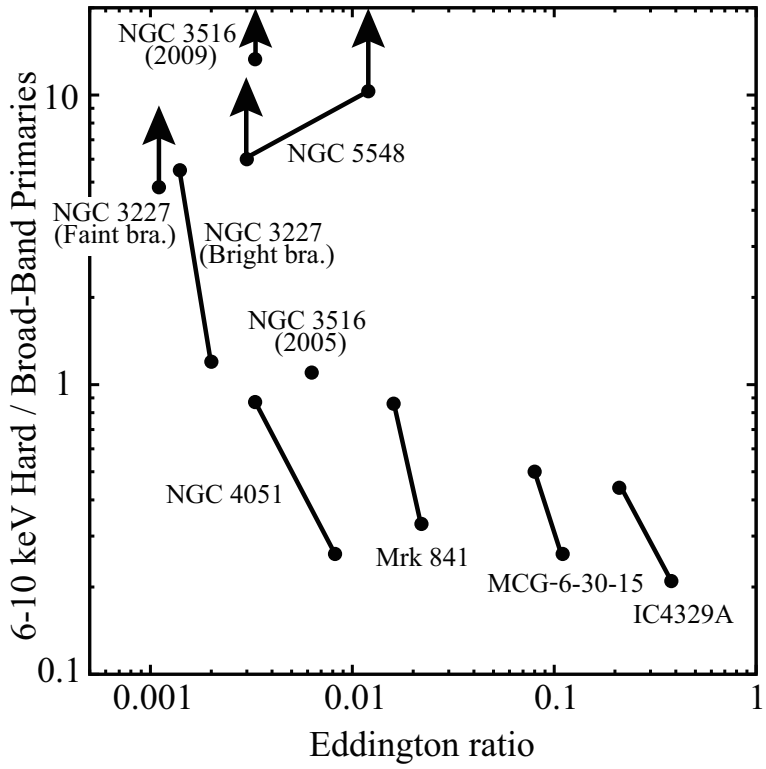

Figure 7.12: Same as Fig. 7.11, but the variable PL components of NGC 3516 in 2009 and NGC 5548, once considered in Fig. 7.12 as the Broad-Band Primary, are re-considered as the Hard Primaries.

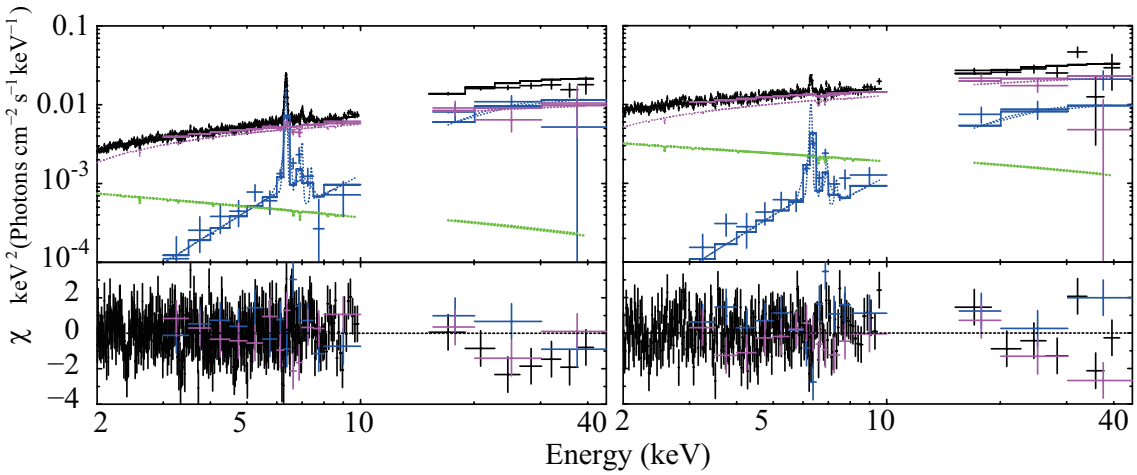

Figure 7.13: Same as Fig. 6.8(a) and Fig. 6.21 (d), but `model_v` is replaced by `model_v'' = Phabs * Ioabs * (PL1 + PL2)`, where `PL1` and `PL2` are the Hard Primary ($\Gamma \sim 1.7$; purple) and Broad-Band Primary ($\Gamma = 2.3$; green) components, respectively. The `PL2` intensity is set at its upper limit.

or "stationary" in the C3PO procedure) through which these components were identified.

With the above suggestion, we modified Fig. 7.11 into Fig. 7.12, by changing ordinate from the variable-PL vs stationary-PL ratio into those between the flatter-slope PL to the steeper-slope one, which we identify with the ratios of the Hard and Broad-Band Primaries. Obviously, data points other than NGC 3516 (in 2009) and NGC 5548 have remained unchanged, because the two classifications schemes are equivalent for them. Now, all the objects consistently follow a common dependence, and define a kind of state transition at $\eta \sim 0.01$.

In creating Fig. 7.12, we carried out some additional analysis shown in Fig 7.13. There, we refitted the same spectra of NGC 3516 (2009) and NGC 5548 as in Fig. 6.8(a) and Fig. 6.21(d), but including an additional softer PL (in green), representing Broad-Band Primary, with its slope fixed at 2.3. The obtained upper-limit normalizations for the additional softer PL were then converted to the lower limits shown in Fig. 7.13. Thus, the C3PO-derived variable spectra in these two exceptional cases were interpreted to consist of a stronger flatter-slope PL, and a weaker steeper-slope PL. Based on the above results, we consider that the variable $\Gamma \sim 1.7$ PL of NGC 3516 in 2009 (Fig. 6.8a) and NGC 5548 (Fig. 6.21d), though derived as the variable part of the data, should in reality be regarded as the Hard Primary components of the other AGNs, and of NGC 3516 itself in 2005. Actually, the light curves of NGC 3516 in 2009 (Fig. 6.1b) and NGC 5548 (Fig. 6.18d) lack rapid variations that are seen in NGC 3227, NGC 4051, and MCG–6-30-15.

7.6 A possible geometry of the AGN central engine

Let us qualitatively consider a possible geometry of the AGN central engine, which is suggested by the present work. The most important conditions are the following five.

1. The geometry must accommodate at least these PL-shaped primary components, i.e., the Broad-Band Primary, the Soft Primary, and the newly found Hard Primary.

2. The Hard Primary component is less variable on short timescales, and is more strongly absorbed, than the Broad-Band Primary component.

3. The Hard Primary component requires an optical depth which is about twice higher than the Broad-Band Primary one (Fig. 7.10), when the same $kT_{\rm e}$ (e.g., ~ 200 keV) is assumed.

4. When the accretion rate gets lower, the Hard Primary component relative to the Broad-Band Primary one increases.

5. The Soft Primary component representing the long-known soft excess phenomenon is yet another Comptonized emission with a relatively low $kT_{\rm e}$ and a high τ (§7.4), presumably near the accretion-disk surface.

A difficult part of this attempt is how to explain, in a natural way, the differences between the Hard Primary and Broad-Band Primary continua. The 3rd condition above may provide a clue,

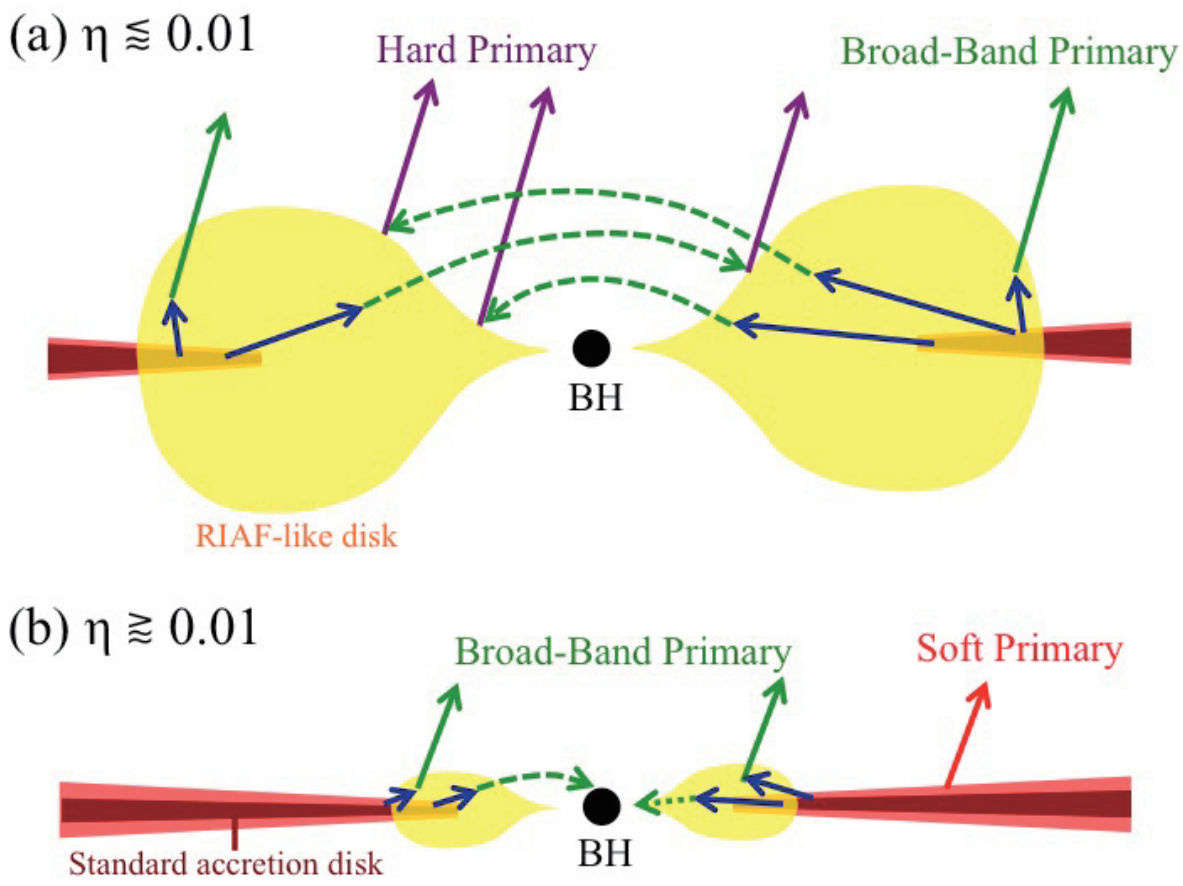

Figure 7.14: A geometry of the AGN central engine suggested by the present work in the case of (a) $\eta \lesssim 0.01$ and (b) $\eta \gtrsim 0.01$. Green, red, purple, and blue lines represent the Broad-Band Primary component, Soft Primary, Hard Primary, and the black body radiation from the accretion disk, respectively.

suggesting that the Hard Primary photons are generated after Compton scattered twice, while the Broad-Band Primary ones only once. If this condition is somehow realized, the slower variability of the Hard Primary PL (2nd condition) is automatically satisfied, because variations in the single-scattered photons would be smeared out in the second scattering. The 4th condition must be considered on the basis of the generally accepted view (§2.2.3) of geometrical changes of the accretion flow, from an standard disk to an optically-thin and geometrically-thick flow like the idea of RIAF (§2.2.3), which will take place as the accretion rate decreases. In short, the key point is how to improve the generally accepted disk-corona picture (§2.2.3), so that the distinction between the Broad-Band Primary (presumably single-scattered) continuum and the Hard Primary one (scattered twice) in physically natural and reasonable ways.

The above consideration leads us to propose a quantitative geometry of the AGN central engine as shown in Fig. 7.14. There, an optically-thick accretion disk (red) is considered to intrude partially into an inflated RIAF-like region, or corona (yellow), where electrons are expected to attain a high temperature (e.g., 200 keV) presumably through Coulomb collisions by ions which are much hotter

due to their larger mass. Soft photons from the disk will be Comptonized in the corona into hard X-ray signals, which are considered to take either of the following three paths. (Path 1) Escape from the corona and directly reach distant observers (located in various directions). (Path 2) Reach the other side of the corona, and again scattered therein. (Path 3) Swallowed into the BH due to the gravitational light bending. As the scattering point becomes closer to the central BH, the probability of Path 1 is expected to decrease, while that of Path 3 to increase. The Broad-Band Primary component is considered to be just these hard X-ray photons which emerged via Path 1, particularly those created at relatively outer coronal regions where the corona is cooler due to efficient cooling by the soft photons. On the other hand, Path 2, particularly in regions close to the BH, is considered to produce the Hard Primary component, because the second scattering will naturally double the Compton optical depth, and will smear out fast variations as the photons travel from the first scattering points to the second.

When $\eta < 0.01$, the corona will increase in both radial and vertical directions, as theoretically predicted by Fig. 2.8. Then, as illustrated in Fig. 7.14 (a), a mutual viewing factor between the nearer and farther sides of the corona will increase, and hence the Hard Primary component via Path 2 will be enhanced. When $\eta > 0.01$, the corona presumably diminishes in size (Fig. 2.8). Even through the Path (1) will remain relatively unaffected, a larger fraction of photons that are scattered in the corona into forward directions (towards smaller radii) will take Path 3 rather than Path 2. As a result, the Hard Primary component will diminish.

The above scenario can, at least qualitatively, explain the origin of the two hard X-ray continua and the $\dot{M}$-dependence of their relative strengths. Quantitative enhancement of the scenario may be achieved by, e.g., numerical simulations considering general relativity. However, we must here admit that a few issues still remain unaccounted. One is the Faint branch of NGC 3227, in which the Broad-Band Primary component disappeared while the Hard Primary component still persisted. This property cannot be readily explained by the present scenario, and requires its further refinement/modification.

Another problem is the relatively strong absorption seen in the Hard Primary. Except in MCG–6-30-15, the effect can be well explained by neutral absorption. Actually, if fitting hard PL components with a model of a power law absorbed by ionized matters, an upper limit of the ionization parameter is obtained as $\xi \lesssim 10^{1-2}$ erg s^{-1} cm, which is essentially consistent with being neutral. The absorber under consideration must affect the Hard Primary photons, but not those in the Broad-Band Primary continuum. Then, the only possible location of such an absorber is the conical opening region above (and below) the BH. Assuming a typical size of such a region as, e.g., 1×10^{-3} pc $= 3 \times 10^{15}$ cm $\sim 300\ R_{\rm S}$ (for a BH mass of $3 \times 10^7\ M_\odot$), the average absorber density to create a column density of $\sim 10^{23}$ cm^{-2} should be $n \sim 3 \times 10^7 f^{-1}$ cm^{-3}, where f is filling factor of the absorbing gas. Then, from eq. (2.9), such an absorber is estimated to have an ionization parameter $\xi \sim 300 f$ for an assumed luminosity of 10^{42} erg s^{-1}, and the observed constraints can be fulfilled if $f \lesssim 0.3$. Interestingly, these conditions of the absorber is similar to those of clouds in the the broad-line region (§2.1.4; Table 2.2). Therefore, the absorption of the Hard Primary continua may be related to the broad-line region.

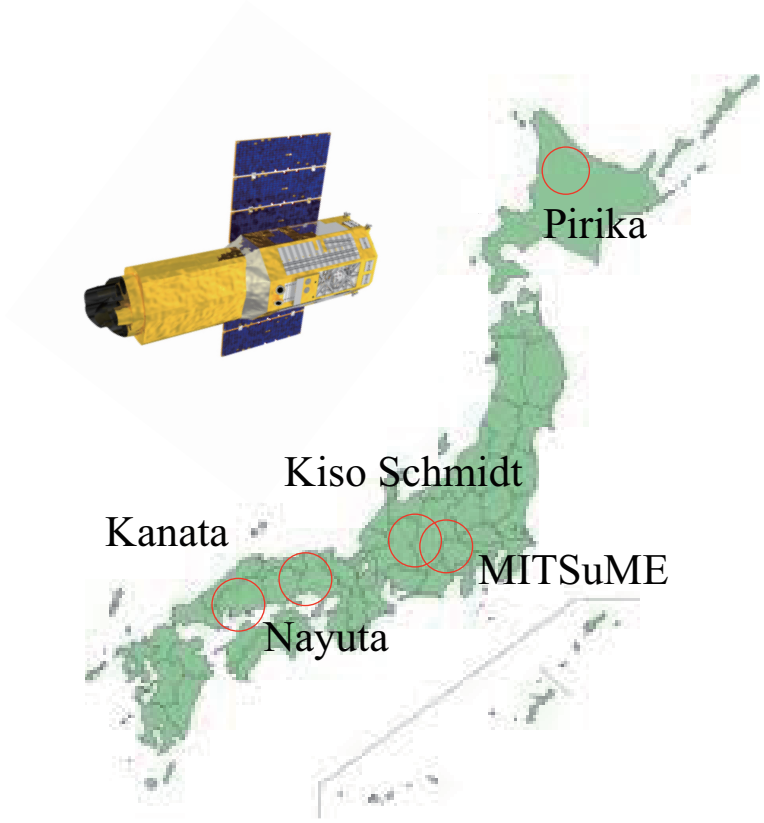

Figure 7.15: Positions of 5 medium-size the Japanese optical telescopes utilized in the 6 simultaneous observations of NGC 3516 with *Suzaku*.

However, the values of $N_{\rm H}$ and ξ of the absorption to the Hard Primary continuum are subject to considerable uncertainties, due to the problem of the C3PO method explained in §7.1.4, as well as the selection effect mentioned in §7.5. This difficulty in explaining the difference of absorption between the two primary components remains another unanswered problem in the present work.

7.7 Future Work

To strengthen our new spectral view (Fig. 7.4) and new geometry (Fg. 7.14) and to better understand the nature of the Hard Primary component, the following two ways are considered effective; one is multi-wavelength simultaneous observations in the X-ray and optical wavelengths, and the other is use of the next X-ray satellite *ASTRO-H* with unprecedented capability.

7.7.1 Simultaneous observations with *Suzaku* and optical telescopes

Although X-ray observations are powerful in studying the AGN central engine, two pieces of important information are missing. One is the condition of the optically-thick accretion disk, of which the emission does not reach the X-ray energies. The other is accurate measurements of the accretion rate, since X-ray emission from optically-thin accretion flows, as represented by the name of RIAF (§2.2.3), may not be proportional to the accretion rate, $\dot{M}$. These two shortcomings are compensated

simultaneously, by the information of optical continuum, which is considered to arise from the optically-thick accretion disk. This urges us to attempt simultaneous optical and X-ray observations of suitable AGNs.

For the above purpose, we have proposed 6 *Suzaku* observations of NGC 3516, all of which were successfully accepted for the AO-8 cycle. We have also succeeded in having these X-ray observations all simultaneously followed up by Japanese 5 optical telescopes shown in Fig. 7.15; from north to south, Pirika (Hokkaido), Kiso Schmidt (Nagano), MITSuME (Yamanashi), Nayuta (Hyogo), and Kanata (Hiroshima). Each *Suzkau* observation has a net exposure of ~ 50 ksec, and intervals between them are taken as 2 weeks, 1 month, 2 month, half a year, and a year. Thus, we can extract the variable and the stationary components by the C3PO method in each observation, and compare their individual intensity variations with those of optical signals, on various timescales from several weeks to 1 year.

In the past, a number of X-ray and optical simultaneous observations have been conducted. As a result, some AGNs such as NGC 3227 and NGC 5548 showed tight X-ray vs. optical correlations, while other AGNs such as NGC 4051 and MCG–6-30-15 did not (e.g., Suganuma et al. 2006; Uttley et al. 2006; Breedt 2009). In the light of the present studies, this may be because the Broad-Band Primary and Hard Primary components (and sometimes the Soft Primary component) were all mixed up together. In our studies, we can compare the intensity of each X-ray component with that of optical signals, and hopefully identify which X-ray component is best correlated with, or even following/leading the optical emission.

7.7.2 Studies with *ASTRO-H*

Being developed under an extensive international collaboration, the 6th Japanese X-ray astronomical satellite *ASTRO-H* will be launched in 2015, as a powerful successor to *Suzaku*. Major capabilities of *ASTRO-H* include the extremely high energy resolution ($\sim 0.1\%$ at 6 keV) realized by the Soft X-ray Spectrometer (SXS) placed at a focal plane of the Soft X-ray Telescope (SXT), and an extremely wide (0.3–600 keV) energy coverage with high sensitivity, jointly realized by the Soft X-ray Imager (SXI), the Hard X-ray Imager (HXI) at the focus of the Harf X-ray Telescope (HXT), and the Soft Gamma-ray Detector (SGD). As exemplified by a simulated 0.3–600 keV spectrum of Mrk 509 in Fig. 7.16, a combination of the SXI, the HXI, and the SGD will allow us to detect an AGN X-ray spectrum from ~ 0.3 keV to ~ 300 keV, to apply the C3PO decomposition to the entire energy range, and to measure the electron temperature (and hence the optical depth) of the coronae which have remained poorly constrained. Furthermore, utilizing the SXS, we can study absorption and emission lines in detail, and physical conditions of absorbers and reprocessors. This will also help us to study primary emission, by correctly eliminating the secondary components.

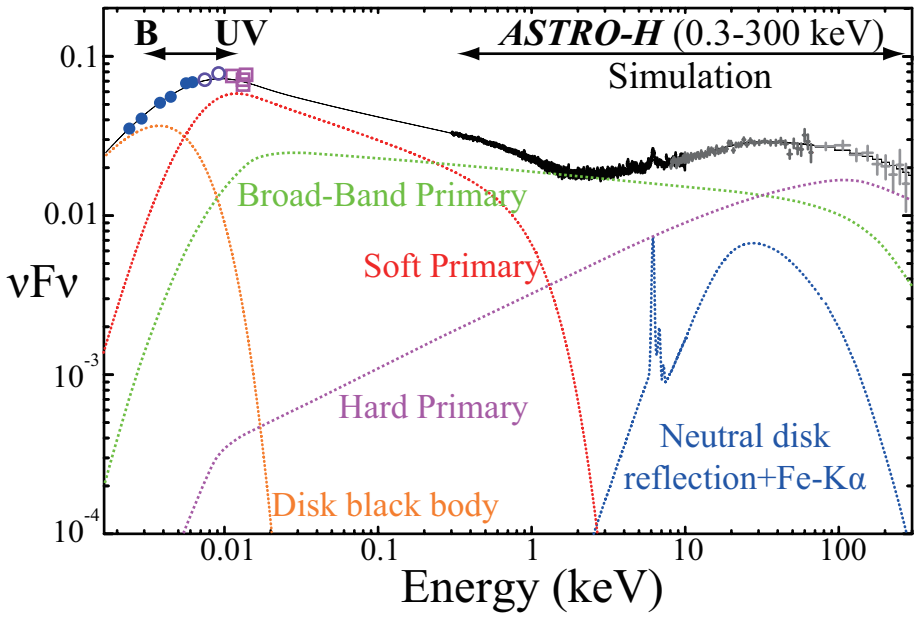

Figure 7.16: The same wide-band spectra of Mrk 509 as presented in Fig. 7.8, but with the *XMM-Newton* actual data replaced with simulations for *ASTRO-H* for an exposure of 100 ksec. The assumed spectral composition refers to Fig. 7.4. Green, red, purple, blue, and brown lines show models of the Broad-Band, Soft, Hard Primary component, neutral disk reflection accompanied by Fe-Kα emission line, and the black body radiation of the accretion disk, respectively.

Chapter 8

CONCLUSION

In the present thesis, we developed a variability-assisted spectral analysis method called C3PO, which allows us to model-independently decompose a time-averaged spectrum of an AGN into a variable and stationary components during an observation. With the method, we analyzed a dozen of *Suzaku* data sets of type I AGNs, focusing on separately their soft and hard X-ray bands, and obtained the following results.

1. The soft X-ray (0.5–3 keV) signals of the AGNs with relatively high luminosities of $\gtrsim 10^{44}$ erg s^{-1} are composed of a rapidly (on several hours) variable component with $\Gamma \sim 1.8$, and a slowly (on several days–weeks) varying soft component with a slope equivalent to $\Gamma \sim 4$. The former can be interpreted as a main broad-band Comptonization component, to be called the Broad-Band Primary component, which has been well recognized as the primary component in many AGN X-ray studies. The latter can be identified with the "soft excess" feature which has long been known in many AGNs, and was successfully interpreted also as a thermal Componization, to be called the Soft Primary component with an electron temperature of ~ 0.5 keV and an optical depth of 10–15. Thus, the mysterious soft-excess phenomenon has been understood as a part of the primary continuum.

2. The hard X-ray (3–45 keV) spectra of those AGNs that show the largest variations among the *Suzaku* data sets consists of; the same Broad-Band Primary component (with $\Gamma = 1.7$–2.2) as identified in 1, the stationary neutral disk reflection component accompanied by the narrow Fe-Kα line, and a slowly (on several days–weeks) variable hard PL-shaped ($\Gamma = 1.5$) continuum. While the first component is weakly absorbed with $N_{\rm H} \lesssim 10^{22}$ $\rm cm^{-2}$, the last one is strongly absorbed with $N_{\rm H} \sim 10^{23}$ $\rm cm^{-2}$, sometimes partially. Because the last component exhibits independent time variations from the first one, and has a significantly harder spectral shape without accompanied by Fe-K emission lines (but sometimes with the Fe-K edge feature), it can be interpreted as another independent primary component in the hard X-ray band, to be called the Hard Primary component.

3. The 0.5–45 keV spectra from the AGN central engine, which used to be regarded in the past

studies as a single primary component, have been found to consist of the multiple primary components with different spectral shapes and time variability. This means that the central engine of AGNs include several coronal regions with different physical parameters and distances from the central super massive black hole.

4. The primary X-ray emission from AGNs can no longer be approximated by a single PL (with a high-energy cutoff). Its spectrum becomes concave in the 0.5–10 keV band, and exhibits some hump in the 15–45 keV range which was previously attributed entirely to the secondary Compton hump. These results require a significant revision in the determination of the secondary features, including "broad" Fe-K lines and the reflector's solid angle.

5. On top of these primary continua, the reflection signal with clear Fe-K line and strong Fe-K edge is superposed as the only secondary component. The reflection, with neither strong ionization nor relativistic effects, is considered to be produced by (nearly-) neutral materials, at large ($\gtrsim 1000\ R_{\rm g}$) distances from the central black hole.

Appendix A

X-ray spectral models utilized in the present thesis

In the present thesis, we utilize X-ray spectral models in XSPEC12. The models and their references are summarized in Table A.1, with parameters, effective ranges of those models, and abbreviated names by which we replaced the model names in XSPEC12, for simplicity.

Table A.1: X-ray spectral components and spectral models for them in XSPEC12, utilized in the present thesis, with parameters, effective rages, and alternative names.

XSPEC12 model	Rename	Parameter (unit)	Effective range
Neutral photoelectric absorption with Wisconsin cross-sections (Morrison & McCammon 1983)			
`wabs`	`Phabs`	Equivalent hydrogen column density $N_{\rm H}$ (10^{22} cm^{-2})	0.001–10^6
Partial covering absorption by partially ionized material (Reeves et al. 2008)			
`zxipcf`	`Ioabs`	Equivalent hydrogen column density $N_{\rm H}$ (10^{22} cm^{-2})	0.1–500
		Ionization paramter $\log \xi$ (erg cm s^{-1})	$-$3–6
		Covering fraction C	0–1
		Redshift z	$-$0.999–10
Gaussian line profile used for Fe-Kα emission line			
`zgaussian`	`Fe-K`	Center energy in rest frame E (keV)	0–10^6
		Line width σ (keV)	0–10
		Redshift z	$-$0.999–10
		Normalization N (photons cm^{-2} s^{-1}.)	0–10^{24}
Power law with high energy exponential cutoff			
`cutoffpl`	`PL`	Photon index Γ	$-$3–10
		Cutoff energy $E_{\rm cut}$ (keV)	0.01–500
		Normarilation N (photons keV^{-1} cm^{-2} s^{-1} at 1 keV)	0–10^{24}
Multi-black body components of accretion disk (Mitsuda et al. 1984)			
`diskbb`	`Diskbb`	Temperature of inner edge $T_{\rm in}$ (keV)	0–1000
		Normalization $(((R_{\rm in}/{\rm km})/(D/10\ {\rm kpc}))^2 \cos\theta^*)$	0–10^{24}

Table A.1: (Continue) X-ray spectral components and spectral models for them in XSPEC12 utilized in the present thesis, with alternative names.

XSPEC12 model	Rename	Parameter (unit)	Effective range
Reflected power law at neutral medium (Magdziarz & Zdziarski 1995)			
`pexrav`	`Refl`	Photon index Γ	-10–10
		Cutoff energy $E_{\rm cut}$ (keV)	1–10^6
		Reflection fraction $f_{\rm ref}^{\dagger}$	-10^6–0
		Redshift z	-0.999–10
		Abundance of elements heavier than He A ($Z_\odot$)	0–10^6
		Abundance of iron $A_{\rm Fe}$ ($Z_{\rm Fe,\odot}$)	0–10^6
		cosine of inclination angle	0.05–0.95
		Normalization (photons keV^{-1} cm^{-2} s^{-1} at 1 keV)	0–10^{24}
Neutral Compton reflection with self-consistent Fe and Ni lines (Nandra et al. 2007)			
`pexmon`	`ReflFe`	Photon index Γ	-10–10
		Cutoff energy $E_{\rm cut}$ (keV)	1–10^6
		Reflection fraction $f_{\rm ref}^{\dagger}$	-10^6–0
		Redshift z	-0.999–10
		Abundance of elements heavier than He A ($Z_\odot$)	0–10^6
		Abundance of iron $A_{\rm Fe}$ ($Z_{\rm Fe,\odot}$)	0–10^6
		inclination angle (degree)	0–85
		Normalization (photons keV^{-1} cm^{-2} s^{-1} at 1 keV)	0–10^{24}
Reflection by a constant density illuminated atomosphere (Ross & Fabian 2005)			
`reflionx`	`Iorefl`	Abundance of iron $A_{\rm Fe}$ ($Z_{\rm Fe,\odot}$)	0.1–20
		Photon index Γ	1.4–3.3
		Ionization parameter ξ (erg cm s^{-1})	10–10000
		Redshift z	0–5
		Normalization	0–10^{24}
Relativistically-blurred refection by illuminated gases (Ross & Fabian 2005)			
`kdblur*reflionx`	`RBR`	Emissivity index q (scales as R^{-q})	-10–10
		Inner radius $R_{\rm in}$ ($R_{\rm g}$)	1.235–400
		Outer radius $R_{\rm out}$ ($R_{\rm g}$)	1.235–400
		Inclination i (degree)	0–90
		Abundance of iron $A_{\rm Fe}$ ($Z_{\rm Fe,\odot}$)	0.1–20
		Photon index Γ	1.4–3.3
		Ionization parameter ξ (erg cm s^{-1})	10–10000
		Redshift z	0–5
		Normalization	0–10^{24}
Thin-thermal plasma emission (Smith et al. 2001)			
`apec`	`TTP`	Plasma temperature kT (keV)	0.008–64
		Abundance A ($Z_\odot$)	0–5
		Redshift z	-0.999–10
		Normalizaiton $((10^{-17}/4\pi(D_{\rm A}(1+z))^2)\int n_{\rm e} n_{\rm H} dV$, where $D_{\rm A}$)	0–10^{24}‡

Table A.1: (Continue) X-ray spectral components and spectral models for them in XSPEC12 utilized in the present thesis, with alternative names.

XSPEC12 model	Rename	Parameter (unit)	Effective range
Thermal Comptonization (Titarchuk 1994)			
`comptt`	`Compton`	Redshift z	-0.999–10
		Input soft photon (Wine) temperature T_0 (keV)	0.01–100
		Electron temperature T_e (keV)	2–500
		Optical depth τ	0.01–200
		Geometry switch	0–5
		Normalization N_comp (photons keV^{-1} cm^{-2} s^{-1} at 1 keV)	0–10^{24}

* Parameters of R_in, D, and θ are "an apparent" inner radius of the disk, the distance to the source, and the angle of the disk ($\theta = 0$ is face-on), respectively.

† When an incident PL and reflection component are emitted simultaneously, the f_ref value of 1 gives a solid angle of reflectors against a primary emitter 2π.

‡ Parameters of D_A, n_e, and n_H show the angular diameter distance to the source (cm), the electron densities, and the H densities (cm^{-3}), respectively.

Appendix B

Figures and Tables Used in Chapter 5

B.1 Light curves

Figure B.1 shows 2–3 keV, 3–10 keV, and 15–45 keV light curves of the AGNs which passed the selection in §5.2. Although they commonly show $\sim 10\%$ peak-to-peak variations, the CCPs between the 3–10 keV and the 2–3 keV bands of these AGNs shown in Fig. 5.12 do not have a tight correlation with a significantly positive slope and offset (Table 5.7). Thus, in the present thesis, we did not apply the C3PO method to them.

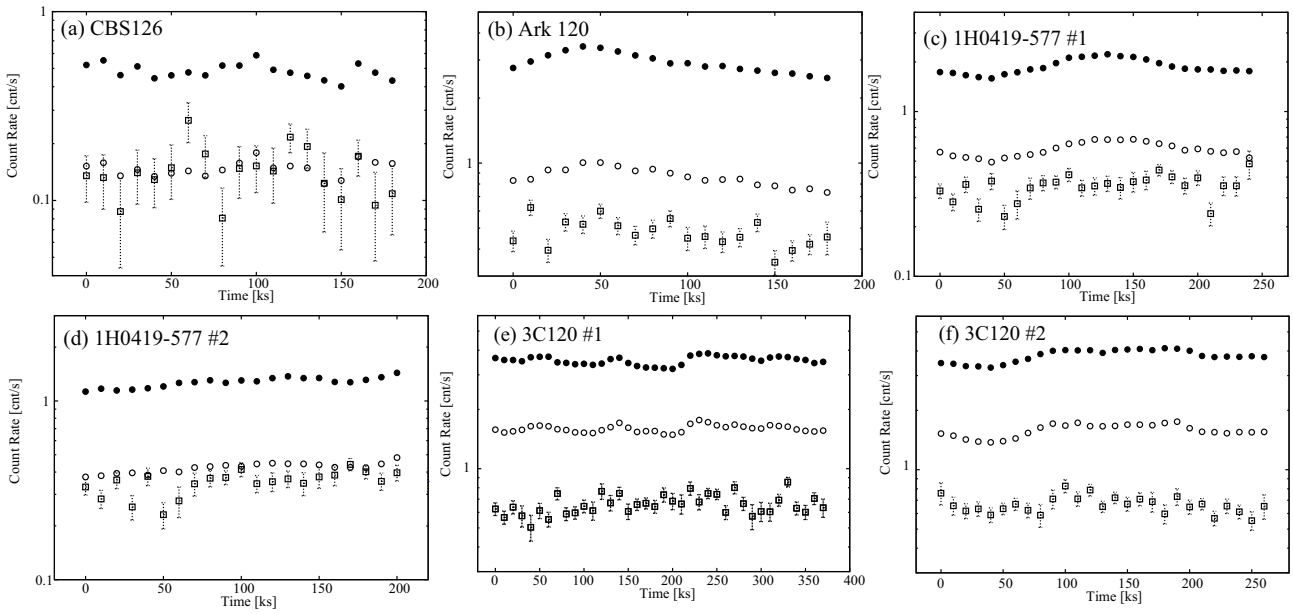

Figure B.1: Same as Fig.5.11, but of the AGNs which are not handled in §5.3.

B.2 Count-count plots

Figures A.2–A.6 show the 7 CCPs of each AGN (35 CCPs in total) which were utilized, in §5.3.2 and §5.3.3, to extract the variable and stationary components by the C3PO method in the soft X-ray bands of the selected 5 AGNs. Almost all of them show positive slopes and offsets as summarized in Table 5.8, and the C3PO-derived components obtained from them are shown in Fig. 5.14.

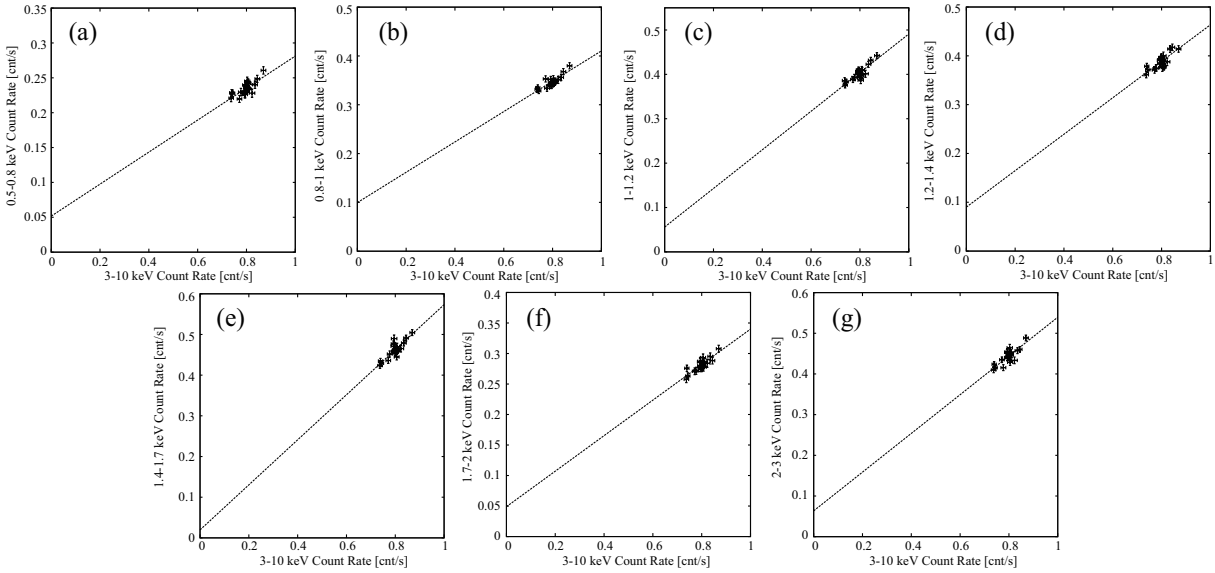

Figure B.2: The same as Fig. 5.5, but of Fairall 9 (Noda et al. 2013a).

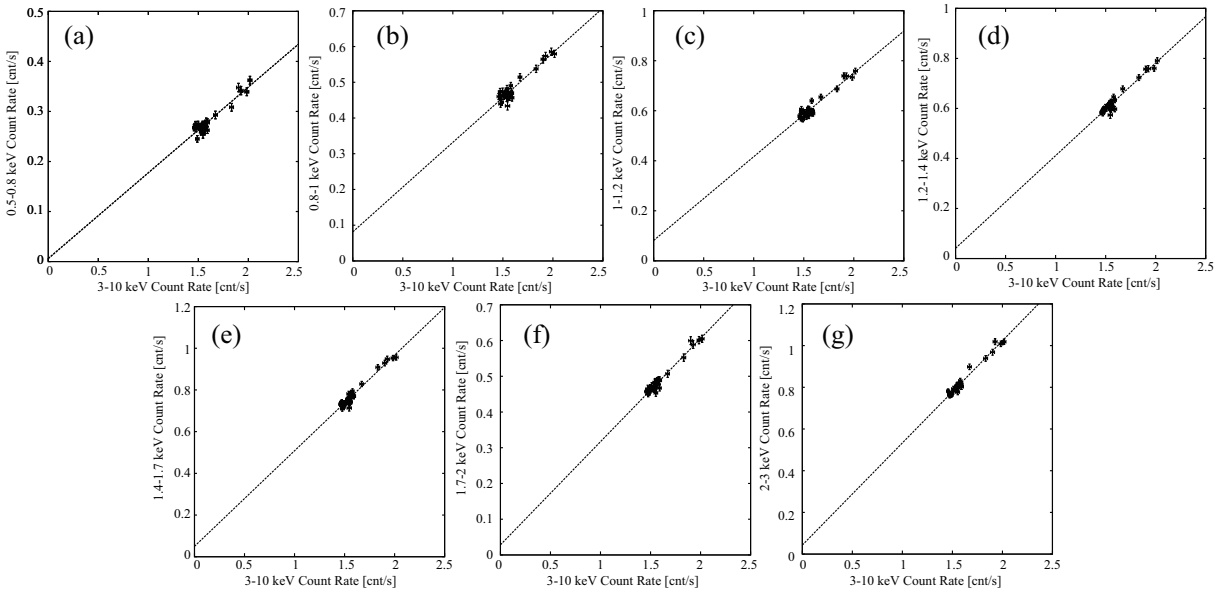

Figure B.3: The same as Fig. 5.5, but of MCG-2-58-22 (Noda et al. 2013a).

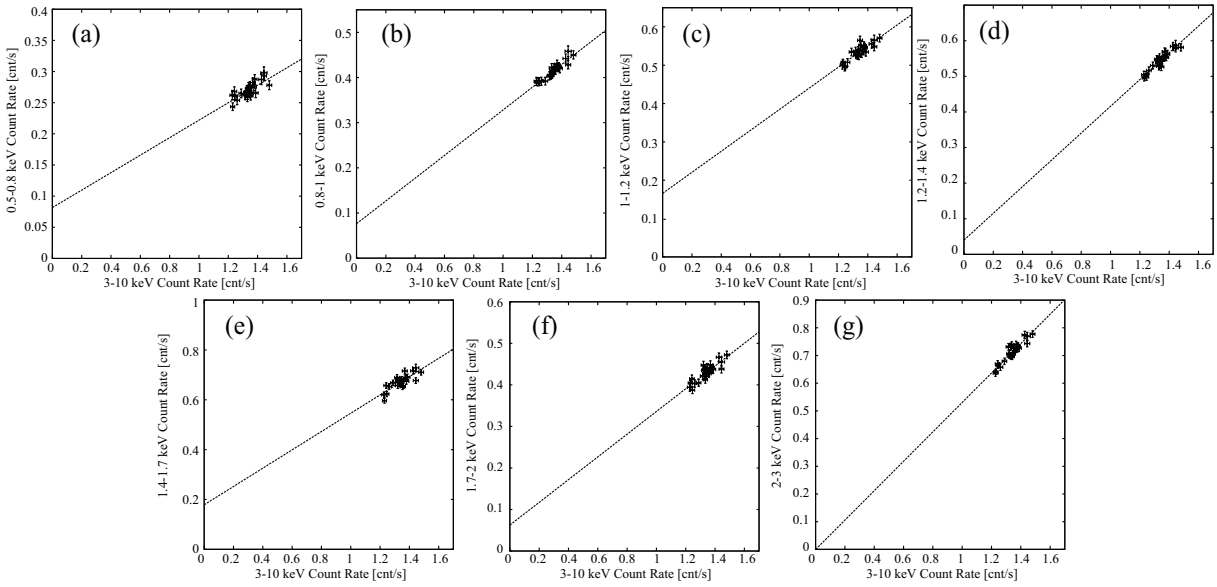

Figure B.4: The same as Fig. 5.5, but of 3C382 (Noda et al. 2013a).

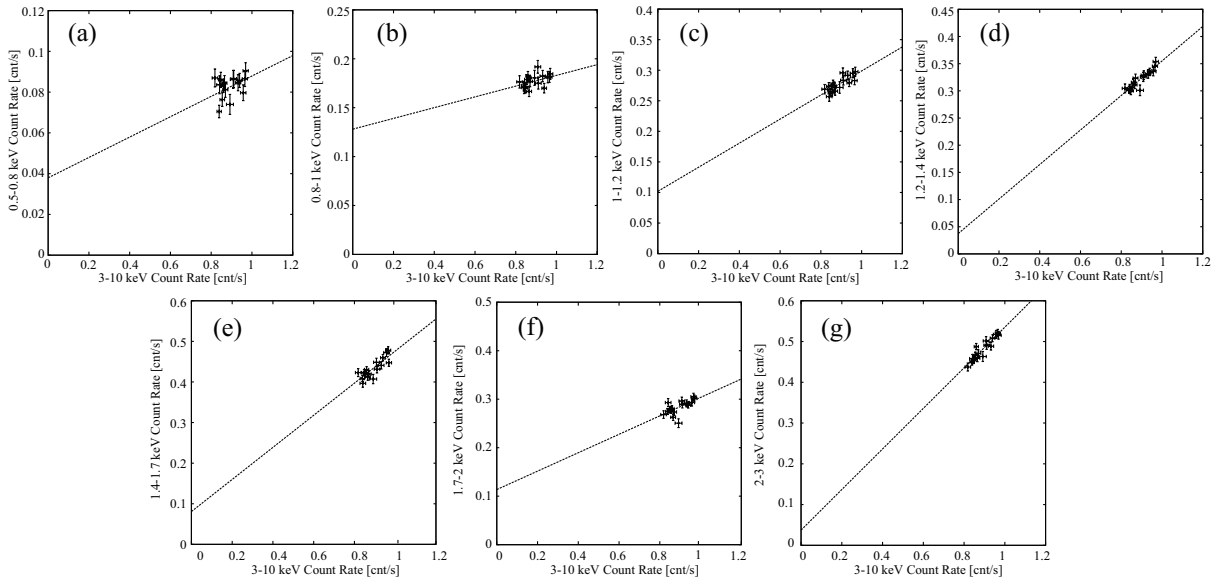

Figure B.5: The same as Fig. 5.5, but of 4C+74.26 (Noda et al. 2013a).

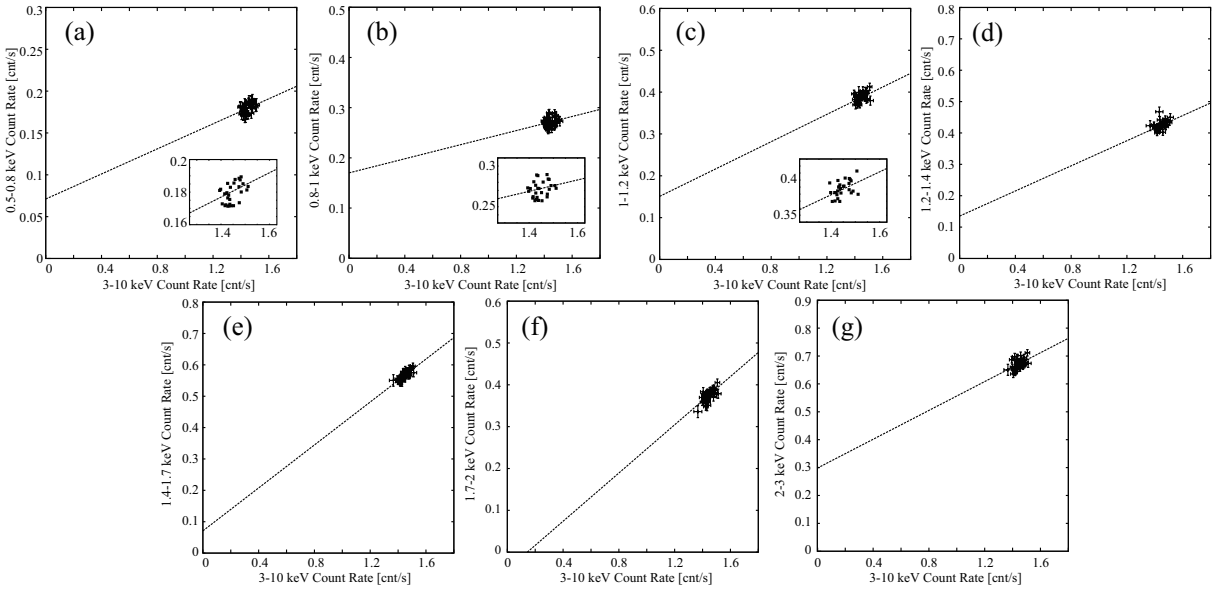

Figure B.6: The same as Fig. 5.5, but of MR2251-178 (Noda et al. 2013a).

B.3 Triplet spectral analysis in the soft X-ray band

In §5.3.4, we fitted spectral triplet in the soft X-ray bands of the 5 AGNs, with several different models including `TTP`, `BRB`, and `Compton` as the soft-excess model. Conditions of the fits are summarized in §5.3.4. As shown in Fig. A.7–A.8 and Table A.1–A.2, some results with the `TTP` and `RBR` model were unsuccessful, while those with `Comtpon` shown in Fig. 5.15 and Table 5.11 were all successful.

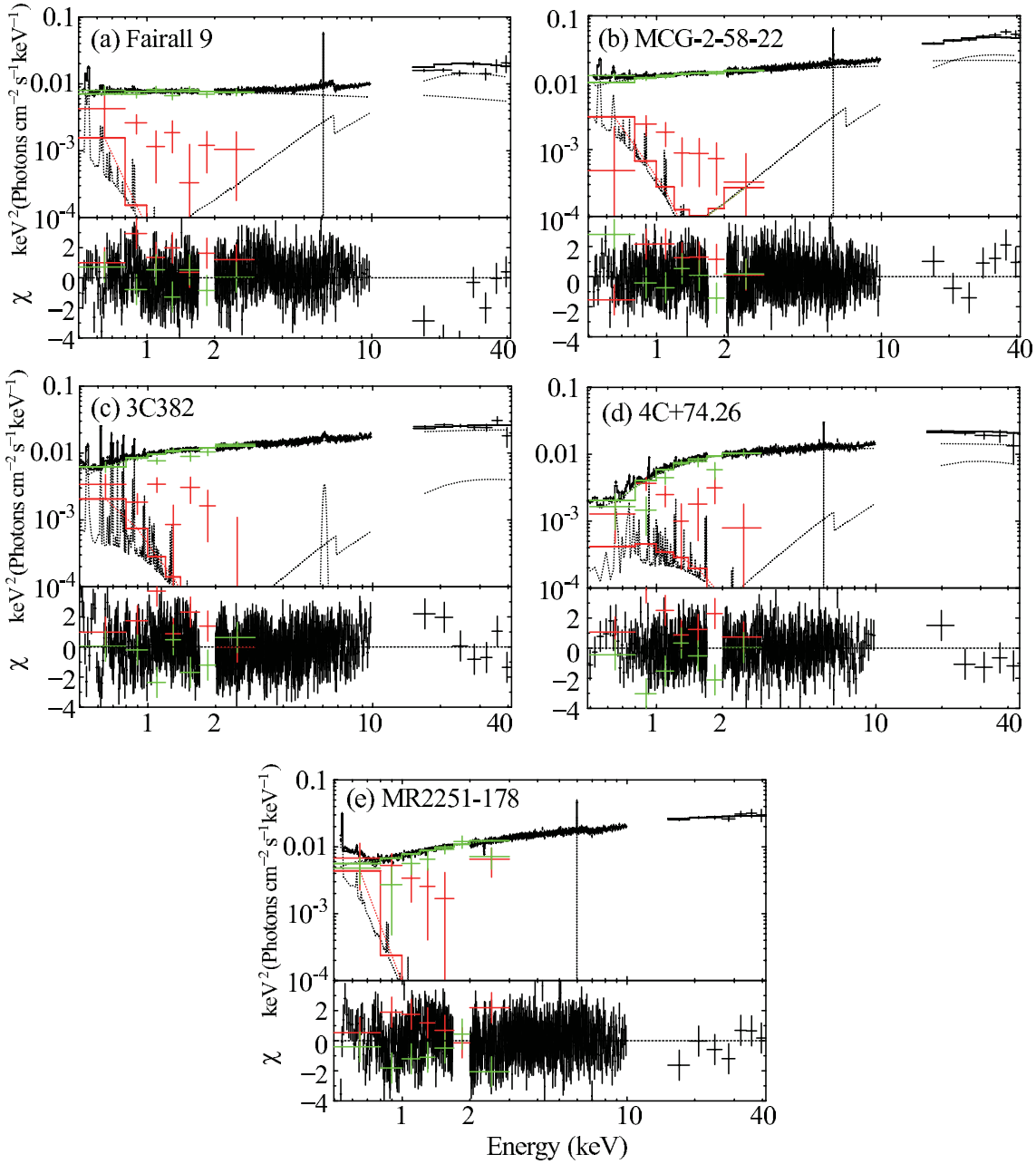

Figure B.7: Fits to the time-averaged spectra of the six AGN, with a model of `Phabs * Ioabs * (PL + Refl + Fe-K + TTP)` (Noda et al. 2013a).

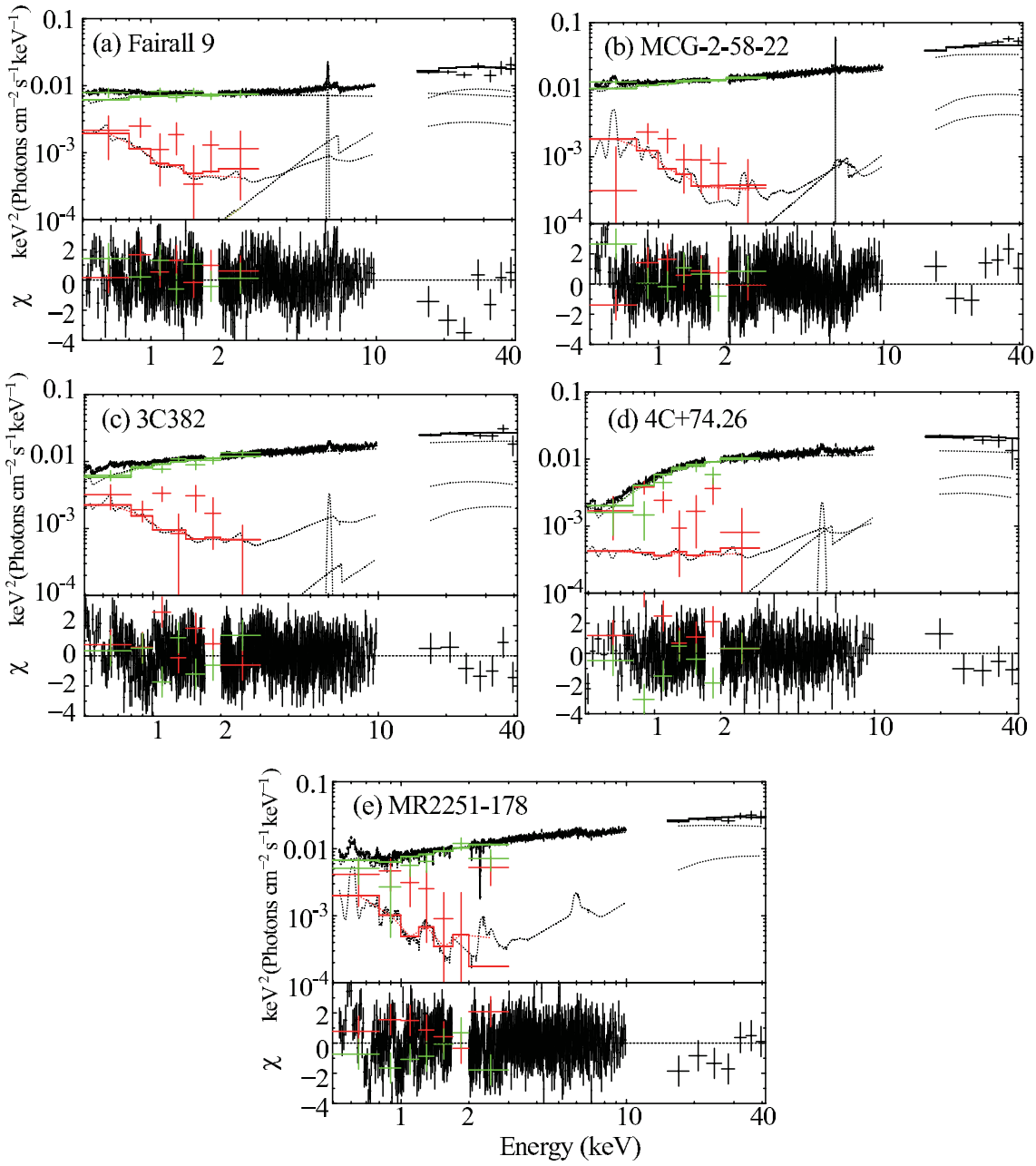

Figure B.8: Same as Fig. B.7, with the `apec` component replaced by a `kdblur * reflionx` model. The fitted model is `Phabs * Ioabs * (PL + Refl + Fe-K + RBR)` (Noda et al. 2013a).

Table B.1: Same as Table 5.4 left, but obtained in the fits to the 5 AGNs.

Model	Parameter	Fairall 9	MCG-2-58-22	3C382	4C+74.26	MR2251-175
`Phabs`	$N_{\rm H}^{*}$	0.032(fix)	0.035(fix)	0.074(fix)	$0.21^{+0.03}_{-0.01}$	0.028(fix)
`Ioabs`	$N_{\rm H}^{*}$	–	$7.27^{+5.52}_{-4.41}$	$0.07^{+0.19}_{-0.02}$	$1.36^{+0.28}_{-0.05}$	1.07 ± 0.02
	logξ	–	$4.35^{+1.63}_{-0.57}$	$2.55^{+0.53}_{-0.16}$	$0.53^{+0.11}_{-0.09}$	$0.40^{+0.01}_{-0.03}$
	Cvr frac.	–	$0.58^{+0.12}_{-0.38}$	> 0.62	$0.61^{+0.04}_{-0.05}$	$0.86^{+0.01}_{-0.02}$
PL	Γ	$1.99^{+0.02}_{-0.03}$	1.85 ± 0.01	1.82 ± 0.01	$1.92^{+0.08}_{-0.08}$	1.72 ± 0.01
	$N_{\rm PL}^{\dagger}$	0.78 ± 0.01	$1.34^{+0.02}_{-0.01}$	1.11 ± 0.01	$1.10^{+0.06}_{-0.08}$	$1.15^{+0.06}_{-0.01}$
`Refl`	$f_{\rm ref}$	$1.9^{+0.4}_{-0.3}$	1.8 ± 0.1	$0.5^{+0.1}_{-0.2}$	$0.9^{+0.4}_{-0.5}$	< 0.2
`Fe-K`α	$E_{\rm c}^{\ddagger}$	6.37 ± 0.02	6.25 ± 0.02	6.41 ± 0.03	6.40 ± 0.04	$6.38^{+0.04}_{-0.03}$
	σ (keV)	10^{-4}(fix)	10^{-4}(fix)	0.099 ± 0.032	10^{-4}(fix)	10^{-4}(fix)
	$N_{\rm Fe}^{\S}$	$2.30^{+0.21}_{-0.22}$	1.84 ± 0.32	$2.25^{+0.44}_{-0.43}$	$1.42^{+0.35}_{-0.34}$	$1.15^{+0.30}_{-0.29}$
	EW (eV)	77^{+40}_{-62}	33^{+54}_{-32}	49^{+27}_{-15}	30^{+32}_{-12}	21^{+8}_{-6}
`TTP`	kT (keV)	$0.32^{+0.02}_{-0.04}$	$0.18^{+0.02}_{-0.03}$	$0.25^{+0.03}_{-0.04}$	$0.68^{+0.08}_{-0.07}$	0.31 ± 0.01
	A ($Z_{\odot}$)	< 0.005	< 0.007	< 0.004	< 0.005	0.002 ± 0.001
	$N_{\rm apec}^{\#}$	$0.52^{+0.15}_{-0.12}$	$1.41^{+0.64}_{-0.42}$	$1.09^{+0.45}_{-0.24}$	$0.73^{+0.09}_{-0.12}$	$8.06^{+1.47}_{-0.87}$
χ^2/d.o.f.		728.62/651	846.70/832	883.80/842	612.45/601	983.20/865

* Equivalent hydrogen column density in 10^{22} cm^{-2} for the Galactic or the intrinsic line-of-sight absorption.

† The power-law normalization at 1 keV, in units of 10^{-2} photons keV^{-1} cm^{-2} s^{-1} at 1 keV.

‡ Center energy in keV in the rest frame.

§ The Gaussian normalization in units of 10^{-5} photons cm^{-2} s^{-1}.

|| Center energy in units of keV.

The `apec` normalization, in units of $(10^{-15}/4\pi(D_{\rm A}(1+z))^2) \int n_{\rm e} n_{\rm H} dV$, where $D_{\rm A}$ is the angular size distance to the source (cm), $n_{\rm e}$ and $n_{\rm H}$ are the electron and H densities (cm^{-3}).

Table B.2: Same as Table 5.4 right, but obtained in the fits to the 5 AGNs.

Model	Parameter	Fairall 9	MCG-2-58-22	3C382	4C+74.26	MR2251-175
`Phabs`	$N_{\rm H}$	0.032(fix)	0.035(fix)	0.074(fix)	$0.26^{+0.03}_{-0.02}$	0.028(fix)
`Ioabs`	$N_{\rm H}$	–	< 0.36	< 0.12	$0.24^{+1.11}_{-0.07}$	3.15 ± 0.02
	logξ	–	$0.73^{+0.32}_{-0.24}$	2.52 ± 0.16	$2.26^{+0.16}_{-0.13}$	$2.16^{+0.66}_{-0.58}$
	Cvr frac.	–	< 0.25	> 0.43	> 0.21	$0.65^{+0.09}_{-0.15}$
PL	Γ	1.99 ± 0.03	$1.84^{+0.02}_{-0.01}$	1.82 ± 0.02	$1.92^{+0.06}_{-0.04}$	$1.83^{+0.01}_{-0.02}$
	$N_{\rm PL}$	0.74 ± 0.01	1.22 ± 0.02	$1.04^{+0.01}_{-0.02}$	$0.99^{+0.08}_{-0.06}$	$1.23^{+0.04}_{-0.02}$
`Refl`	$f_{\rm ref}$	0.8 ± 0.3	< 0.3	< 0.2	< 0.5	< 0.2
`Fe-K`	$E_{\rm c}$	$6.38^{+0.04}_{-0.03}$	6.39 ± 0.03	$6.42^{+0.03}_{-0.04}$	6.39 ± 0.04	$6.40^{+0.04}_{-0.03}$
	σ (keV)	10^{-4}(fix)	10^{-4}(fix)	$0.095^{+0.025}_{-0.029}$	10^{-4}(fix)	10^{-4}(fix)
	$N_{\rm Fe}$	$2.45^{+0.25}_{-0.20}$	$2.01^{+0.21}_{-0.28}$	$2.25^{+0.44}_{-0.43}$	$1.46^{+0.31}_{-0.38}$	0.91 ± 0.25
	EW (eV)	91^{+40}_{-62}	33^{+44}_{-31}	52^{+27}_{-15}	37^{+32}_{-12}	25^{+12}_{-10}
`RBR`	q^{*}	$4.48^{+2.70}_{-0.98}$	$5.15^{+4.19}_{-0.81}$	$4.87^{+3.11}_{-0.68}$	$3.96^{+0.89}_{-1.35}$	$2.45^{+2.31}_{-0.27}$
	$R_{\rm in}$ ($R_{\rm g}$)	$2.30^{+0.49}_{-0.16}$	$1.24^{+0.35}_{-0.0}$	$2.44^{+0.56}_{-0.22}$	$1.24^{+0.31}_{-0.0}$	$1.24^{+0.27}_{-0.0}$
	$\xi^{\dagger}$	$58.9^{+27.2}_{-31.2}$	$101.8^{+53.2}_{-48.4}$	$103.5^{+56.6}_{-50.8}$	$94.1^{+42.9}_{-34.8}$	$20.2^{+12.1}_{-5.2}$
	$N_{\rm reflionx}^{\ddagger}$	$3.11^{+0.34}_{-0.12}$	$4.97^{+0.64}_{-0.42}$	$2.39^{+0.45}_{-0.24}$	$2.44^{+0.30}_{-0.12}$	$1.28^{+0.23}_{-0.09}$
χ^2/d.o.f.		785.06/651	945.79/832	886.26/842	660.51/601	1145.17/865

Appendix C

Figures and Tables Used in Chapter 6

C.1 CCPs for the hard band C3PO applications

Figure B.1–B.5 show 6 of the 16 CCPs of each selected AGN in §6.3, and Table B.1–B.3 show parameters obtained by the fits to the 16 CCPs with eq. (5.1) in each AGN. In the C3PO analysis in §6.4, the slopes and the offsets in Table B.1–3 are utilized to extract the variable and stationary components, respectively, in each AGN. Because these AGNs are brighter than NGC 3516, we included 3% systematic errors into the 3–10 keV band in the CCP fits for the same reason as in §5.1.3 and §6.1.3.

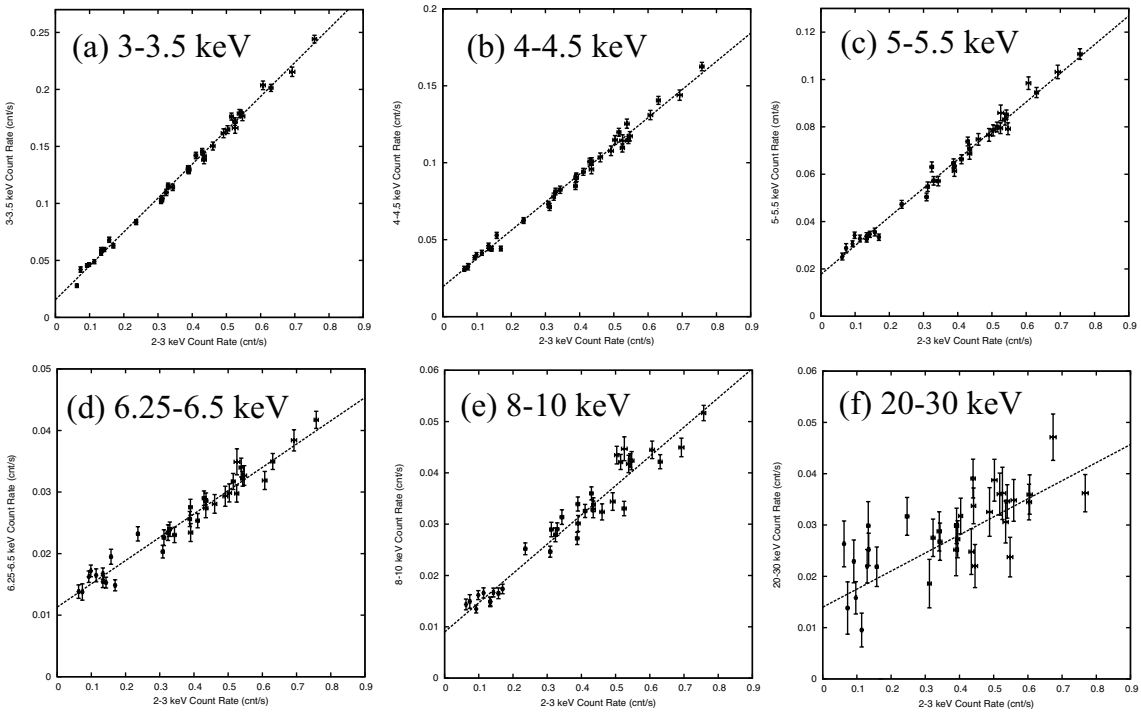

Figure C.1: The same as Fig.6.5, but of NGC 4051.

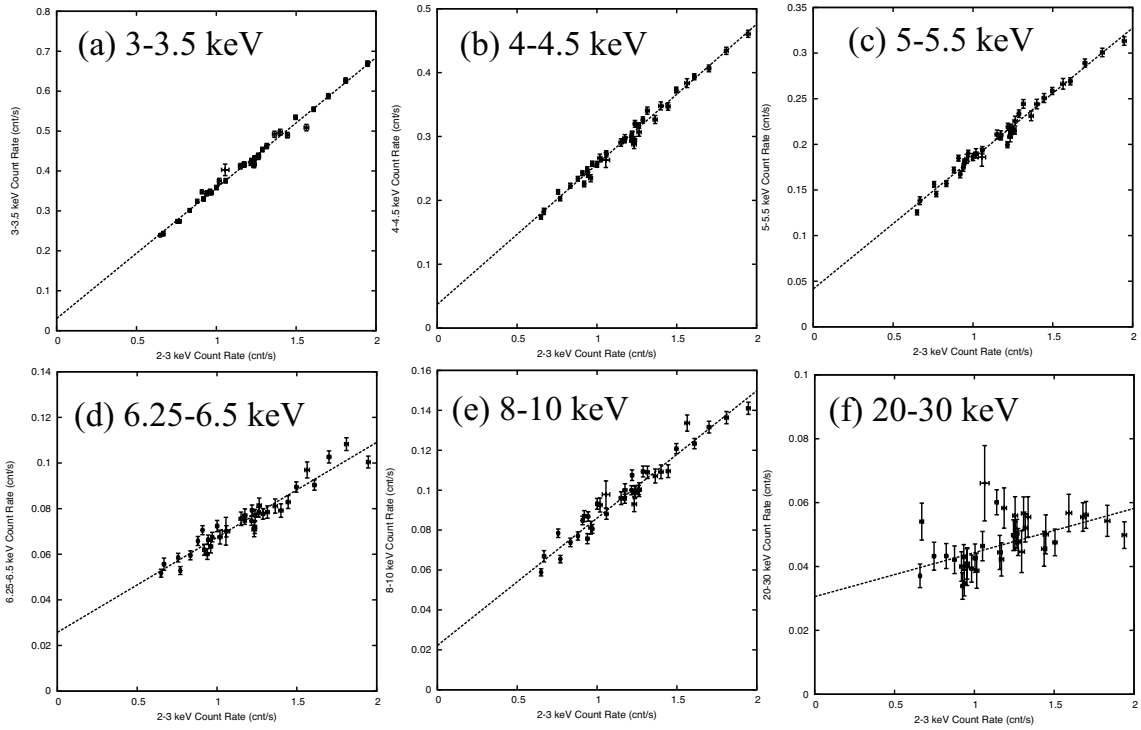

Figure C.2: The same as Fig.6.5, but of MCG–6-30-15.

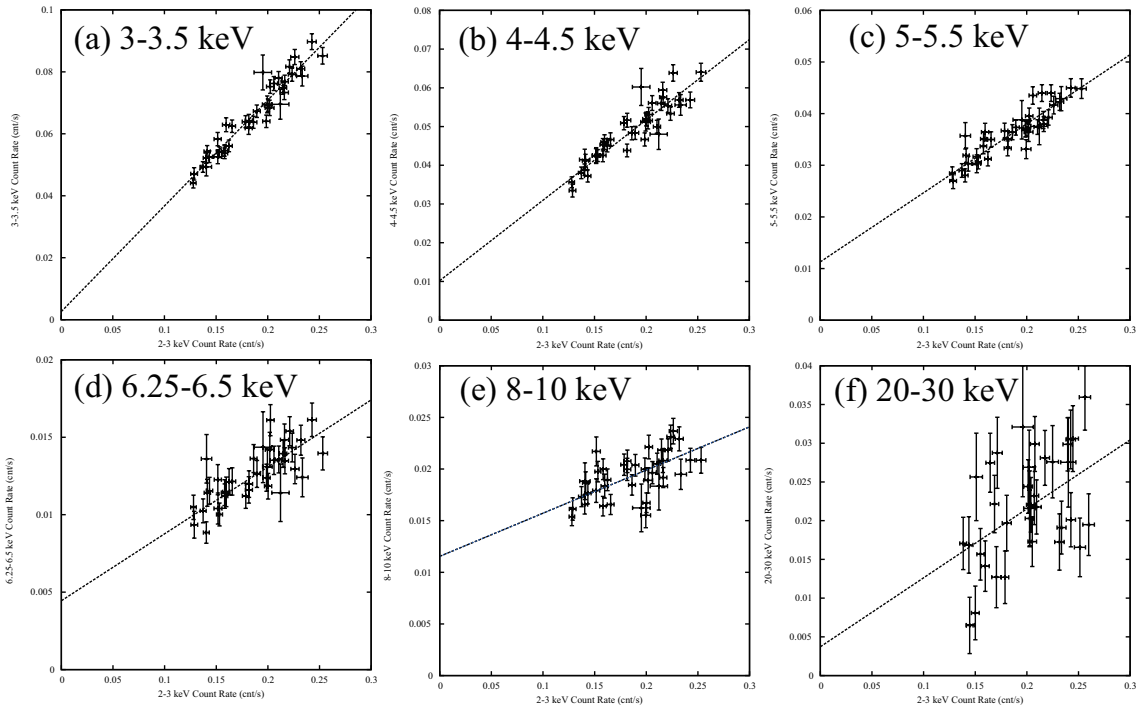

Figure C.3: The same as Fig.6.5, but of Mrk 841.

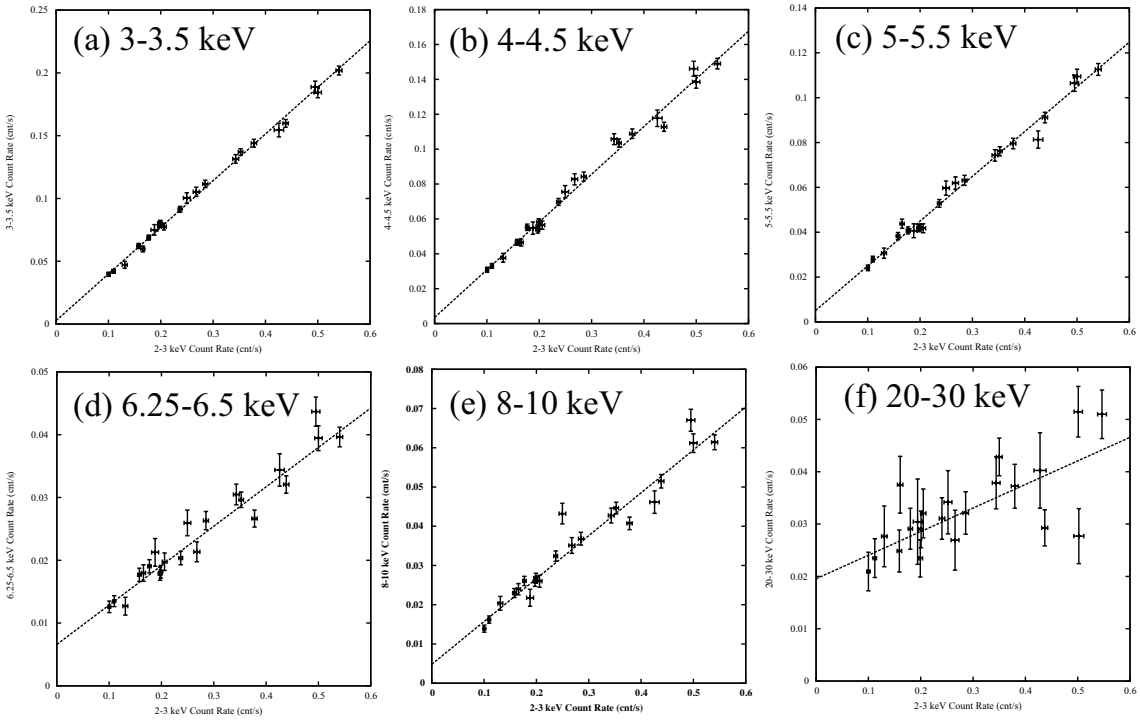

Figure C.4: The same as Fig.6.5, but of NGC 5548.

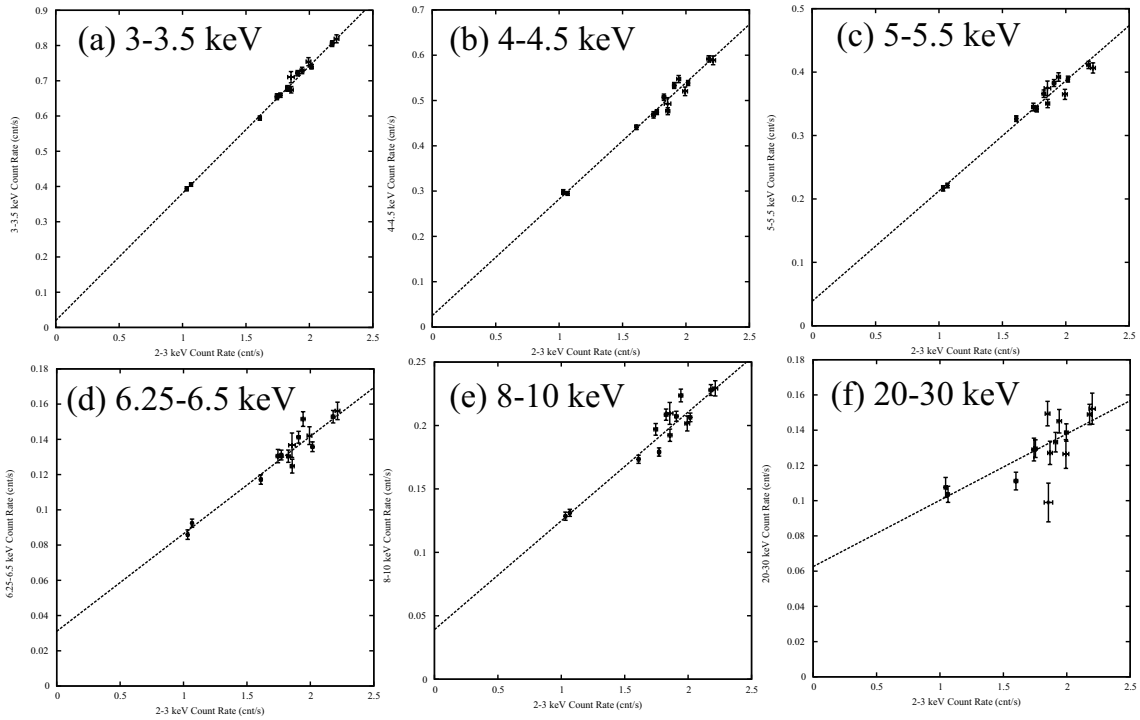

Figure C.5: The same as Fig.6.5, but of IC4329A.

Table C.1: Parameters obtained by fitting to 16 CCPs of NGC 4051*.

	NGC 4051		
Range (keV)	Slopes	Offsets$\times 10^2$	χ^2/d.o.f.
3–3.5	0.30 ± 0.01	1.55 ± 0.11	34.9/34
3.5–4	0.23 ± 0.01	1.86 ± 0.09	30.8/34
4–4.5	0.18 ± 0.01	1.98 ± 0.09	33.9/34
4.5–5	0.15 ± 0.01	1.91 ± 0.10	57.6/34
5–5.5	0.12 ± 0.01	1.79 ± 0.08	39.6/34
5.5–6	0.09 ± 0.01	1.67 ± 0.07	38.8/34
6–6.25	0.04 ± 0.01	0.76 ± 0.04	36.5/34
6.25–6.5	0.04 ± 0.01	1.13 ± 0.05	45.1/34
6.5–6.75	0.03 ± 0.01	0.63 ± 0.04	60.3/34
6.75–7	0.03 ± 0.01	0.49 ± 0.03	33.5/34
7–7.5	0.04 ± 0.01	0.70 ± 0.05	61.9/34
7.5–8	0.03 ± 0.01	0.53 ± 0.03	41.5/34
8–10	0.06 ± 0.01	0.90 ± 0.07	79.1/34
15–20	0.04 ± 0.01	2.21 ± 0.22	61.0/34
20–30	0.03 ± 0.01	1.70 ± 0.19	56.4/34
30–45	0.01 ± 0.00	0.47 ± 0.12	40.3/34

* Systematic errors of 3% are included.

Table C.2: Parameters obtained by fitting to the 16 CCPs of MCG–6-30-15 and Mrk 841*.

	MCG–6-30-15			Mrk 841		
Range (keV)	Slopes	Offsets$\times 10^2$	χ^2/d.o.f.	Slopes	Offsets$\times 10^2$	χ^2/d.o.f.
3–3.5	0.33 ± 0.01	3.08 ± 0.59	17.4/35	0.34 ± 0.01	0.29 ± 0.25	32.6/37
3.5–4	0.26 ± 0.01	4.14 ± 0.54	19.7/35	0.25 ± 0.01	1.02 ± 0.22	32.9/37
4–4.5	0.22 ± 0.01	3.65 ± 0.48	20.8/35	0.21 ± 0.01	1.01 ± 0.23	44.7/37
4.5–5	0.17 ± 0.01	4.32 ± 0.54	36.1/35	0.18 ± 0.01	0.82 ± 0.18	32.1/37
5–5.5	0.14 ± 0.01	4.04 ± 0.42	29.1/35	0.13 ± 0.01	1.14 ± 0.17	39.2/37
5.5–6	0.11 ± 0.01	4.29 ± 0.39	34.0/35	0.13 ± 0.01	0.71 ± 0.16	40.4/37
6–6.25	0.05 ± 0.01	1.97 ± 0.28	57.6/35	0.05 ± 0.01	0.78 ± 0.12	46.8/37
6.25–6.5	0.04 ± 0.01	2.56 ± 0.22	38.4/35	0.04 ± 0.01	0.44 ± 0.09	39.5/37
6.5–6.75	0.04 ± 0.01	1.40 ± 0.21	52.6/35	0.02 ± 0.01	0.63 ± 0.08	33.2/37
6.75–7	0.03 ± 0.01	1.14 ± 0.16	37.6/35	0.03 ± 0.01	0.40 ± 0.09	49.6/37
7–7.5	0.05 ± 0.01	1.12 ± 0.24	49.8/35	0.05 ± 0.01	0.45 ± 0.11	57.7/34
7.5–8	0.04 ± 0.01	0.84 ± 0.15	33.2/35	0.03 ± 0.01	0.35 ± 0.07	38.4/37
8–10	0.07 ± 0.01	2.18 ± 0.29	48.6/35	0.04 ± 0.01	1.16 ± 0.15	65.8/37
15–20	0.02 ± 0.01	3.88 ± 0.46	58.3/35	0.07 ± 0.03	1.47 ± 0.55	64.0/37
20–30	0.01 ± 0.00	3.01 ± 0.35	41.3/35	0.09 ± 0.03	0.32 ± 0.49	60.7/37
30–45	0.00 ± 0.00	0.88 ± 0.24	46.5/35	0.03 ± 0.01	0.11 ± 0.44	37.3/37

* Systematic errors of 3% are included.

Table C.3: Parameters obtained by fitting to the 16 CCPs of NGC 5548 and IC4329A*.

	NGC 5548			IC4329A		
Range (keV)	Slopes	Offsets$\times 10^2$	χ^2/d.o.f.	Slopes	Offsets$\times 10^2$	χ^2/d.o.f.
3–3.5	0.37 ± 0.01	2.19 ± 0.13	10.0/20	0.36 ± 0.01	1.82 ± 0.90	2.0/12
3.5–4	0.32 ± 0.01	4.44 ± 0.14	13.8/20	0.32 ± 0.01	0.40 ± 1.08	3.9/12
4–4.5	0.28 ± 0.01	3.01 ± 0.15	20.3/20	0.25 ± 0.01	2.86 ± 1.34	7.8/12
4.5–5	0.24 ± 0.01	3.88 ± 0.13	20.0/20	0.21 ± 0.01	4.16 ± 1.01	5.8/12
5–5.5	0.20 ± 0.01	5.12 ± 0.12	20.4/20	0.17 ± 0.01	3.91 ± 1.08	8.9/12
5.5–6	0.17 ± 0.01	3.96 ± 0.12	24.5/20	0.14 ± 0.01	5.06 ± 1.22	14.5/12
6–6.25	0.07 ± 0.01	0.54 ± 0.07	20.4/20	0.06 ± 0.01	3.02 ± 0.59	11.3/12
6.25–6.5	0.06 ± 0.01	6.53 ± 0.83	28.0/20	0.06 ± 0.01	3.01 ± 0.58	11.7/12
6.5–6.75	0.05 ± 0.01	0.27 ± 0.05	15.6/20	0.05 ± 0.01	2.50 ± 0.50	12.0/12
6.75–7	0.05 ± 0.01	0.40 ± 0.05	15.2/20	0.04 ± 0.01	1.91 ± 0.36	7.6/12
7–7.5	0.08 ± 0.01	0.32 ± 0.08	28.8/20	0.07 ± 0.01	2.42 ± 0.58	10.9/12
7.5–8	0.06 ± 0.01	0.26 ± 0.07	30.0/20	0.05 ± 0.01	1.86 ± 0.60	19.2/12
8–10	0.11 ± 0.01	0.46 ± 0.12	40.3/20	0.09 ± 0.01	3.90 ± 0.91	15.9/12
15–20	0.07 ± 0.01	2.41 ± 0.32	32.4/20	0.06 ± 0.01	6.03 ± 1.42	21.8/12
20–30	0.04 ± 0.01	1.97 ± 0.29	33.2/20	0.04 ± 0.01	6.34 ± 1.23	21.6/12
30–45	0.00 ± 0.01	0.91 ± 0.15	19.4/20	0.01 ± 0.00	2.45 ± 0.66	20.1/12

* Systematic errors of 3% are included.

C.2 Triplet Spectral Analysis in Faint Occasions

In §6.4, we analyzed all data set of the selected AGNs in the triplet spectral analysis, but showed only the result of the brightest occasion in each AGN, except for Mrk 841 of which the brightest one has the shortest exposure among all the observations. Thus, in the present section, we show results of the other observations, which are not included in §6.4, in each AGN. Figure B.6, B.7, B.8, B.9, and B.10 show fainter observations of NGC 4051, MCG–6-30-15, Mrk 841, NGC 5548, and IC4329A, respectively. Almost all of the triplet fits were successful.

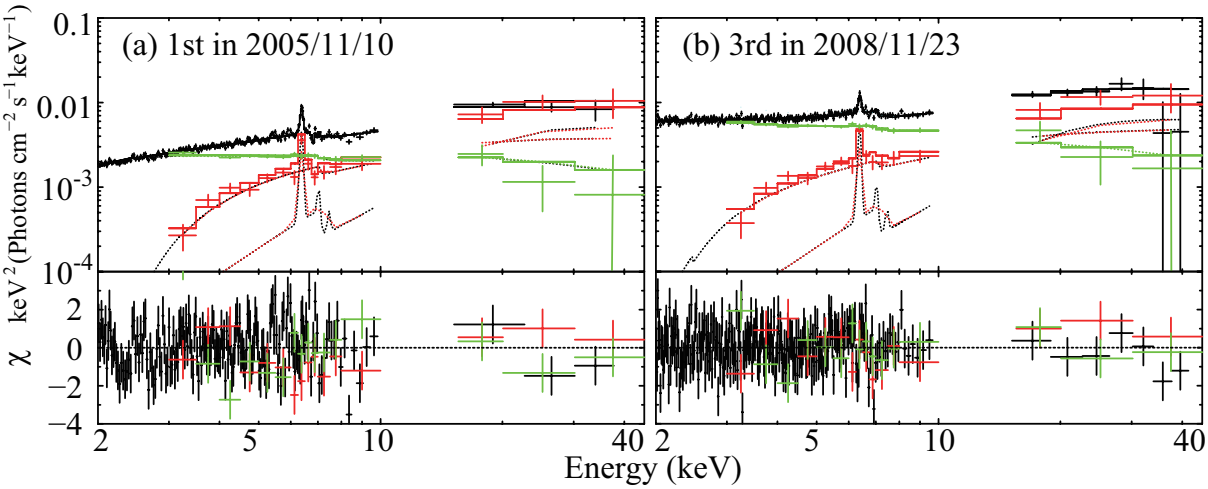

Figure C.6: The same as Fig. 6.21 (a), but of the other observations of NGC 4051.

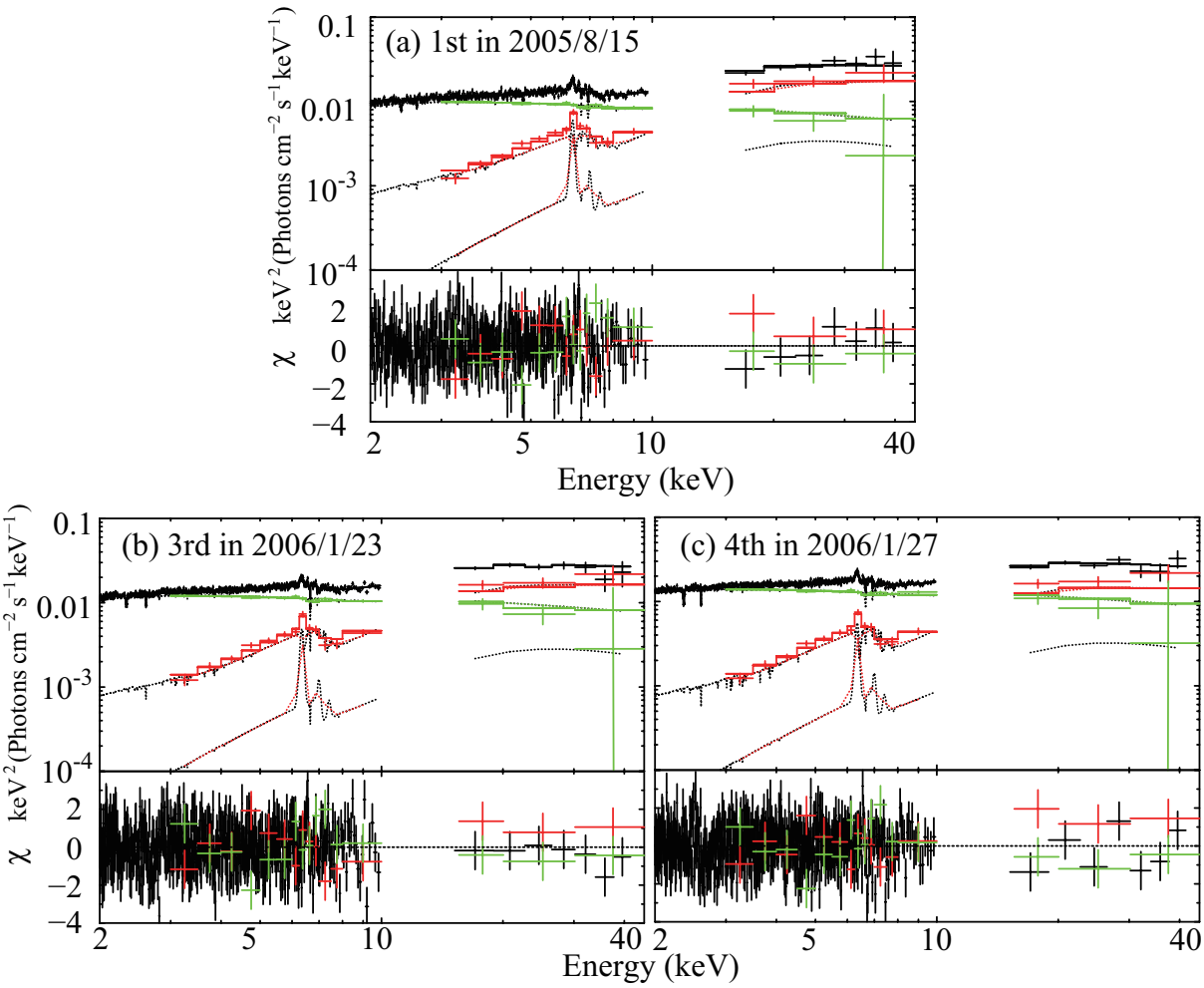

Figure C.7: The same as Fig. Fig. 6.22, but of the other observations of MCG–6-30-15.

Table C.4: The obtained parameters in the triplet fitting of MCG–6-30-15 in §6.4.2[†].

		2005/8/15	2006/1/23	2006/1/27
Absorption to all				
`Phabs`	$N_{\rm H}^{*\dagger}$	$0.74^{+0.08}_{-0.13}$	$0.72^{+0.05}_{-0.10}$	0.65
`Ioabs`	$N_{\rm H0}\dagger$	$11.1^{+22.5}_{-5.1}$	$0.9^{+2.5}_{-0.5}$	0.9
	logξ	$4.4^{+0.5}_{-0.1}$	$3.5^{+0.4}_{-0.1}$	3.6
	Cvr frac.	> 0.96	> 0.97	> 0.97
	z		0.0023 (fix)	
Broad-Band Primary component*				
`PL`	Γ_0	2.20 ± 0.04	2.18^{+}_{-}	2.19
	$E_{\rm cut}$ (keV)		200 (fix)	
	$N_{\rm PL}^{\ddagger}$	1.39 ± 0.09	1.67^{+}_{-}	1.92
Reflection component				
`ReflFe`	$\Gamma_{\rm ref}$		$= \Gamma_0$	
	z		0.0078 (fix)	
	A ($Z_\odot$)		1 (fix)	
	$A_{\rm Fe}$ ($Z_{\rm Fe,\odot}$)		1 (fix)	
	$f_{\rm ref}$	0.8 ± 0.1	$0.5\pm$	0.5
	i (degree)		60 (fix)	
	$N_{\rm ref}$		$= N_{\rm PL}$	
Hard Primary component*				
`Ioabs'`	$N_{\rm H0}\dagger$	$103.6^{+10.2}_{-15.4}$	92.0^{+}_{-}	90.2
	logξ	$2.4^{+0.3}_{-0.2}$	2.3^{+}_{-}	2.4
	Cvr frac.	$0.80^{+0.07}_{-0.06}$	$0.86\pm$	0.87
	z		0.0023 (fix)	
`PL'`	Γ_1	$1.57^{+0.24}_{-0.26}$	$1.70^{+0.10}_{-0.11}$	1.70
	$E_{\rm cut}$ (keV)		200 (fix)	
	$N_{\rm PL}^{\ddagger}$	$0.39^{+0.46}_{-0.21}$	0.60 ± 0.03	0.55
χ^2/d.o.f.		484.6/396	640.3/544	566.2/570

* Identified in §7.1 and 7.2.

† Same as Table 6.11.

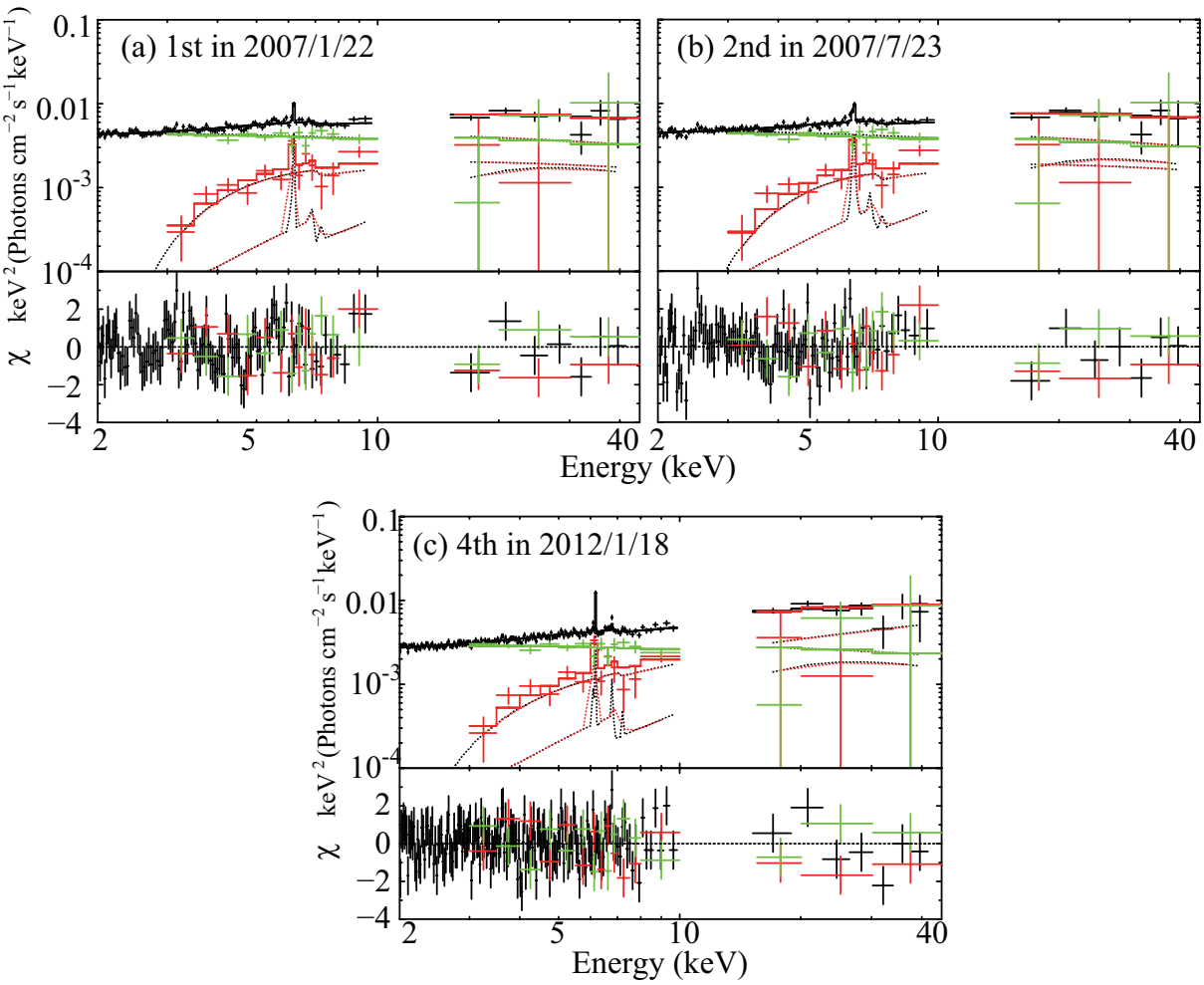

Figure C.8: The same as Fig. 6.21 (c), but of the other observations of Mrk 841.

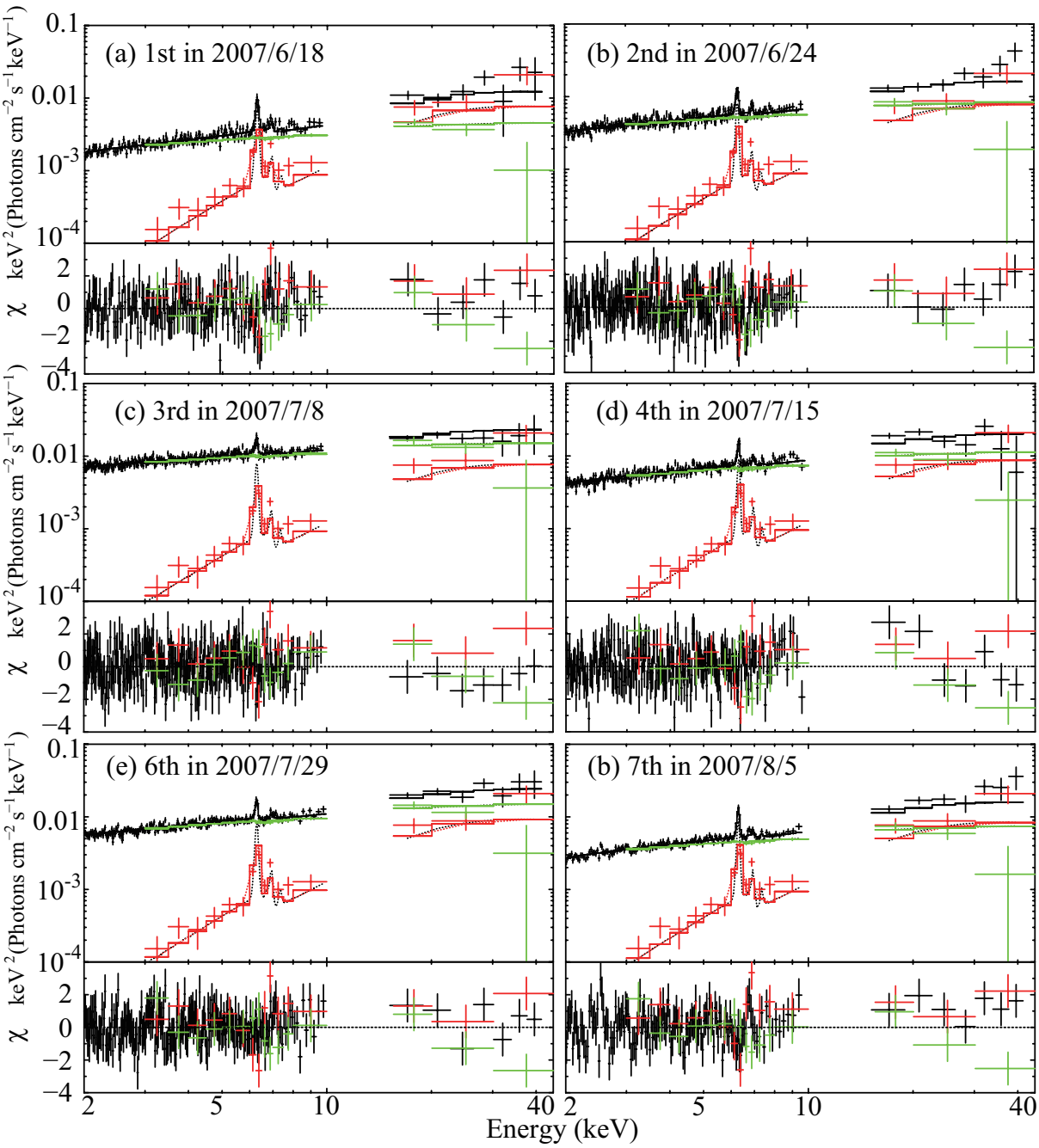

Figure C.9: The same as Fig. 6.21 (d), but of the other observations of NGC 5548.

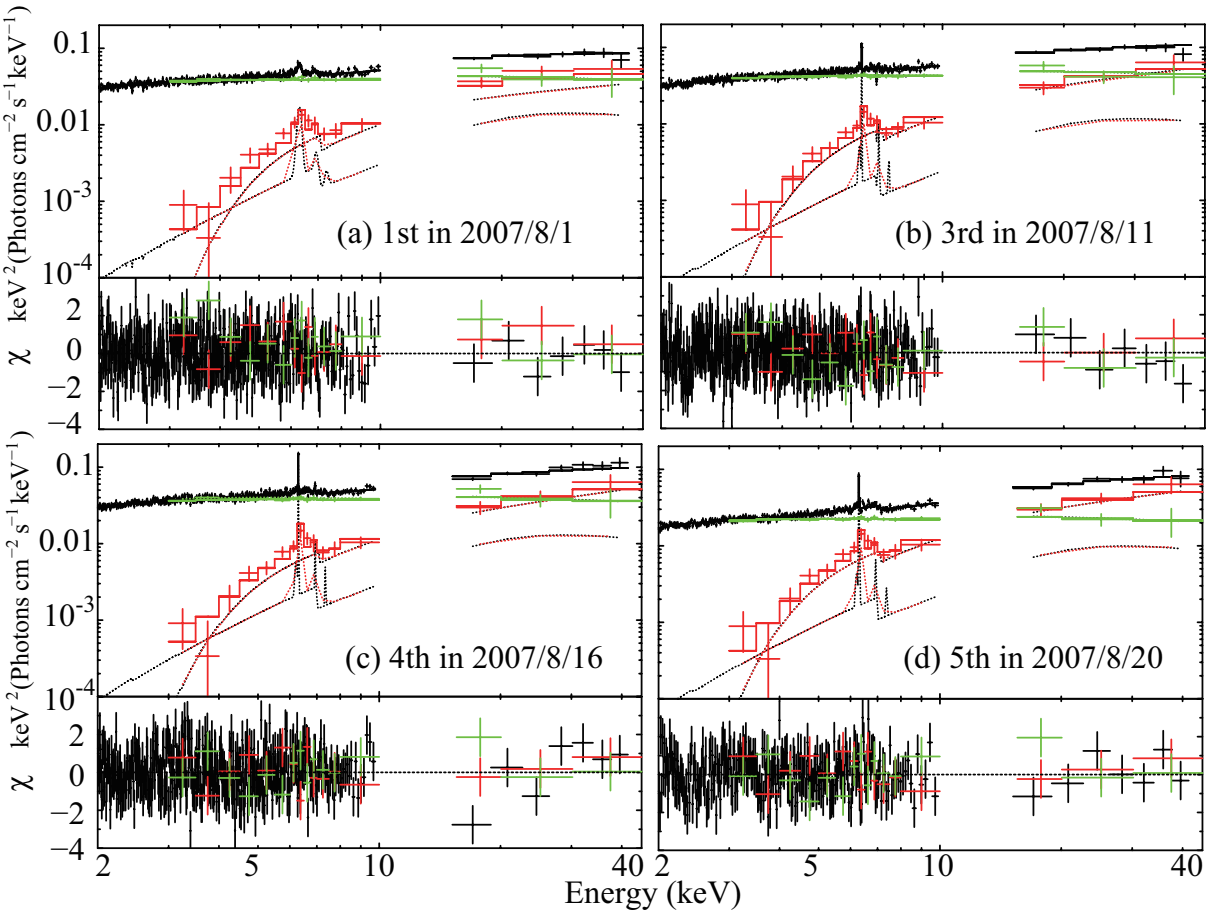

Figure C.10: The same as Fig. 6.21 (e), but of the other observations of IC4329A.

Bibliography

[1] Abramowicz, M. A., Chen, X., Kato, S., Lasota, J.-P., & Regev, O. 1995, ApJL, 438, L37

[2] Akizuki, C., & Fukue, J. 2006, PASJ, 58, 469

[3] Andrade-Velázquez, M., Krongold, Y., Elvis, M., et al. 2010, ApJ, 711, 888

[4] Arnaud, K. A., Branduardi-Raymont, G., Culhane, J. L., et al. 1985, MNRAS, 217, 105

[5] Awaki, H., Koyama, K., Kunieda, H., & Tawara, Y. 1990, Nature, 346, 544

[6] Awaki, H., Koyama, K., Inoue, H., & Halpern, J. P. 1991, PASJ, 43, 195

[7] Beckmann, V., Soldi, S., Ricci, C., et al. 2009, A&A, 505, 417

[8] Boldt, E., & Leiter, D. 1987, ApJ, 322, L1

[9] Breedt, E. L., 2009, the Doctoral thesis, the University of Southamtpon

[10] Cerruti, M., Ponti, G., Boisson, C., et al. 2011, A&A, 535, A113

[11] Chiang, C., Reis, R. C., Fabian, A. C., Grupe, D., Tsuruta, S. 2012, MNRAS, 425, 1299

[12] Di Matteo, T. 1998, MNRAS, 299, L15

[13] Dove, J. B., Wilms, J., Maisack, M., & Begelman, M. C. 1997, ApJ, 487, 759

[14] Ebisawa, 2006, lecture note in the University of Tokyo

[15] Elvis, M., Wilkes, B. J., McDowell, J. C., et al. 1994, ApJS, 95, 1

[16] Fabian, A. C., Iwasawa, K., Reynolds, C. S., & Young, A. J. 2000, PASP, 112, 1145

[17] Fabian, A. C., & Miniutti, G. 2005, arXiv:astro-ph/0507409

[18] Field, G. B., Arp, H., & Bahcall, 1974, JRASC, 68, 276F

[19] Ford, H. C., Harms, R. J., Tsvetanov, Z. I., et al. 1994, ApJL, 435, L27

[20] Francis, P. J., Hewett, P. C., Foltz, C. B., et al. 1991, ApJ, 373, 465

[21] Fukazawa, Y., Botoya-Nonesa, J. G., Pu, J., Ohto, A., Kawano, N. 2006, ApJ, 636, 698

[22] Fukazawa, Y., Mizuno, T., Watanabe, S., et al. 2009, PASJ, 61, 17

[23] Fukue, 2007, textbook, 「Kagayaku burakku horu koucyaku emban (in Japanese)」, Pureadesu syuppan (in Japanese)

[24] Gebhardt, K., Bender, R., Bower, G., et al. 2000, ApJL, 539, L13

[25] George, I. M., & Fabian, A. C. 1991, MNRAS, 249, 352

[26] George, I. M., Mushotzky, R., Turner, T. J., et al. 1998, ApJ, 509, 146

[27] George, I. M., Turner, T. J., Netzer, H., et al. 2002, ApJ, 571, 265

[28] Gofford, J., Reeves, J. N., Turner, T. J., et al. 2011, MNRAS, 414, 3307

[29] Gruber, D. E., Matteson, J. L., Peterson, L. E., & Jung, G. V. 1999, ApJ, 520, 124

[30] Haardt, F., & Maraschi, L. 1991, ApJL, 380, L51

[31] Haardt, F., & Maraschi, L. 1993, ApJ, 413, 507

[32] Haardt, F., Maraschi, L., & Ghisellini, G. 1994, ApJL, 432, L95

[33] Haba, Y., Liebmann, A. C., Fukumura, K., Kunieda, H., & Tsuruta, S. 2008, PASJ, 60, 1257

[34] Harms, R. J., Ford, H. C., Tsvetanov, Z. I., et al. 1994, ApJL, 435, L35

[35] Heckman, T. M., 1980, A&A, 87, 152H

[36] Ho, L., Filippenko A. V., & Sargent, W. L. W. 1994, in Multi-Wavelength Continuum Emission of AGN, ed. T. J.-L. Courvoisier and A. Blecha, (Klurwer Academic Publishers: Dordrecht) p. 275

[37] Ishisaki, Y., Makishima, K., Iyomoto, N., et al. 1996, PASJ, 48, 237

[38] Ishisaki, Y., Maeda, Y., Fujimoto, R., et al. 2007, PASJ, 59, 113

[39] Iyomoto, N., Makishima, K., Matsushita, K., et al. 1998, ApJ, 503, 168

[40] Kaastra, J. S., de Vries, C. P., Steenbrugge, K. C., et al. 2011, A&A, 534, A37

[41] Kaspi, S., Netzer, H., Chelouche, D., et al. 2004, ApJ, 611, 68

[42] Kelley, R. L., Mitsuda, K., Allen, C. A., et al. 2007, PASJ, 59, 77

[43] Khachikian, E. Y., & Weedman, D. W. 1974, ApJ, 192, 581

[44] King, A. L., Miller, J. M., & Raymond, J. 2012, ApJ, 746, 2

[45] Kokubun, M., Makishima, K., Takahashi, T., et al. 2007, PASJ, 59, 53

[46] Kormendy, J., 1988, ApJ, 325, 128K

[47] Koyama, K., Inoue, H., Tanaka, Y., et al. 1989, PASJ, 41, 731

[48] Koyama, K., Awaki, H., Iwasawa, K., & Ward, M. J. 1992, ApJL, 399, L129

[49] Koyama, K., Maeda, Y., Sonobe, T., et al. 1996, PASJ, 48, 249

[50] Koyama, K., Tsunemi, H., Dotani, T., et al. 2007, PASJ, 59, 23

[51] Larsson, J., Fabian, A. C., Ballantyne, D. R., & Miniutti, G. 2008, MNRAS, 388, 1037

[52] Lohfink, A. M., Reynolds, C. S., Miller, J. M., et al. 2012, ApJ, 758, 67

[53] Longinotti, A. L., Costantini, E., Petrucci, P. O., et al. 2010, A&A, 510, A92

[54] Lubiński, P., Zdziarski, A. A., Walter, R., et al. 2010, MNRAS, 408, 1851

[55] Machida, M., Hayashi, M. R., & Matsumoto, R. 2000, ApJL, 532, L67

[56] Magdziarz, P., & Zdziarski, A. A. 1995, MNRAS, 273, 837

[57] Magorrian, J., Tremaine, S., Richstone, D., et al. 1998, AJ, 115, 2285

[58] Makishima, K., Fujimoto, R., Ishisaki, Y., et al. 1994, PASJ, 46, L77

[59] Makishima, K., Takahashi, H., Yamada, S., et al. 2008, PASJ, 60, 585

[60] Manmoto, T., Mineshige, S., & Kusunose, M. 1997, ApJ, 489, 791

[61] Markowitz, A., Reeves, J. N., Serlemitsos, P., et al. 2006, Astronomische Nachrichten, 327, 1087

[62] Matsumoto, C., Inoue, H., Fabian, A. C., & Iwasawa, K. 2003, PASJ, 55, 615

[63] Merritt, D., & Ferrarese, L. 2001, MNRAS, 320, L30

[64] Miller, K. A., & Stone, J. M. 2000, ApJ, 534, 398

[65] Miller, L., Turner, T. J., & Reeves, J. N. 2008, A&A, 483, 437

[66] Miniutti, G., & Fabian, A. C. 2004, MNRAS, 349, 1435

[67] Miniutti, G., Fabian, A. C., Anabuki, N., et al. 2007, PASJ, 59, 315

[68] Mitsuda, K., Inoue, H., Koyama, K., et al. 1984, PASJ, 36, 741

[69] Mitsuda, K., Bautz, M., Inoue, H., et al. 2007, PASJ, 59, 1

[70] Miyakawa, T., Ebisawa, K., & Inoue, H. 2012, PASJ, 64, 140

[71] Miyoshi, M., Moran, J., Herrnstein, J., et al. 1995, Nature, 373, 127

[72] Morrison, R., & McCammon, D. 1983, ApJ, 270, 119

[73] Nandra, K., O'Neill, P. M., George, I. M., & Reeves, J. N. 2007, MNRAS, 382, 194

[74] Narayan, R., & Yi, I. 1994, ApJL, 428, L13

[75] Nobukawa, M., Koyama, K., Tsuru, T. G., Ryu, S. G., & Tatischeff, V. 2010, PASJ, 62, 423

[76] Noda, H., Makishima, K., Uehara, Y., Yamada, S., & Nakazawa, K. 2011a, PASJ, 63, 449

[77] Noda, H., Makishima, K., Yamada, S., et al. 2011b, PASJ, 63, 925

[78] Noda, H., Makishima, K., Nakazawa, K., et al. 2013a, PASJ, 65, 4

[79] Noda, H., Makishima, K., Nakazawa, K., Yamada, S., 2013b, ApJ, 771, 100

[80] Osterbrock, D. E. 1981, ApJ, 249, 462

[81] O'Sullivan, E., Duncan, A. F., & Ponman, T. J. 2001, MNRAS, 328, 461

[82] Patrick, A. R., Reeves, J. N., Lobban, A. P., Porquet, D., & Markowitz, A. G. 2011, MNRAS, 416, 2725

[83] Peterson, B. M. 1997, textbook "An Introduction to Active Galactic Nuclei", Cambridge, New York Cambridge University Press, Physical description xvi, 238 p. ISBN 0521473489

[84] Peterson, B. M., Ferrarese, L., Gilbert, K. M., et al. 2004, ApJ, 613, 682

[85] Reynolds, C. S., & Nowak, M. A. 2003, PhR, 377, 389

[86] Rees, M. J. 1978, The Observatory, 98, 210

[87] Reeves, J., Done, C., Pounds, K., et al. 2008, MNRAS, 385, L108

[88] Rivers, E., Markowitz, A., & Rothschild, R. 2011, ApJ, 732, 36

[89] Rodes-Roca, J. J., Page, K. L., Torrejón, J. M., Osborne, J. P., & Bernabéu, G. 2011, A&A, 526, A64

[90] Ross, R. R., & Fabian, A. C. 2005, MNRAS, 358, 211

[91] Sambruna, R. M., Tombesi, F., Reeves, J. N., et al. 2011, ApJ, 734, 105

[92] Salpeter, E. E. 1964, ApJ, 140, 796

[93] Schmidt, M., & Green, R. F. 1983, ApJ, 269, 352

[94] Schmoll, S., Miller, J. M., Volonteri, M., et al. 2009, ApJ, 703, 2171

[95] Schödel, R., Ott, T., Genzel, R., et al. 2002, Nature, 419, 694

[96] Schödel, R., Ott, T., Genzel, R., et al. 2003, ApJ, 596, 1015

[97] Serlemitsos, P. J., & Soong, Y. 1996, Ap&SS, 239, 177

[98] Serlemitsos, P. J., Soong, Y., Chan, K.-W., et al. 2007, PASJ, 59, 9

[99] Shakura, N. I., & Sunyaev, R. A. 1973, A&A, 24, 337

[100] Smith, R. K., Brickhouse, N. S., Liedahl, D. A., & Raymond, J. C. 2001, ApJL, 556, L91

[101] Stark, A. A., Elmegreen, B. G., & Chance, D. 1987, ApJ, 322, 64

[102] Stern, B. E., Poutanen, J., Svensson, R., Sikora, M., & Begelman, M. C. 1995, ApJL, 449, L13

[103] Shapley, A., Fabbiano, G., Eskridge, P. B. 2001, ApJS, 137, 139

[104] Steenbrugge, K. C., Kaastra, J. S., Sako, M., et al. 2005, A&A, 432, 453

[105] Suganuma, M., Yoshii, Y., Kobayashi, Y., et al. 2006, ApJ, 639, 46

[106] Sunyaev, R. A., & Titarchuk, L. G. 1980, A&A, 86, 121

[107] The *Suzaku* Technical Description, URL: http://www.astro.isas.ac.jp/suzaku/doc/suzaku_td/node6.html

[108] Takahashi, T., Abe, K., Endo, M., et al. 2007, PASJ, 59, 35

[109] Tanaka, Y., Nandra, K., Fabian, A. C., et al. 1995, Nature, 375, 659

[110] Terashima, Y., Gallo, L. C., Inoue, H., et al. 2009, PASJ, 61, 299

[111] Titarchuk, L. 1994, ApJ, 434, 570

[112] Urry, C. M., & Padovani, P. 1995, PASP, 107, 803

[113] Uttley, P. 2006, Astronomical Society of the Pacific Conference Series, 360, 101

[114] Turner, T. J., & Pounds, K. A. 1989, MNRAS, 240, 833

[115] Turner, T. J., Reeves, J. N., Kraemer, S. B., & Miller, L. 2008, A&A, 483, 161

[116] Tuner, T. J., Miller, L., Kraemer, S. B., Reeves, J. N., Pounds, K. A. 2009, ApJ, 698, 99

[117] Turner, T. J., Miller, L., Kraemer, S. B., & Reeves, J. N. 2011, ApJ, 733, 48

[118] Vasudevan, R. V., & Fabian, A. C. 2009, MNRAS, 392, 1124

[119] Vikhlinin, A., et al. 1999, ApJ, 520, 1

[120] Weaver, K. A., Nousek, J., Yaqoob, T., Hayashida, K., & Murakami, S. 1995, ApJ, 451, 147

[121] Yamada, S., Itoh, T., Makishima, K., & Nakazawa, K. 2009, PASJ, 61, 309

[122] Yamada, S., Makishima, K., Done, C., Torii, S., Noda, H., Sakurai, S., 2013, PASJ, in press

[123] Young, P. J., Westphal, J. A., Kristian, J., Wilson, C. P., & Landauer, F. P. 1978, ApJ, 221, 721

[124] Zel'dovich, Y. B., & Novikov, I. D. 1964, Soviet Physics Doklady, 9, 246

[125] Zhou, X. L., Zhao, Y. H., Soria, R. 2011, MNRAS, 413, 61

Acknowledgement

First of all, I am deeply grateful to Prof. K. Makishima for his considerable and continuous supports on my studies of Active Galactic Nuclei (AGNs) with *Suzaku* and thermal designs of instruments onboard *ASTRO-H*. In any situations, he taught me how to think physically, and showed an attitude toward researches, with an impressive expression, "Discard preconceived notions, and listen to what data say!". This word greatly helped me obtaining the new interesting results in the complicated situations which confront X-ray researches of the AGN central engine, and making out the present thesis. In my life of research, it has become my cherished motto, with which I would like to continue my AGN studies.

I also would like to express many thanks to Dr. S. Yamada for his respectable helps. Many talks and discussions with him brought up my interest and knowledge in black hole studies, and made me come up with new ideas, which are directly connected to the results in the present thesis. Not only in the researches, but also at various situations including my private life, he kindly gave a helping hand to me, and supported me to solve problems.

I wish to thank Lecturer K. Nakazawa, and Dr. H. Uchiyama, who gave me many valuable advices and big helps, especially in working on the thermal designs of the *ASTRO-H* instruments. I also thank Dr. L. Gu for giving me a lot of cleaver opinions and having many discussions with me about my results. My wonderful graduate school life is owing to my colleagues, Mr. S. Torii, Mr. K. Nakajima, Mr. H. Nishioka, Mr. S. Sakurai, Mr. M. Sasano, Mr. T. Nakano, and the other members of the Makishima-Nakazawa laboratory. I shared good times and bad times with them, encouraging each other.

Finally, I give a special thanks to my father, mother, brothers and Ayaka Morita, who allowed and committedly supported me anytime to concentrate on my studies. If it were not for their significant helps, I could not have continued my research, and would have given up studies of astrophysics. I owe what I am to them.